UNIVERSITÀ DEGLI STUDI DI CATANIA

DIPARTIMENTO DI SCIENZE BIOLOGICHE, GEOLOGICHE ED AMBIENTALI

SEZIONE SCIENZE DELLA TERRA

Dottorato di ricerca in Scienze della Terra

XXVI ciclo

Investigation on Mt. Etna dynamics by seismic and acoustic signals (August 2007 – December 2010)

Dott.ssa Laura Spina

Coordinatore: Prof. Carmelo Monaco

Tutor:

Prof. Stefano Gresta

Co-tutors:

Dott. Andrea Cannata

Dott. Eugenio Privitera

DICEMBRE 2013

PREFACE

Volcanoes are the most intriguing challenge among Earth Sciences.

Indeed, volcanic activity is the most dreadful and fascinating fingerprint of Earth inner activity. Nevertheless, the occurrence of eruptions is not exclusively a matter of interest of the scientific community, but it rather has huge consequences on the common life of people. Populations leaving nearby, indeed, are exposed to several kinds of hazards. However, the influence of volcanic activity may be not exclusively restricted at local scale, as shown in recent years by the effects on the aviation and air traffic played by entrained ash in the stratosphere. Therefore, it is fundamental to investigate the mechanisms and achieve more knowledge on the moody behaviors of volcanoes. With this aim, the analysis of infrasound signals, produced by volcanoes, has acquired growing importance in last decades.

In this thesis infrasound signals from Mt. Etna, continuously recorded from August 2007 to December 2010, are analyzed. Our goal is to investigate the shallow plumbing system and the relations among eruptive vents by acoustic and seismic data. Furthermore, we aim also to define the source mechanism of infrasound signals of Mt. Etna. In addition, acoustic signals from a temporary experiment carried out at Mt. Yasur volcano are analyzed in order to compare the dynamics of Mt. Etna with other basaltic volcanoes.

The thesis is structured in four chapters. In **Chapter 1** a brief introduction, regarding volcano monitoring and the main seismo-acoustic signals produced by volcanoes, is given first (**sections 1.1** and **1.2**). Successively, the analytical methods applied in this study are described (**section 1.3**). **Chapter 2**, which comprises the main body of the thesis, regards signals recorded at Mt. Etna. Initially a wide background on the regional setting, volcanic activity and acoustic studies, previously performed on the volcano, is given (**section 2.1**). Successively, data from August 2007 to December 2009 are analyzed (**section 2.2**). A dedicated section focuses on signals recorded from the eruptive fissure of the 2008-2009 eruption (**section 2.3**). Finally, the analyses carried out on signals recorded during 2010 are depicted (**section 2.4**). **Chapter 3** contains a description of acoustic signals recorded at Mt. Yasur during a temporary experiment. First, the volcano is contextualized in its geographical and tectonic setting (**section 3.1**), then the characteristics of the experiment and the performed analyses are described (**sections 3.2, 3.3. 3.4, 3.5**). Finally, **Chapter 4** summarizes the conclusions, which are more widely discussed in the previous chapters, in order to give a general overview of the achievements of the work.

Please note that several part of this manuscript has been drawn from published or submitted papers, of which the undersigned is respectively co-author or author.

Contents

Chapter 1: Introduction

1.1 Seismic and acoustic signals: source models and relevance for research and monitoring purpose

1.1.1 Volcanic hazard and monitoring systems

Volcanoes are undoubtedly one of the major hazards on the Earth, representing a multifaceted challenge for risk management and life safeguard during volcanic crisis.

Indeed, most of the volcanic areas are characterized by favourable weather condition for agricultural activities, and provided of fertile lands, thanks to the nutrients deriving from the rapid weathering of volcanic ejecta [Dahlgren et al., 1989]. It was estimated that 10 % of the global population lives near active or potentially active volcanoes [Peterson and Tilling, 2000]. The hazards, they might be exposed to, are several. Amongst others, the most striking reports come from sites covered by falling pyroclastic flows or surges or lahars. Well known examples are the eruption at Mt. Pelée, Martinique, in 1902, with 29000 victims, or the 1902 eruption of St. Maria, Guatemala, killing 6000 people [Nakada, 2000]. Luckily, in well monitored volcanic areas, the knowledge of volcanoes mechanisms and behaviour, together with a dense monitoring network, has strongly limited the loss of life. A famous example is given by Mt. Monserrat eruption, 1999-2004, where most of the people have been preventively evacuated from dangerous areas before the major paroxysms, in 1995 [Kokelaar, 2002; see **Fig.1.1**]. Nevertheless the cost of this exodus in terms of social and economic aspect of the island was terrible, as in early 1998 roughly 70 % of the population has left the island [Kokelaar, 2002].

Moreover, volcanic eruptions may also trigger other catastrophic phenomena, such as earthquakes and tsunami, and release abundant quantity of ash in atmosphere. Recently -in response to the growing amount of flight traffic- the hazard posed to aviation from the presence of ash in atmosphere has been object of several studies. Volcanic ash could travel along considerable distances and are totally see-through to the radar of the aircraft. The injection of ash particles into the engine is known to have caused several times the loose of thrust of the hit engine [Miller and Casadeval, 2000].

Quantitative forecasting of volcanic eruptions is far from being a real solution for such issues. Nevertheless, researches on the behaviour of each specific volcano, joined with the development

of a surveillance system nearby, are proved to be -so far- an effective way to mitigate risk. During its ascent toward the surface, the out-coming magma may produce different kinds of perturbations of the surrounding medium. The detection of such perturbations reveals the renewal of volcanic activity. Among these, the most important are seismicity, ground deformation and release of magmatic gases [Sparks, 2003].

Figure 1.1: Image from the destroyed city of Plymouth, once capital of Montserrat. Buildings that are holding up where located at the margin of the impacted area. The main part of the city was destroyed and completely buried by a pyroclastic flow.

Seismic signals are temporal series, recording the shaking of the ground at the surface due to seismic waves travelling from the source. There is a variety of eruptive processes, related to magma movement at depth, or alternatively occurring during the emission at the surface of the solid, liquid, or gaseous products, able to generate different seismic signals [Zobin, 2012]. Volcano-tectonic seismicity often occurs before the majority of eruptions. Once the background activity for a given volcano is well known, the rate of occurrence, location and characteristic of volcano seismic signals give indications about the dynamics of the ongoing eruption. For instance, it is possible to gain information about the physic condition of magmatic fluid in the system, or regarding their position into the volcano edifice [e.g., Kumagai and Chouet, 1999; Morrissey and Chouet, 2001; Almendros et al., 2002; Battaglia and Aki, 2003], or identify active faulting processes as well as the spatial position of the fault plane [Azzaro, 1999]. Recently, an increasing number of broadband seismic network have been deployed, allowing for an improvement of data quality.

Furthermore, in the last decades, a new branch of seismology has developed, thanks to the many observations of the acoustic field in volcanic environment [e.g., Firstov and Kravchenko, 1996; Ripepe et al., 1996; Johnson and Lees, 2000]. Indeed, the recordings of volcanic acoustic emission, which are mainly in the infrasound range, are proved to be really efficient in terms of source location, and they can also provide several information on the explosive and degassing source dynamics [e.g., Ripepe et al., 2007].

Geodetic monitoring is undoubtedly another milestone of the surveillance system of active volcanoes. Surface displacements occur in response to the movement or increase of volume of magmatic bodies at depth. Consequently, the pattern and rate of the displacement reveal fundamental information such as depth and rate of magma accumulation. Furthermore, while rapid changes are likely to be linked to an individual eruption, long term variations of the displacement are linked to processes taking place on longer scale such as subsidence [Dvorak and Dzurisin, 1997]. The geodetic network may comprise traditional EDM (electronic distance measurement) theodolites, GPS (Global position system) stations, as well as extensimeters and tiltmeters. Recently, interferometer analyses have been done on images periodically taken by satellites, the SAR (Synthetic Aperture Radar) techniques.

The geochemistry approach is based on the evidence that any change of the volume or position of the magma, is reflected by variation in the properties of the volatiles discharged during magma degassing. Thus, monitoring should focus on fumaroles, diffused soil degassing, degassing associated with geothermal waters and plumes [Inguaggiato et al., 2011]. However, direct sampling of the gas at the source is commonly not safe for hot volcanic plumes, especially during the ongoing activity. In order to solve this problem, remote sensing techniques have been developed, as the COSPEX (Correlation Spectrometer) and TOMS (Total Ozone Mapping Spectrometer) for Sulfure Dioxide emissions, and FTIR (Fourier Trasform Infrared) to obtain the ratio between the many other gas species [Stix and Gaonach'h, 2000].

Finally, surveillance systems can avail themselves of gravimetric and magnetic observations, which has been found to be capable of detecting precursory changes of the incoming eruption, especially if they are provided on a wide area and combined together [McNutt et al., 2000].

In the following pages, we provide a brief focus on seismo-acoustic volcanic signals, on their source mechanisms and the analytic methods commonly used to analyze them.

1.2 Characterization of the signals

Volcano seismology deals with different kinds of seismic and acoustic signals produced by volcanoes. Despite the proliferation of terms to define them, there is a general consensus on a frequency based classification. In the following paragraphs, the characteristics, as well as the main source models proposed for the different seismic events and for infrasound, are described.

1.2.1 Volcano Tectonic Earthquakes

Volcano Tectonic (VT) Earthquakes are characterized by a frequency content above 5 Hz and up to 15-20 Hz, and clear arrivals of both P and S waves [Zobin, 2012, see **Fig. 1.2a**]. Higher frequencies may be generated at the source, but they are not recorded because of instrumental limitation or local attenuation [McNutt, 2005]. They derive by shear failure or slip on faults, thus they can be used to determine stress orientations using focal mechanisms and stress tensor inversion [e.g., Moran, 2003; Sanchez and McNutt, 2004; Waite and Smith, 2004]. The main difference between VT and tectonic earthquake consists in their rate of occurrence. Indeed, VTs occur in swarms, with less than 0.5 of difference in magnitude between the largest earthquake and the second one [McNutt, 2005]. The stress that triggers the seismic release is likely to be linked to different phenomena, such as regional tectonic forces, gravitational loading, pore pressure effects or hydro fracturing, thermal and finally volumetric forces associated with magma intrusion, withdrawal, cooling [McNutt, 2005].

According to some authors [Wassermann, 2009], a second type of VT-earthquakes occur at very shallow depth (above 1-2 km). The relatively superficial position of the hypocenter determines a large amount of scattering, especially at higher frequencies, thus lowering the dominant frequency content to 1-5 Hz.

Finally, although the source mechanism of VTs is generally double-couple source, several papers, dealing with the inversion of the seismic moment tensor, showed a significant contribution of non double-couple parts [Dahm and Brandsdottir, 1997].

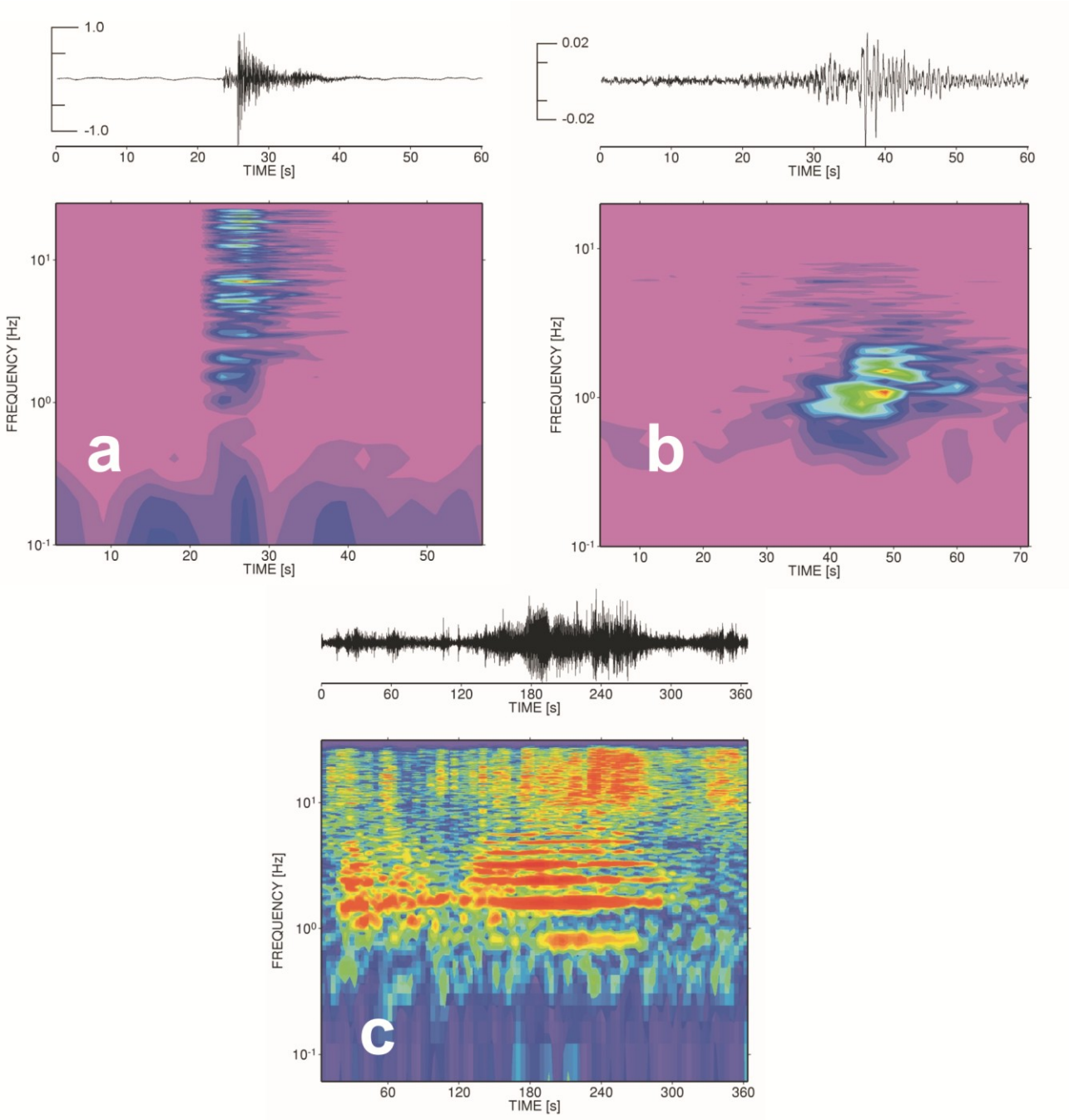

Figure 1.2: Seismic traces and spectrograms of a) VT earthquake, b) LP event from Mt. Merapi, and c) volcanic tremor from Mt. Semeru. Modified from Wasserman [2009].

1.2.2 Long Period Events

Long period (LP) events, also called low frequency (LF) events, are characterized by frequency content comprised between 0.5 and 5 Hz, absence of a clear and distinct S arrival, and often emergent P wave arrival (**Fig. 1.2b**). Commonly, they occur in families, with a high level of steadiness of the waveforms [Zobin, 2012]. Furthermore, they display longer codas than common

seismic signals [McNutt, 2005]. According to Chouet [2003], the simple decaying harmonic oscillations nature of these signals is due to movement of a fluid-filled oscillator in response to time-localized excitation, i.e. a crack resonating because of pressure disturbances active during magma ascent toward the surface. Other authors [Seidl et al., 1981] propose as source model the resonance of the magma body, triggered by transient in the fluid-gas mixture. In felsic volcanoes, LP events were interpreted as seismic energy released from brittle failure of magma at the conduit wall, with the long tail representing energy trapped in the conduit [Neuberg et al., 2006]. More generally, they are likely to be linked to processes involving the movement of fluids at depth, transfer of magma, gas and heat or finally magma-water interaction at depth. Therefore, their occurrence rate suggests an evaluation of magma and gas flux in the conduit [Neuberg, 2000]. However, despite their pervasiveness, their source mechanism is still matter of debate.

Recently, the installation of an increasing number of broadband seismic network, has allowed for the identification of another type of LP events, the so called Deep LP events, occurring beneath 20 km of depth. Even though their frequency content could be due to filtering effect of the travel path through the fluid rich deep crust, some studies linked their occurrence with anomalous content of CO_2 in volcanic area [Hill, 1996; Wassermann, 2009], suggesting possible connections with fluid release and pressure at the depths. They have been recorded at different volcanoes [e.g., Aki and Koyanagi, 1981; Hasegawa and Yamamoto, 1994; Pitt and Hill, 1994; White, 1996; Nakamichi et al., 2003]. For instance, it has been found that 9 volcanoes out of 27 in Alaska produce this kind of signals [Power et al., 2004]. Such widespread diffusion of Deep LP observation suggests that this kind of signals must be focused in the future studies.

1.2.3 Very long period events

Seismic signals with periods in the range 2 - 100 s (frequencies between 0.5 and 0.01 Hz) are defined very long period (VLP) events [Chouet, 2009]. They are characterized by impulsive onset (see **Fig. 1.3c**), and they are usually recognized by low filtering the signal. Like LP signals, families of VLP are commonly observed at several volcanoes as Stromboli [Chouet et al., 2003], Popocatepetl [Arciniega-Ceballos et al., 1999], Erebus [Aster et al., 2008], among others. Some studies [i.e., Kawakatsu et al., 1994] demonstrate that the source area of VLP is particularly small, and consequently they exhibit a departure from the linear behavior. Several different source mechanisms have been proposed. According to Chouet [1999], they are resulting from inertial

forces associated with perturbations in the flow of magma and gases through conduits. At Aso Volcano, they have been interpreted as draining of super-saturated crack at shallow depth [Kawakatsu et al., 1994; McNutt, 2005], whereas at Stromboli they are believed to be caused by upward movement of gas slugs [Neuberg et al., 1994]. Further, an almost continuous signal, where the single pulses were merging into a tremor like signal, was found at Stromboli, and called *long period tremor*. This long lasting signal was interpreted as linked to the interaction of hot magma fluid with an overlying aquifer [Aso Volcano; Kawakatsu et al., 2000]. Finally at Kilauea, VLP have been interpreted as connected to the movement of pulses of magma through sill-crack [Ohminato et al.,1998].

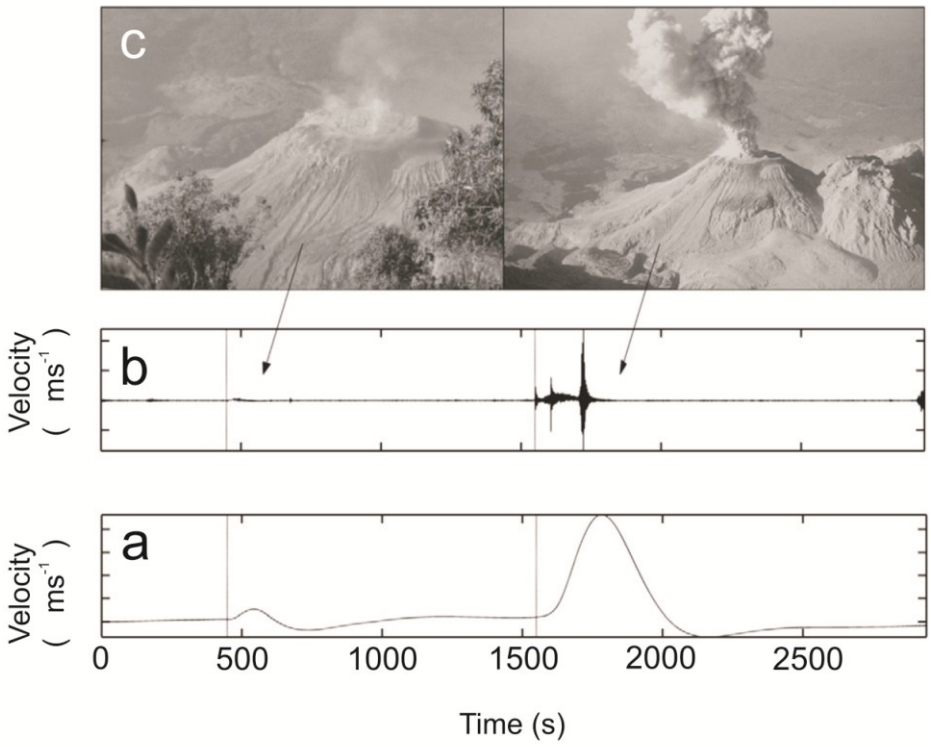

Figure 1.3: a) Band pass filtered (600-30 s) and b) raw signals for VLP events recorded at Santiaguito volcano. Images in c) show the corresponding volcanic activity. Modified from Zobin [2012].

1.2.4 Volcanic tremor

Volcanic tremor is a persistent seismic signal, lasting from several minutes to several days or even months, often preceding or accompanying volcanic eruptions [e.g., Kostantinou and Schlindwein**,** 2002]. Even if the frequency content may be characteristic of the individual volcano, volcanic tremors are generally characterized by similar frequency content to LP signals, that is roughly 0.5-5 Hz. Furthermore, in some cases, it is possible to identify a fundamental frequency and the relative

harmonics; the corresponding signal is called *volcanic harmonic tremor*. In most cases the wavefield is composed of Rayleigh and Love waves, and it is strongly affected by path effects [e.g., Kostantinou and Schlindwein**,** 2002], but some studies proved that a mixed composition of both body and surface waves may be dominant at other volcanoes [i.e., Deception Island, Almendros et al., 1997]. According to Kostantinou and Schlindwein **(**2002), several interpretations of the volcanic tremor source mechanism are possible: for instance, fluid oscillation induced by external causes to the fluid, i.e. like fracturing of the surrounding bedrock and formation of a new feeding branch, or a sudden variation in the fluid supply [St Lawrence and Qamar, 1979; Ferrick et al., 1982]. Aki et al. (1977) proposed that tremor is due to the vibration of a crack chain as the magma ascent to the surface through the network. Chouet [1986, 1988] proposed as a source of tremor the wall vibration of a magma filled crack, due to a pressure disturbance. In hydrothermal area, tremor-like signals are likely to be due to water boiling processes at depth [Kieffer, 1984; Kedar et al., 1996]. Crosson and Bame [1985] found, by realizing a model of a spherical cavity in the hosting rock containing a smaller gas filled cavity, that tremor at Stromboli could be explained as magma resonance in consequence of the expansion of the slug.

It is noteworthy that onset, evolution and conclusion of the summit paroxysmal activity are typically well-correlated with the pattern of the volcanic tremor. However, the relationship between amplitude variations of volcanic tremor and magmatic activity is not univocal. Indeed, in some cases there is a good correlation between the occurrence of the former and the renewal of shallow volcanic activity, as reported for a few volcanoes [e.g. Kilauea, Dvorak and Okamura, 1985; Pavlof, McNutt, 1986; Etna, Cannata et al., 2008]. Alternatively, the variation in amplitude of volcanic tremor may be related to the movement of fluid at great depth and not accompanied by any variation in observable volcanic activity [Aki and Koyanagi, 1981].

1.2.5 Infrasound signals

Acoustic waves are longitudinal waves due to the compression-expansion of the medium in which they propagate, in response to the vibration of the source of sound. For frequencies below 20 Hz, the threshold of hearing of human being, they are called infrasound. Volcanoes radiate acoustic energy mainly in this range of frequencies. Infrasound was first recorded by microbarometers after the violent 1883 eruption of Krakatau [Strachey, 1888], which induced low frequency oscillations that propagated around the Earth several times, as also audible sounds of “heavy

gunfire" as far as 5000 km away [Simkin and Fiske, 1983]. Since then, and especially in the last decades, infrasound has become a widespread method of investigation and monitoring of volcanoes. Infrasonic transients (hereafter: infrasonic events) have been frequently recorded. During paroxysmal activity or during intense degassing, the can merge giving rise to an almost continuous signals named infrasonic tremor [Montalto et al., 2010].

Several processes have been recognized as sources of infrasound.

A group of source models for infrasound events deals with phenomena linked to explosions of strombolian bubbles. For instance, Vergniolle et al. [2004] suggest that infrasound is produced from the oscillation of gas slugs prior to the bursting, when they reach the free magma surface. This model will be used to fit some data in the following pages, thus it is worthy to add some more information about it. According to the authors, bubbles reach the surface with some excess pressures. As a consequence, strong volumetric vibration of the bubble wall, (corresponding to a thin layer of magma), pushed by variation of pressure inside the bubble prior to bursting, occur, producing sound. The bubble shape is approximated by a hemispherical head and a cylindrical tail, as expected in slug-flow [Vergniolle et al., 2004]. The propagation of pressure waves is radial and the waveform of the resulting infrasound signal consists of a first energetic part roughly composed of one cycle (or one cycle and a half), corresponding to the bubble vibration, followed by a second part with weaker oscillations [Vergniolle et al., 2004]. The experimental data may be fitted by synthetic waveforms obtained by the equation [Vergniolle and Brandeis, 1996]:

$$p_{ac} - p_{air} = \left[2\dot{R}^2(t - {}^{r}/_{c}) + R(t - {}^{r}/_{c})\ddot{R}(t - {}^{r}/_{c})\right]\frac{\rho_{air}R(t - \frac{r}{c})}{r} \quad \textbf{(1)}$$

where the first term is excess pressure in air, t is time, r is the distance source-sensor, c is the sound speed in air, R is the bubble radius and ρ_{air} is the air density.

It is worth noting that several parameters are needed to solve this equation: density of magma, thickness of magma above the vibrating bubble, magma viscosity, length of the bubble and initial overpressure [an exhaustive discussion can be found in Vergniolle and Brandeis, 1996]. However, some of them (i.e. viscosity and density of the magma) can be derived from complementary studies. Concerning the thickness of the magma wall, for instance, it is likely to be on the same order of magnitude of the diameter of the ejecta, thus it can be easily inferred [Vergniolle et al., 2004]. Once all the parameters are fixed, we can easily calculate the characteristic features of the bubble (overpressure, length and radius) by equation (**1**).

Another model based on volcanic slugs suggests that very large bubbles are forming at the shallow part of the conduit for coalescence processes. The escape of gas through a tiny hole, that breaks the bubble walls, produces a low monochromatic sound [Vergniolle and Caplan Auerbach, 2004].

Differently, there is a class of models that links infrasound sources with resonance phenomena. Acoustic resonance can be defined as the acoustic response of a contained region to pressure disturbances, a feature of a perturbed sound field interacting with two or more boundaries or fluid discontinuities [Fee et al., 2010a]. Indeed, resonance is due to multiple reflection of pressure disturbances at the boundary of the resonator, and can be defined as a propagation path effect [Garces and McNutt, 1997], which gives us useful information about the geometry and/or the characteristics of the resonator.

Resonance of the shallow portion of the conduit, for instance, have been hypothesized at several volcanoes [i.e., Buckingham and Garces, 1996; Hagerty et al., 2000]. For example, at Kilauea and Villarica were found evidences of a resonant monotonic and long lasting tremor, whose source coincides with skylights above lava tubes [Garces et al., 2003; Matoza et al., 2010a] and central vents [Ripepe et al., 2010].

Such kind of resonance is likely to occur when the ratio between the wavelength and the cavity dimension is comprised between 1/3 to 3 [Fee et al., 2010a; Morse and Ingard, 1968]. For a fluid filled fracture of length *L* and width *W*, longitudinal and lateral sets of resonance modes are expected (respectively 2*L*/*n* and 2*W*/*n*, with *n*=1,2,3) [De Angelis and McNutt, 2007]. Nevertheless, it is common to observe only longitudinal modes, coherently with the cylindrical shape of the very shallow conduit inferred at many volcanoes. Indeed, for wavelength much longer than the radius of the conduit, lateral modes are negligible, and only the longitudinal modes must be taken into account [Garces and McNutt, 1997].

According to fundamental law for pipe resonance [equation (**2);** Hagerty et al., 2000]:

$$L_r = \frac{c}{2f_0} \tag{2}$$

with c equal to the acoustic velocity and f_0 fundamental frequency of resonance, while L_r is the length of the resonator.

However, the type of triggered resonance depends on the boundary conditions. For a resonant pipe with matched boundary condition, thus having both the termination closed or both open, the resulting spectra show integer harmonics of the fundamental. In the opposite case (open-closed termination), odd harmonics of the fundamental will be observed. It is noteworthy that the

condition of closure is due to change of the impedance contrast, i.e. cross sectional variations or drastic discontinuity in the magma properties [Garces and McNutt, 1997; De Angelis and McNutt, 2007]. Furthermore, it must be remarked that the observation of an open vent does not imply acoustically open termination, and vice versa [Garces and McNutt, 1997].

Finally, an end correction must be taken into account when dealing with open vent [Morse and Indegard, 1968]. Indeed, in the near field, the movement backwards and forwards of the air due to the vibration of the surface of the source, adds inertial mass to the vibrating mode, thus affecting the frequency of resonance. For this reason, a term, namely end correction, is introduced to extend the length of an open-ended vibrating column [Rossing, 2007]. For a closed pipe the end correction is zero, while for an open pipe is 0.6*a, with a radius of the pipe [Miklos et al., 2001].

Other possible kinds of resonance have been recognized at active volcanoes [i.e., Goto and Johnson, 2011; Fee et al., 2010a]. When the wavelength is much larger than any dimension of the resonator, harmonic oscillation with only one degree of freedom, i.e. the volume, may occur [Fee et al., 2010]. This kind of resonator is called lumped acoustic element [Kinsler, 1982], and the most common example of it is the Helmholtz resonator. A simple Helmholtz resonator is made up of a cavity connected with the outside space through a narrow neck or through an opening [see **Fig. 1.4**; Alster, 1972]. The resonator reverberates with a single frequency, computed on the basis of the following equation [Kinsler et al., 1982]:

$$f = \frac{c}{2\pi}\sqrt{\frac{S}{Vk'}} \quad \textbf{(3)}$$

Where S is the area of the neck, V is the volume of the cavity and k' is the effective length of the neck, provided of end correction by the equation:

$$k' = l + 1.45A \quad \textbf{(4)}$$

with A and l equal to the radius and length of the neck, respectively.

Indeed, the compressible fluid in the resonator acts like a spring with constant:

$$k_{sp} = \frac{\rho_{air} c^2 S^2}{V} \quad \textbf{(5)}$$

where ρ_{air} is the density of the air. The behavior of the fluid in the neck is correspondent to a lumped acoustic element [Rossing, 2007]. The magnitude of the lumped mass resonator is given by:

$$m = \rho_{air} S k' \quad \textbf{(6)}$$

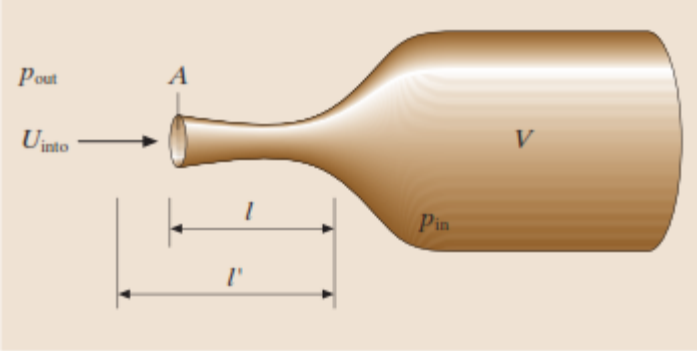

Figure 1.4: Simplified scheme showing an Helmholtz resonator. Modified from Rossing [2007].

At Halema'uma'u Crater (Kilauea Volcano), Fee et al. [2010a] inferred the presence of a double resonance mechanism to justify the presence of two spectral bands in both infrasonic tremor and events, namely: "f1" at 0.3-0.6 Hz, and "f2" at 1-3 Hz. Authors claim that the former spectral band is due to Helmholtz resonance of the gas filled cavity beneath the vent, whereas the latter and higher frequency band is due to standing waves of the same cavity (see **Fig. 1.5**).

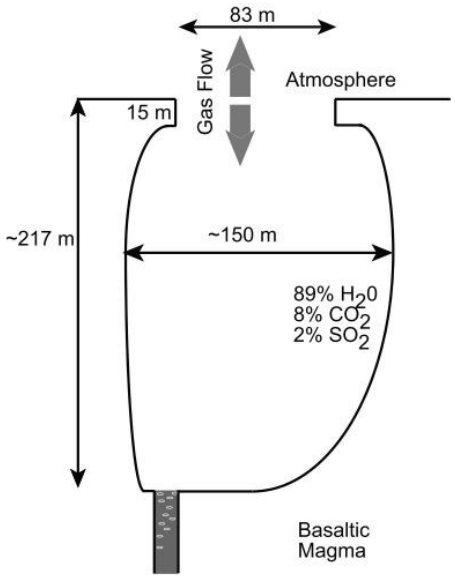

Figure 1.5: Cartoon of Halema'uma'u double resonant cavity [Fee et al., 2010].

Obviously, different dynamics may be active at other volcanoes. For example, infrasound may be related to the sudden uncorking of the volcano, when the pressure exceeds the critical threshold releasing acoustic energy. This mechanism is believed to be more common in presence of intermediate viscosity magma, where Vulcanian eruption -disrupting the plug obstructing the conduit- may occur [Johnson and Lees, 2000; Uhira and Takeo, 1994]. Another example of source

model in which more violent level of activity is implied is given by the 8 March 2005 Vulcanian eruption of Mt. Helens, for which during the initial emission of gas, quite fast ejection of gas and ash is likely to have occurred [Matoza et al., 2007]. The acoustic signals corresponding to this phase of the eruption were compared to low frequency jet noise, on the basis of a similarity with the physical mechanism of noise radiation from the aircrafts [Matoza et al., 2009a].

Sometimes the occurrence of infrasound may be due to hydrothermal phenomena. For instance, at Mt. St. Helens, from November 2004 to March 2005 the eruption was characterized by repetitive infrasound signals associated to LP events that were probably linked to hydrothermal processes. It was suggested [Matoza et al., 2009b] that the repeated and rapid pressure loss from a hydrothermal crack system caused both acoustic and seismic radiation. Indeed, heated fluid may cause the pressure buildup required to open the crack system. The sudden release of pressure produces a broadband infrasound signal, and, in the meanwhile, induces the crack collapse, thus generating infrasound signals.

Finally, it must be taken into account that also landslides and pyroclastic flows, both common phenomena in volcanoes environment, are able to produce infrasound [Oshima and Maekawa, 2001; Moran et al., 2008a].

1.3 Analytical methods

1.3.1 Transient detection

Detection algorithms are the fundamental first step of every research study or monitoring activity based on continuously recorded signals. Indeed, dealing with big amount of temporal traces requires the use of an automatic algorithm to detect the occurrence of transients. On the base of the characteristics of the investigated signals, and thus on the base of the type of alterations we expect to detect in correspondence of an arrival of a seismic/infrasonic wave, different trigger algorithms can be used. For instance, they can be based either on the time or frequency domain, they can search for a specific expected pattern, or make use of the particle motion or the polarization characteristics of the signal, such as rectilinearity or planarity [Withers et al., 1998].

One of the most extensively used algorithm, named STA/LTA (*Short time average/long time average*), is based on the evaluation of the ratio between energy density on short and long terms

[Whiters et al., 1998]. This method requires the definition of two time windows, one relatively shorter than the other. It has been estimated that ideal conditions for the algorithm are given when the two windows are respectively 3 and 27 times the central period of the frequency band of interest [Whiters et al., 1998]. The energy density in each window is computed by using root mean square (hereafter RMS) and then the ratio between the values estimated for the two windows is calculated. Thus, the two windows are simultaneously shifted along the traces, and a transient is detected when the value of such energy density ratio overcomes a fixed threshold.

It must be noted that this algorithm tends to produce false arrivals in condition of irregular noise [Havskov and Alguacil, 2004].

Alternatively, an effective trigger algorithm used in this work is the percentile method [for an example see **Fig. 1.6**; Cannata et al., 2011b].

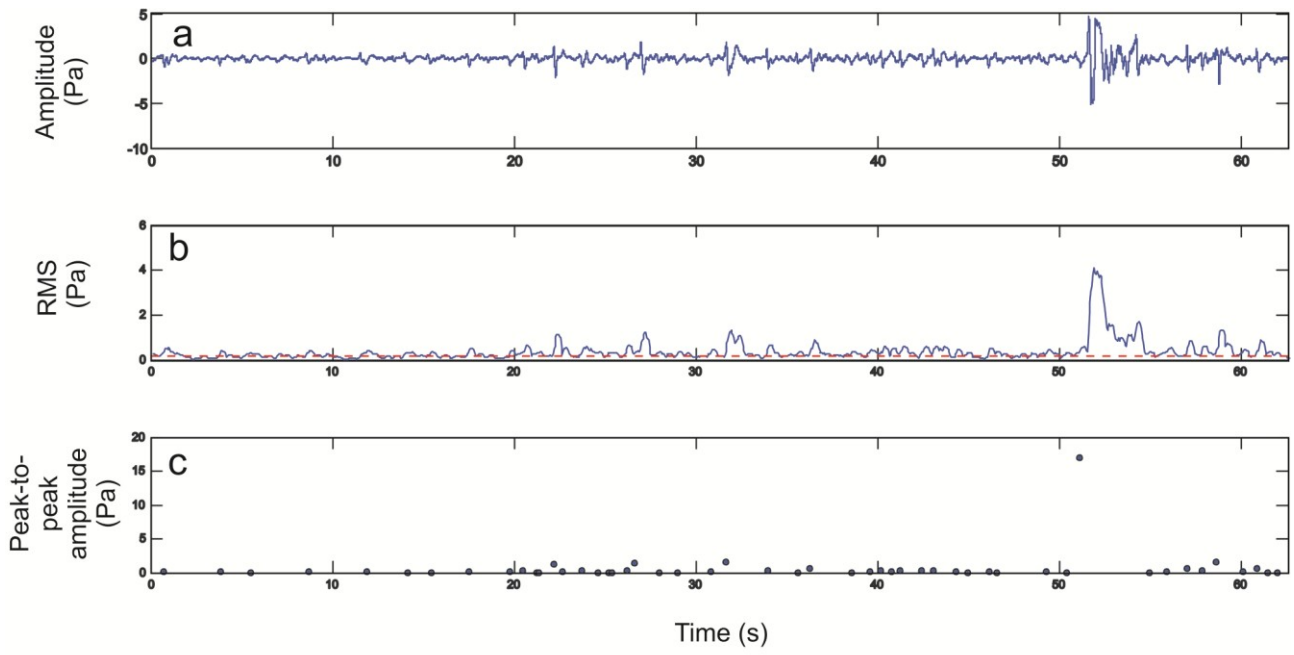

Figure 1.6: Example of percentile trigger analysis applied to moderate puffing activity at Mt. Yasur. a) Raw signal (begin time: July, 7th 2011, 06:01:54). b) RMS envelope of signal shown in a); the red dotted line represents the percentile threshold value. Blue dots in c) represent triggered events.

The RMS envelope is computed by using a sliding window with a fixed duration. Successively, the percentile of RMS envelope is computed by using another moving window. A percentile threshold p_{tr} is established, as the value for which at most (100 × p_{tr}) per cent of the measurements are less than this value and 100(1 – p_{tr}) per cent are greater. A transient arrival is detected every time the RMS percentile overcomes the fixed threshold. This method was found to be more effective than STA/LTA when dealing with closely spaced events [Cannata et al., 2011b].

1.3.2 Location analyses

1.3.2.1 Infrasound location

Unlike seismic signals, whose epicentral location errors are generally larger than 100 m, infrasound location can be much more precise [up to 3 m; Johnson, 2005]. This difference depends on several factors. Firstly, considering the lower velocity of acoustic waves in respect of seismic ones, small changes in the source position affect more the infrasound travel and arrival times than in the case of seismic signals [Johnson, 2005]. Secondly, the propagation velocity of the seismic waves [Johnson, 2005; Arrowsmith et al., 2010] is often poor-known and identifying correlated phases for emergent or sustained seismic signals is still difficult [Arrowsmith et al., 2010]. Infrasound location techniques, using semblance or cross correlation functions to compare signals recorded at several sensors, have allowed recognizing active vents in multivent systems such as Stromboli [Ripepe and Marchetti, 2002], Mt. Etna [Cannata et al., 2009a] and Kilauea [Garces et al., 2003]. Different techniques have been developed to locate the infrasound sources [e.g. Ripepe and Marchetti, 2002; Garces et al., 2003; Johnson, 2005; Matoza et al., 2007; Jones et al., 2008; Jones and Johnson, 2010; Montalto et al., 2010]. Among them grid search methods are particularly suited for dense network recordings.

These methods are based on the designation of a grid, spread all over the region of interest for the determination of the source position. For infrasound, it is convenient to define a bi-dimensional grid of assumed source positions coincident with the topography, since the vent radiating infrasound can be considered a source point located on the topography. Successively, the procedure requires to find a source position on the grid that allows for a set of theoretical arrival times (τi, i =1,…, N), that yields maximum value of a similarity function calculated on the N-channel data.

The procedure includes several steps common to other location methods [e.g., Almendros and Chouet, 2003; Ripepe et al., 2007]. In particular, a start time t_s is fixed as the time of first arrival at a reference station (generally chosen on the basis of the highest signal to noise ratio). The source is iteratively assumed to be in each node of the grid, and for each node the origin time is calculated, assuming a certain value of propagation velocity of the infrasonic waves c, as follows:

$$t_0 = t_s - r/c \quad \textbf{(7)}$$

where *r* is the distance between the reference station and the node of the grid assumed as source location. The theoretical travel times are calculated at all the sensors t_i (*i* =1,…, *N*, number of stations):

$$t_i = r_i/c \quad \textbf{(8)}$$

where r_i is the distance between the station *i*-th and the node of the grid assumed as source location. Then, using these theoretical travel times and the origin time, signals at the different stations are delayed and a function is applied in order to compare the windows of signals obtained and define the level of similarity among them. The source coincides with the point of the grid where the maximum of such function is observed.

Two functions have been used in this work, the semblance function [Neidel and Tarner, 1971] and the brightness function [Kao and Shan, 2004]. In some cases, in order to obtain high precision location, the two functions were also combined together [Cannata et al., 2011a].

Let us consider traces *U*, acquired by a certain number of sensors *N*; the semblance is defined as [Neidel and Tarner, 1971; Almendros and Chouet, 2003]:

$$S = \frac{\sum_{j=1}^{M}(\sum_{i=1}^{N}(U_i(\tau_i + j\Delta t))^2)}{N\sum_{j=1}^{M}\sum_{i=1}^{N}U_i(\tau_i + j\Delta t)^2} \quad \textbf{(9)}$$

where Δt is the sampling interval, τ_i is the origin time of the window sampling the *i*-th trace, $U_i(\tau_i+j\Delta t)$ is the *j*-th time sample of the *i*-th *U* trace, and *M* represents the number of samples in the window. *S* is a number between 0 and 1. The value 1 is only reached when the signals are identical, not only in waveform but also in amplitude. Eventually, in order to make *S* values unrelated to the different amplitudes of the signals recorded at distinct stations, it is useful to normalize the waveforms dividing each trace by its maximum absolute value. Indeed, as also argued by Almendros and Chouet [2003], the semblance location technique is mainly based on the quantification of the similarity among waveforms recorded at different stations, and then we are not interested in the relative differences in amplitudes. However, when many stations, located at very different distances from the source, are used, it can be useful not to normalize the amplitudes before calculating the semblance values. Thus, greater "weight" is given to the stations nearest to the source and characterized by the highest signal to noise ratio [Cannata et al., 2009c]

The definition of brightness was given by Kao and Shan [2004], and was used to map the space distribution of seismic sources by the so-called Source-Scanning Algorithm. Here we use the following slightly modified brightness definition:

$$B = \frac{1}{N}\sum_{i=1}^{N}(\max(W_i))$$

(10)

where W_i is a time window of the signal U_i multiplied by a hanning window:

$$W_i = hanning|U_i(\tau_i + j\Delta t)|$$

(11)

with j =1,…,M. Even in this case the signals U_i have to be normalized such that, if all the largest amplitudes are aligned at the centre of the considered time windows, B is equal to 1.

In **Fig. 1.7** is shown the space distributions of both semblance and brightness values for the same event. Both the advantages and disadvantages of each method are evident in the picture. For instance, the drawback of the semblance distribution is the presence of pronounced lobes extending over almost the whole grid, giving rise to many relative maxima. On the other hand, the drawback of the brightness distribution is the wide area characterized by high brightness values that does not allow locating the source precisely.

The joint semblance-brightness distribution [Cannata et al., 2011a] overcomes the drawbacks of both the methods. Indeed, once the space distributions of both semblance and brightness values are determined, the two grids of values are normalized, by subtracting the minimum value and dividing by the maximum one. Thus, the values belonging to two grids range from 0 to 1, and the same weights are assigned to semblance and brightness. Then, the two normalized grids are summed node by node. The source is finally located in the node where the delayed signals show the largest composite semblance brightness value. This joint method not only shows the high location resolution of the semblance method, but also, by the brightness function, strongly reduces the side lobes characterizing semblance locations [Jones and Johnson, 2010; Montalto et al., 2010].

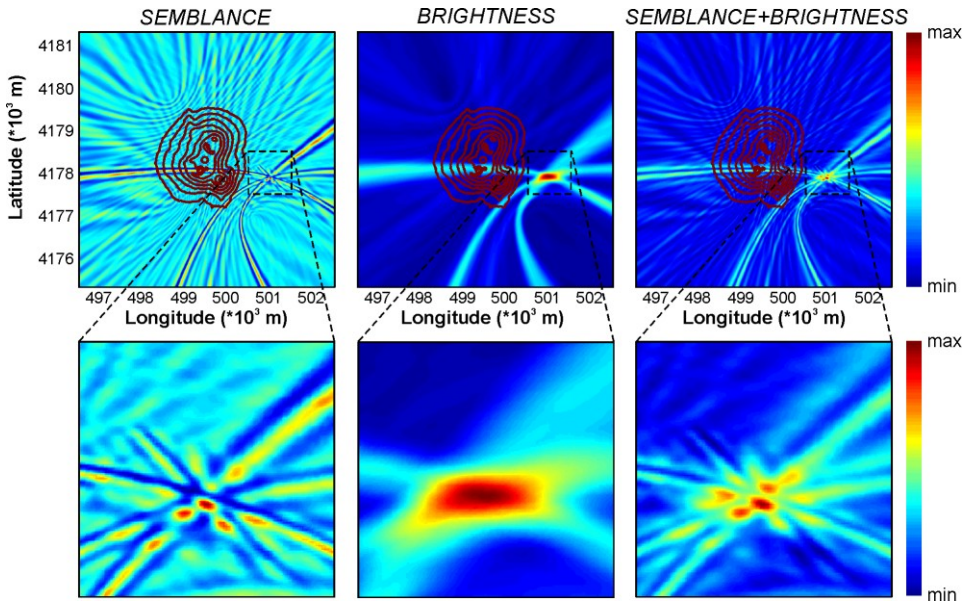

Figure 1.7. Example of semblance, brightness and semblance+brightness space distribution for an infrasound event generated by the eruptive fissure. The concentric lines in the top plots are the altitude contour lines from 3 to 3.3 km a.s.l.

1.3.2.2 Seismic tremor location

As previously said, volcanic tremor is a continuous or long-lasting signal for which no method based on the inversion of the travel time could be used. For this reason, the localizations of volcanic tremor are usually based on the spatial distribution of the amplitudes at all the stations of the network, the so called amplitude decay method, which takes into account the expected amplitude decay through the path source/station [e.g., Battaglia et al., 2005; Di Grazia et al., 2006; Patanè et al., 2008].

Thus, according to these methods, the first step is the definition of a 3D grid, whose nodes are iteratively assumed coincident with the source of tremor. Indeed, fixing a node as the source, a distribution of expected amplitude of the signal is computed at each station. The decay in amplitude during the travel path is computed by the following general law:

$$A(f,s) = A_0(f)s^{-b}e^{-\alpha s} \quad \textbf{(12)}$$

where f is the frequency, s the distance, b is the exponent, which takes values of 0.5 or 1 for the cases of surface and body waves, respectively, A_0 the initial amplitude at frequency f, A the amplitude at frequency f and distance s, and α, the frequency dependent absorption coefficient, given by:

$$\alpha = \frac{\pi f}{Qc}$$

(13)

with *c* corresponding to the wave velocity and *Q* equal to the quality factor, indicating the loss of energy during each cycle of the wave, and quantified with the following equation [Knopoff, 1964]:

$$\frac{1}{Q} = \Delta E / 2\pi E$$

(14)

where E is equal to the peak energy reached in each cycle, and ΔE is the energy loss in same cycle. The equation (**12**) can be linearized in the following form:

$$lnA_i + \alpha s_i = a - blns_i$$

(15)

where a ($\ln A_0$) and b are constant, A_i is the amplitude at the station ith, and s_i is the distance source–station ith. The RMS value is used for quantifying the amplitude of the volcanic tremor. The location of the source is found by evaluating the goodness of the regression fit between the theoretical and the experimental amplitude (R^2), as the amount of variance explained by the linear fit with respect to the total variance of $\log A(s)$ [Di Grazia et al., 2006]. Finally, the position of the source is found as the centroid of the 3D points whose R^2 does not differ more than 1 % from the maximum R^2.

Even though the frequency dependent absorption coefficient does not affect excessively the source location [Battaglia et al., 2005], it must be estimated in order to apply the method. At Mt. Etna it was evaluated by systematically attributing different values to α, and then searching for the best values achieved for R^2. Thus, values comprised between 0 and 0.2 were obtained for α [Patané et al., 2008].

1.3.2.3 LP events location

LP events in this work were located by combining together two location methods above described: semblance and amplitude decay (Neidel and Tuner, 1971; Battaglia et al., 2005). Indeed, as in the previous case a grid is defined, and then each node of the grid is iteratively assumed to be the source. Successively, both semblance and amplitude decay functions are computed. Thus, the source is located where is the maximum of the two combined function.

1.3.3 Spectral analyses

In order to investigate the characteristics of a temporal series in the frequency domain it is necessary to apply different spectral analyses methods. Basically, a spectral analysis is the conversion of signals, made up of sinusoids in the time domain, into spectral peaks in the frequency domain [Hasada et al., 2001]. In the present thesis two spectral analysis methods have been applied: FFT analysis and Sompi method.

1.3.3.1 FFT analysis and pseudospectrograms

The most common way to perform a signal de-convolution into the frequency domain is the Fourier analysis. Indeed, signals characterized by periodicity can be projected into the mathematical base of the Fourier series, thus into a sum of sinusoidal components. However, this kind of mathematical process is not valid for not periodic signals, such as short-time lasting transient. Therefore, in order to achieve information about the weight of each frequency component in a given transient signal *x*, we need to apply the Fourier Transform, given by:

$$X(f) = \int_{-\infty}^{+\infty} x(t) e^{-i2\pi t} dt \quad \textbf{(16)}$$

with *f* frequency and *t* time, *X*(*f*) is the signal in the frequency domain while *x*(*t*) is the signal in the time domain, and *i* is equal to $\sqrt{-1}$. The opposite mathematical operation is called Fourier anti-transform, and it is used to express in the time domain a frequency based signal.

As we are commonly dealing not with continuous signal, but rather with temporal series sampling the physical phenomenon at a given interval of time, the Fourier transform is defined Discrete Fourier Transform (DFT) and it is applied only to the portion of signal investigated.

The fastest way to solve a Discrete Fourier Transform is by using the Fast Fourier Transform (FFT) algorithm [Cooley and Turkey, 1965]. The N point signal is divided in N signals with one point each, then the spectrum is computed, and finally all the spectra obtained are averaged [Smith, 1999].

The data obtained can be represented in different ways. One of the most extensive representations, particularly useful when dealing with big amount of data -for instance in order to identify spectral variation through time- is the spectrogram. It is obtained by putting each

spectrum near to the other along x-axis and representing frequency along the y axis and spectral amplitude as color shading. However, in this thesis extensive use of pseudospectrograms (an example in **Fig. 1.8)** was made, thus it is worthy to spend some words about this.

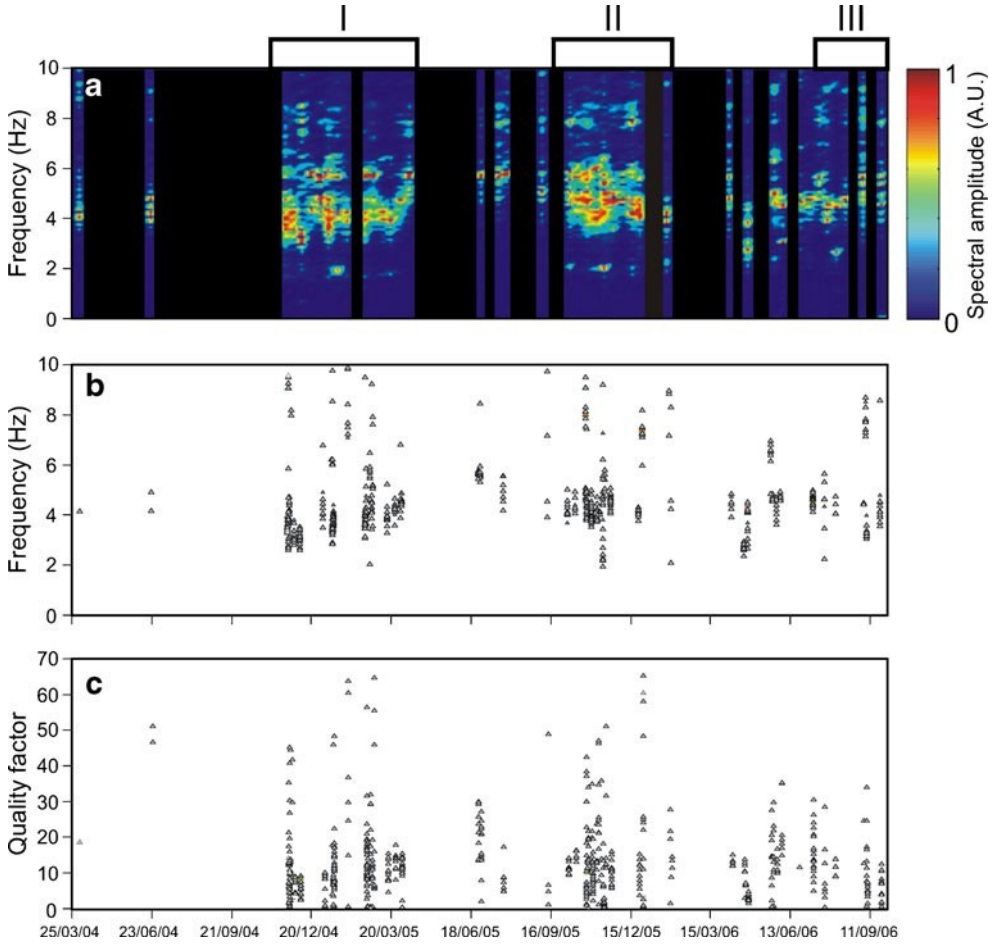

Figure 1.8: a) Normalized pseudospectrogram of the so called Mixed- Events (MX) recorded at the vertical component of IVCR station, at Volcano (Sicily). Each spectrum was calculated by averaging the spectra of the MX events occurring during 10-days long interval. The black rectangles, located inside the plot, show time intervals with no MX events. The top empty rectangles and roman numbers indicate the periods characterized by the seismic sequences; b) and c) Peak frequency and quality factor of the vertical component of the seismic signal of IVCR station, obtained by Sompi method for autoregressive (AR) orders ranging between 4 and 60 (see section 1.3.3.2. for details) . From [Alparone et al., 2010].

Indeed, since for many volcanoes infrasound events are discrete transients lasting from a few seconds to tens of seconds and occurring tens of seconds to hours, and occasionally days, apart, the classic representations of FFT analysis (i.e. the spectrograms) would mainly be made up of noise spectra (mostly wind noise), that would hide the spectral features of infrasound events related to volcano activity. In light of this, in place of classic spectrograms, pseudospectrograms were drawn as follows. For each event a spectrum is calculated. Next, to maintain the temporal information, an averaging process of the spectra, falling in sliding time windows, was performed. The duration of such sliding windows is a critical factor, since it must be a compromise between the need for detailed time information (short time interval), and continuity in the representation

that takes into consideration the occurrence rate of infrasound events (long time interval). Each averaged spectra is gathered as column in a single matrix, arranged in temporal order. This matrix was visualised as a pseudospectrogram. Hence, in the x-axis the time is reported, the y-axis represents the frequency and the colour scale shows the spectral amplitude. In order to gather the most complete information, it is useful to produce pseudospectrograms using both normalized averaged spectra and the original spectra, as non-normalized spectra will be dominated by high-amplitude phenomena that obscure the spectral content of low amplitude events. In the normalized pseudospectrogram the latter information is preserved, but, on the other hand, the information on the amplitude of observed phenomena is lost. It is noteworthy that pseudospectrograms, even if differently named, have been used several times in literature to analyze group of "discrete" seismic and acoustic signals [e.g., Saccorotti et al., 2007; Molina et al., 2008; Moran et al., 2008b; Di Grazia et al., 2009; Alparone et al., 2010].

1.3.3.2 Sompi analysis

The FFT algorithm it is not suited for really short time signal. In fact, the resolution in the frequency domain depends on the length of the time window applied to the signal. Furthermore, the decomposition of the signal in harmonic components is not really representative of signals growing or decaying in time, like in presence of energy dissipation or supply, where the frequency must be defined in the complex rather than real frequency domain.

An alternative procedure to acquire information on the signal in the frequency domain is the Sompi method [Hori et al., 1989; Kumazawa et al., 1990] . According to this method, the temporal series is de-convolved into a linear combination of a finite number of sinusoidal wave-elements. The latter are defined by two complex numbers, *z* and α, defined as (Kumazawa et al., 1990):

$$z = \exp(\gamma_z + i\omega_z) \tag{17}$$

where are γ_z and ω_z are respectively the real and imaginary part of the complex angular frequency, and:

$$\alpha = A_z e^{i\theta} \tag{18}$$

with A_z and θ, real amplitude and phase at the origin time. The ordinary frequency f and the growing rate *g* are defined as (Kumazawa et al., 1990):

$$f = \frac{\omega_z}{2\pi} \tag{19}$$

$$g = \frac{\gamma_z}{\omega_z} \tag{20}$$

while the quality factor is [O'Connell e Budiansky, 1978]:

$$Q^{-1} \cong \frac{-2g}{f} \tag{21}$$

where a smaller value of *Q* corresponds to major losses of energy during each oscillation. The general law for the amplitude decay is given by [Kumazawa et al., 1990]:

$$x(t) = \sum_{v=1}^{m} A_v \exp(\gamma_v t) \cos(\omega_v t + \theta_v) \tag{22}$$

where *m* represents the number of wave-element in which the signal is decomposed, and is defined as the order of the regression mode. The choice of the order is fundamental because it defines the number of elements in which the signal must be decomposed. Many authors use a wide range of orders to discriminate coherent elements (i.e., Kumagai et al., 2005; De Angelis and McNutt, 2005)

In the **Fig. 1.9**, an example of Sompi analysis in the bidimensional plane frequency - growth rate is shown. All the scattered points represent incoherent noise, whereas the densely populated lines, that remain stable when the order of the regression order changes, are resolved dominant modes [Hori et al., 1989]. Another example of Sompi analysis is given in **Fig. 1.8**.

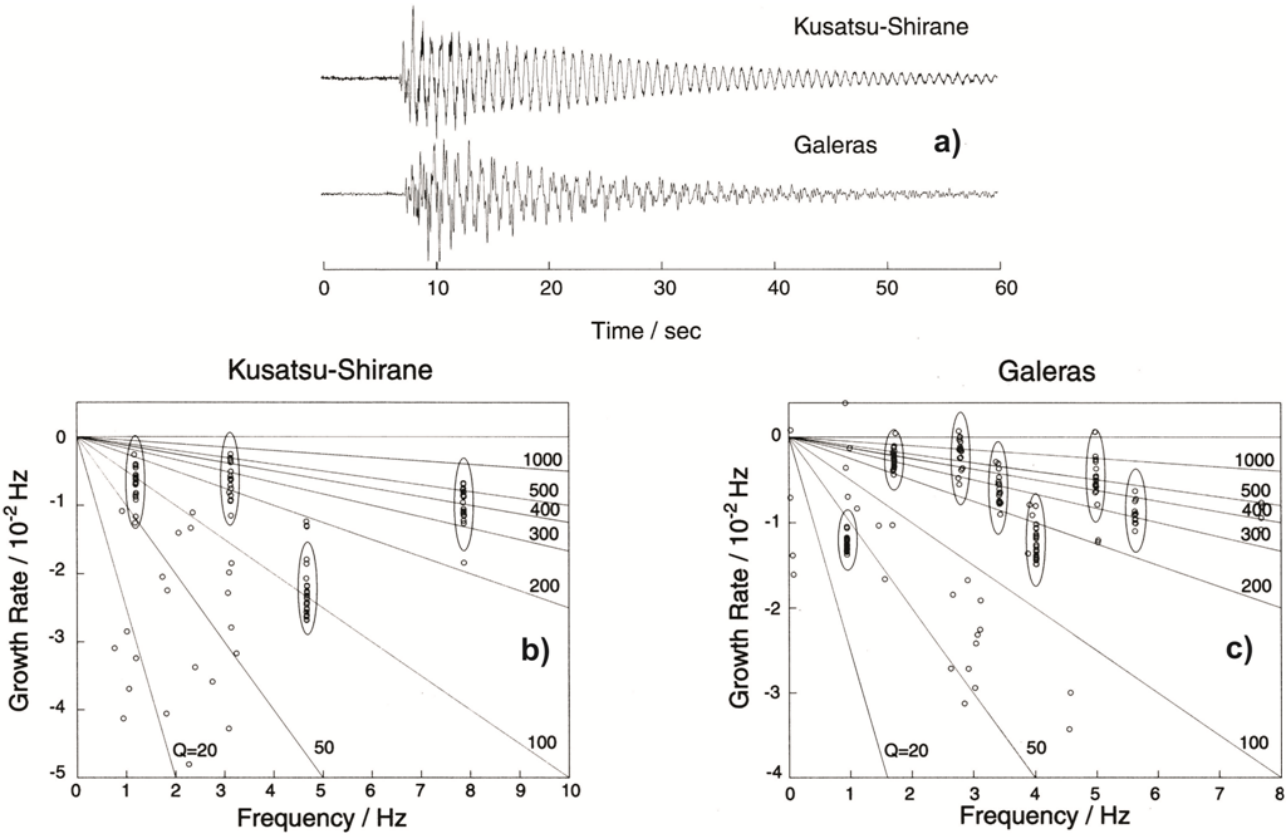

Figure 1.9: Example of Sompi analyses. The two signals at the top, respectively an LP event from Kusatsu-Shirane and from Galeras, are analyzed below by Sompi method. Indeed, the two graphs below plot the complex frequency of individual wave element versus growth rate for all the performed autoregressive order (AR) trial (20 to 60). The solid lines represent couple of points with same value of Q. Dominant modes are highlighted by circles. Modified from Kumagai and Chouet (1999).

1.3.4 Cross-correlation

In order to identify pattern in the huge amount of seismic/infrasonic signals that accompany an eruption, signal classification methods are required. Indeed, acoustic or seismic events are commonly grouped on the basis of their frequency content. Nevertheless, much information could be achieved by comparing waveforms, which can be grouped into clusters with a physical meaning.

In order to do that, a time window of fixed length is extracted from the signal. Then, all the events are compared by using the following cross-correlation function:

$$r_{xy}(i, i-l) = \frac{\sum_{i=1}^{n}(x_i - \bar{x})(y_{i-l} - \bar{y})}{\sqrt{\sum_{i=1}^{n}(x_i - \bar{x})^2}\sqrt{\sum_{i=1}^{n}(y_{i-l} - \bar{y})^2}} \quad \textbf{(23)}$$

with x_i *i*th sample of the signal *x*, y_{i-l} is the (*i*-*l*)th sample of the signal y, *n* is the number of events to be compared, and the over-bar represents the mean value of the signal [Green, 2005]. The relative position of the two windows of signal is expressed by the lag *l*. A value of cross correlation coefficient r_{xy} equal to 1 means that the signals are identical, whereas -1 stands for opposite signals, and 0 for total absence of correlation. Using this function, each event is cross-correlated with the other.

Successively, a matrix, with size *n x n*, is realized by plotting the maximum correlation coefficient. For instance, a generic value m_{xy} of the matrix represents the maximum correlation coefficient obtained for signals *x* and *y*, for different trial lags [Green and Neuberg, 2006].

In order to detect families of events from the matrix, a coefficient threshold is established. A "master event" is selected as the event with the biggest number of threshold excesses. Then, there are mainly two procedures to obtain individual families:

- Bridging technique [e.g., Barani et al., 2007]: All the events with r_{xy}, in respect of the master event, over the threshold are grouped into the same family and removed from the dataset. Secondly, all the events with r_{xy} , in respect of the removed events, over the fixed threshold, are grouped in the same family, independently from their similarity to the master event. The procedure is completed when all the possible families are grouped.
- Green and Neuberg method [Green and Neuberg, 2006]: An average waveform is obtained by stacking all the events with r_{xy}, in respect to the master event- over the threshold. Then the cross-correlation values are computed again in reference to the stacked event, and all the events that overcome the fixed threshold are grouped as a family and removed from the dataset. Even in this case, the procedure is completed when all the possible families are grouped.

1.3.5 Seismo-acoustic energy partitioning

The evaluation of the partition between seismic and acoustic energy during volcanic eruptions has proven to be really useful in order to acquire information about the dynamics active at different volcanoes [i.e., Johnson and Aster, 2005] and at the same volcano during different episodes [i.e. Sahetapy-Engel et al., 2008]. Estimations of elastic energies of acoustic and seismic wave field can

be useful in order to infer physical constraints about the eruptive mechanisms and to provide quantitative information about condition and intensity of the eruption [Johnson and Aster, 2005].

Seismo-acoustic partition is computed from seismic and infrasonic traces by calculating individually the energy radiated from the source in the acoustic and in the seismic field, and then successively their ratio, namely VASR (Volcano acoustic seismic ratio; Johnson and Aster, 2005).

The total acoustic energy radiated into the atmosphere can be estimated by integrating in space and time, over an hemi-spherical surface, the energy density, which is proportional to the square of the excess pressure Δ*P* [Johnson and Aster, 2005; Firstov and Kravchenko, 1996; Johnson, 2003; Vergniolle et al., 2004]:

$$E_{acu} = \frac{2\pi r^2}{\rho_{air} c_{air}} \int \Delta P(t)^2 dt \quad \textbf{(24)}$$

with *r* distance source-station, ρ_{air} and c_{air} respectively air density and sound speed in the air. Equation (**24**) requires the assumptions of linear propagation and isotropic travel path of the acoustic wave through the atmosphere. The first statement is verified for moderate explosions, with VEI smaller than 2 [Johnson and Aster, 2005]. The assumption of isotropy of the travel path, instead, is a valid only if the recording stations are located at few kilometers of distance from the source. Bias, due to the noise produced by high intensity winds and/or eventual limitations related to the instrumental response, must be taken into account when evaluating the radiated energy from the recorded signal.

Seismic energy can be estimated through the following equation [Johnson and Aster, 2005; Boatwright, 1980]:

$$E_{seism} = 2\pi r^2 \rho_{earth} c_{earth} \frac{1}{A} \int S^2 U(t)^2 dt \quad \textbf{(25)}$$

where ρ_{earth} and c_{earth} are respectively density and *P* wave velocity into the volcanic edifice, *A* is the attenuation due to intrinsic and scattering dissipation and *S* is the site response. Equation (**25**) assumes that the dominant wave field is made up of pure body waves propagating with a single velocity toward the station. Furthermore, the radiation is considered isotropic and the attenuation negligible. The validity of these assumption, have already been verified at several volcanoes [Etna; Sciotto et al., 2013; Karymsky and Erebus; Johnson and Aster, 2005]. Nevertheless, the application of the equation, require verifying them for the specific studied volcano.

Finally, VASR is computed by [Johson and Aster, 2005]:

$$VASR = \frac{E_{acu}}{E_{seism}}$$

(26)

The VASR parameter is basically an indicator of the coupling among the source, the surrounding medium and the atmosphere. Good coupling with the atmosphere is favored by low density of eruptive plumes, or from the absence of a cap rock plugging the conduit. Similarly, the energy associated to seismic waves, traveling inside rock medium from the source to the station, is affected by conduit conditions (e.g., explosive source depth, conduit width) as well as intrinsic attenuation and scattering [Andronico et al., 2013].

Chapter 2: Insights into Mt. Etna shallow conduit dynamics

2.1 Mt. Etna: an introduction

2.1.1 Geographical and tectonic setting

Mt. Etna is a Quaternary stratovolcano, characterized by Na-alkaline magmatism [e.g., Cristofolini and Romano, 1982]. It is located on the eastern coast of Sicily, nestled into a peculiar convergence of tectonic elements. Indeed, it lies at the front of the collision belt (Apenninic-Maghrebian Orogen) -developed at the margin of the Africa promontory- and at termination of the Malta Escarpment fault, a Mesozoic discontinuity separating the continental crust of the Pelagian Block [Barreca et al., 2012; Burollet et al., 1978] from the oceanic crust of the Ionian See [Makris et al., 1986; Monaco et al., 2005]. Such characteristic position reflects on the complexity of the structural elements affecting the volcano (see **Fig. 2.1**). Indeed, the eastern flank is characterized from the presence of a normal fault system, with direction SSW-NNE in the north-eastern sector of the volcano, and NNW-SSE toward south-east, where a slight right lateral component of motion was inferred [Monaco et al., 1995, 1997, 2005; Lanzafame et al., 1996; Azzaro, 1999]. Most of the segment faults are accompanied at the surface by steep slopes called “Timpe”, with Late Pleistocene to Holocene vertical slips ranging from 1 to 2 mm/y [Monaco et al., 1997]. A shallow level (<3) seismicity, with M <4.5 is associated to this system [Azzaro et al., 2000]. The southernmost termination extends offshore at the base of the Malta Escarpment fault [Monaco et al., 1995]. According to some authors, the northward prosecution of the system corresponds to the Tindari-Letojanni system, which marks the alignment of the islands Salina, Lipari and Vulcano [Ghisetti, 1979; Continisio et al., 1997; Lanzafame and Bousquet, 1997].

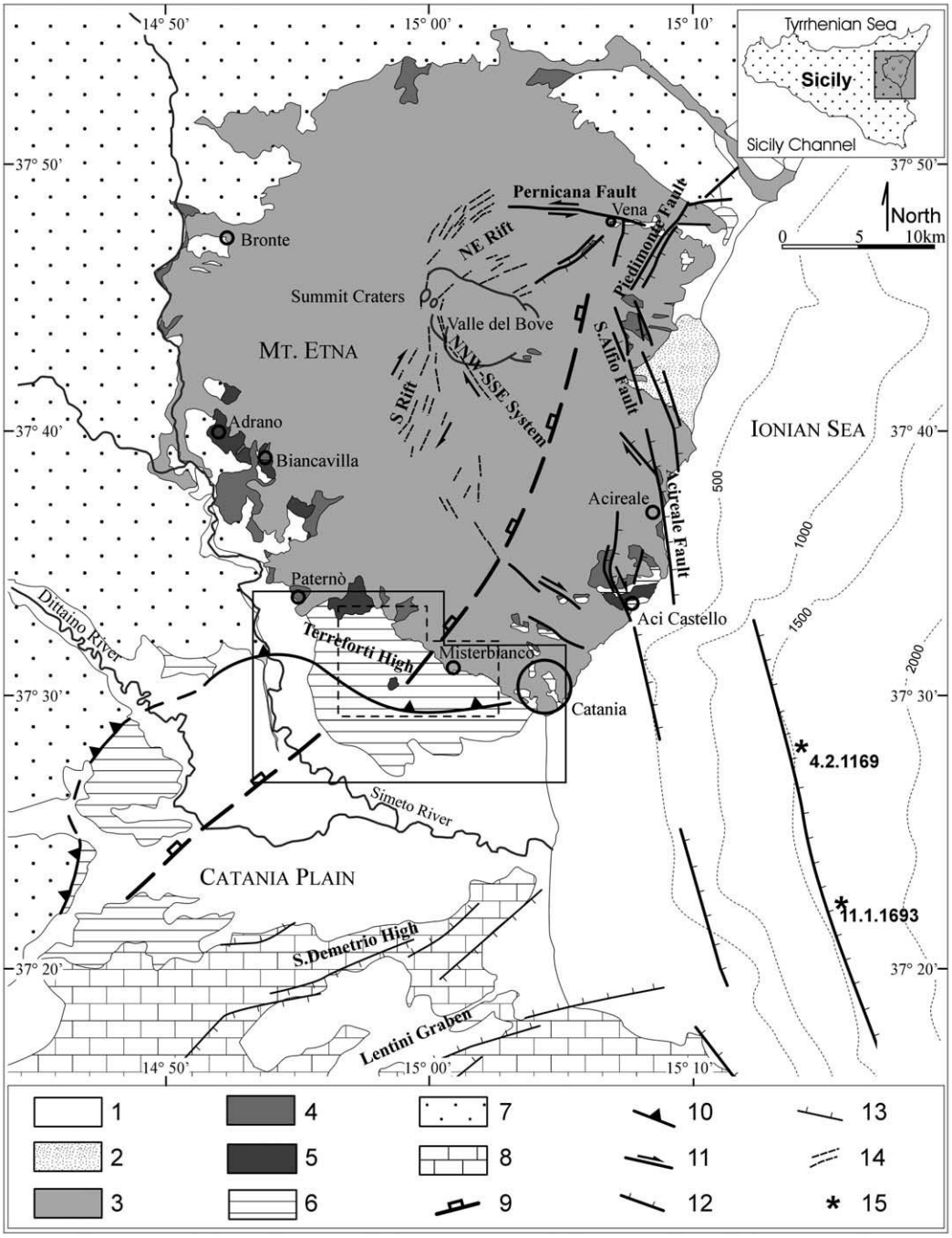

Figure 2.1: Geological sketch-map of the Mt. Etna region. Key: (1) Alluvial deposits ; (2) Late Wurmian alluvial fan; (3) Trifoglietto, Ancient and Recent Mongibello lava flows (80 ka to Present); (4) Ancient Alkaline Centres lava flows (180-100 ka); (5) Sub-alkaline lava flows (580-250 ka); (6) Middle-Upper Pleistocene foredeep sequences ; (7) Units of the Apenninic-Maghrebian collisionbelt; (8) Hyblean Plateau sequences; (9) Front of the buried Gela Nappe; (10) Major thrust-ramp; (11) Strike-slip fault; (12) Late Quaternary normal fault of the 'Siculo-Calabrian Rift Zone ; (13) Plio-Pleistocene normal fault; (14) Dry and eruptive fissures; (15) Ms7 earthquakes since AD 1000.From Catalano et al., [2004].

Another fundamental tectonic structure, whose movement is deeply connected to the volcanic activity, is the Pernicana Fault: one of the most active fault systems of Mt. Etna. It is located in the NE sector of the volcano edifice with strike E-W, and it extends from the North East Rift until the coastline, with a total length of 18 km [Neri et al., 2004]. Along the Pernicana fault the motion

changes from normal dip-slip at the westernmost termination to the left-strike slip motion at the eastern one [Azzaro et al., 2001]. Jointly with the NNW-SSE Rift, it is believed to accommodate, on the summit area and on the NE rift, the extension, related to the regional tectonic contest, [Monaco et al., 1997; 2005]. Furthermore, together with the Mascalucia-Tremestieri-Trecastagni fault system –characterized by strike NNW, right lateral movement and superficial seismicity- delimitates the boundaries of an unstable edifice sector, with movement toward ESE.

Extensional features affect also the summit area of the volcano edifice, where these tectonic elements are deeply linked to the major magma feeding system [Catalano et al., 2004]. Indeed, Mt. Etna summit area is marked by the presence of three rifts, known as NE, NNW-SSE, and N-S rifts. The former is an eruptive fissures network with strike 42-47°C and with dispersion axes comprised between 15-62°C [Branca et al., 2003]. The second rift is comprised between the South East Crater and the south-western rim of the Valle del Bove, and shows an overall geometry NNW-SSE, implying a right-lateral component of motion [Monaco et al., 1997, 2005]. Finally, the N-S rift, in the southern slope of the volcano, consists of a series of N-S, to SSW-NNE striking fissures extending for a total length of 10 km.

The first evidences of volcanic activity in the etnean area are dated 500-700 ka, and they are mainly tholeitic/transitional products, likely linked to fissural activity, emplaced in the pre-etnean Gulf (nowadays correspondent to emerged land). The successive phase was characterized by the presence of the so called ancient alkaline center (150-80 ka), which marked a sharp change in the eruptive style and in the composition of the volcanic products. Successively, activity focused in the area of the Valle del Bove, where actually it is possible to see the traces of the different eruptive centers that succeeded in time in the exposed valley rock walls. The stratigraphical sequence is according with a movement of the eruptive center westward through time [Doglioni et al., 2001].

However, since 35 ka, the activity has been persistently occurring at the eruptive center of Mongibello that accounts for one third of the total volume of Mt. Etna [Giacomelli and Pesaresi, 2003]. The history of Mongibello is commonly split in two parts by the occurrence of a violent episode, 14 ka, that led to the formation of a caldera, named “Caldera dell’Ellittico”. Such depression has been filled through time, and above it, a new central summit cone developed and it is actually the theatre of eruptive activity at the volcano.

The summit area of Mt. Etna is currently made up of four active craters: Voragine, Bocca Nuova, South East Crater and North East Crater (hereafter referred to as VOR, BN, SEC and NEC, respectively, **Fig. 2.2**). Indeed, at the beginning of the century the summit area was characterized

by the presence of a Central Crater, filled by the almost not interrupted eruptions [Patanè et al., 2004]. VOR developed in the North-east sector of the summit chasm in 1945 and, successively, a new crateric depression, corresponding to new-born BN, formed and enlarged in the Central Crater. The NEC, instead, developed in 1911 as a pit depression decentred in respect of the Central Cone, and grew up in time reaching lately the maximum altitude of the volcano, since nowadays. Also SEC developed initially as a simple pit crater, in 1971. Its activity increased drastically after 1978, leading to the development of the actual cone. Furthermore, during 2011-2013 a large new pyroclastic cone, named "New South East Crater", formed on south-east flank of SEC [Patanè et al., 2013].

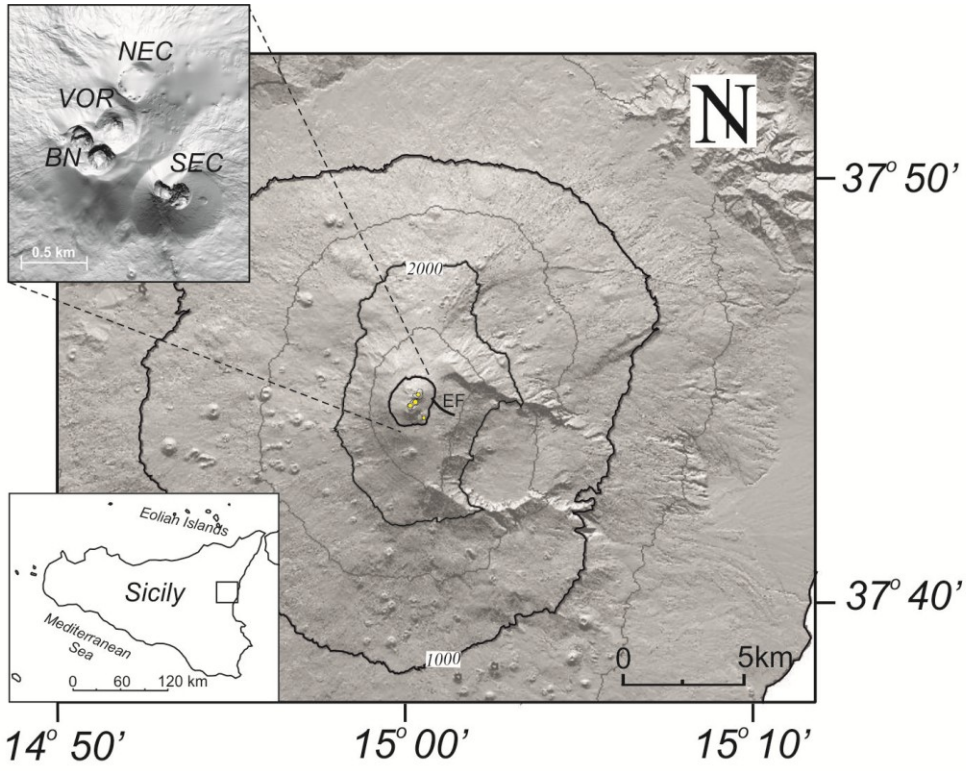

Figure 2.2. Digital elevation model of Mt. Etna with the eruptive fissure opened on 13 May 2008 (thick black line "EF"). The digital elevation model in the upper left corner shows the distribution of the four summit.

Volcanic activity may be divided into activity at the summit craters and flank eruptions. The former is characterized by phases of degassing alternating with mild Strombolian activity, occasionally fire fountains, and lava overflows [e.g., Cannata et al., 2008]. In contrast, flank eruptions occur from lateral vents, which are usually located along fracture systems and often related to regional tectonics [e.g., Monaco et al., 2005].

2.1.2 Recent volcanic activity

During the August 2007 – December 2009 different kinds of volcanic activity at Mt. Etna [INGV staff, 2007-2013] were observed, including quiet degassing, ash emission, Strombolian activity, fire fountain episodes and effusive activity. Therefore, it could be useful to clarify what is defined with each word adopted in this thesis. The term "fire fountain", a typical activity of Hawaiian-type eruptions, refers to an almost continuous to fully sustained vigorous magma jet [Alparone et al., 2003] driving lava clots [Vergniolle et al., 1996] that can typically be tens to hundreds of metres in height [Parfitt, 2004]. The term "Strombolian" is used here to refer to eruptions characterized by discrete explosions due to the breaking of overpressurized bubbles at the surface of the magma column [Vergniolle et al., 1996]. Finally, the term "ash emission" indicates mild explosive activity with ejection of ash into the atmosphere, rising up from few tens of meters to about 1 km [e.g., Andronico et al., 2013].

After 15 months of quiet degassing, in July 2006 Mt. Etna interrupted the rest of the eruptive activity, which followed the 2004-2005 eruption, with Strombolian explosions both at SEC and NEC. It is noteworthy that this episode was the last NEC superficial eruptive activity to be observed and sampled, until November 2010. Interestingly, pyroclastic products coming from both NEC and SEC overlap in the CaO/Al_2O_3 versus FeO_{tot}/MgO graph [INGV staff, 2007-2013]. Furthermore, temperature estimations obtained by the geo-thermometer based on the total composition of MgO into the glass [Pompilio et al., 1998] highlight the same temperature for the magma [INGV staff, 2007-2013]. Successively, the activity renewed on 31 August, and continued until October, with almost 20 paroxysms interrupted only by few days of rest.

After the end of the 2006 eruption, in December, Mt. Etna activity consisted of several short duration eruptive events from a pit crater on the eastern SEC flank [Napoli et al., 2008; Aiuppa et al., 2010; Bonaccorso et al., 2011a]. Indeed before June four fire fountains occurred [29 March, 11 and 29 April, and 6 May; INGV staff, 2007-2013]. They were characterised by explosive phases (fire fountaining and strombolian activity), ash falls, and lava output emplacing along the eastern flank of the cone towards the Valle del Bove [e.g., INGV staff, 2007-2013; Patanè et al., 2008; Bonaccorso et al., 2011a].

Mild explosive activity resumed at SEC in mid-August 2007 [Aiuppa et al., 2010]. This explosive phase culminated on 4-5 September in one of the most powerful fire fountains among those occurring in the last decade, both in terms of duration, about 12 hours, and of lava and tephra

volume, ~2-4 x 10^6 m^3 [Andronico et al., 2008]. This fire fountain was followed on 23-24 November by a second fire fountain episode that lasted about 6 hours.

Thereafter, until the beginning of May 2008, the eruptive activity at Mt. Etna consisted of discontinuous and mild explosive activity at SEC. On 10 May 2008, a fire fountain occurred at SEC and on 13 May a new eruption took place from an eruptive fissure that opened east of the summit area. This eruption was characterized at the beginning by spectacular fire fountaining activity and during the following months by phases of variably intense lava flows and Strombolian activity [Bonaccorso et al., 2011a]. This eruptive phase ended on 6 July 2009. More and detailed information about the 2008-2009 eruption, which are necessary in order to interpret high precision location analyses performed, can be found in the **section 2.3.1**.

In the evening of 6 November 2009, bright incandescence marked the birth of a new degassing vent (a few meters wide and deep) within the pit crater. The incandescence at the pit crater continued up to the end of February 2010, then resumed in the night between 16 and 17 March, when an almost continuous glow was again visible (INGV staff, 2007-2013). In the first months of 2010, the pit crater was characterized by discontinuous but intense output of whitish plumes, accompanied by profound rumbling from the pit, which were able to rise for tens to hundreds of meters before being dispersed laterally. The resumption in March of high-temperature degassing at SEC (signaled by visible incandescence during night hours) heralded the resumption of volcanic activity. Afterward, several episodes of short lasting ash emissions occurred at two of the four summit craters (mainly BN and secondarily SEC) up to the end of 2010. Notably, an ash emission episode occurred in November 2010 also from NEC. Three of these ash emission episodes are analyzed in details in the following pages. Therefore, a more precise description of their occurrence is given in **section 2.4.1**.

The 2011-2013 time interval is characterized by recurrent paroxysmal activity at NSEC, often accompanied or alternated with explosive activity at BN and VOR. Indeed, on the first January 2011 the renewal of activity at the “pit crater” (hereafter referred to as NSEC), close to the SEC, marked the beginning of a new eruptive phase that lasted until November 2011, characterized by a total number of 18 fire fountains, occurring regularly and with relatively short interval time of rest. In the meanwhile, strombolian activity at BN was observed in June-July 2011. The “leading actors” of 2012 were still NSEC and BN. The former was characterized by 7 paroxysmal episodes, similarly to 2011, until April, when strong strombolian activity and ash emission occurred at BN in July and August. Furthermore, BN, together with VOR, reactivated in the very first months of 2013,

with several strombolian episodes. Since the end of January, NSEC started again his paroxysmal activity, producing up to 14 fire fountains (**Fig. 2.3**).

Figure 2.3: Eruptive activity at the New South East Crater on February 28th, 2013. (Copyright, Marco Fulle; http:// www.swisseduc.ch/stromboli/)

2.1.3 Previous acoustic studies at Mt. Etna

The first infrasound investigations at Mt. Etna were performed by temporary experiments [e.g., Ripepe et al., 2001a; Gresta et al., 2004; Vergniolle and Ripepe, 2008].

In particular, Ripepe et al. [2001] performed a seismo-acoustic experiment in 1998 during Strombolian activity occurring contemporaneously at SEC, BN and VOR. They found that volcanic tremor at Voragine -at that time the main source of infrasound- was modulated according to the release of burst of infrasonic energy. Indeed, correlating RMS amplitude of acoustic pressure and volcanic tremor amplitude they found high correlation coefficients, suggesting a coupled dynamics between the source of infrasound and tremor. Consequently, the authors inferred a source linked to degassing and composed by the superposition of small point sources, occurring at 1-2 s rate and due to pressure flux instabilities.

Another temporal experiment was performed in July-August 2001, during the ongoing flank eruption by Gresta et al. [2004]. A small array (four microphone, one of which coupled with

thermal camera) was emplaced close to the eruptive vents, located in the southern flank of the volcano at about 2100 and 2550 m a.s.l. . Authors [Gresta et al., 2004] were able to define the depth (below the pre-existing ground surface) of both the explosions causing infrasound radiation and the seismic source. Interestingly, the results are in agreement with a shallow, phreato-magmatic origin of the explosive activity at the 2550 crater vent.

Furthermore, during the same eruption, Vergniolle and Ripepe [2008] analyzed acoustic signals recorded in coincidence of Strombolian activity (4th July 2001) and explosive activity evolving toward fire fountain (12th July 2001). They found that the transition toward the paroxysmal state is accompanied by an increase in the occurrence rate, and according to the adopted model for infrasound source, also by an increase in the length of the bursting slug. Furthermore, they estimated the gas volume within the foam, assuming the foam coalescence as the mechanism at the base of both kinds of activity. Efficiency of the foam coalescence was found to be higher for fire fountain rather than Strombolian explosion.

Another 4 elements temporary array was deployed at September-November 2006 by Marchetti et al. [2009] at Cratere del Piano, summit area. Analyzing the recordings, two main sources were identified: i) SEC and ii) a second source coming from an area in between VOR and NEC (hereafter VNEC). Indeed, the array was not able to resolve difference of location among the those two craters. Authors [Marchetti et al., 2009] found a shifting behavior between the two identified sources, active at least until the end of October. Such shift was systematically associated with changes of the excess pressure. Indeed, higher amplitudes were commonly linked to events located within the SEC. On the contrary, infrasonic transients coming from the VNEC were associated to lower amplitude values. Consequently, they inferred the existence of a bifurcation in common feeding system, which allowed the SEC branch to activate only for higher values of gas/magma flux.

Since 2006, a permanent infrasound network has been deployed by Istituto Nazionale di Geofisica e Vulcanologia (INGV), Osservatorio Etneo - Sezione di Catania (see also **section 2.1.4**), which has allowed the continuous recording of infrasound and investigations of its linkages with volcanic activity [e.g., Cannata et al., 2009a,b; Di Grazia et al., 2009; Sciotto et al., 2011, 2013]. Until 2009, two summit craters were recognised as active from the infrasound point of view: SEC and NEC [Cannata et al., 2009a,b]. SEC crater was characterised by sporadic explosive activity with different intensity, from mild ash emission to fire fountaining, while NEC crater was mainly characterised by pulsatory degassing and loud booming sounds with no visible eruptive activity [INGV staff, 2007-

2013]. During the 2008–2009 eruption a third infrasound source, coinciding with vents along the lowest portion of the eruptive fissure (hereafter referred to as EF), was also active, producing infrasonic signals called "EF events" during explosive activity [Cannata et al., 2011a]. BN also generated infrasound during sporadic episodes of mild ash emission in 2010 [Andronico et al., 2013] and during episodic Strombolian activity in 2011-2013 [INGV staff, 2007-2013]. Finally, even the NSEC generated infrasound signals during 2011–2013 [INGV staff, 2007-2013]. In February-March 2013, also VOR emitted infrasound signals during Strombolian activity [INGV staff, 2007-2013].

Several analyses have been performed on short-term recordings of Mt. Etna infrasonic events. According to them, the infrasonic signal at Mt. Etna is generally made up of infrasonic events characterized by durations of less than 1 to over 30 s, impulsive compression onsets, and peaked spectra with most of the energy in the frequency range 0.3–6.0 Hz [e.g., Cannata et al., 2013; Sciotto et al., 2013]. Sometimes infrasonic tremor (a continuous infrasound signal lasting from minutes to days) is recorded and in association with both paroxysmal activities and degassing processes [e.g., Cannata et al., 2009a, 2013; Sciotto et al., 2011]

Interestingly, it has been shown how distinct craters generate infrasound signals with different spectral features and duration [Cannata et al., 2009a,b, 2011a,b]: SEC and EF events have dominant frequencies above 2.5 Hz, impulsive compression onsets and short duration (~1 s), while NEC events generally have a frequency content lower than 2.5 Hz , a duration up to tens of seconds, and are characterised by a first pulse followed by decaying sinusoidal oscillations. Furthermore, in Sciotto et al. [2013], two frequency bands were identified for NEC events occurring during 12-13 May 2008: the lower one comprised between 0.4 and 0.7 Hz, and the upper one between 1.5 and 2 Hz.

Even the occurrence time of each type of event is characteristic of its own source, with NEC events occurring almost continuously even during non-eruptive periods, whereas SEC, NSEC, BN, EF and VOR events are mainly recorded during explosive activity at their respective source craters [e.g., Cannata et al., 2011a,b; Andronico et al., 2013]. On the basis of their waveform and spectral features, as well as their occurrence time, SEC and EF events have been interpreted as resulting from a Strombolian bubble vibration model [Cannata et al. 2009a, 2011a], while NEC events from resonance phenomena [e.g., Sciotto et al., 2011, 2013].

2.1.4 The Mt. Etna infrasound and seismic network

From August 2007 to December 2009, the permanent infrasound network at Mt. Etna consisted of between 2 and 5 stations. At the beginning of this period the stations were EBEL, ECPN and ESLN, and in September 2007 EPLC and EPDN were installed (**Fig. 2.4**). Station EBEL had the longest time series and the best signal to noise ratio, and hence was chosen as the reference station. The distance of this station from NEC, SEC and the EF (southernmost ending) is around 2 km, 1.2 km and 1 km, respectively. The infrasound sensors consist of Monacor MC-2005 condenser microphones, with a "theoretical" sensitivity of 80 mV/Pa in the 1–20 Hz infrasound band. At the beginning of November 2009, a G.R.A.S. 40AN microphone was installed in place of the Monacor sensor at EBEL station. Successively, during 2010, six G.R.A.S. sensors have been deployed, as shown in the map. The G.R.A.S. sensor shows a flat response with sensitivity of 50 mV/Pa in the frequency range 0.3-20,000 Hz, and ±3 dB in the range 0.1-0.3 Hz. Since the Monacor microphones do not have flat response in the frequency range of interest (~0.3 - 6.0 Hz), laboratory experiments were performed on recording ambient noise at both Monacor and G.R.A.S. sensors. On the basis of the response of G.R.A.S. sensor, the "experimental" response curve of the Monacor microphones was calculated to correct the amplitude values, spectra and pseudospectrograms (reported in the following pages).

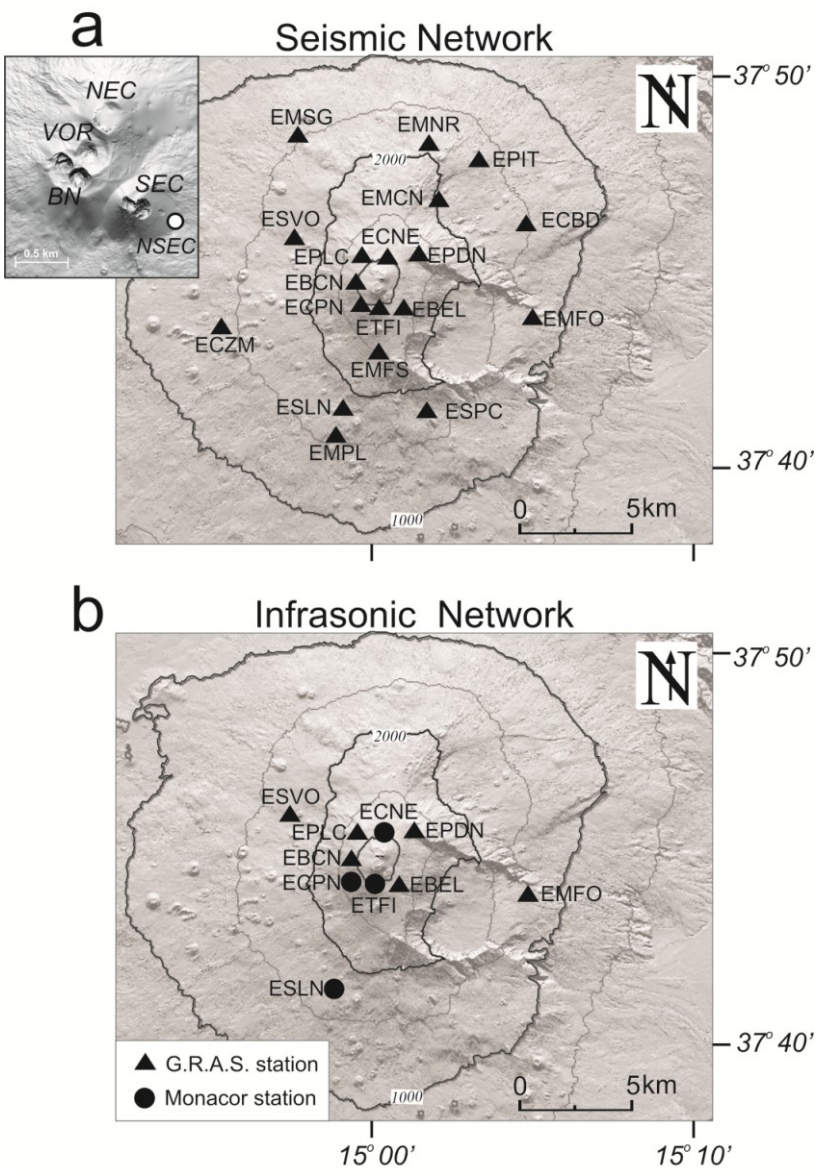

Figure 2.4. a) Mt. Etna seismic network. The top right inset shows the distribution of the summit crater. Please note that NSEC is indicated by a with circles. b) Mt. Etna infrasonic network at the end of 2010. Triangles represent G.R.A.S. stations, while dots represent Monacor stations.

It is worth noting that from the replacement of the Monacor-sensors with the G.R.A.S. microphone a very low frequency peak (<0.5 Hz), accompanying the previously observed frequency content of NEC events (≈1-2.3 Hz), was recorded. Before the installation of the new sensor, these frequency values were observed only prior to the lava fountain of 10 May 2008 and on 12-13 May 2008 before the onset of the 2008-2009 eruption [Di Grazia et al., 2009; Sciotto et al., 2013]. In both cases they were clearly recorded, although their frequency was not in the flat interval of Monacor's response curve. In order to discard the existence of instrumental artefacts on the detection of this signal, experimental tests were carried out on the G.R.A.S. microphone. A 10 cm^3 cylinder-piston device was coupled with a G.R.A.S. 40AN microphone, equipped with a

G.R.A.S. 26HG pre-amplifier, to ensure a flat (± 3 dB) 50 mV/Pa response curve (experimentally calculated for each sensor) in the range 0.1 – 20,000 Hz. The simple experiment consisted of the instantaneous release of 10 cm^3 of air in front of the microphone and recording the pre-amplifier output with a digitizer similar to those used in the permanent network. The output observed is the expected damped response of the microphone to an impulsive input with no very low frequency peak, indicating that the observed low frequency peak at station EBEL was real and not an instrumental artefact (see **Fig. 2.5**).

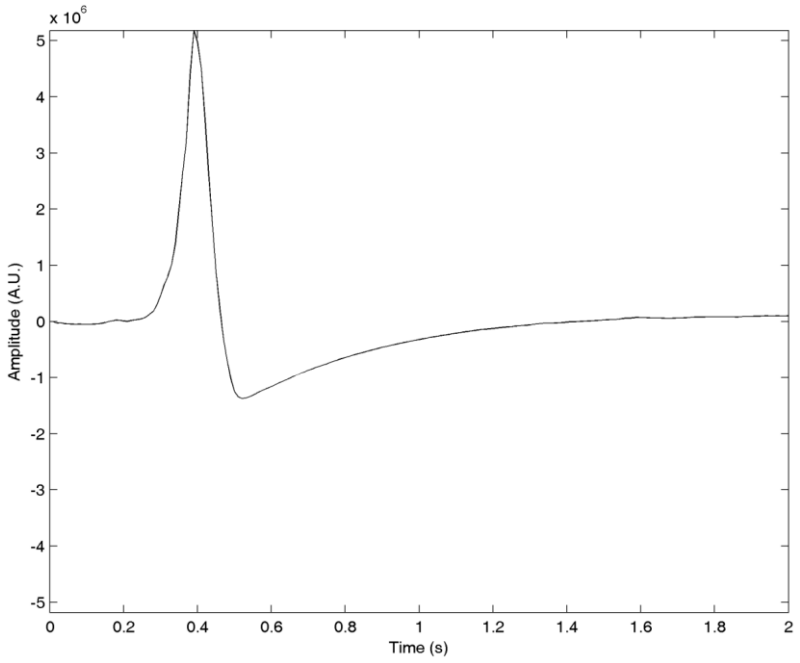

Figure 2.5: Waveform obtained from an experimental test of the Grass microphone. It can be noticed that low frequency tail is absent.

This evidence, plus the observation that such low frequencies were recorded by the Monacor sensor for large-amplitude signals despite its non-flat response at these frequencies, suggests that such low frequency (<0.5 Hz). is a real feature of NEC events rather than instrumental artefact.

The seismic data used in this work were recorded by 19 stations equipped with broadband (40 s period) three component Trillium seismometers (Nanometrics) (**Fig. 2.4a**). Infrasound stations are located at the same place as some seismic stations (**Fig. 2.4b**).

Seismic and infrasound signals are transmitted in real-time by radio link to the data acquisition center in Catania where they are acquired at a sampling rate of 100 Hz. Since August 2010, sampling rate of infrasound signal was lowered at 50 Hz. It must be noted that, due to adverse weather conditions at the Mt Etna summit, infrasound recordings might be affected by wind noise, worsening the signal to noise condition. For such reason, data analysis is not always continuous.

2.2 : Insights into the Mt. Etna shallow plumbing system from the analysis of infrasound signals, August 2007-December 2009

2.2.1 Long term analyses on Mt. Etna acoustic signals (2007-2009):

2.2.1.1 Dataset

Infrasound signals generated by volcanic activity at Mt. Etna consist mostly of discrete events with a duration of seconds. To investigate Mt. Etna infrasound activity during August 2007-December 2009, 40,000 infrasound events were detected by using an STA/LTA algorithm, and analysed. Successively, three periods were chosen, considering their relevance for the ongoing volcanic activity and for coverage of seismic and infrasonic stations, that are: i) 14 August-15 September 2007; ii) 20 November-8 December 2007; iii) 3-29 June 2008. On each period detailed analyses were performed. Finally, in order to further investigate the dynamics active at the Eruptive Fissure of 2008-2009, all the signals from the EF were isolated and analyzed in details from May to September 2008, when EF signals were effectively recorded.

2.2.1.2 Spectral and location analyses

In order to study the spectral variations of the infrasound events over time, FFT analysis was performed and results were displayed by means of pseudospectrograms.
Furthermore, about 3500 events, characterised by high signal to noise ratio at least at 3 out of 4 summit stations (EBEL, ECPN, EPLC, EPDN), were selected to perform location analysis by joint semblance and brightness method [Cannata et al., 2011a]. The location of the infrasound source was estimated by a 2D grid searching procedure, using a 3 km × 3 km grid, with spacing of 25 m, covering the summit area and coinciding with the topographic surface .A point source was assumed and a speed of sound of 340 m/s in the air. There were no infrasound source locations for August 2007 and the whole of 2009 because of the small number of properly working stations (only 1-2 stations).

2.2.1.3 Analysis of the seismic counterparts

The joined analysis of seismic and acoustic signals has proven to be an effective tool for the analysis of volcanic signals. Indeed it was previously used to define the depth of the explosive source [Gresta et al., 2001; Sciotto et al., 2013], or the efficiency of the coupling of the source with atmosphere/medium [Andronico et al., 2013]. Therefore, the existence of seismic transients, linked to the analyzed dataset of infrasonic events was verified. To do that, STA/LTA algorithm was applied on the seismic signal, searching for arrivals in proximity of the arrival time of each infrasonic event. By fixing a STA/LTA threshold of 2.5, 5000 (out of 40000 events) seismic transients were found, as the seismic counterparts of the co-respective infrasound events (**Fig. 2.6b**). However, the seismic-infrasonic lag of these 5000 events showed that some of the seismic transients were not truly related to the infrasound events. Thus, the STA/LTA threshold was raised up to 3, and the number of seismic transients related to the infrasonic events obviously decreased, but many false arrivals were avoided (**Fig. 2.6a**).

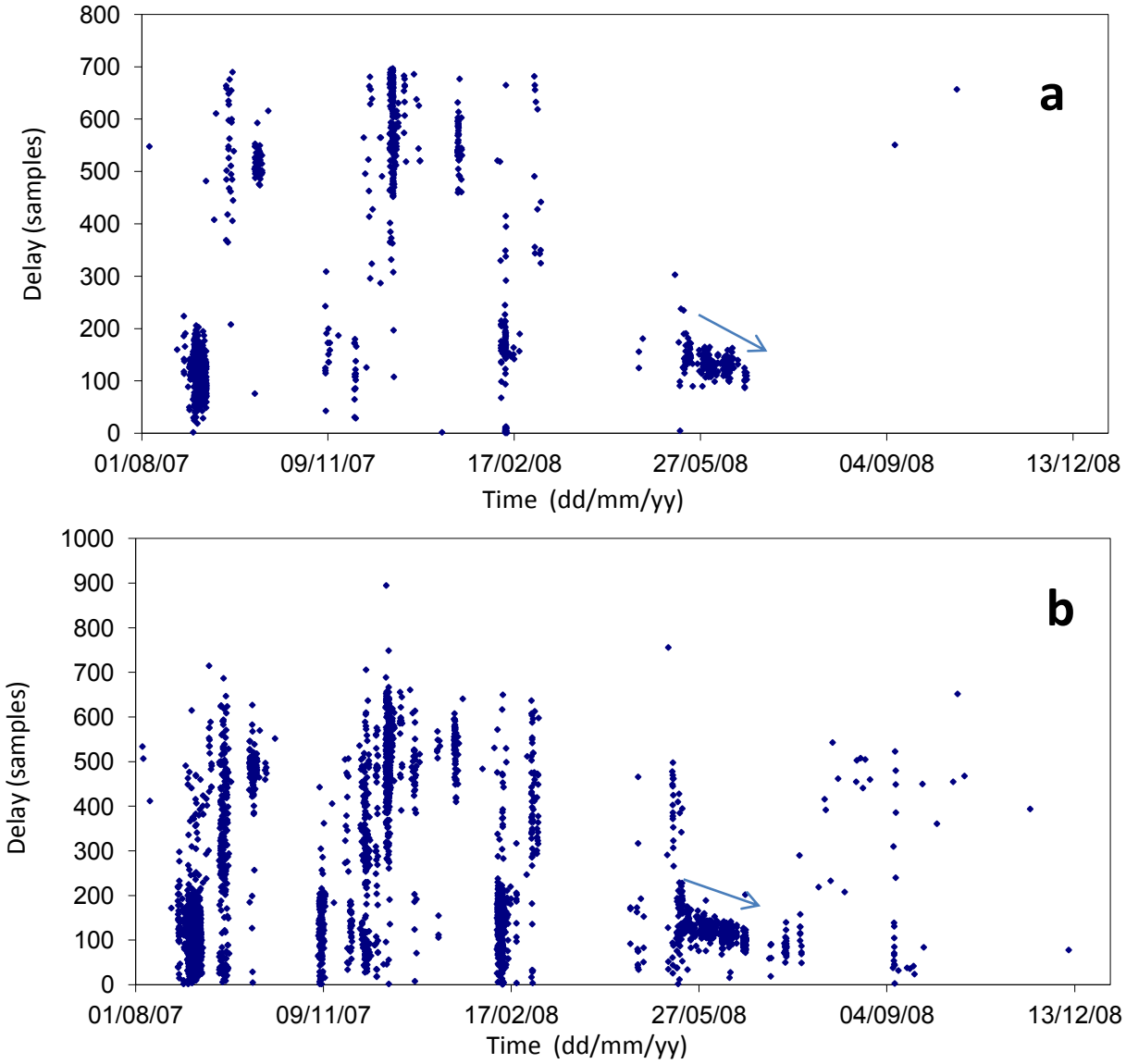

Figure. 2.6: Infrasonic arrival time delay in respect of seismic arrivals for the all the events with both infrasonic and seismic counterparts, by using threshold of a) 2.5 and b) 3 for the STA/LTA algorithm (ref. station: EBEL).

If we consider **Fig. 2.6a**, which is clearly more reliable in terms of true detections of seismic counterparts, it is possible to notice that points tend to be roughly clustered in two groups: delay time around 500 samples (5 s), are coincident with events from NEC, whereas values around or below 2 s are consistent with activation of SEC or Eruptive Fissure. Thus, it is evident that, although the NEC events are numerically dominant in respect of those from EF or SEC, only a small percentage of them has seismic counterparts. Furthermore, those seismo-acoustic events are not homogeneously distributed along the dataset. Further analyses are required to acquire more insights on the processes dealing with the seismic emission for NEC events.

It is noteworthy during May-June 2008 the decrease in the delay time, highlighted by both graphs in **Fig. 2.6a,b** (see the arrows). Considering the position of the ref. station EBEL, and the infrasonic

sources active at that time, it can be interpreted as a movement of the infrasound radiating source upward along the eruptive fissure. This evidence is extensively discussed, on the basis of the acoustic signal, in **section. 2.3.3.**

Spectral and amplitude analyses have been carried out on the whole dataset, in order to detect the existence of meaningful trend. However, no clear trends are evident, not in the whole time interval neither in the three periods (not reported in this text). In any case, it must be noted that most of the seismic-infrasound signals are representative of explosive activity (and then SEC/EF events), and a very few are recorded during non-eruptive periods (NEC events). Consequently, the absence of evident pattern related to changes observed in infrasound events at NEC may be an effect of the discontinuity of NEC seismic counterpart occurence.

2.2.1.4 Results

Different infrasound sources can be recognised during August 2007 – December 2009: SEC, EF and NEC (see **Fig. 2.7, Fig. 2.8**). As already observed in other eruptive episodes and mentioned in **section 2.1.3**, the first two sources were systematically active at the same time as sporadically explosive activity took place at the source vents, while the NEC source was characterized only by pulsatory degassing and generated infrasound events almost continuously even during non-eruptive periods.

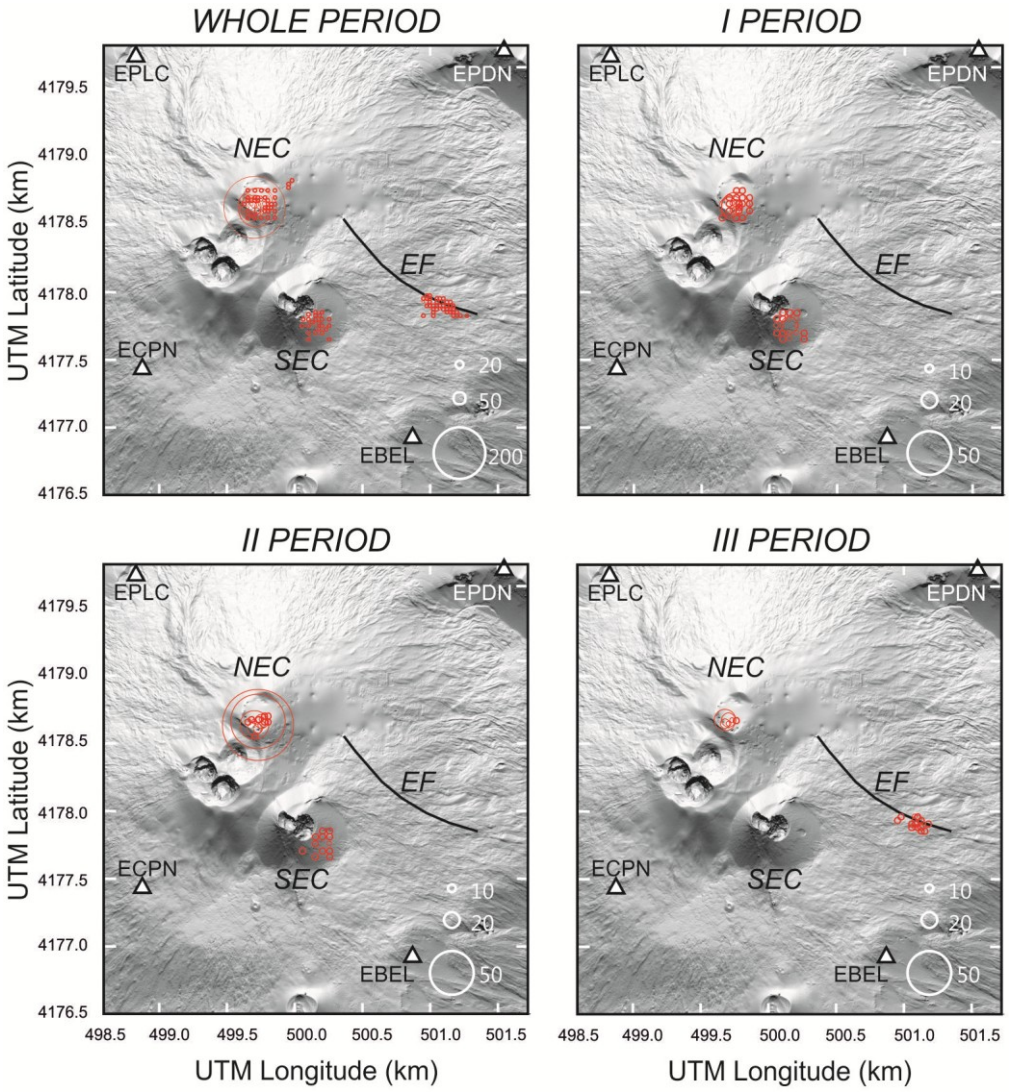

Figure 2.7: Digital elevation model of Mt. Etna summit with the source locations of the infrasound events, indicated by red circles, occurring during September 2007 – December 2008 (top left panel), and during each of the three analysed periods (I Period: 15 August - 14 September 2007; II Period: 20 November – 8 December 2007; III Period: 3 June – 29 June 2008). The radii of the circles are proportional to the number of locations in each grid node (see white circles and numbers reported in the lower right corner of the maps). The sites of the four summit infrasound sensors are indicated with triangles.

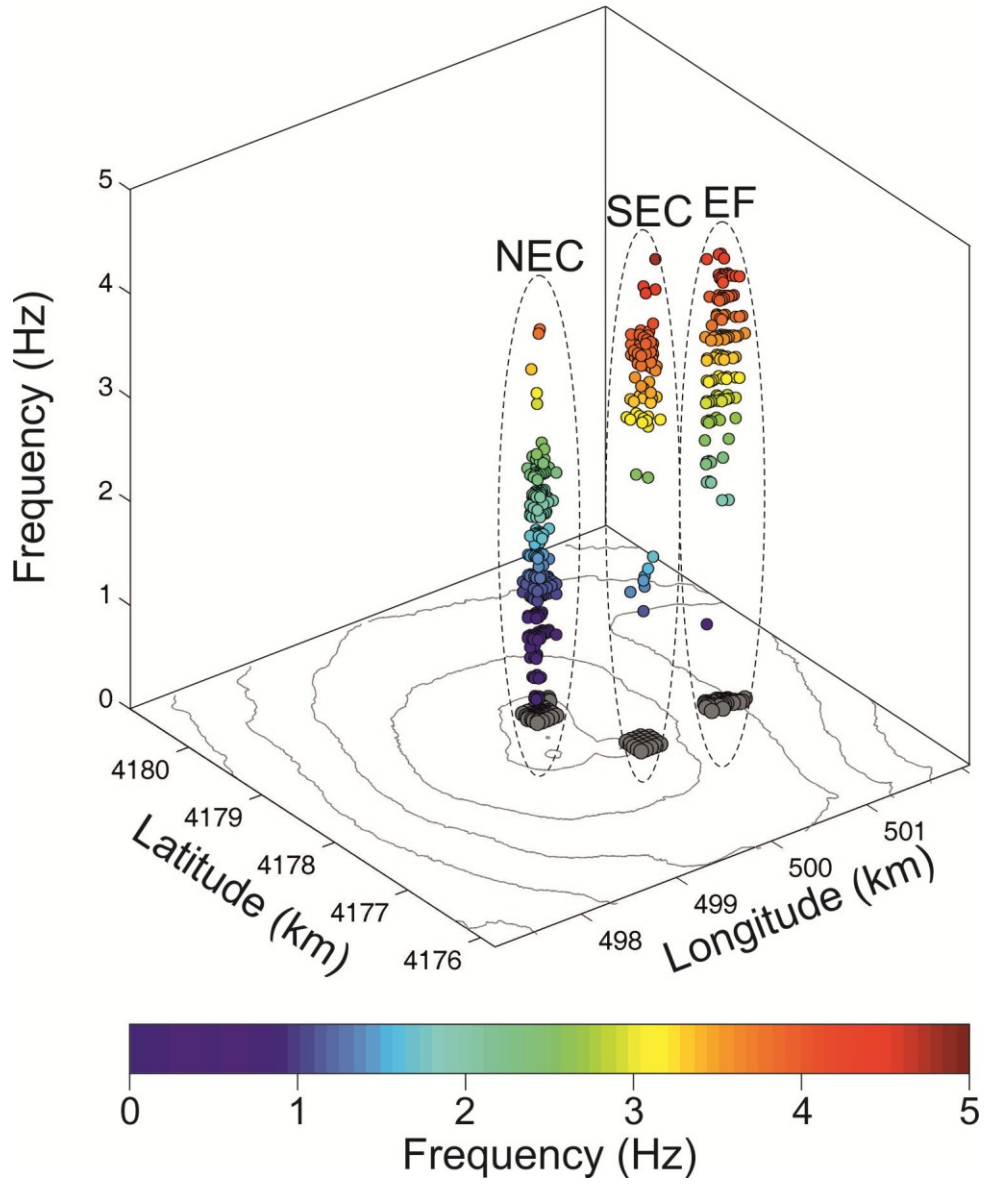

Figure 2.8: Relation between source/vent location and frequency content of infrasound events. Coloured dots represent infrasound event locations plotted against their peak frequencies (reported in z-axis and color bar, too). Gray dots indicate the projection of the coloured dots on the x-y plane.

In agreement with the previous studies (**section 2.1.3**), the frequency content of the SEC and EF events studied in this work mostly ranged from 2.5 to 5 Hz, while NEC events had frequencies below 2.5 Hz (**Figs. 2.8, 2.9**).

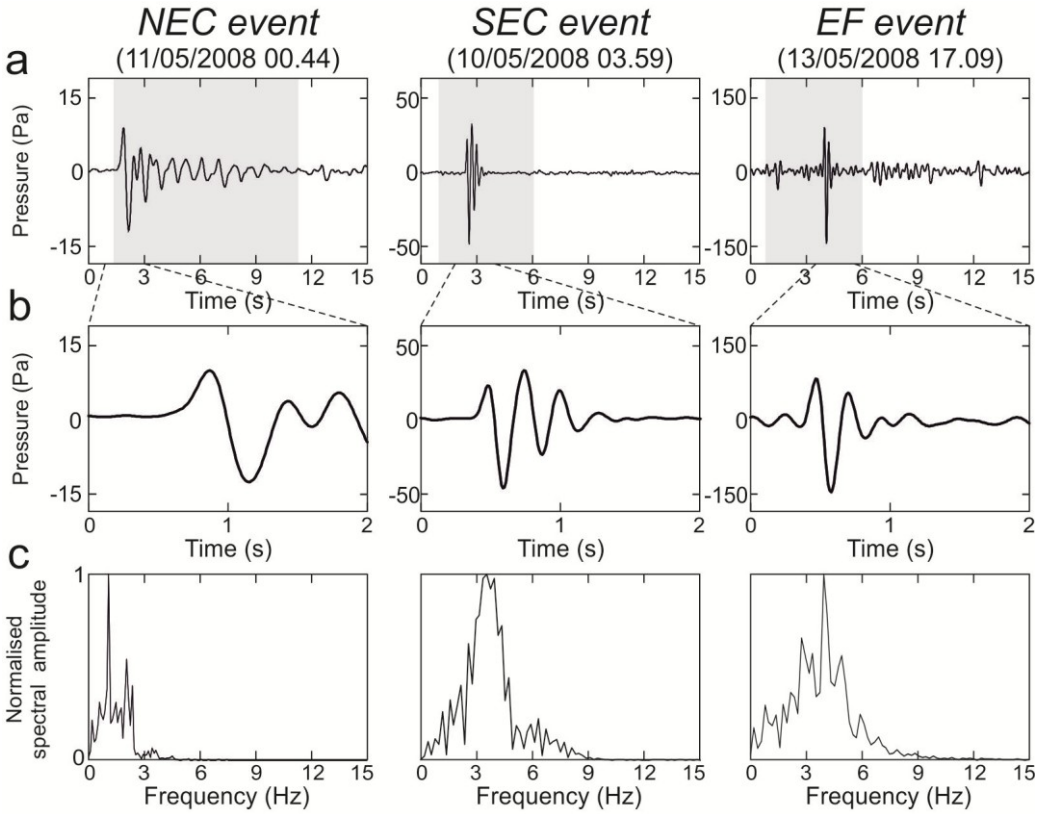

Figure 2.9: Infrasound events recorded by EBEL station and related spectra, performed on 10.24 (NEC event) and 5.12 s (SEC and EF events) time windows. The grey areas in the top plots show the signal windows used to calculate the spectra.

Furthermore, in **section 2.2.1.3** it was noted how most NEC events lacked any seismic counterpart or were accompanied by very weak seismic signals. On the contrary, SEC and EF events were often associated to seismic signals, related to explosive activity.

NEC events featured periods with very steady waveforms and spectral features lasting from days to months, with slow or sudden variations. Some examples of NEC event waveforms and spectra are shown in **Fig. 2.10**, to highlight their variability, as well as the common characters. The repeatability of the NEC waveforms is clearly evident from **Fig. 2.11**, where all the events gathered in interval of 6 consecutive hours (**Fig. 2.11a, b, c and d**) are overlapped. Finally, a clear example of steady spectral features a few-month-long period is shown in **Fig. 2.12a**, exhibiting the pseudospectogram during July-October 2008.

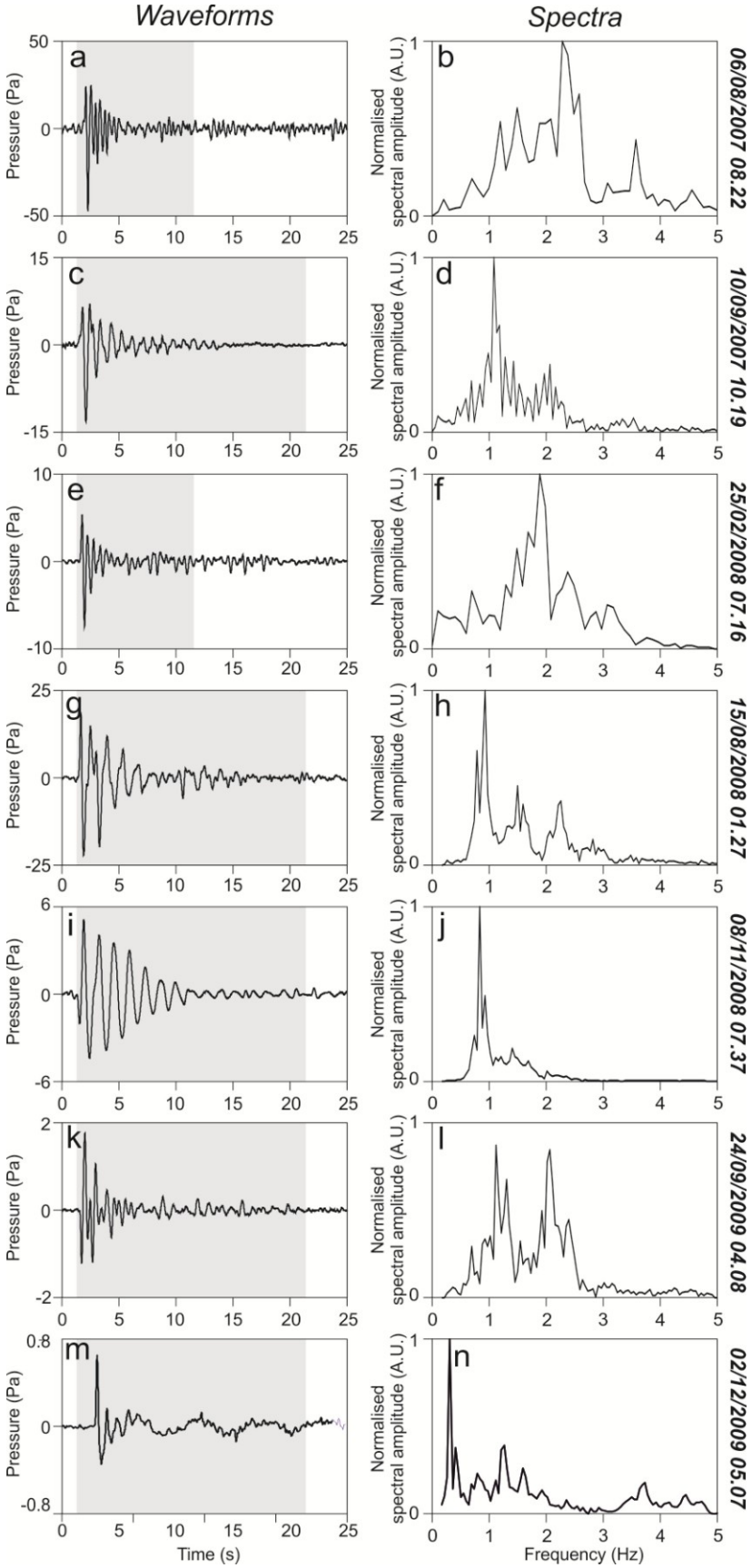

Figure 2.10: Infrasound events generated by NEC and recorded by EBEL station (the recording time is reported on the right of the plots) and corresponding spectra. The grey areas show the signal windows used to calculate the spectra. The event in (m) was recorded with broadband microphone (G.R.A.S. 40 AN).

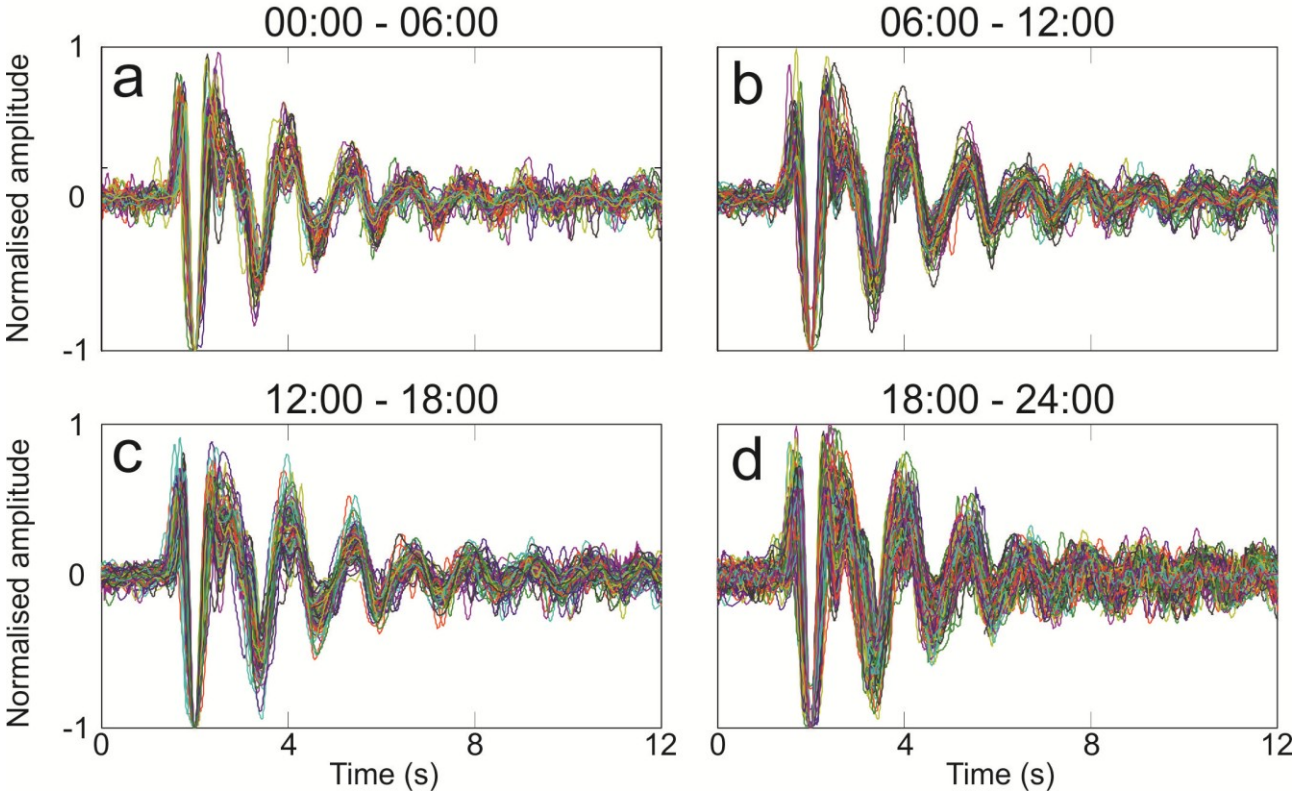

Figure 2.11: Superimposed traces of infrasonic events, recorded at EBEL station, taking place during 27 September 2008 at 00:00 – 06:00 (a), 06:00 – 12:00 (b), 12:00 – 18:00 (c) and 18:00 – 24:00 (d).

The NEC event changes mostly coincided with variations in the activity at SEC or EF. One of the most evident spectral content variations of the NEC events took place during the 2008-2009 eruption at EF. It is difficult to determine the frequency range of the NEC events preceding the beginning of the eruption on 13 May 2008 because of the fire fountaining on 10 May at SEC, and the consequent modifications of the NEC events [see Di Grazia et al., 2009]. After the eruption beginning at EF the NEC events, during June 2008, were characterised by two peaks at ~1 and 2 Hz, successively by three peaks at ~0.8, 1.5 and 2.2 Hz and finally the two higher peaks (1.5 and 2.2 Hz) gradually disappeared giving rise to an almost monochromatic signal (**Fig. 2.12**). At the end of the eruption (6 July 2009), the dominant frequency was 0.8 Hz, one of the lowest frequency values observed during the studied interval. During the months following the end of the eruption, the dominant frequency peak was gradually at higher frequencies (up to ~1.2 Hz at the end of the analysed time interval), confirming that such low frequency peaks of NEC events were somehow related to the eruption at EF (**Fig. 2.12b**).

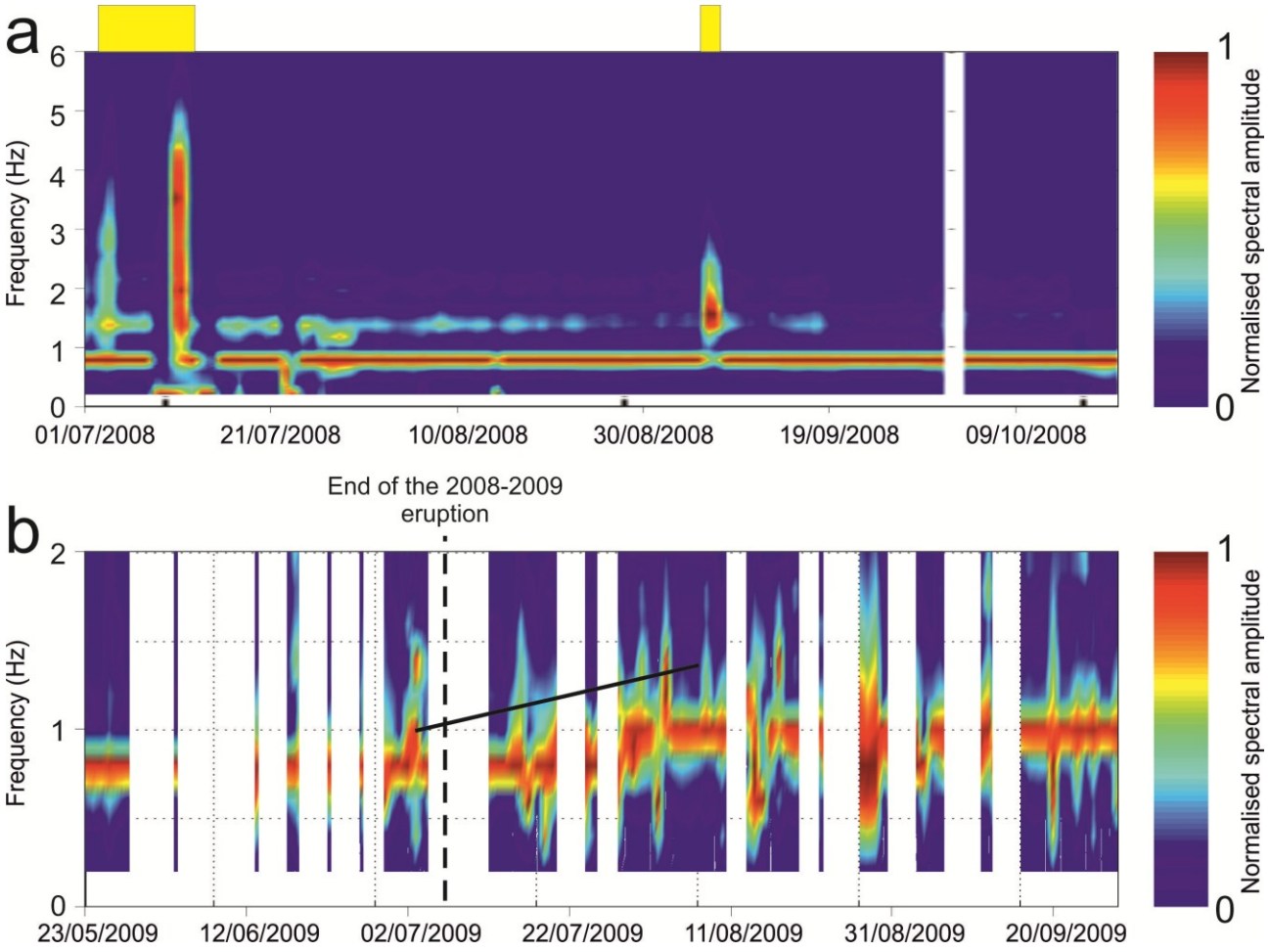

Figure 2.12: (a) Normalised pseudospectrogram of the infrasound events occurring at Mt. Etna during 1 July - 20 October 2008 and recorded by EBEL station. (b) Normalized pseudospectrogram between 23 May and 23 September 2009. Due to the long duration of the considered periods and the low occurrence rate, pseudospectrograms averaging process was performed on 24 hour windows. The dashed vertical line in (b) represents the end of 2008-2009 eruption. Black arrow in (b) highlights the post-eruption frequency increase. Please note that white stripes in (a-b) take into account: i) stations out of order, ii) noisy periods (due to strong wind) and iii) lack of infrasound events. The yellow bars at top of the plots indicate the time intervals characterised by Strombolian activity at EF. It is worth of noting that spectral changes smaller than the spectral resolution (~0.2 Hz) cannot be detected in these plots.

The evolution in time of the spectral features of infrasound events during three short periods is shown in **Figs. 2.13, 2.14** and **2.15**: i) 15 August – 14 September 2007; ii) 20 November – 8 December 2007; iii) 3-29 June 2008.

The first period was characterised by explosive activity at SEC, consisting of ash emission and Strombolian activity, culminating in an episode of fire fountaining on 4-5 September (**Fig. 2.13b**). In the normalized pseudospectrogram of **Fig. 2.13e** such activity is highlighted by high spectral amplitudes at frequencies above 3 Hz, with the frequency content of SEC infrasound events accompanying explosive activity mostly ranging from 2.5 to 5 Hz . The lack of detected infrasound events during the fire fountaining is due to the powerful infrasound tremor accompanying this eruptive activity preventing the detection of individual events, as also observed during the SEC fire

fountaining on 10 May 2008 and during the very first days of the 2008-2009 eruption [Cannata et al., 2009a]. In contrast, the events radiated by NEC mostly had peak frequencies below 2.5 Hz, with spectral content changing during the activity at SEC. Indeed, most of the infrasound energy radiated at NEC was in the 1.5-2.4 Hz band at mid-August (before both Strombolian activity and fire fountaining), whereas the events were mostly monochromatic with a frequency peak of ~1.2 Hz after the fire fountaining (**Fig. 2.13e, f**), with these peaks remaining invariant throughout the end of the first period .An increase in the duration of the NEC events is clearly highlighted by the waveform examples shown in **Fig. 2.13a**. Furthermore, slightly lower average peak-to-peak amplitude of the NEC events was observed in the ten days after the fire fountain compared to the values during the few days preceding it (**Fig. 2.13g**).

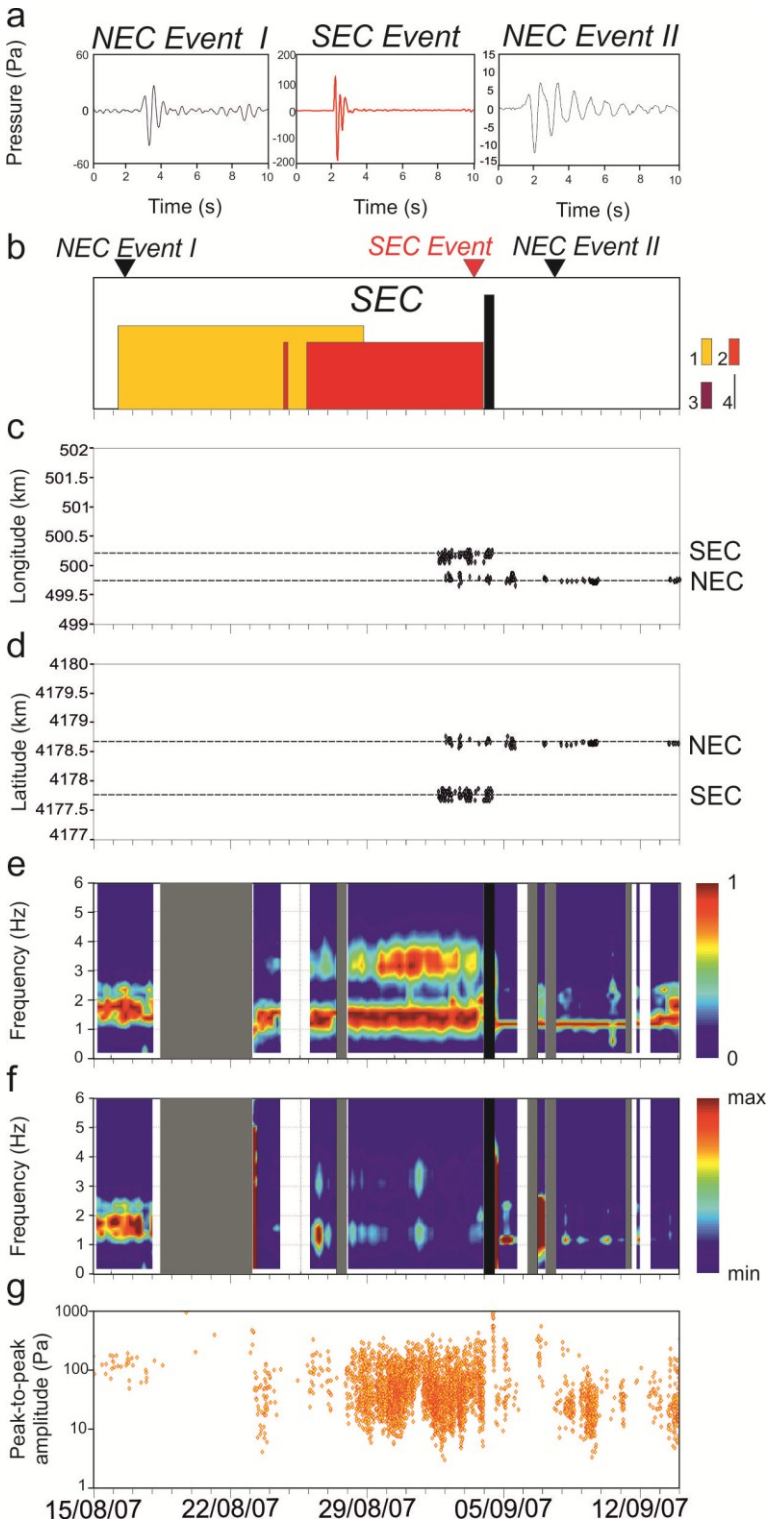

Figure 2.13: (a) Waveforms of two NEC infrasound events and a SEC infrasound event recorded by EBEL station during period I (15 August - 14 September 2007). (b) Sketch of the volcanic activity of Mt. Etna at SEC during period I (1: ash emission; 2: Strombolian activity; 3: effusive activity; 4: fire fountain). (c) Longitude and (d) latitude of infrasound events located during the first period. (e) Normalised pseudospectrogram, (f) pseudospectrogram, (g) peak-to-peak amplitude of the infrasound events occurring at Mt. Etna during period I and recorded by EBEL station. Triangles at top of (b) indicate the time of occurrence of the events shown in (a). In (e) and (f) grey rectangles represent periods of partial or complete lack of triggered events for bad weather conditions/station malfunctioning. In (e) and (f) black rectangles show periods of partial or complete lack of triggered events because of infrasonic tremor. White rectangles in (e) and (f) indicate periods when the pseudospectrograms could not be calculated because of the small number of triggered events even in good signal to noise ratio conditions.

The second period was characterised by a fire fountain occurring at SEC on 23-24 November 2007, which was preceded by some hours of Strombolian activity (**Fig. 2.14b**). Similarly to the previous period, the infrasound events radiated by SEC during such explosive activity produced peak frequencies above 2.5 Hz. Likewise in this case, the frequency peak of NEC events changed from ~2 Hz to 1.0-1.2 Hz at the end of the eruptive activity (**Fig. 2.14e,f**). Concerning the peak-to-peak amplitude, although during the 5 days following the fire fountain (strongly affected by bad weather conditions preventing detecting infrasound events clearly) very low amplitude events were recorded, no significant variations were observed (**Fig. 2.14g**).

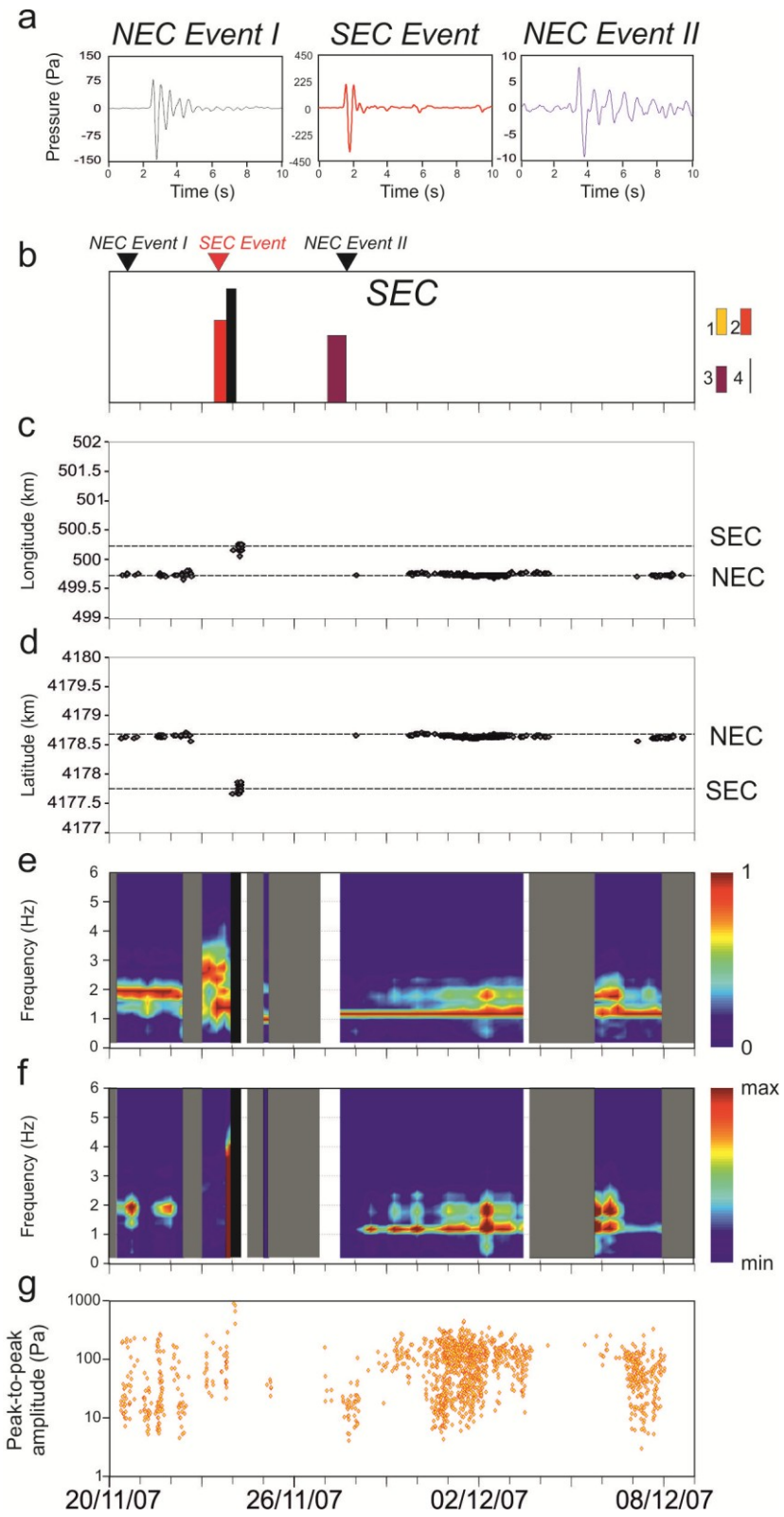

Figure 2.14: (a) Waveforms of two NEC infrasound events and a SEC infrasound event recorded by EBEL station during period II (20 November – 8 December 2007). (b) Sketch of the volcanic activity of Mt. Etna at SEC during period I I(1: ash emission; 2: Strombolian activity; 3: effusive activity; 4: fire fountain). (c) Longitude and (d) latitude of infrasound events located during the second period. (e) Normalised pseudospectrogram, (f) pseudospectrogram (g) peak-to-peak amplitude of the infrasound events occurring at Mt. Etna during period II and recorded by EBEL station. Other symbols as in Figure 2.13.

Finally, the third period (3-29 June 2008) belongs to the 2008-2009 eruption starting on 13 May 2008. This period was considered meaningful from the eruptive point of view because a renewal of explosive activity at EF took place at that time (**Fig. 2.15a**). In particular, intense Strombolian activity took place from 8 to 21 June 2008. The infrasound events radiated by EF during the Strombolian activity showed frequencies above 2.5 Hz (**Fig. 2.15e**). NEC infrasound events were characterised by two sharp frequency peaks at ~1 and 2 Hz before this activity, and by three peaks at ~0.8, 1.5 and 2.2 Hz after (**Figs. 2.15e,f**). The peak-to-peak amplitude values of the NEC events slightly decreased after the Strombolian activity at EF (**Fig. 2.15g**).

It is noteworthy that all the observation that were done in the present thesis by using the pseudospectrograms of **Fig. 2.13, 2.14** and **2.15** are fully confirmed by the pseudospectrograms, drawn without any averaging process, (see **Fig. 2.16)** demonstrating that averaging process, provided the choose of the proper time window for the average process, is not affecting at all the analysis of the datum.

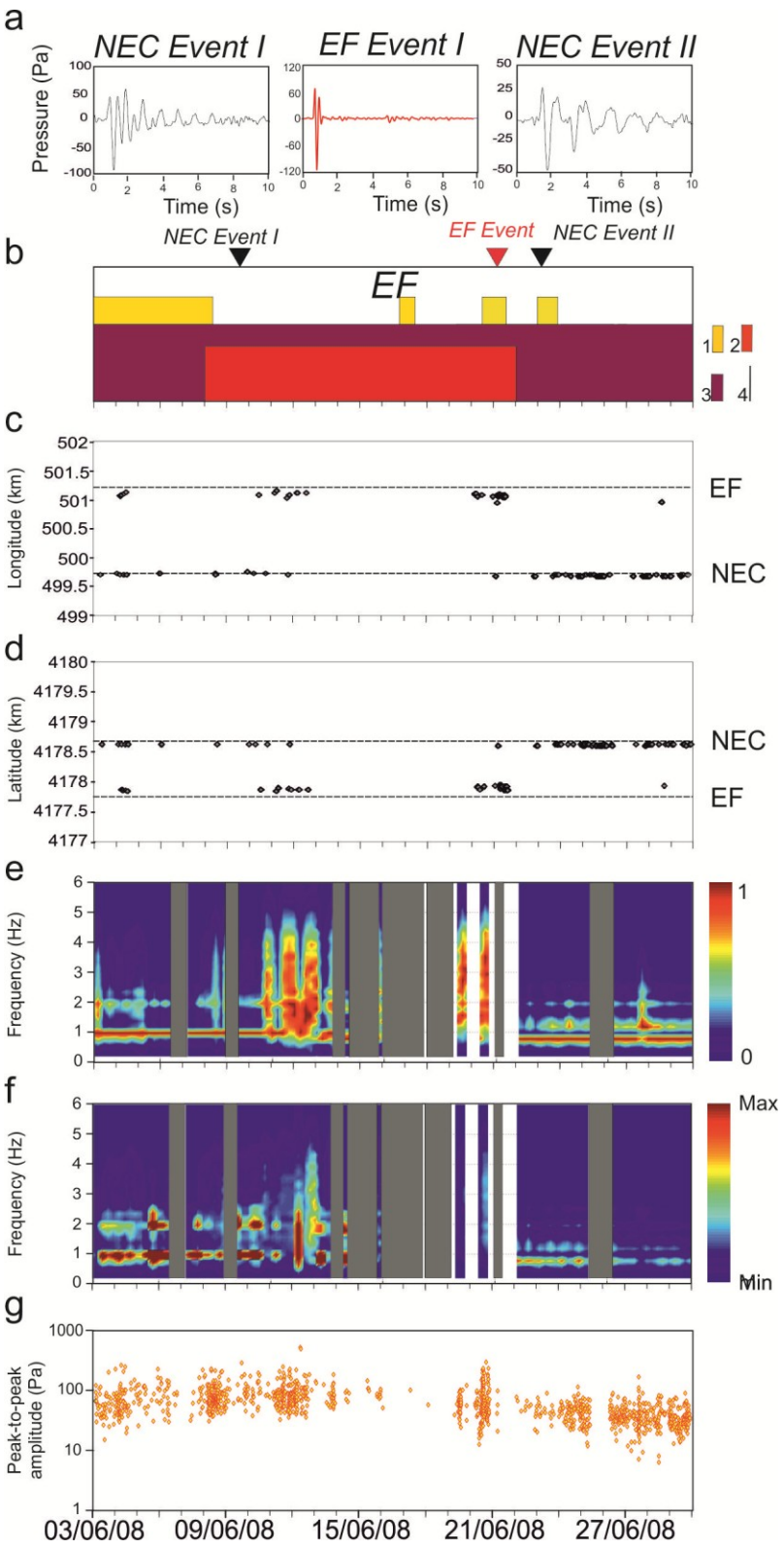

Figure 2.15: (a) Waveforms of two NEC infrasound events and an EF infrasound event recorded by EBEL station during period III (3 June – 29 June 2008). (b) Sketch of the volcanic activity of Mt. Etna at EF during period III(1: ash emission; 2: Strombolian activity; 3: effusive activity; 4: fire fountain). (c) Longitude and (d) latitude of infrasound events located during the third period. (e) Normalised pseudospectrogram, (f) pseudospectrogram (g) peak-to-peak amplitude of the infrasound events occurring at Mt. Etna during period III and recorded by EBEL station. Other symbols as in Figure 2.13.

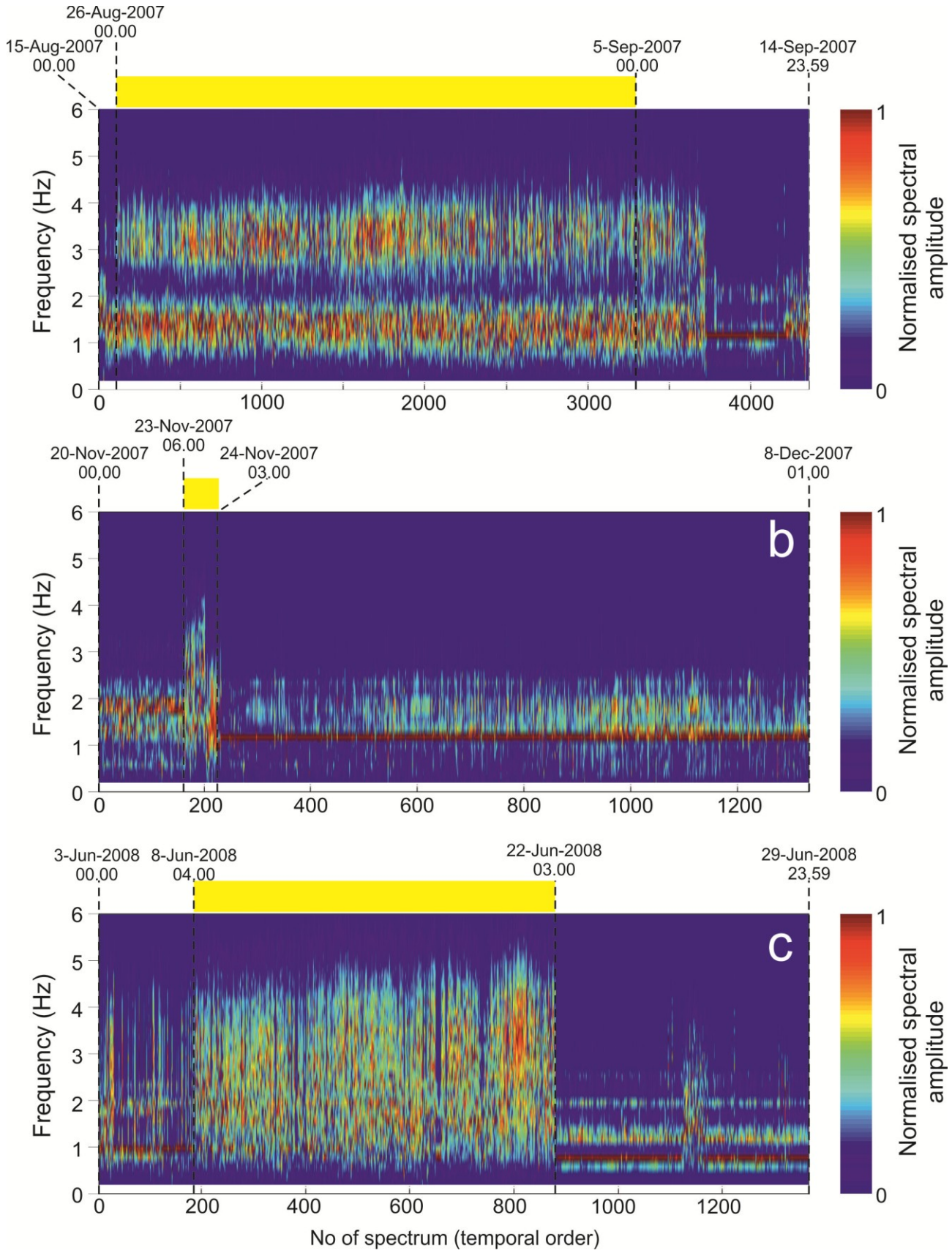

Figure 2.16: Pseudospectrograms gathering the spectra of the infrasound events taking place during 15 August – 14 September 2007 (a), 20 November – 8 December 2007 (b) and 3– 29 June 2008 (c). Unlike the pseudospectrograms in Figures 2.13-2.15, these do not involve averaging process and then show in the x-axis the number of spectrum in place of the time. The yellow bars at top of the plots indicate the time intervals characterised by Strombolian activity and/or fire fountain at SEC (a,b) and EF (c).

2.2.2 Development of a model for North East Crater shallow feeding system from acoustic and seismic data (12-13 May 2008)

In **section 2.1.3** some of the characteristics of NEC events, evidenced from previous studies, have been described. In particular, as previously said, Sciotto et al. [2013] found two dominant spectral components (0.4–0.7 Hz and 1.5–2.0 Hz) in NEC events recorded some hours before the onset of the 2008-2009 eruption. Contemporaneously, as described in details in **section 2.2.1.4**, similar observations were done in the dataset used for this work, since the replacement of the Monacor station with a G.R.A.S. microphone (November 2009). It is noteworthy that also nowadays the analysis of the recordings reveals that these features are peculiar of NEC events (Cannata, personal communication).

Therefore, together with the Dr. Mariangela Sciotto of University of Catania, a unique source model was developed in order to fit both datasets. The application of the model to the 12-13 May 2008 dataset is fully described in Sciotto et al. [2013]. Here a short description of the model, whose validity will be proved for the dataset of the present thesis, is provided.

NEC events usually display regularly decaying sinusoidal waveforms and often their spectra showed harmonics [Cannata et al., 2011; present thesis], exclusively in the higher frequency band (1.5-2.0 Hz). Consequently, is reasonable to assume that sound emission is related to phenomena of standing wave-resonance in the conduit. Degassing processes at the free magma surface inside the NEC conduit are likely to excite these resonance phenomena. There is no evidence, not in this work neither in previous analyses, of two sets of resonance modes, as we would expect for a bi-dimensional resonator source such as a dyke. Therefore, the resonating source is assumed to be cylindrical. Indeed, radial resonance modes are negligible for wavelength much longer than the radius of the conduit (see also **section 1.2.5**). The shallow portion of the conduit, directly connected with the atmosphere, is believed to correspond to such cylindrical resonator. In particular, according to the observations of the present work, only integer harmonics are present, therefore the resonating part must correspond to an open-open or either closed-closed resonating system (see **section 1.2.5).** The lowest termination of the resonator was assumed to correspond to the magma surface. It is noteworthy that the same assumption was already done in literature for acoustic resonance occurring at other volcanoes [i.e., Shishaldin, Petersen and McNutt, 2007; Kilauea, Fee et al., 2010a]. Therefore, for NEC, a closed termination is expected to be at the upper

end, and it was identified with the cross-section restriction at the base of the funnel shaped crater, below the termination of NEC funnel shaped crater, as clearly recognizable from visual inspection. As previously observed, indeed, the lack of obstruction, a necessary condition for acoustic waves to propagate, does not imply the acoustically opening of the resonator, which is dependent on the impedance contrast at the termination. Thus, the resonating portion of the NEC conduit was inferred to be comprised between the free magma surface and a narrowing (upper end), filled with a gas-mixture. The fundamental frequency of resonance is given by equation (**2**).

However, the upwards-narrowing of the conduit makes it to behave also like a Helmholtz resonator, akin to a bottleneck through which gas can escape, radiating low frequency and monochromatic infrasound. Equation (**3**) indicates the relation between the observed frequency of radiated sound and the geometry of the Helmholtz resonator. Therefore, the high frequency peak (1.5-2.0 Hz) of the NEC infrasound events investigated by Sciotto et al. [2013] was interpreted as resulting from pipe resonance, while the low frequency peak (0.4-0.7 Hz) from Helmholtz resonance.

Accurate analyses have been done in order to prove the consistency of the model, and the observance of the required conditions in order to have both kinds of resonance simultaneously. Unknown parameters in the equation (**3**), such as the radius of the conduit or the length of the neck of the Helmholtz resonator, were determined by cross checking the geometry calculated with equation (**2**) and (**3**) from the spectral observations [Sciotto et al, 2013]. A whole range of acoustic velocity (400-750 m/s) was taken into account, on the basis of the composition of NEC plume measured from La Spina et al. [2010] and considering several temperatures up to a maximum of 1200 °K. Conduit radius was found to be comprised between 25 and 45 m, in agreement with previous literature studies [see also Bonaccorso and Davis, 1999], while the length of the neck was found to affect marginally the determination of the frequency. Furthermore, the amount of energy transmitted or reflected through the narrowing was computed by using the transmission and reflection coefficients [Raichel, 2006].

As clearly visible in **Fig. 2.17,** in the frequency band of interest for this work, assuming a conduit radius of 25 or 45 m, good level of acoustic energy transmission through the narrowing is observed. Nevertheless, the transmitted energy decreases for higher frequencies. It is noteworthy that, according to **Fig. 2.17**, assuming that the resonance is triggered from the bursting of a slug at the free magma surface, the high frequency acoustic waves, expected for such type of acoustic

source, would not be detectable outside from the crater, as the constriction acts as low pass filtering.

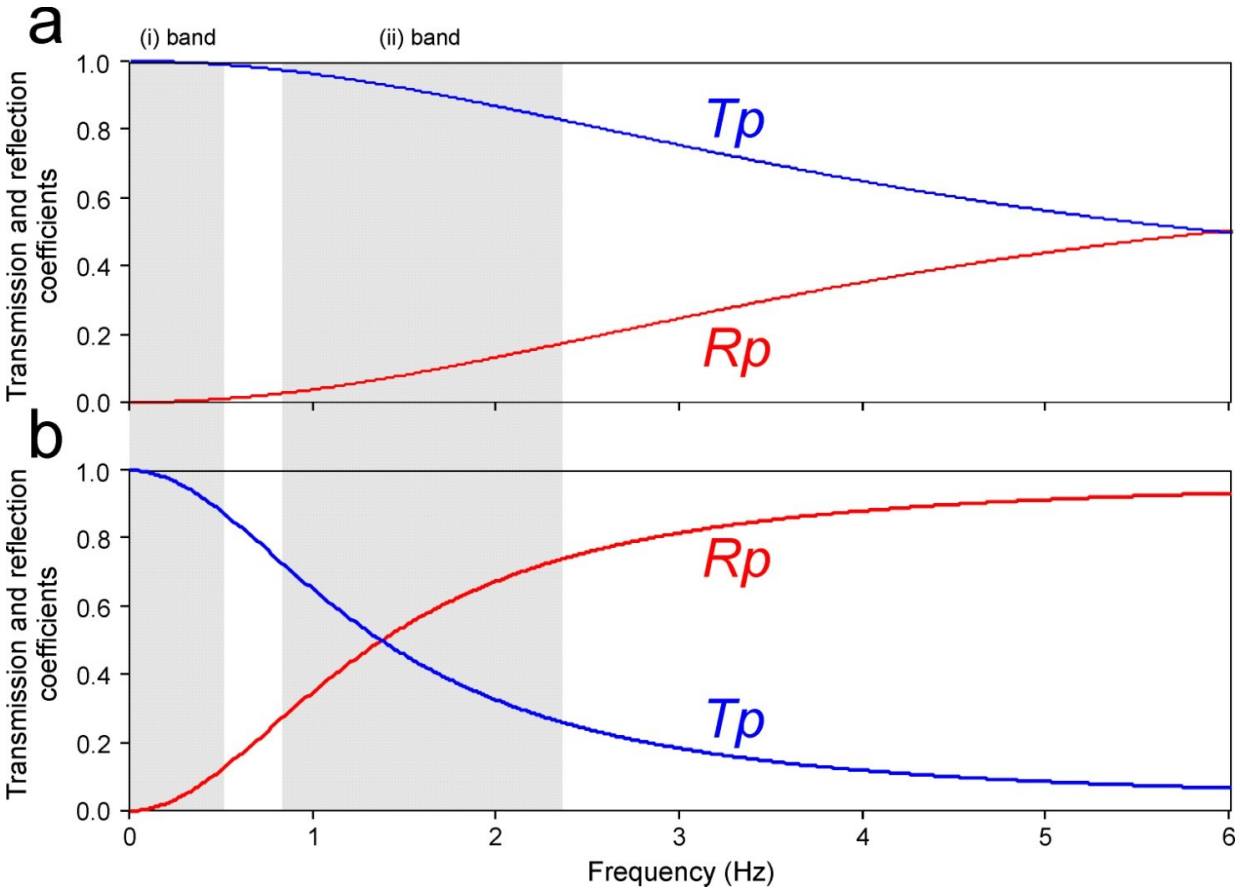

Figure 2.17: Frequency dependence of power transmission (*Tp* blue lines) and reflection (*Rp* red lines) coefficients through the narrowing, assuming a conduit radius of 25 (a) and 45 m (b). The gray areas highlight the two frequency components characterizing NEC events as observed in the present thesis (redrawn from Sciotto et al., 2013).

Finally and interestingly, it should be noticed that a similar example of double resonance exists already in nature, in the human vocal system. Indeed, when pronouncing the vowel "i", the jaw and the tongue body are raised, creating a narrow front cavity, and the tongue body is moved forward, enlarging the back cavity [e.g. Diehl, 2008]. Therefore, the front cavity resonates as an open-closed pipe whereas the back cavity is contemporaneously resonating as a closed-closed pipe and as a Helmholtz resonator. [e.g. Johnson, 1997; Diehl, 2008]. The interaction of the sound field produced from these sources gives the vowel "i".

2.2.3 Discussion

The infrasound signals continuously recorded from August 2007 to December 2009 at Mt. Etna by a permanent network were analyzed. About 40,000 infrasound events were detected, most of which were generated by NEC. Indeed, as already mentioned, although NEC has only been characterized by pulsing degassing, it has almost continuously emitted infrasound events. The source of these events, characterized by frequency lower than 2.5 Hz, has been attributed by previous papers [Sciotto et al., 2011, 2013] to resonance phenomena of the shallowest portion of the NEC plumbing system. It has sporadically been noted that the spectral features of NEC events changed before, during and/or after eruptive activity at other vents [e.g., Sciotto et al., 2011, 2013].

The large dataset analyzed in this work gives us the opportunity to investigate the NEC infrasound that until now was only investigated during short time intervals, in a long and continuous period. In particular, the following questions are addressed:

1. How steady (or vice versa variable) are the waveform features of the NEC events investigated during year-long time periods?
2. How systematic (or vice versa sporadic) are the spectral changes of the NEC events time-related to eruptive activity at other vents?
3. Is the two resonator NEC model, proposed in previous papers, suited to explain all the observations made during 2007-2009?
4. Are the interpretations given to spectral changes found in previous investigated eruptions confirmed? If so, may the changing sizes of resonating structures, due to level oscillations of magma column, be used to estimate pressure fluctuation in the main plumbing system?

Regarding the first issue, it was noted how NEC events featured periods with very steady waveforms and spectral features lasting from days to months (for instance July-October 2008 in **Fig. 2.12a**), with slow or sudden variations. The steadiness of the waveforms during long periods highlights the repetitive nature of the NEC infrasound events, and then of their source mechanism. This behavior has also been noted at other volcanoes, such as St. Helens [Matoza et al., 2007], Fuego [Erdem and Waite, 2013] and Shishaldin [Petersen and McNutt, 2007]. The detected waveform changes consisted of variations of amplitude, duration and frequency content, and in

particular spectral peak shifts and disappearances/appearances. The most important eruptive episodes taking place during the analyzed time interval were accompanied by sudden variations of NEC events: the infrasonic NEC changes during the 4-5 September and 23-24 November 2007 fire fountains at SEC are documented here; during the 10 May 2008 fire fountain at SEC and the onset of the 2008-2009 eruption at EF on 13 May are described in Di Grazia et al. [2009] and Sciotto et al. (2013), respectively; during the Strombolian activity occurring from 8 to 21 June 2008 at EF here; and finally during the entire 2008-2009 eruption (considered as a single episode) here, too (**Table 2.1**).

The same behavior was also observed during the explosive activity at SEC on 16 November 2006, that was preceded and accompanied by dominant frequency increases and decreases, respectively [Sciotto et al., 2011]. Therefore, these NEC infrasound variations can be considered systematic, hence answering to the second issue. In all the cited cases taking place during 2006-2009 (**Table 2.1**, documented both in this thesis and in previous papers), at least the spectral content changed and, in particular, a decrease in the dominant frequencies was noticed right after (or during, taking into account the whole 2008-2009 eruption) the eruptive episodes, or vice versa their increase right before (it was clearly noted once, before the 2008-2009 eruption onset).

An important implication of this systematic behavior regards the plumbing system geometry and in particular the relationship between the systems feeding the distinct considered vents (NEC, SEC, and EF). Indeed, on the basis of this study it is possible to state that the connection between NEC and SEC/EF plumbing systems is not simply temporary and related to a given considered episode (such as the onset of the 2008-2009 eruption on 13 May for EF-NEC connection, or the 16 November 2006 episode for SEC-NEC), but rather it is stable even considering a relatively years-long time interval. The relationships among summit craters at Mt. Etna have also been studied on the basis of volcanological and geochemical information. Corsaro and Pompilio [2004] made an integrated study of compositional, volcanological and geophysical data, and found that during 1995-1999 the products emitted by NEC, VOR and BN craters displayed common petrographical and geochemical features, whereas SEC products were more highly differentiated than those of the other craters until January 1999. As specified in **section 2.1.2,** Corsaro and Miraglia [INGV staff, 2007-2013], analyzing the similarity in major element compositions and the inferred temperature of pyroclastic products emitted from NEC and SEC in July 2006, pointed to a possible common feeding system of these two vents. More recently, during 2008-2009, analysis of the composition of the main gases from NEC and VOR-BN volcanic plumes suggested that NEC

branches off from the central conduit at depths of 2.3 km from the volcano summit [La Spina et al., 2010].

In order to answer the third and fourth issues, concerning the interpretation of such systematic changes, it could be useful to briefly recall NEC event features and source model, fully described in **sections 2.2.1.4** and **2.2.2**. NEC events, analyzed in this thesis, are characterized by two frequency bands: <0.5 Hz (see **Fig. 2.10m,n**) and 0.8-2.3 Hz (see **Fig. 2.10a-n**), both consisting of decaying sinusoids, with the highest frequency peak showing integer harmonics [see **Figs. 2.10g,h,k,l** and **2.15e,f**]. According to the double resonator model, the lower frequency band is due to Helmholtz resonance of the volume of conduit comprised between the free magma surface and a narrowing at the base of the funnel shaped crater. However, the same portion of the conduit is responsible for a standing wave resonance, which produces the higher frequency band. Our data (also thanks to the G.R.A.S. microphone installed in November 2009) and analyses confirm the validity of the model in a much longer period, and, consequently, the double source mechanism previously described is inferred to generate NEC events during the entire interval investigated in this work. Therefore, on the basis of such a model, the spectral content variations time-related to the eruptive activity, that in this thesis involved the NEC higher frequency band, could be related to an increase in the length of the resonator and/or decrease in the acoustic waves velocity, according to the equation (**2**).

Fig. 2.18 displays the values of the frequency for different values of conduit length and acoustic waves velocity. In particular, since infrasound waves propagating in a hot gas mixture above the free magma surface were hypothesized, the acoustic waves velocity is a function of the composition and temperature of the medium, in which the acoustic waves propagate. In this thesis the limits of the range of possible values of acoustic velocity were chosen as follow: the sound velocity in air at 20°C was considered as the lower limit for *c* (340 m/s), whereas the value of 750 m/s as upper one, according to Sciotto et al. [2013], wherein it was calculated on the basis of the composition of NEC plume measured from La Spina et al. [2010] and considering a temperature of 1200 °K.

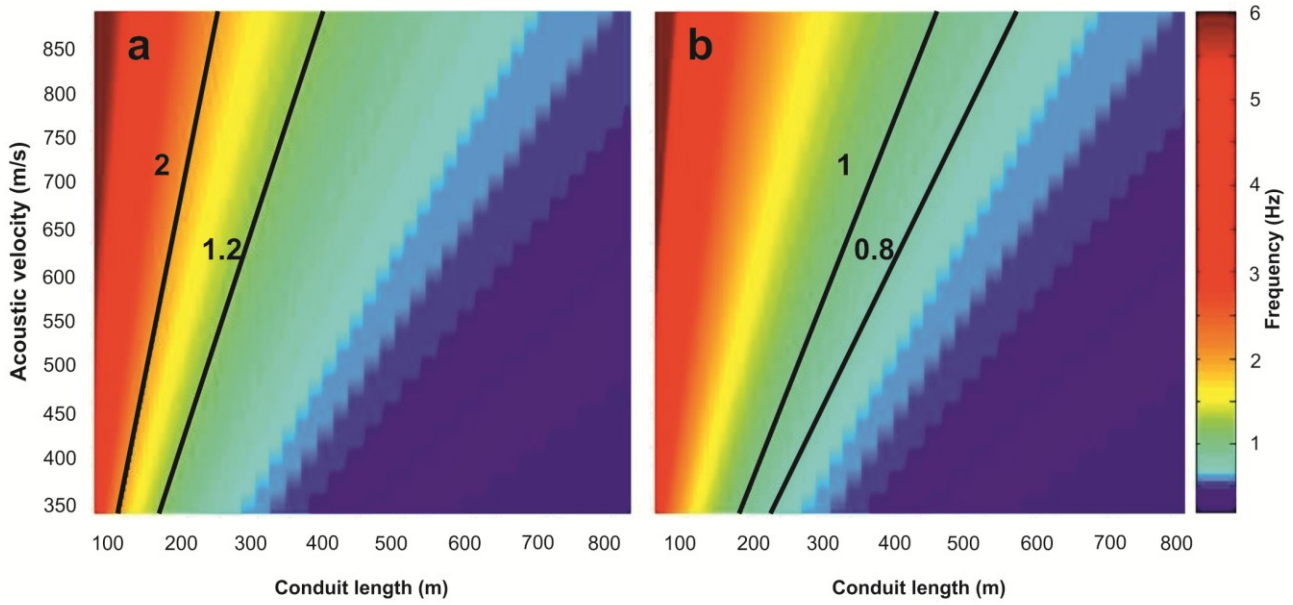

Figure 2.18: Fundamental frequency of the resonating conduit for variable length and acoustic velocity. The solid black lines represent the observed dominant frequencies before and after eruptive activity, corresponding respectively to values of 2 and 1.2 Hz during the first-second periods (a), 1 and 0.8 Hz during the third period (b).

Focusing on the relationships between acoustic velocity and gas composition, in a pure gas mixture with H_2O, acoustic velocity decreases with the increasing content of SO_2 (or CO_2). Indeed, for a H_2O rich gas mixture at 800 °K, adding 50% in weight of SO_2 (or CO_2), acoustic velocity decreases from 695 m/s to 560 and 550 m/s, respectively [Morrissey and Chouet, 2001]. For the same gas mixture, Kumagai and Chouet [2000] found that, with varying composition and temperature, acoustic velocity ranges from several hundred to 1000 m/s (the latter for a pure H_2O gas at 1600 °K). On the basis of these studies, a decrease in the acoustic wave velocity would imply an increase of SO_2 (or CO_2) in the gas mixture filling the conduit. On the other hand, fixing the acoustic velocity at 500-600 m/s, the decrease in the dominant frequency leads us, by using equation (**2**), to infer a lengthening of the resonating conduit from 125-150 m to about 200-250 m after the end of the first and second eruptive episodes. In the third episode, we can infer that the length of the conduit increased from 250-300 m to about 310-380 m (**Table 2.1**).

Between the two described possibilities, namely changes in acoustic wave velocity or in geometrical resonance properties of the conduit, the latter is more reasonable for the following reasons. First, neglecting the frequency component < 0.5 Hz, the lowest frequency values at NEC (0.8-1.0 Hz) were reached during the eruption at EF and increased only after its end. In light of this evidence, the maximum lengthening of the resonating conduit is reasonable during the 2008-2009 eruption, considering the effective magma drainage within the shallow plumbing system (and

consequently magma surface drop) concomitant with the activity of the topographically low EF vents (**Fig. 2.19b**).

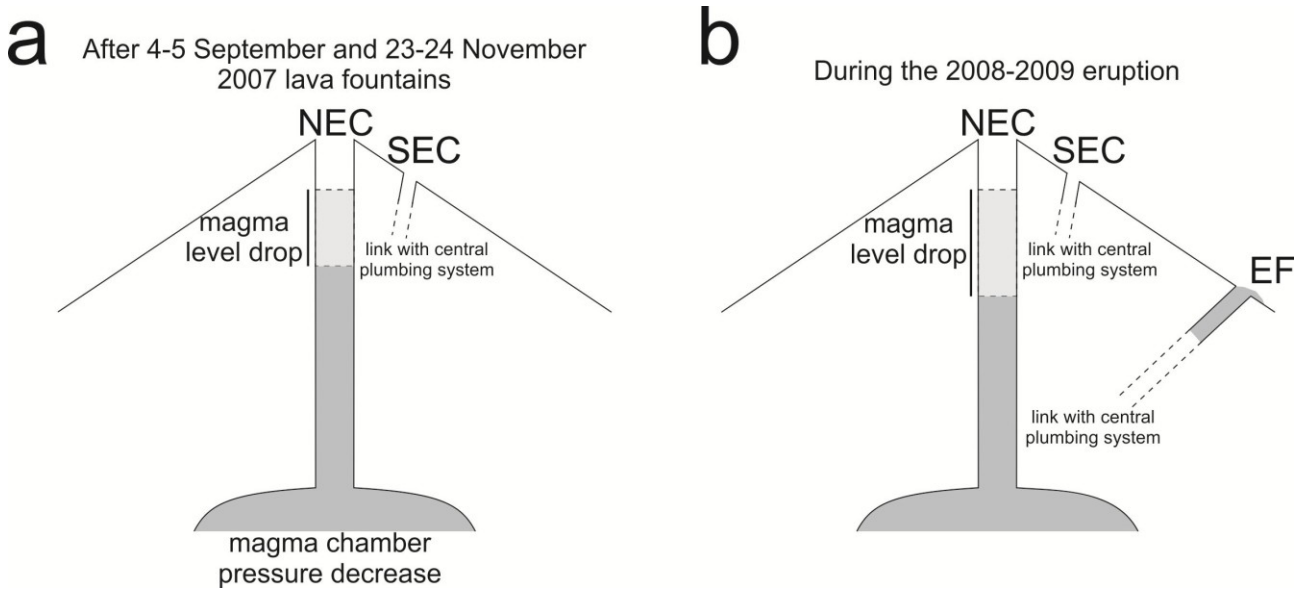

Figure 2.19.:(a) Mt. Etna sketch section showing the drop in the magma level inside the NEC conduit due to the pressure decrease in the magma chamber, taking place after the fire fountains of 4-5 September and 23-24 November. (b) Mt. Etna sketch section showing the drop in the magma level inside the NEC conduit due to the effective magma drainage from the topographically low EF vents. See text for details. Note that this model is purely qualitative.

Moreover, the mismatch between the stability of the dominant frequency at 0.8 Hz, lasting from the end of the third period (end of June 2008) to the end of the eruption (6 July 2009), and the large variability of the gas plume composition during the same period, evidenced by the CO_2/SO_2 ratio values reported by Aiuppa et al. [2010], suggests that the spectral variations were likely generated by changes in geometry rather than in acoustic wave velocity. In any case, we cannot rule out minor contribution by the latter or by the interplay between the two factors. The inferred drop in the magma level inside the plumbing system, giving rise to the observed infrasound spectral feature changes, is also reasonable after the fire fountainings taking place during 4-5 September and 23-24 November 2007 (periods I and II, respectively). Further support for this inference comes from the observation that the occurrence of fire fountains is generally accompanied/followed by slight deflation due to plumbing system depressurization, as shown by tilt data during the 10 May 2008 fire fountain [Bonaccorso et al. 2011b]. If we consider a simple plumbing system composed of a magma chamber connected to a vertical open-conduit, in equilibrium conditions the pressure inside the chamber must be balanced by the magmastatic pressure of the conduit [e.g., Witham and Llewellin, 2006]. Therefore, a pressure decrease in the magma chamber causes the magma to flow from the conduit back into the chamber, with a consequent magma level drop inside the conduit (**Fig. 2.19**). In the light of these evidences, the

answer to the third issue is: the observations made in this work strengthen the interpretations of the NEC infrasound changes, time-related to eruptive activity, in agreement with the double resonance model and those given in previous studies [especially Sciotto et al., 2013]. In any case, only multidisciplinary investigations focused on NEC acoustic wave velocity and gas composition measurements may definitively assess the role of changes in composition and temperature of the gas in the NEC infrasound variations.

Date	Eruptive phenomena	Frequency variation	Inferred conduit length variation (c = 575 m/s)	Inferred magmastatic pressure variation (magma density = 700 to 2700 kg/m^3)	Reference
16 Nov 2006	Strombolian activity	1.2 → 1.0 Hz	~50 m	-0.3 to -1.3 MPa	Sciotto et al., 2011
4 - 5 Sep 2007	Lava fountain	2.0 → 1.2 Hz	~100 m	-0.7 to -2.6 MPa	Present work
23 - 24 Nov 2007	Lava fountain	2.0 → 1.2 Hz	~100 m	-0.7 to -2.6 MPa	Present work
10 May 2008	Lava fountain	2.0 → 1.2 Hz	~100 m	-0.7 to -2.6 MPa	Di Grazia et al., 2009
13 May 2008	2008-2009 eruption onset	0.4 → 0.7 Hz	~-200 to -400 m	1.5 to 11.0 MPa	Sciotto et al., 2013
8 - 21 Jun 2008	Strombolian activity	1.0 → 0.8 Hz	~70 m	- 0.4 to -1.9 MPa	Present work

Table 2.1. Documented episodes of explosive activity at SEC and EF, accompanied by changes of NEC event features. The frequency peak variations, together with the inferred conduit length variations, the corresponding magmastatic pressure variations and the references, are also indicated. The negative and positive inferred conduit length variations correspond to decrease and increase of the length of the resonating portion of the column. The negative and positive inferred variation of magmastatic pressure indicates decrease and increase of the pressure inside the plumbing system.

Such a geometrical interpretation has important implications concerning the pressure changes over time inside the plumbing system. Indeed, the fragmentation level drop was estimated roughly equal to ~ 60-100 m in all the three considered episodes (**Figs. 2.13, 2.14, 2.15**). Assuming a constant value of magma density inside the conduit in the range 700-2700 kg/m^3 [gas-magma foam and bubble-free magma, respectively; e.g., Pinkerton et al., 2002], the pressure decrease inside the plumbing system, consequent to the drop of the magmastatic pressure, of ~0.4-2.6 MPa (**Table 2.1**), was calculated following the explosive activities at SEC and EF. Since there are major uncertainties in this evaluation related to the several assumptions, the order of magnitude of such pressure variations has to be taken into account.

Finally, it is worthy to briefly focus on the slight amplitude decreases of NEC events, observed during episodes I and III (**Figs. 2.13, 2.15**), after the end of SEC fire fountain and EF Strombolian phase, respectively. The resonance is likely to be triggered by an impulsive event (a Dirac function), that can be induced by repetitive bursting of large bubbles at the top of the magma column. In that case, the decrease in amplitude of NEC events, observed after an eruptive phase, could be related to the decrease of the inner gas overpressure within the bubbles triggering the phenomenon. However, none of the mechanisms already proposed at the origin of the slug overpressure, such as the crossing of a flare [James et al., 2004; 2006] or the massive foam coalescence at depth [Vergniolle and Brandeis, 1996], can explain the decrease in amplitude after the eruptive phase. Alternatively, for longitudinal modes of a resonating conduit, the amplitude of

the pressure fields scales directly with the volume of the source (i.e., the bursting slugs) and/or with the acoustic impedance at the vent [Garces and McNutt, 1997]. According to the latter, the observed amplitude decrease derives by a change in the properties of the medium in which acoustic waves propagate, i.e. changes in the composition of gas filling NEC conduit. We discard this hypothesis, basing on the same considerations previously exposed. Diminishing the volume source (i.e., volume of bursting slug) plays the same effect. Similar considerations could be derived by Del Bello et al. [2010] for cylindrical bubble, such as slugs. Their study indicates that, although a minor role is played by magma properties (viscosity and density) and conduit geometry (i.e., conduit radius), volume is the main factor affecting slug overpressure. Thus, a decrease in slug volume causes a decrease in overpressure of the source triggering resonance. Such reduction in slug dimension is likely to be linked, among the other causes, to a drop in gas flux at the end of the eruptive activity. Accordingly, the deepening of the magma free surface inside the NEC conduit could result in a decrease in overpressure of these gas slugs, producing the observed decline in NEC event amplitudes.

2.3 Insights into explosive activity at closely-spaced eruptive vents using infrasound signals: Example of Mt. Etna 2008 eruption

In the following sections, a detailed focus on the eruptive activity at the EF is given, in order to provide more information on the dynamics of the eruptive vents during the ongoing activity, and on the evolution of the feeding system at the EF. The reconstruction of the volcanic activity at the Eruptive Fissure was realized in collaboration with Dr. Letizia Spampinato of Istituto Nazionale di Geofisica and Vulcanologia, Section of Catania.

2.3.1 Further details on the eruptive activity at 2008-2009 eruptive fissure

On 13 May 2008, the episodic 2007–2008 activity culminated in a proper explosive-effusive eruption preceded by an intense and shallow earthquake swarm, that started at 08:39 (all times are GMT) with locations between −1.5 and 1.5 km a.s.l. [Cannata et al., 2009b], and pronounced ground deformation marking the rising of a shallow dike [Aloisi et al., 2009; Di Grazia et al., 2009; Bonaccorso et al., 2011a]. This intersected the surface opening at first (from 09:30 to 11:00) a NW-SE-trending eruptive fissure [~3000 m a.s.l.; INGV-staff, 2007-2013], which fed lava fountaining and lava flows [Aloisi et al., 2009]. Then after 11:00, the number of earthquakes abruptly declined and the rupture direction moved down to the ESE, towards the volcano upper eastern flank between ~2900 and 2650 m a.s.l. [Bonaccorso et al., 2011a]. This segment of the eruptive fissure produced lava fountains, strombolian activity and lava flows from up to five vents during the first days following the onset [**Fig. 2.20**; Bonaccorso et al., 2011a].

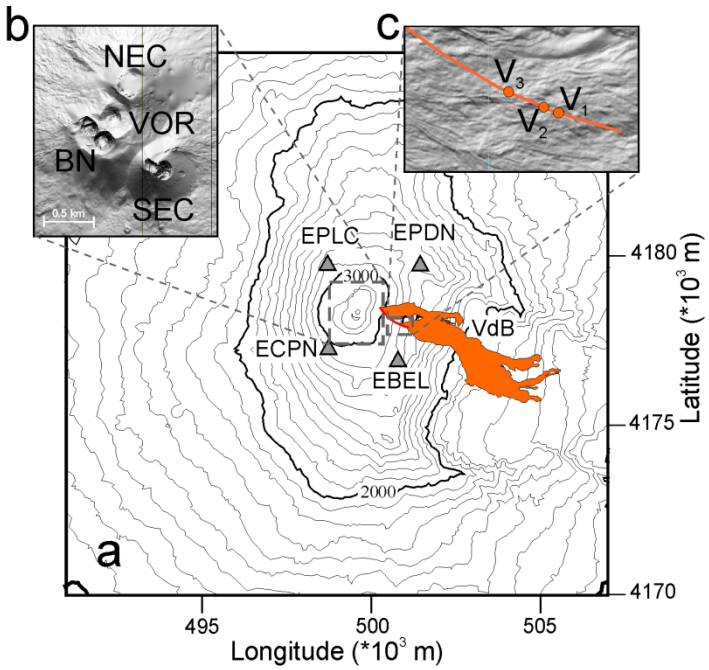

Figure 2.20: (a) Map of the summit area of Mt. Etna showing the locations of the infrasound sensors (triangles), the 13 May 2008 eruptive fissure (red line) and the area covered by the 2008–2009 lava flow field (orange area; INGV-staff 2007-2013). (b) Digital elevation model of the summit area (VOR: Voragine; BN: Bocca Nuova; SEC: South-East Crater; NEC: North-East Crater). (c) Eruptive fissure with the locations of V1, V2, V3 (see Section 2.3.3 for details). VdB in (a) is the Valle del Bove.

Here along the eruptive event, explosive activity fluctuated between ash emissions and strombolian explosions, commonly from the upper part of the fissure and strombolian activity and lava effusion from the topographically lowest parts [Bonaccorso et al., 2011a]. Over time, lava

output produced a lava flow field with features including lava tubes, ephemeral vents, and tumuli [INGV staff, 2007-2013]. Overall, the eruptive event was characterized by phases of increasing and decreasing activity [Bonaccorso et al., 2011a]. During episodes of increase, renewal of the explosive activity were frequently observed, greater number of active vents with the reactivation of the topographically higher vents, increase in both intensity and frequency of explosions, and higher lava supply rate from the effusive vents [Bonaccorso et al., 2011a]. Since this analysis focuses only on the explosive activity between mid May and early September 2008, in the following lines are provided only details on the style of the activity gathered in this ~4 month-temporal window. Indeed after September 2008, the infrasonic activity at the EF was negligible. In the targeted period, observation of the eruptive activity allowed discriminating between a numbers of eruptive phases consisting of sudden short-lived increases in the overall eruptive activity followed by gradual declines (**Table 2.2**).

DATE	ERUPTIVE PHASE	LOCATION (m a.s.l.)	TYPE OF ERUPTIVE ACTIVITY
13 May	Opening of two eruptive fissures (N-S and ENE-WSW oriented)	~3000 N-S 2900-2650 ENE-WSW	From the upper part of the fissures towards the lowest segments: lava fountaining, strombolian explosions with detonations, and effusive activity.
14 May	Activity decline and concentration at only the ENE-WSW eruptive fissure	~2900-2650	Discontinuous ash emissions, strombolian activity, and lava output.
15-16 May	Further decline of the intensity of the eruptive activity	~2800-2750	On 15 May: no activity at the upper part of the fissure. Gas explosions and ash with emission of ejecta between ~2800-2750 m a.s.l.. Ballistic-dominated explosions and lava flows from the very low part of the fissure. On 16 May, two vents (here named V_1 and V_2) fed strombolian activity and rare ash emissions. Lava output persisted through both days from 2750 m elevation.
17-22 May	Increase of the eruptive activity	~2800-2750	On 17 May, V_1 and V_2 produced strombolian activity and sporadic ash emissions except for the temporal interval between 17:30-19:00, when any explosion was detected. Lava output still continued from 2750 m elevation.
23 May-7 Jun	Decrease of the eruptive activity	~2800-2750	On 23 May, strombolian activity only at V_1. On 7 June, weak strombolian explosions from V_1. Progressive decrease of lava effusion from 23 May to 7 June.
8-15 Jun	Increase of the eruptive activity	~2800-2750	Ash-rich explosions from V_1 and V_2. Lava output still continued from 2750 m elevation.
15-16 Jun	Decrease of the eruptive activity	~2800-2750	Strombolian activity at V_1 and V_2. Lava output still continued from 2750 m elevation.
17-20 Jun	Increase of the eruptive activity	~2800-2750	Increasing explosive activity at V_1 and V_2. Lava output still continued from 2750 m elevation. On 20 June, the high frequency of the explosions produced a small ash plume and widening of the lava flow field.
End of Jun	Gradual decline of the eruptive activity	~2800-2750	Strombolian activity from V_1 and V_2. Lava flows fed from 2750 m elevation via lava tubes.
End of Jun - early Jul	Increase of the eruptive activity	~2800-2750	Strombolian activity and opening of a further eruptive vent (V_3) ~100 m above V_1 and V_2. V_3 produced closely-spaced, ash-rich explosions. Lava output through lava tubes.
9-12 Jul	Further increase of the eruptive activity	~2800-2750	Intense and continuous explosions at V_1 and V_2. Lava output through lava tubes.
12-24 Jul	Progressive decline of the eruptive activity	~2800-2750	On 15 July, the explosive activity focused only at V_2. This fed mild strombolian explosions with weak ash emissions. On 22 July, only mild degassing from the fissure. On 24 July, V_2 was characterised by degassing and small gas explosions. Lava output through lava tubes and ephemeral vents.
28 Jul-6 Sept	Steady decrease of the eruptive activity	~2800-2750	Passive degassing from the eruptive fissure. Lava effusion from lava tubes and ephemeral vents.
7 Sept	Slight increase of the eruptive activity	~2800-2750	Explosive activity renewal with weak strombolian explosions from V_3.

Table 2.2: Synthesis of the main phases and features of Etna's 2008 eruptive activity from 13 May, day of the onset of the eruption, to early September.

The period between 13 and 16 May, was characterised by the opening of the eruptive fissure followed by the deactivation of its highest segment and stabilisation of the activity at the mid and low portions [Bonaccorso et al., 2011a]. Explosive activity produced mainly ash emissions and gas explosions accompanied by strong detonations from the upper vents and Type-1 strombolian explosions [ballistic-dominated, with faintly visible plumes; Patrick et al., 2007] from the lowest. On the 14th, the vigorous activity of the first day gradually diminished with discontinuous ash emission at the upper and explosive activity at the lower vents, as well as lava erupted from the topographically lowest vents [INGV staff, 2007-2013]. On 15th, no ash emission from the upper part of the fissure was recorded. Between 2800–2750 m elevation, four vents were active of which the topographically highest was generating gas explosions and ash with slight emission of ejecta [INGV staff, 2007-2013]. The very low part of the fissure showed Type-1 strombolian activity even if with decreased frequency and intensity. The following day, at ~2750–2800 m elevation, two 15–20 m spaced vents (hereafter referred to as V1 and V2) were feeding strombolian activity and sporadic ash emission. This was more intense at the upper part of the fissure [INGV staff, 2007-2013]. The period between 17 May and 7 June was characterised by an increase of the eruptive activity that subsequently diminished smoothly. On the 17th, V1 and V2 produced strombolian explosions and discontinuous ash emissions [INGV staff, 2007-2013]: however, late on the same day (17:30–19:00), no explosive activity was recorded. On the 23 rd, only one of the explosive vents was active (V1 V2) producing strombolian explosions [INGV staff, 2007-2013]. Between 2 and 7 June, weak strombolian activity and rare ash emissions were fed by only one vent V1 and V2 [INGV staff, 2007-2013]. From 8 to 15 June, a further increase in the intensity of the eruptive activity was recorded [INGV staff, 2007-2013]. Particularly, on the 8th, V1 and V2 were producing ash-rich explosions. The heightened activity declined eventually on the 15th [NGV staff, 2007-2013]. From 17 to 19 June, the intensity of the activity at V2 and V1 increased gradually, and on the 20th the high frequency of explosions produced a small plume [INGV staff, 2007-2013]. Between the end of June and early July, a further increase in the eruptive activity led to the activation of one of the vents (V3) that opened on 13 May, sited ~100 m above the two vents currently active V1 and V2.V3 showed vigorous Type-2 strombolian activity (characterized by conspicuous ash plume; Patrick et al., 2007) with explosions at brief intervals [NGV staff, 2007-2013].

2.3.2 Dataset

In this thesis acoustic signals, produced by the EF during the period comprised between 13 May and 8 September 2008 (when the main explosive activity took place) are analyzed. In order to select only the infrasound events generated by EF activity, a first extraction based on the spectral content was performed. Indeed, as previously mentioned, NEC events are characterized by frequency lower than 2 Hz, while SEC and EF events by frequency higher than 2 Hz. This spectral feature was shown to be rather stable during the investigated period. Thus, taking into account only the events characterized by dominant frequency higher than 2 Hz we could exclude NEC events. To exclude also SEC events the differences between the arrival times at the stations were considered. In **Fig. 2.21** two examples of SEC and EF events are shown highlighting the different time delays between the station pairs for the two sources. In particular, the time delay EBEL-ECPN and EBEL-EPDN are indicative of the different infrasound sources. Thus, roughly 500 EF events, whose daily number and peak-to-peak amplitudes at EBEL are reported in **Fig. 2.23**, were selected with good signal quality (visually evaluated) at EBEL. However, only a part of these events were also well recorded at the other stations: in particular ~190 at ECPN, ~90 at EPLC and ~400 at EPDN.

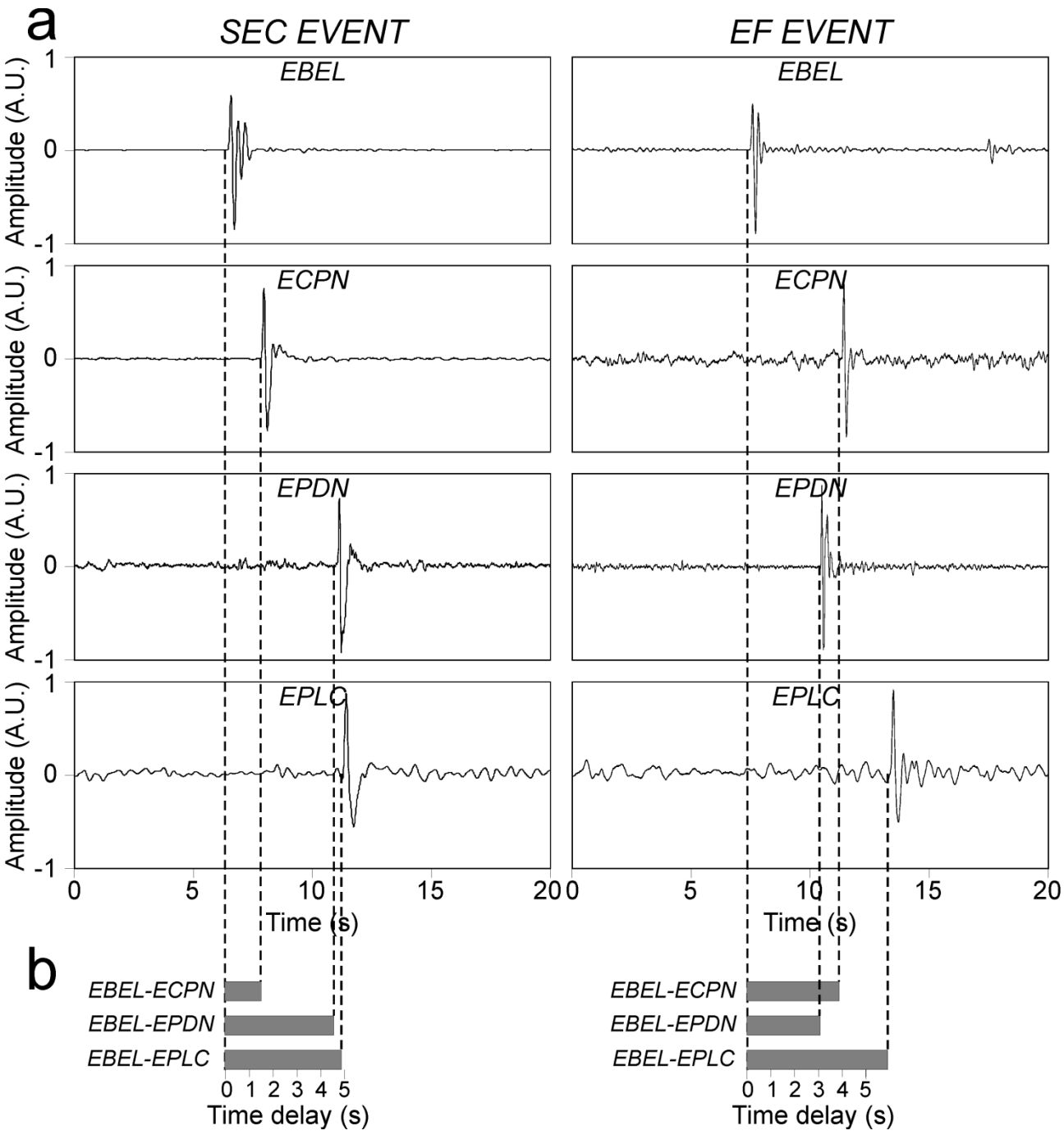

Figure 2.21: (a) Infrasound signals generated by SEC and the eruptive fissure (EF) and recorded by four stations (EBEL, ECPN, EPDN and EPLC). (b) Time delays (grey bars) between station pairs.

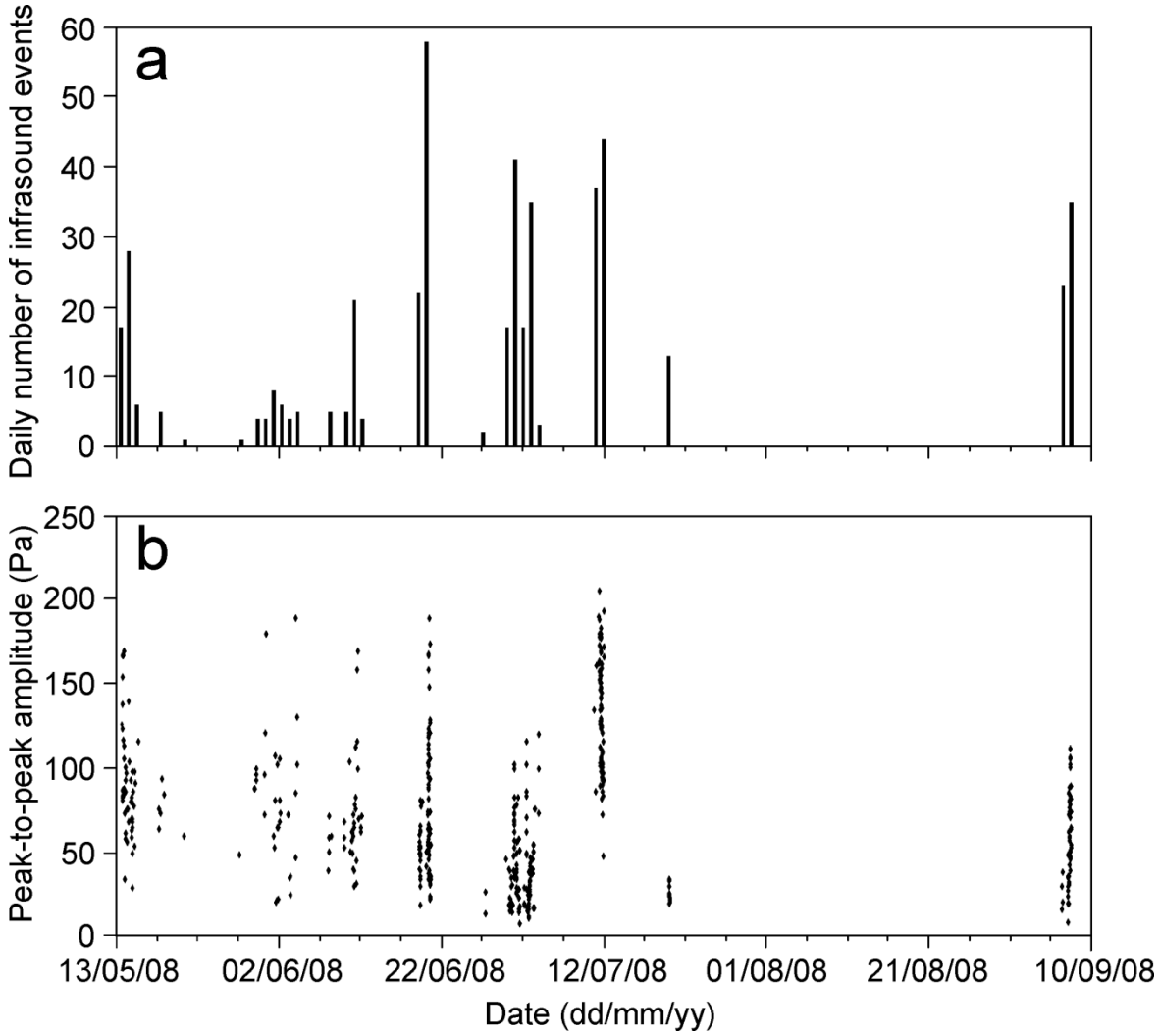

Figure. 2.22: (a) Daily number of selected EF infrasound events and (b) their peak-to-peak amplitudes calculated at EBEL station.

2.3.3 Analyses and results

2.3.3.1 Location analyses

The joint semblance-brightness method (see **section 1.3.2.1.** for further details) was applied in order to locate the selected events. By this technique roughly 250 events, clearly recognizable by visual inspection in the signals recorded at least at three stations, were located (**Fig. 2.23**). A grid of 6×6 km^2 with spacing of 12.5 m, centered on the volcanic edifice, and 3-second-long signal windows was used. The sound speed was fixed to 340 m/s [Lighthill, 1978]. It is worth noting that the sound propagation velocity can be time-dependent, because it is affected by several factors

such as air temperature and wind [e.g. Ripepe et al., 2007; Marcillo and Johnson, 2010]. For infrasonic microphones located at short distances (within 5 km of the vent) these effects are generally negligible, and can cause location errors of tens of meter depending on the wind speed. For instance, if we consider wind speed equal to 10 m/s in the direction of sound propagation and a source-station distance of 1 km, the calculated source location gets closer to the stations downwind of the source and further from the stations upwind (~30 m) in respect to the real source location. All the locations aligned along EF, highlighting the reliability and high precision of the joint semblance-brightness location method (**Fig. 2.23a, b**). **Fig. 2.23c** shows a time variability of the source location.

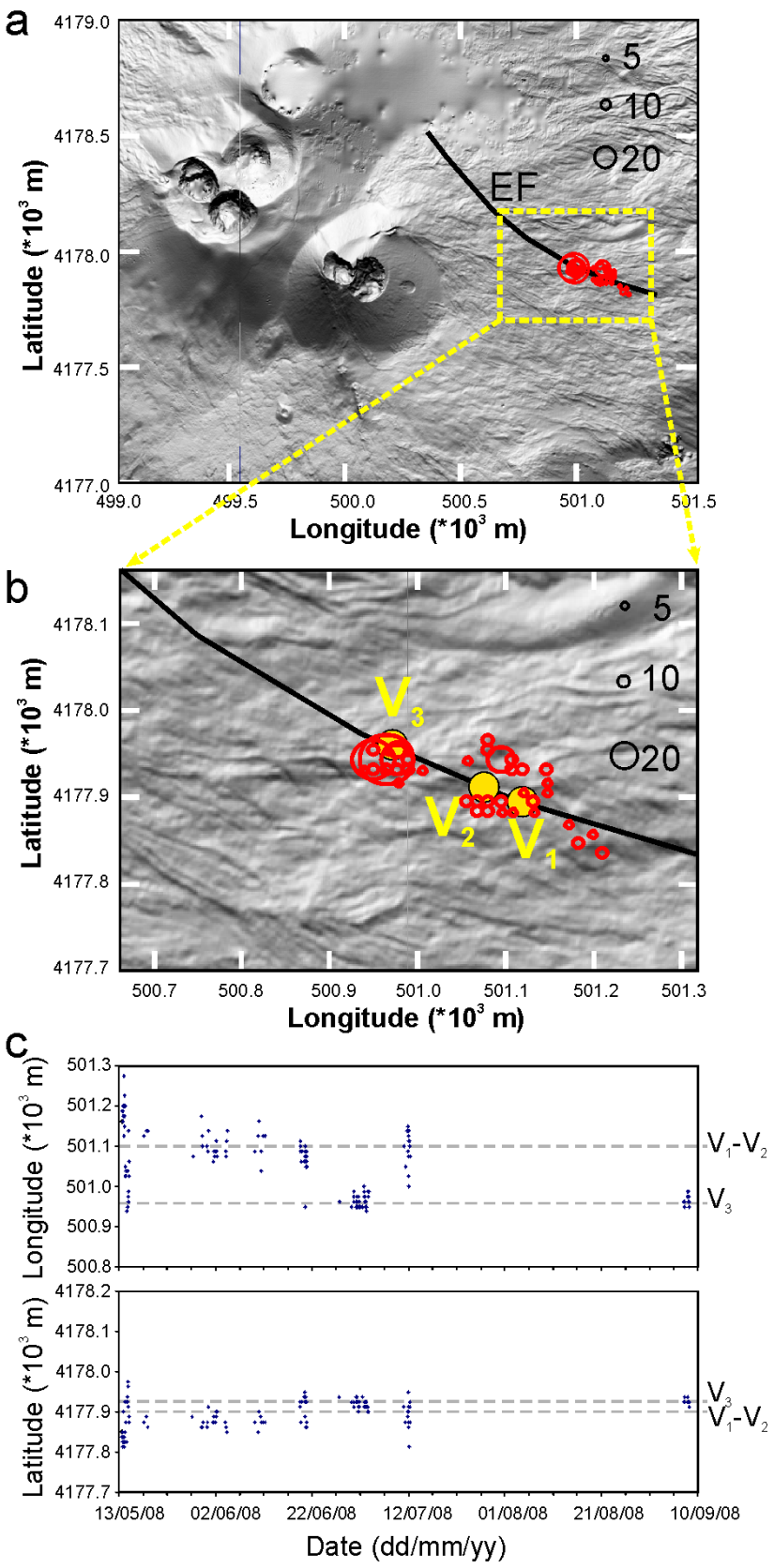

Figure 2.23: (a and b) Digital elevation model of Mt. Etna summit area with the source locations of the infrasound events, indicated by red circles, occurring during May-September 2008. The radii of the circles are proportional to the number of the locations in each grid node (see black circles and numbers reported in the upper right corner of the map). The black line (indicated by EF in a) represents the eruptive fissure. (c) Time variation of the source location of infrasound events plotted in (a and b). The dashed grey lines in (c) indicate the coordinates of the vents.

During the first few days of the eruption (13–15 May), the infrasound locations were fairly spread out along a roughly 200 m long portion of the EF. From mid May to the end of June, the infrasound activity was concentrated at the lowest part of EF, where two vents V1 and V2 fed the explosive activity. Successively until the end of the analyzed period, the source locations periodically shifted about 100–150 m upstream towards the vent V3. In particular, the infrasound activity of 11 and 12 July was characterized by the same location as mid May - end of June. On the basis of the example previously reported, the observed variations in source locations of 100–150 m cannot be an artifact due to changes in wind direction or intensity because the average wind speed was equal to 10 m/s during the studied period. Moreover, there were no significant variations in wind direction or intensity at the same time as infrasonic time delay, and then source location, changed.

In order to further investigate the migration of the infrasound source along the eruptive fissure, the time delays between station pairs were analyzed. EBEL was chosen as a reference station, because it was the least affected by noise due to bad weather and had the longest time series and successively EBEL–ECPN and EBEL–EPLC pairs were evaluated allowing better investigation of the east-westward source migrations than the other station pairs.

About 190 EF events recorded at ECPN and 90 at EPLC were visually selected on the basis of the good quality of the recordings. The corresponding events recorded at EBEL were aligned and the signals at ECPN and EPLC were plotted according to the alignment time at EBEL. Then, two complementary visualizations were created. In the first visualization (**Fig. 2.24**) in the x-axis the time elapsed from the onset to the end of the waveforms is reported, while the y-axis represents the time of occurrence of the events. To obtain the second visualization (**Fig. 2.25**), the waveforms of each station were grouped into a matrix, where each row is a waveform. Thus, in the x-axis the time elapsed from the onset to the end of the waveforms is reported, and the y-axis represents the event number in temporal order. The amplitude of the signal is visualized with the color scale. It is evident that the time arrival of EF events at ECPN and EPLC changed in time. In particular, the first few days of the eruption (13–15 May) were characterized by variable time arrivals (**Fig. 2.24b**, **d** and **f**), confirming the above described variability of the infrasound source location during this time interval. The most important variation, consisting of a decrease in the time delay EBEL–ECPN and EBEL–EPLC of roughly 0.5 s, took place at the end of June (**Figs. 2.24** and **2.25**), as also observed by the infrasound source location (**Fig. 2.23c**).

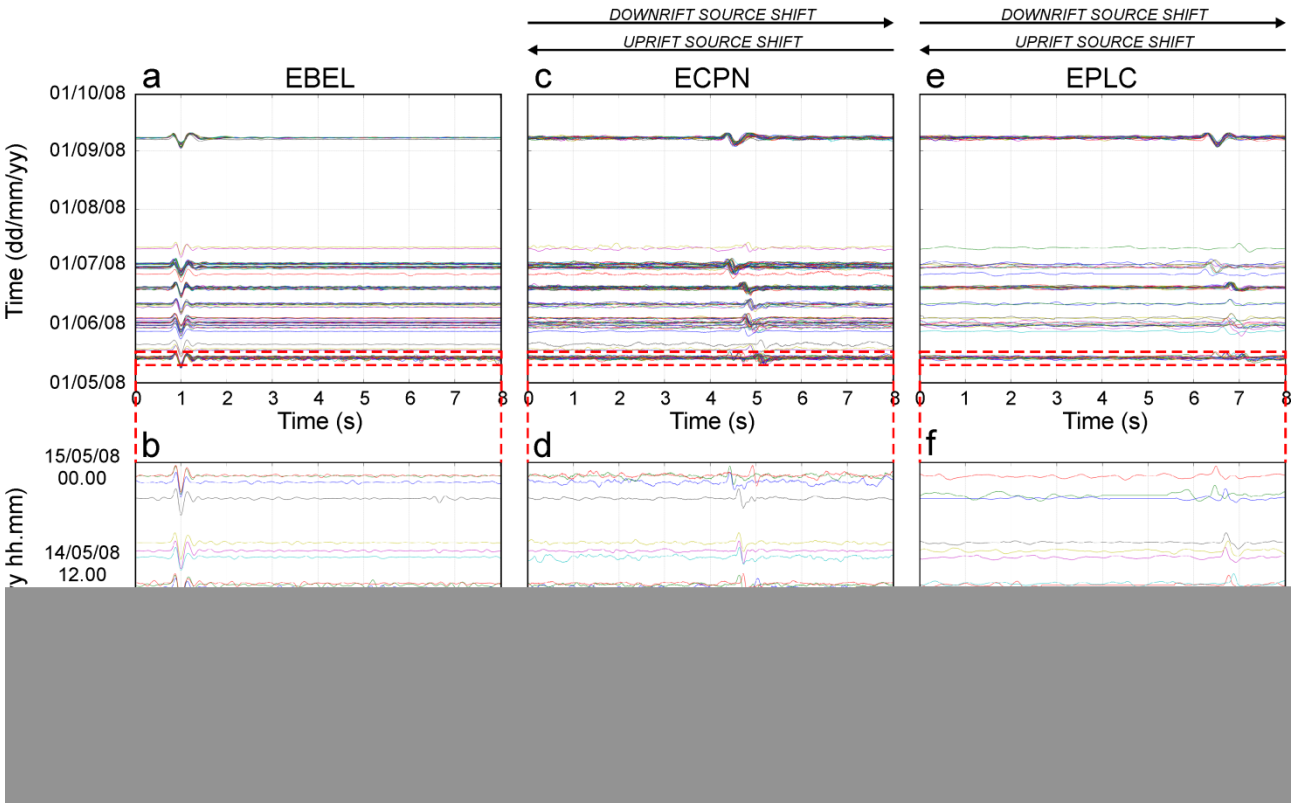

Figure 2.24: Infrasound events recorded by EBEL, ECPN and EPLC stations from 13 May to 8 September 2008 (a, c and e) and during 13–14 May 2008 (b, d and f). In the x-axis the time elapsed from the onset to the end of the waveforms is reported, while the y-axis represents the time of occurrence of the events. See text for details.

Figure 2.25: Surface plots visualizing matrixes, each of which is composed of the waveforms of the infrasound events of each station (each row is a waveform). In the x-axis the time elapsed from the onset to the end of the waveforms is reported, the y-axis represents the event number in temporal order. The amplitude of the signal is visualized with the color scale. See text for details.

2.3.3.2 Waveform analysis and classification

Since the waveforms of infrasound events, recorded at short distance from the source, largely depend on the source characteristics [mechanism, size, vent/shallow plumbing system geometry; e.g. Vergniolle et al., 2004; Fee et al., 2010b], we expect that shifts of the infrasonic source, and

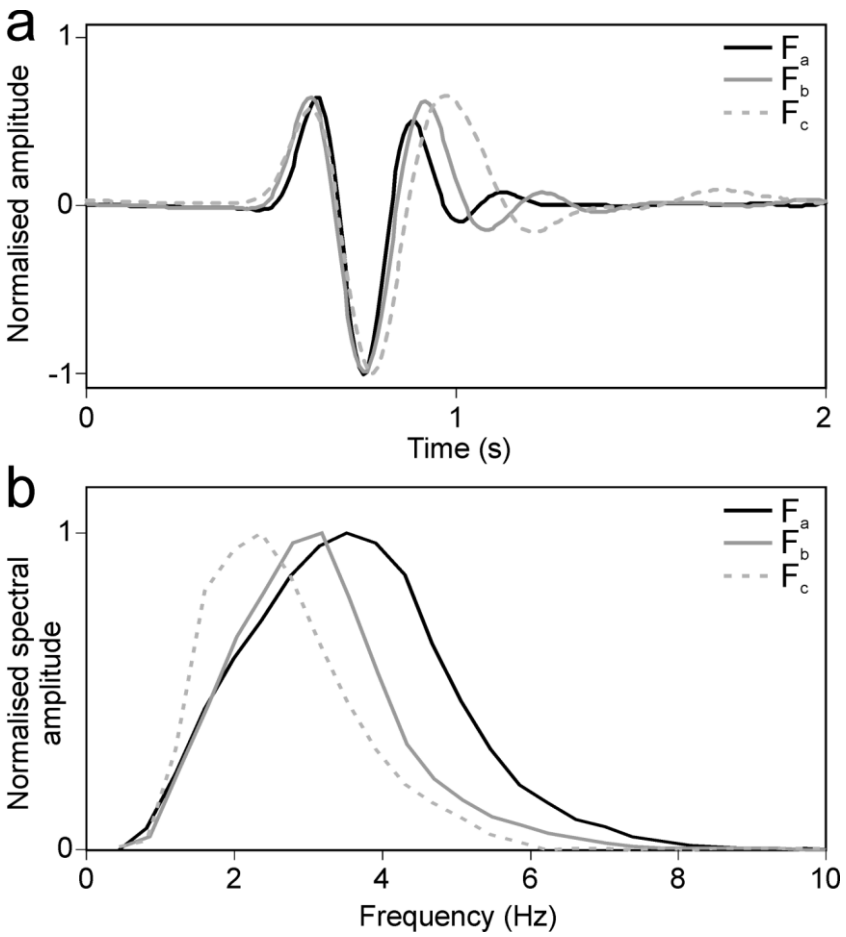

Figure 2.27: (a) Waveforms and (b) spectra of the stacked events of the three detected families (see legend in the right upper corner).

2.3.3.3 Waveform inversion

Waveform inversions were performed on the stacked waveforms of the three families (see **section 2.3.3.2**) by the Cannata et al. [2009a] and Montalto et al. [2010] method. The synthetic waveforms were obtained by the equation (**1**).

	Fa	Fb	Fc
Bubble radius (m)	2.1	3.3	3.5
Bubble length (m)	7.6	7.2	7.2
Bubble overpressure (kPa)	382	123	200

Table 2.3: Best-fit strombolian bubble parameters obtained by the waveform inversion for the stacked waveforms of Fa,Fb and Fc.

The values of density of magma and thickness of magma above the vibrating bubble were fixed to 2700 kg/m^3 and 0.1 m, respectively [Vergniolle and Ripepe, 2008], and magma viscosity to 100 Pa s [e.g. Spera, 2000]. Thus, the synthetic waveform only depends on three unknown source parameters: radius and length of the bubble, and initial overpressure. Then, by genetic algorithms [Montalto et al., 2010] the values of these unknown parameters were constrained, finding the best fit between synthetic and stacked waveforms of the three families. The comparison between synthetic and stacked waveforms is reported in **Fig. 2.28** and shows that the fit is quite good especially for the Fa and Fb stacked waveforms. The results of the inversions (**Table 2.3**) show that the bubble length values are very similar for all the three families (7.2–7.6 m), while the overpressure values ranged from 123 kPa (Fb) to 382 kPa (Fa). Focusing on the bubble radius, on which the spectral content of infrasound signals strictly depends, Fa is characterized by smaller value (2.1 m) than Fb and Fc (3.3 m and 3.5 m, respectively).

Although all the three values of bubble radius seem similar to each other, the slight but persistent spectral differences among the three families suggest that these differences can be considered meaningful. Waveform inversion was also performed by using different values of viscosity (10 to 1000 Pa s) and thickness of magma above the vibrating bubble (0.15 and 0.20 m), in order to investigate the effect of each fixed parameter. While changes in viscosity poorly affect the inversion results, as also shown by Vergniolle and Brandeis [1996] and Bouche et al. [2010], magma thickness variations are able to strongly modify the source parameters. Indeed, for instance by using a thickness of 0.15 m, radius (1.4, 2.2 and 2.5 m for Fa, Fb, Fc, respectively) and length (3.0, 2.9 and 3.0 m for Fa, Fb, Fc, respectively) of the bubble decrease and overpressure increases (1488, 450 and 619 kPa for Fa, Fb, Fc, respectively). However, it is worth noting that the relative differences among the three event families remain similar to those observed with a magma thickness of 0.1 m: Fa showed the smallest radius size and Fc the largest one, and the highest overpressure value was obtained for Fa.

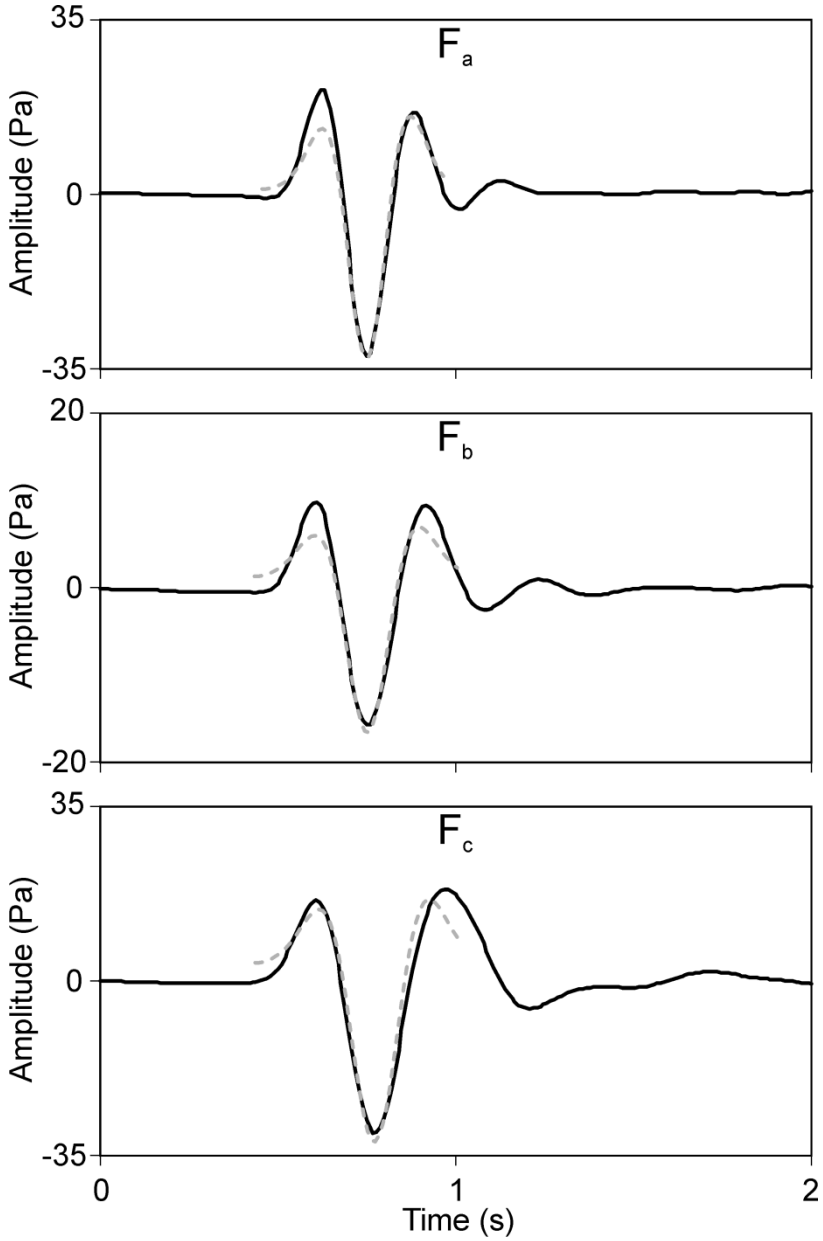

Figure 2.28: Comparison between the stacked waveforms of the three infrasonic event families (black lines) and the best-fit synthetic waveforms using the Vergniolle and Brandeis (1996) model (dashed grey lines).

2.3.4 Discussion

The infrasound activity of a 14 month-long lasting eruptive fissure that opened at Mt. Etna on 13 May 2008 was investigated and compared with the volcanic activity during the first phases of the eruption. Particular attention has been focused on the explosive activity between mid May and early September 2008, providing details on the style of activity. The usefulness of infrasound analysis for monitoring eruptive activity has already been reported by previous studies at Mt. Etna [e.g. Montalto et al., 2010] and at other worldwide active volcanoes [e.g. Stromboli, Ripepe et al.,

2007; Mt. St. Helens, Matoza et al., 2007; Kīlauea, Matoza et al., 2010b]. In this thesis a method based on the joint semblance and brightness functions, allowing accurate locations of infrasound sources, was applied (**Fig. 2.23**). These permitted us to locate closely-spaced eruptive vents and to observe spatial changes in explosive activity over time (**Fig. 2.29**). Both ground deformation data [Aloisi et al., 2009] and volcanic tremor source locations [Di Grazia et al., 2009] indicate that the 2008–2009 eruption was fed by a dike that intruded radially from the central conduit (below 1.5–2.0 km a.s.l.) and intersected the topography at the eastern flank of the volcano. During the very first days following the onset of the eruption (13–14 May), many infrasound sources were aligned along a roughly 200 m-long segment of the eruptive fissure (**Fig. 2.29a**). Successively, the sources clustered in a smaller portion of the eruptive fissure, where two explosive vents (V1 and V2) were active (**Fig. 2.29b**). As already observed during Etna's 2002–2003 southern eruption [Spampinato et al., 2008], such a reduction in the number of active vents was likely due to cooling of the dike's peripheral areas with magma transport being efficient only at the dike core (corresponding at the surface to V1 and V2). At the end of June, a third vent (V3) opened ~100 m upwards and was periodically active (**Fig. 2.29c**). The periods of activity of such a vent lie within the phases of increased eruptive activity described in the chronology section that could be related to short-lasting variations in magma/gas fraction supply rate that might have changed locally the level of magma in vent conduits. In fact, increases in the supply rate might have allowed the reactivation of V3 (which formed during the first days following the onset of the eruptive event) at the surface. The same mechanism was previously documented during the 2002–2003 Etna southern eruption [Spampinato et al., 2008] and the Stromboli flank eruption, where migration of the effusive vents along the Sciara del Fuoco was observed [Calvari et al., 2005]. Accordingly, during periods of V3 activity infrasound events from V1 and V2 were hardly detected at all. This could be explained considering the geometry of the conduits feeding V1/V2 and V3: the gas preferentially uprises through the more inclined conduit, i.e. through V3 conduit [e.g. Penmatcha et al., 1996; Marti and Shoham, 1997; **Fig. 2.29c**].

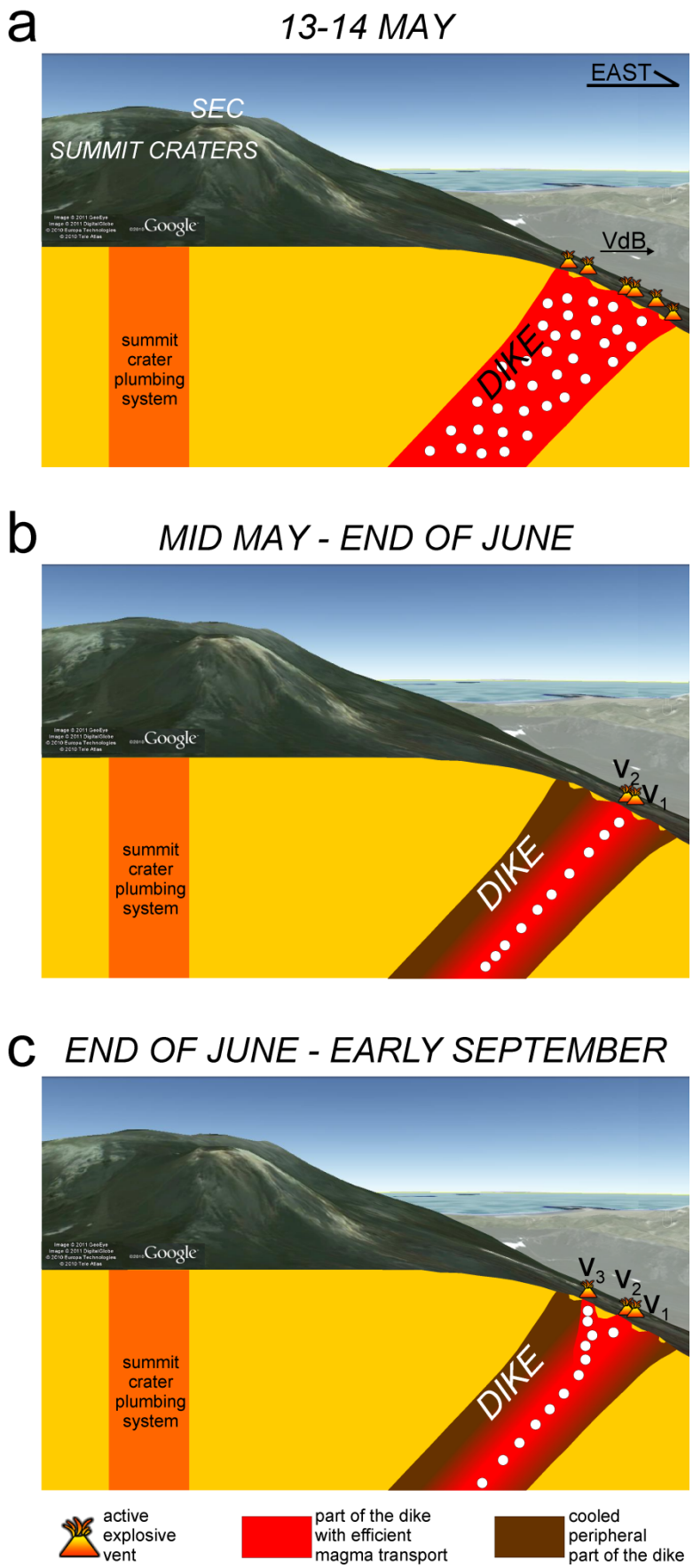

Figure 2.29: Cartoon of Mt. Etna (Google Earth) showing the volcano west–east profile and the eruptive vents along the 13 May 2008 eruptive fissure. a, b and c refer to the three phases of the eruptive activity: 13–14 May, mid May–end of June, end of June–early September.

James et al. [2004] carried out experimental research demonstrating the role of conduit inclination in promoting bubble coalescence, and thus slug formation by locally increasing the gas-volume fraction on the conduit upper wall. James et al. [2004] also considered the control of conduit inclination on vent eruptive style observed at the surface. This is consistent with volcanological observations of the explosive activity along the 2008–2009 eruptive fissure, according to which V2 and V2 displayed mainly the Type 1-strombolian activity of Patrick et al. [2007] and V3 showed predominantly the Type 2. Since the waveforms of infrasound events strictly depend on source characteristics [e.g. Vergniolle et al., 2004; Fee et al., 2010b], it is worthy to investigate further their variations over time. In detail, it was observed that, although all the event waveforms were very similar to each other (duration generally shorter than 1 s and monochromatic frequency content in the range of ~2–4 Hz), they could be grouped into three families (Fa, Fb, Fc; **Figs. 2.26** and **2.27**). Fa showed dominant frequency of 3.5 Hz and was associated to the infrasound activity of both V1 and V2. The other two families (Fb and Fc), characterized by spectral peaks at 3.1 and 2.3 Hz, were generated by the periodic activity of V3 (3.1 Hz between 27 June–4 July, and 2.3 Hz between 7–8 September). Comparing the infrasound activity of V1 and V2 with V3, it can be noted that vents, reasonably characterized by different features (e.g. shape, radius and so on), produced diverse infrasound signals. Similar results were previously obtained comparing signals generated by SEC and NEC summit craters of Mt. Etna [Cannata et al., 2009a], as well as at other volcanoes [e.g. Stromboli; Ripepe and Marchetti, 2002]. Moreover, V3 produced different signals during distinct eruptive periods. In order to shed light on the physical meaning of such changes, the strombolian bubble vibration model [e.g. Vergniolle et al., 2004] was considered and waveform inversions of the stacked events of the three detected families was performed. Among family source parameters, the main difference responsible for the observed event spectral variations is the bubble radius size, i.e. 2.1, 3.3 and 3.5 m for the stacked events of Fa, Fb and Fc, respectively (**Table 2.3**). These values are reasonable and in good agreement with previous values obtained at Etna [Vergniolle and Ripepe, 2008; Cannata et al., 2009a, b], at Stromboli [Vergniolle and Brandeis, 1996], and at Shishaldin [Vergniolle et al., 2004]. Considering the strombolian activity observed at the surface, and thus a slug two-phase flow-type model [e.g. Jaupart and Vergniolle, 1988], where the slug radius is assumed to be of the same size as the shallow conduit [Vergniolle et al., 2004], we can infer that the observed waveform differences might result from differences in vent sizes. While we expected such differences at distinct vents, the change of the bubble radius for V3 event inversions (both Fb and Fc stacked events) might suggest an increase of the V3 size over time.

Many papers have dealt with variations in vent size along basaltic volcanic eruptions [e.g. Valentine and Groves, 1996; Dobran, 2001; Keating et al., 2007; Spampinato et al., 2008] attributing in particular vent size increase to (i) erosion from shear stress of flowing magma; (ii) erosion from particle collision; (iii) conduit wall collapse; (iv) changing style of eruptive activity at the surface, and thus magma transport modalities; and (v) variation of magma supply rate. Since the aforementioned change in V3 infrasound waveforms took place during a period of weak activity/lack of activity of V3 , lasting for almost two months, the conduit wall collapse model can be considered the most reasonable to explain the inferred changes in the V3 size. Alternatively to vent size change, a variation in the fragmentation surface depth can cause different conditions of the infrasound generation, such as a different conduit radius at the depth of bubble bursting. In order to better constrain the mechanisms leading to changes in infrasound waveforms, future work might be based on the integration of the infrasound data with further geophysical observations and geochemical and volcanological data. A multiparametric approach might also help retrieving better constraints for modeling infrasound sources and investigating the magma dynamics in the deeper portion of the feeding systems. The results here presented represent an approach for discriminating and tracking the eruptive activity at individual vents, that will prove useful for monitoring future eruptive-fissure-fed lava effusions at Mt. Etna as well as at other volcanoes.

2.4 Characterization of the superficial feeding systems from 2010 ash emissions: a joined seismo-acoustic and volcanological analysis.

A minor and less known explosive activity, related to ash emissions, without clear volcanological precursors, is also frequent at the summit craters of Etna. These explosions produce low eruption columns which rise up to about 1 km in height above the summit, being dispersed laterally where their tephra load falls over the volcanic slopes. The rather low content of tephra makes these plumes diluted when rising because of the rapid decrease in concentration with height. A considerable number of explosive events were observed in 2010, as specified in **section 2.1.2**, where the term “event” stands for a single explosion or series of explosions occurring within a few seconds of each other. In **Table 2.4**, all the episodes directly observed by camera recordings and/or visual observations in the field are reported; in a few cases, the ash emission has been

validated only by the ash fallout collected from the ground. On the whole, 35 events were counted, including at least three to four other episodes inferred by the seismic and acoustic signals but not observed by video-camera recordings (due to poor visibility at Etna's summit) and/or reported by eyewitnesses. Several ash emissions at BN and SEC, not directly linked to explosive seismic signals, were correlated to small failures involving the rims and/or the inner walls of these craters, in particular those at SEC, considered separately in **Table 2.4**.

In this thesis, three of these events are focused, and in particular they took place from SEC on 8 April, from BN on 25 August, and from NEC on 14–15 November. While the first two events represent largely unexpected explosions, the latter one consisted of a prolonged ash emission into the atmosphere. A detailed chronology (timing and eruption column) of each ash emission episode analyzed is given in **section 2.4.1** Successively, dispersal of the deposit and texture (grain size, componentry, and morphology) of the emitted tephra from each of the studied events is provided. All the volcanological analyses described in the following pages were carried out in collaboration with Dr. Daniele Andronico and Dr. Deborah Lo Castro of Istituto Nazionale di Geofisica e Vulcanologia, Catania. Furthermore, infrasound and seismic signals recorded during the aforementioned eruptive episodes are analyzed, as well as the volcanic tremor acquired during March– December 2010. Finally, volcanological features of the study events are correlated with the associated seismic and infrasound signals in order to better constrain this type of activity, eventually finding possible evidence of short-term variations of these signals preceding minor explosive activity. Sampling site and positions of the video-cameras, as well as of the seismic and acoustic sensors used for this analysis, are reported in **Fig.2.30**.

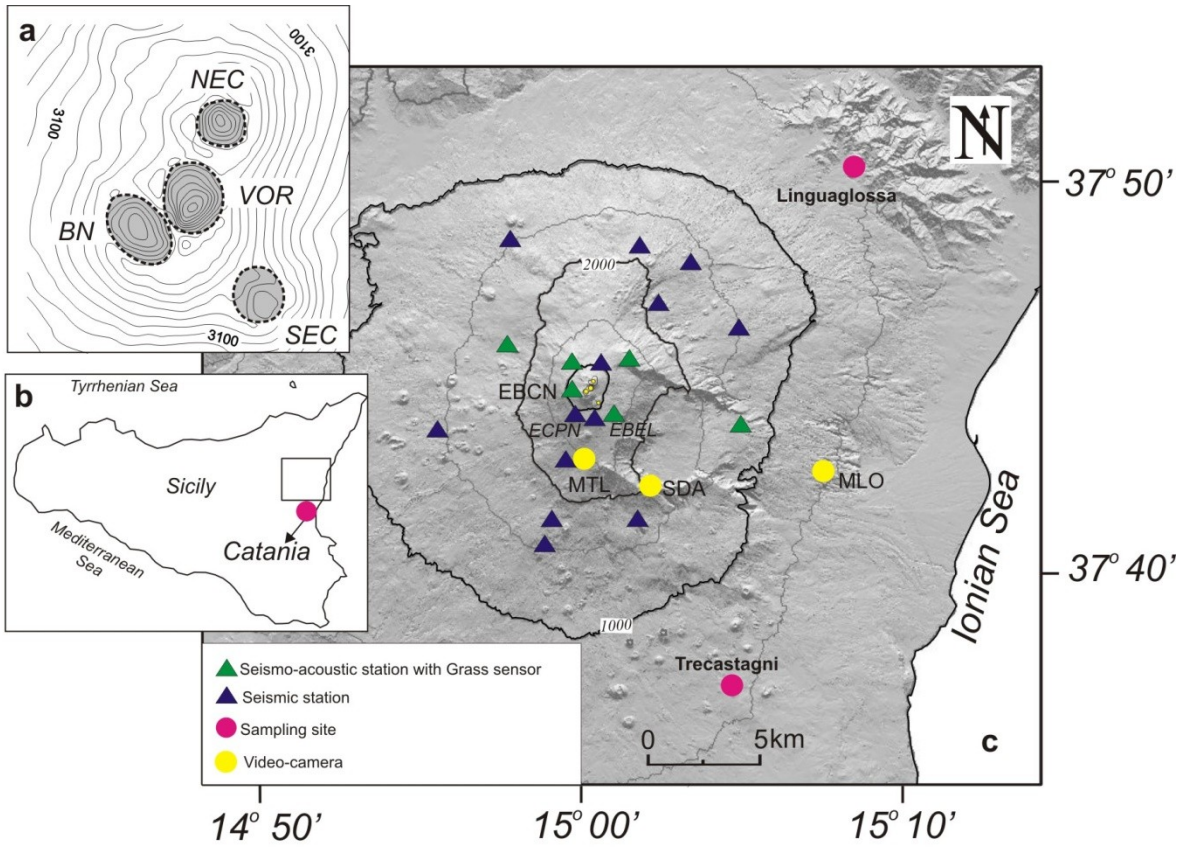

Figure 2.30: a) Digital Elevation Model of Mt. Etna with location of the seismic (solid blue triangles) and seismo-acoustic (G.R.A.S.S. sensor; solid green triangles) stations used in this analysis (see the key in the lower left corner). MLO, MTL and SDA (solid yellow circles) are the Milo, Montagnola and Schiena dell'Asino cameras, respectively. Solid red circles: main localities reported in the text. b) Location of Sicily in the regional context. c) Distribution of the summit craters (VOR = Voragine, BN = Bocca Nuova, SEC = South-East Crater, NEC = North-East Crater).

Such a multidisciplinary comparison of monitoring data allows shedding some light on the dynamic conditions of the shallow plumbing system [e.g., Ripepe et al., 2001b] and improves our capacity to foresee the occurrence of these events, thus reducing the potential associated volcanic risk at Etna.

explosive episodes	probable failure events	glowing episodes	date	Time (GMT)	SEC	CRATER BN	NEC
1			8 April	16:28	**XXX**		
2			7 May	11:04	x		
3			19 June	06:22-06:52	x		
		1	29 June	13:15	glow		
4			5 July	05:01		X	
			8 August	10:01		X	
5			25 August	13:09		**XXX**	
6			25 August	17:28		X	
7			25 August	23:25		X	
		2	26 August	22:20	glow		
8			26 August	02:08		X	
9			27 August	09:28		X	
10			27 August	16:00		X	
11			28 August	09:14		X	
12			28 August	14:18		X	
13			29 August	01:00-01:17		X	
14			29 August	05:39		X	
15			29 August	07:31		X	
16			30 August	07:28		X	
17			3 September	/		X	
18			4 September	13:01		X	
19			6 September	22:42		X	
20			10 September	10:42		X	
21			12 September	11:13		X	
22			13 September	07:04		X	
23			17 September	07:57		X	
	1		18 September	/	X		
24			24 September	12:46		X	
25			30 September	10:02		X	
26			7 October	09:27			
27			8-9 October	23:44		X	
28			9 October	00:35		X	
29			22 October	16:23		X	
	2		31 October	15:33		X	
30			1 November	02:08		X	
31			1-2 November	02:22		X	
	3		2-3-4 November	/	X		
	4		12 November	/	X		
32			14-15 November	05:25			**XX**
33			7 December	14:30			
34			22 December	04:46		**XXX**	
35			29-30 December	16:28	X + Str. Act.		

Table 2.4: List of the ash emissions observed in 2010 subdivided into related to explosive activity and related to the source vent

2.4.1 Timing and eruption columns of major ash emission episodes

Among the roughly 35 ash emission episodes occurred at Mt. Etna, some were particularly relevant for the violence of the explosion, as in the case of ash emissions occurring on 8 April, at SEC, and on 25 August at BN, or because they witness the renewal of activity after long time eruptive quiescence, as for the 14-15 November ash emission at NEC. Below, some information about the eruptive episode are given.

8 April ash emission (SEC)

In the early morning of 8 April, at around 04:36, a seismic sequence, originated below SEC and not accompanied by any superficial volcanic activity, was recorded. From the late morning of 8 April, small, episodic puffs of reddish ash were visible from the surveillance cameras. In good agreement with the forecast of the wind speed indicating values of 15 knots from the south, the low gas and ash plumes pouring out from the pit were able to rise for tens to hundreds of meters before being dispersed laterally. At around 15:58, a first, steady ash emission occurred, producing a thin, lighter steam-rich <1 km-height plume above the pit that lasted about 10 min before dissolving. A new, lower (200–300 m-height) plume rose from the pit at 16:24. However, the major ash emission event occurred at 16:28; a dark, thick convective plume quickly formed, remaining steady for about 2 min up to 600–700 m of height before thinning and further rising, thus bending above the eruptive vent and forming an umbrella region. It is noteworthy that in this case the ash emission was extremely un-expected as well as hazardous in terms of amount of tephra erupted. After 16:34, the plume became whitish, suggesting the cessation of the ash and lapilli material and their gradual replacement by a sustained steam flux persisting for at least another hour (see **Fig. 2.31** for images of the eruption).

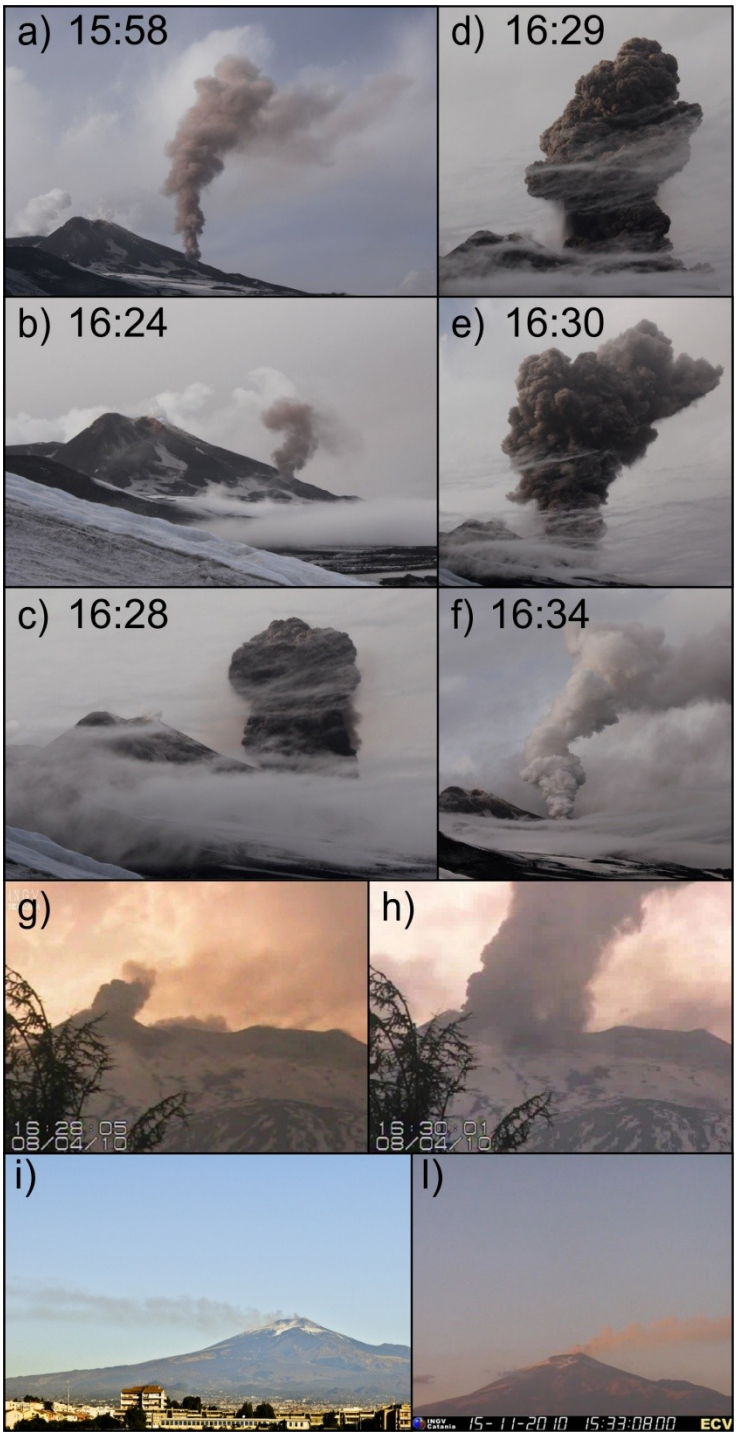

Figure 2.31: (a–h) The ash and steam emissions preceding, accompanying, and following the 8 April explosion. Photos from Thomas Bretscher at http://www.flickr.com/photos/ 34365424@N08/ in a to f. The explosions as recorded by the true-color camera located in Milo in g and h. (i–l) The 14–15 November ash emission from NEC. Image showing the 14 November plume (photo by D. Andronico) in Figure 2i. Image recorded from the CUAD visible camera showing the 15 November plume in l. Note the rotation of the plume direction from west to east by changes of wind direction in about 24 h. See text for details; reported times are GMT.

In the meantime, a light shower of tephra had begun to gradually dirty the white snow cover between the summit and intermediate-low slopes of Etna (**Fig. 2.32a**). Tephra fallout

involved the lower northeast flank of Etna down to the Linguaglossa village, more than 16 km from the SEC, where a light ash shower occurred from 16:50 to 17:45 (about 18 g m $^{-2}$) (**Fig. 2.33**).

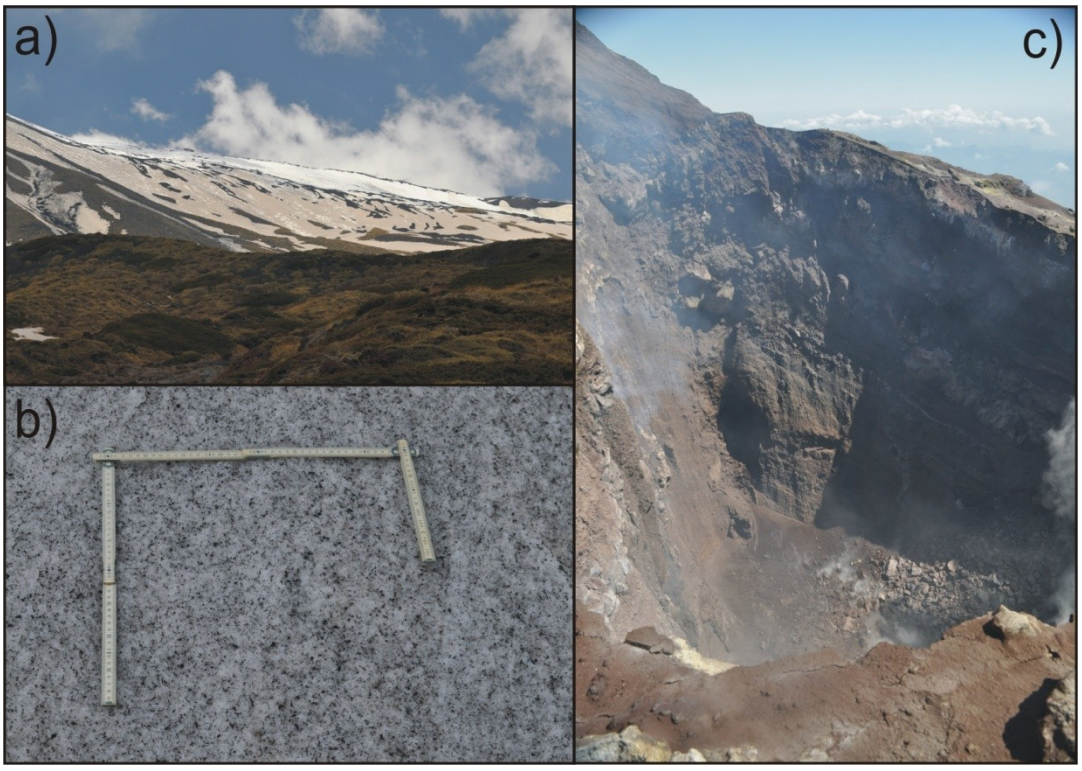

Figure 2.32:. Images related to the 8 April explosive event: (a) the ash fallout leaving a brownish mark on the northeastern snowy slopes of Etna; (b) detail of the ash covering the snow surface; (c) the deepening of the pit crater after the explosions; note the blocks at its base and the reddish thin ash layer around the crater rim and above the bottom. Photos by D. Andronico.

We took four samples between Linguaglossa and the intermediate slopes of Etna, at sites covered by snow located 5–7 km from the vent, where we collected about 80 g m $^{-2}$ of ash. **Fig**. **2.33a** shows the isomass map drawn after the data collection. The sum of the single volumes calculated for each isomass line based on the relative enclosed area provides a rough estimation of the total erupted volume (~10 m^3). The ash covering was discontinuous, with a significant drop in thickness away from the vent, smoother in the intermediate slopes (5–10 km from the vent), and then sharper approaching Linguaglossa. A survey carried out a few weeks later showed that the 8 April explosions caused the significant enlargement and widening of the former pit (estimated between 60 and 100 m), surrounded by steep walls of at least 50 m of height; noteworthy are the metric-sized blocks at its flat base and the reddish film around the rim and above the bottom, most of which was covered by reddish coarse ashes (**Fig. 2.32c**), while lithic material with dimensions from a few centimeters to decimeters was found scattered and entirely covered by reddish ash around the crater rim [INGV staff, 2007-2013].

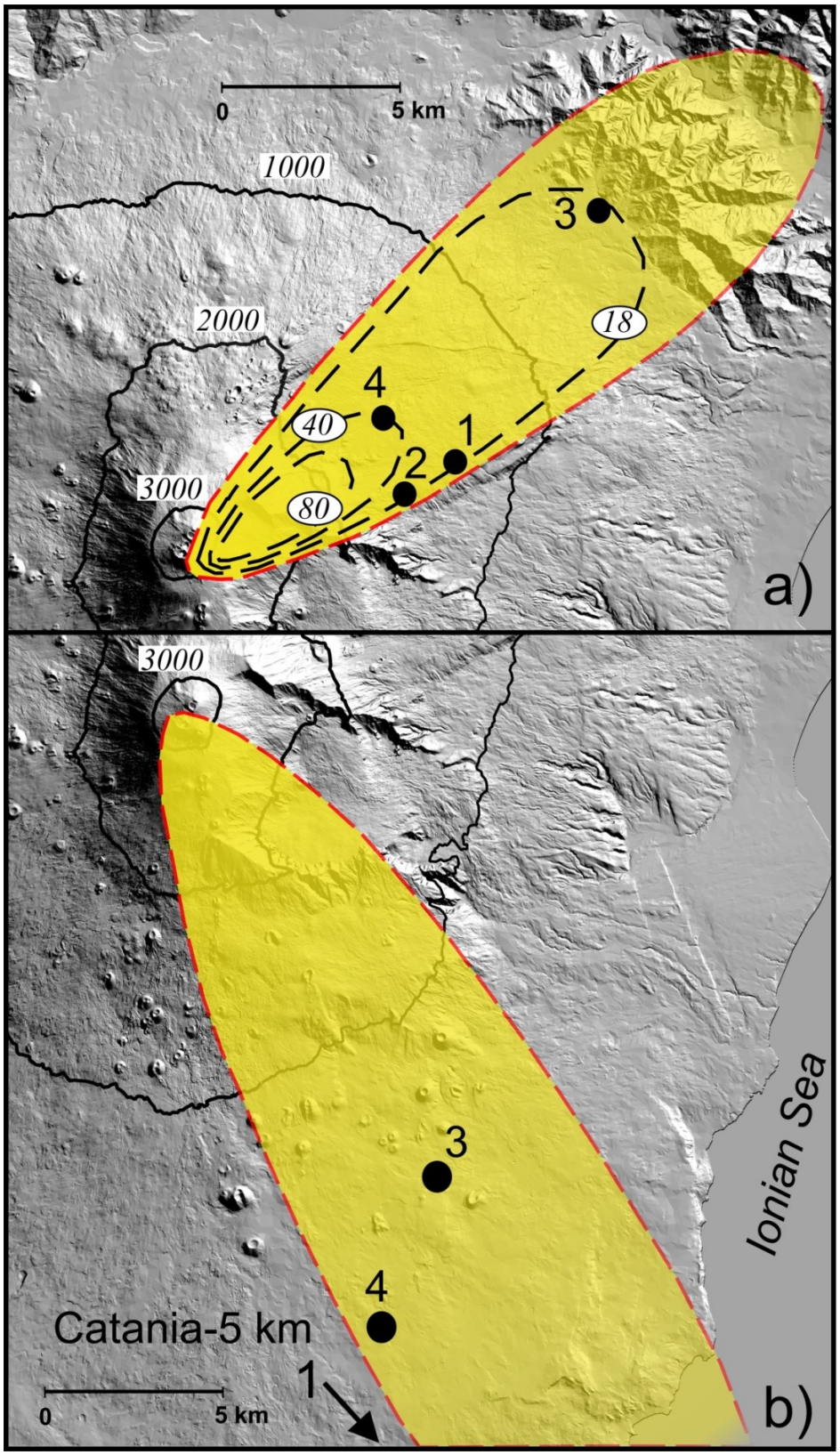

Figure 2.33: (a) Isomass map of the 8 April tephra fallout from SEC drawn based on all the collected samples. CSE08410 analyzed samples: 1, Pineta Ragabo; 2, Monte Conca; 3, Linguaglossa; 4, Piano Provenzana. (b) Map of the tephra fallout after the 25 August explosion. BN250810 analyzed samples: 1, Catania; 3, Trecastagni; 4, Mascalucia.

25 August ash emission (BN)

In the morning of 24 August, the INGV seismic stations recorded a low frequency event sequence lasting about 15 min located at BN, not followed by evidence of volcanic activity. Nevertheless, in the early afternoon of 25 August a violent explosion occurred, as recorded from visible cameras, at 13:09:02. The absence, in the previous hours, in the video-camera recordings of any evidence of higher degassing or small ash emissions, suggests the apparent unpredictability of an explosive event from video monitoring.

The explosion caused the sudden emission of a dense, dark cloud above the BN-1 crater. Both the true-color and thermal images indicate the magnitude of the explosion in terms of duration, height, and width of the eruption columns. Thermal images show high temperatures of up to 169° C at 13:09:04 during the initial tephra pouring, falling rapidly (**Fig. 2.34**). A thick volcanic plume rose up for more than 1 km of height in less than 1 min (estimated ascent velocity about 22 m/s based on the pixel dimension in the first 10 s), being shifted to the SE above the BN-2 and SEC craters by moderate (15 knots) winds between 3000 and 5500 m of elevation. For at least 10 min, the ash output was abundant and continuous, resulting in a brownish, convective plume; afterward, the ash emission became less continuous and intense, and the ash cloud became less sustained, pulsing and gradually whitened by strong degassing. The ash pulses following the main event (the last at about 13:25) were probably related to repeated intracrater collapses or small failures along the inner rim of BN-1. At 17:28 and 23:25, two minor ash emission events again occurred at BN-1. The ash fallout dispersed toward the southern flank of Etna down toward Catania, affecting mainly the upper slopes of Etna. In distal sites, 0.88 g m^{-2} at Trecastagni (at about 17 km from the vent), 0.07 g m^{-2} at Mascalucia (20 km), and 0.065 g m^{-2} at INGV-CT (27.5 km) were collected (**Fig. 2.33b**).

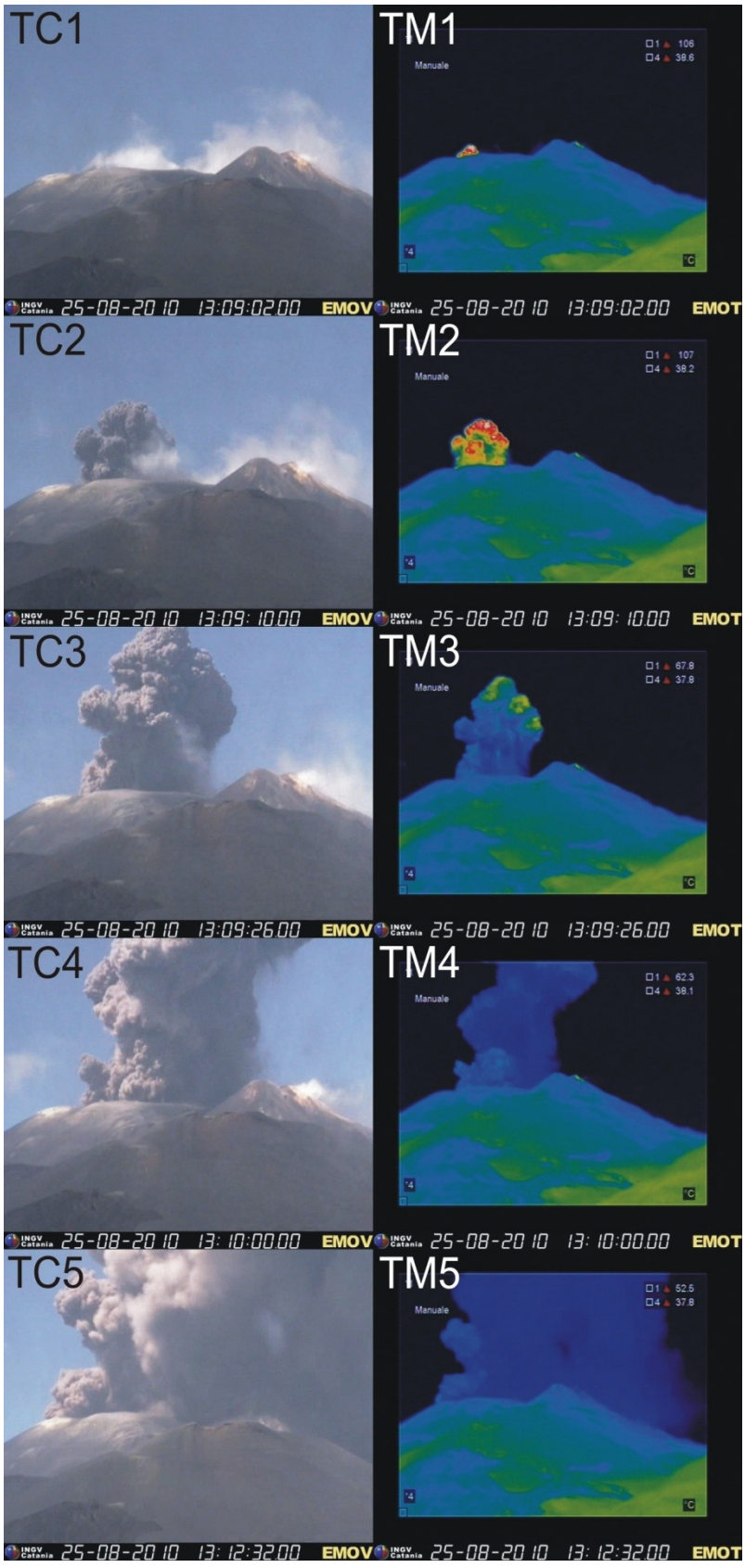

Figure 2.34: Images showing the 25 August explosion by images recorded at La Montagnola video cameras. Left: true-color camera; right: thermal camera. See text for details.

14-15 November ash emissions, NEC

Since 12 November 2010, the summit of NEC has been characterized by intermittent emissions of reddish ashes and steam. This type of activity increased until 14 November when it became less pulsating and sometimes almost continuous, forming a very weak eruption plume, and thereafter it decreased. On 15 November, in particular, NEC seemed to emit only a degassing light reddish plume, dirtied by a very low content of ash (for images of the eruptive activity see **Fig. 2.31i, l**). Finally, in the morning of 16 November INGV cameras recorded the end of the ash emission. The 14 November activity formed a diluted, thin plume extending above the summit of the volcano and dropping a meager amount of fine ash on the ground. However, the volcanic plume did not have sufficient convective power to rise up, thus becoming bent by the winds after reaching only 100–300 m altitude. Due to the prolonged activity, the plume shifted following variations in wind direction; hence, the fallout dispersed southward and westward on 14 November, rotating northward on 15 November and covering the summit area round the rim of NEC with a reddish centimeters-thick layer of ash (B. Behncke, personal communication) and also the volcanic flanks around Etna with a very thin ash film. The ash sample for this study was collected over the rim of NEC by B. Behncke during a rapid survey carried out on 15 November while the volcanic activity was still ongoing. Remarkably, direct observation did not bear any evidence of inner failures within the NEC crater, except for a continuous production of ash due to a persistent, low-energy explosive process.

Further episode: 22 December 2010 BN

On December 22th, a seismic sequence was recorded at 04:40 a.m. . Then, at 04:46 a.m. a notable ash emission occurred at BN, as clearly visible from Montagnola video-camera. [INGV staff, 2007-2013]. The ash emission lasted for few minutes and was dispersed from dominant wind in NE direction, with a fall-out mainly observed at Linguaglossa village. This episode, here reported for the sake of completeness, was not included in this analysis due to the paucity of the sampled ash products.

2.4.2 Volcanological analyses

Volcanic (mainly explosive) activity at Etna is routinely observed by video-recordings from the INGV-CT live-cameras set around the slopes of the volcano [e.g., Andronico et al., 2009a] which can provide images at a rate of 2 FPS. As shown on several occasions, when visibility is good enough, video-recordings from one or more points of view allow a detailed reconstruction of the timing of the explosive activity. For this thesis, in particular, images from the cameras of La Montagnola (thermal and true-color, at about 3.5 km away from the summit), Nicolosi (thermal and true-color, 15 km) and Catania-CUAD (true-color, 27 km), all of them on the Southern slope of Etna, and from the true-color camera of Milo (11 km) on the East flank of the volcano were analyzed (see **Fig. 2.30**). All times reported in the following and in the pictures are given in GMT (local time: GMT+2H for the ash emissions from SEC and BN, GMT+1H for that from NEC).

Sampling of the erupted products is usually carried out by volcanologists of Istituto Nazionale di Geofisica e Vulcanologia within a few hours/days after the end of each explosive event, depending on the formation of an eruption column and weather conditions (mainly poor or absence of intense rain and snow) during and immediately after the tephra fall [Andronico et al., 2009a]. In case of small events, the fallout deposit is often temporary due to the low amount of tephra recovered on the ground. When possible, collection of a sufficient number of samples to estimate the magnitude of the explosive event by the mass load per unit area is done. These operations also allow comparing the intensity of different explosive episodes by evaluating the amount of tephra fallout. Further, on selected ash samples the textural features are investigated. In particular, for this study, grain size, componentry, and morphologic analysis were performed on eight volcanic ash samples described in **Table 2.5**. Sample labels refer to the crater of emission and the day when the ash was erupted. Samples were first carefully cleaned in distilled water and oven dried.

Sample ID	Crater	Date	Location of Sampling sites	Coordinates (Latitude-Longitude)	Location of sampling sites (m) asl)	Distance from the vent (km)	Direction of ash dispersion	Weight (g/m^2)
CSE080410-1	SEC	8/04/2010	Pineta Ragabo	37°47'27.26''N 15°2'31.68''E	1800	4.7	NE	17.3
CSE080410-2	SEC	8/04/2010	Monte Conca	37°47'16.98''N 15°2'20.84''E	1900	4.3	E-NE	17.7
CSE080410-3	SEC	8/04/2010	Linguaglossa Town	37°50'33.77''N 15°8'30.41''E	550	16	NE	17.75
CSE080410-4	SEC	8/04/2010	Piano Provenzana	37°47'36.19''N 15°2'4.98''E	1810	7	N-NE	77.8
BN250810-1	BN	25/08/2010	Catania, INGV	37°30'50.11''N 15°4'55.10''E	40	30	S-SE	0.065
BN250810-1	BN	25/08/2010	Trecastagni Town	37°36'50.79''N 15°4'33.05''E	560	17	S-SE	0.88
BN250810-4	BN	25/08/2010	Mascalucia Town	37°40'10.65''N 15°3'56.20''E	420	19	S-SE	0.07
NEC151110	NEC	15/11/2010	North East Crater rim	37°45'13.38''N 15°59'49.72''E	3300	0.002	E-NE	1.8

Table 2.5: List of Study Samples With the Main Volcanological Features

2.4.2.1 Grain-size analyses:

Grain-size analyses were performed by CAMSIZER® [*Retsch*; www.retschtechnology.com], a laboratory instrument based on digital image processing that measures both size and shape of incoherent materials in a range between 30 µm to 30 mm [e.g. Lo Castro and Andronico, 2008].
In the following, the main results obtained from this analysis are listed for each episode.

The 8 April 2010 eruption from SEC. The proximal samples 080410-1 and 080410-4 consist of more than 90 % of particles with dimensions ranging from 0.125 mm to 1 mm showing a modal value of 0.25 mm, while the sample 080410-2 has a slightly broader trend with a secondary mode peaked at 8 mm (possibly caused by the concurrence of two different pulses of ash emission). Sample 080410-3, collected at 16 km from the vent, is unimodal at 0.25 mm with 60 % of particles ranging between 0.25 and 0.5 mm (**Fig. 2.35**).

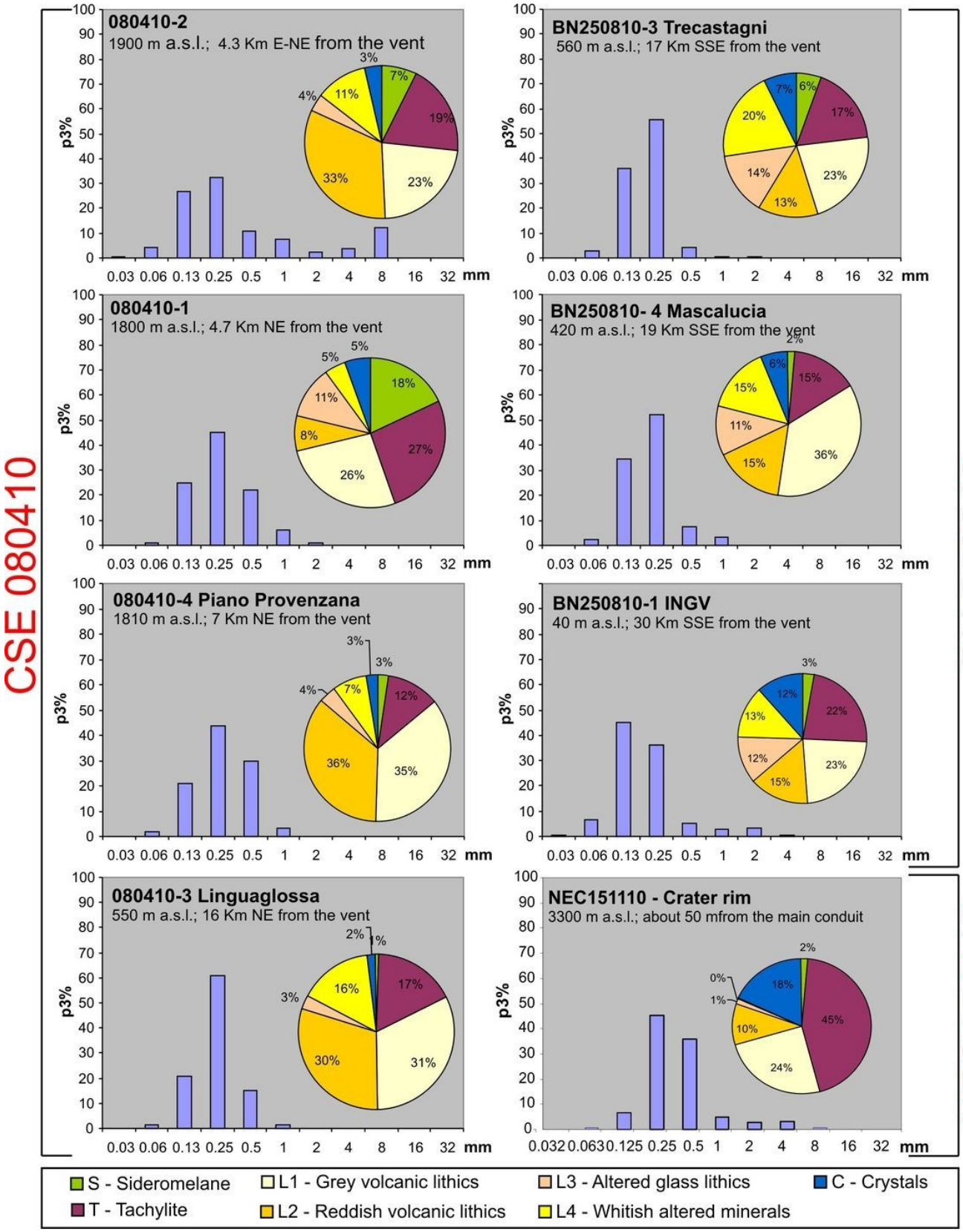

Figure 2.35: Histogram and cake diagram showing, respectively, the grain-size distribution and component percentage of the collected ash samples related to the three eruptive events described in the text (8 April 2010 from SEC, 25 August from BN, and 14–15 November from NEC).

The 25 August 2010 eruption from BN. The samples related to Trecastagni and Mascalucia sites (BN250810-3 and BN250810-4, respectively) show a similar quasi-unimodal distribution with most of the samples (91.8 and 86.8 %, respectively) ranging between 0.125 and 0.5 mm. Sample BN250810-1 (INGV), collected 30 km SSE from the vent, is characterized by a slight decrease of particle dimensions thus ranging from 0.063 mm to 0.5 mm with a lower 1-phi class mode than previous samples at 0.125 mm (**Fig. 2.35**).

The 15 November 2010 eruption from NEC. The only sample collected shows a relatively wide, coarse-grained distribution, with more than 80 % of the sample ranging from 0.25 mm to 1 mm (**Fig. 2.35**).

2.4.2.2 Componentry and Morphological Analysis

Componentry and morphological analyses were performed by binocular stereoscopic microscope (Nikon SMZ1500). In particular, componentry was evaluated by counting 500 particles per sample in order to identify the proportion of the different ash components [e.g. sideromelane, tachylite, lithics and crystals: Taddeucci et al., 2002; Andronico et al., 2009a,b]. It was performed on the highest frequency size class for every sample (i.e. the mode), corresponding to the interval comprised between 0.125 mm and 0.25 mm (0.063-0.125 mm for sample BN250810-1). Furthermore a total of 12 to 30 ash particles from each sample were mounted on three different glass slides, representing the main juvenile and lithic typologies detected under binocular microscope. The particles were then observed with a LEO-1430 scanning electron microscope (SEM) in order to better scrutinize and evidence their morphological and textural features.

We distinguished: a) transparent, light to dark brown glass fragments of sideromelane, with different vesicularity degree (from poor to high) showing variable shapes (see morphological description below for details); b) grey-black, opaque tachylite clasts, poorly or not vesiculated, exhibiting equant and mostly blocky shapes; c) crystals (felsic or mafic); d) different typologies of lithics: I) grey clasts; II) reddish clasts; III) altered glass; IV) whitish altered minerals. The distribution of those component for each ash emission episode is given below.

The 8 April 2010 eruption from SEC – Samples 080410-2, 080410-3 and 080410-4 are characterized by a high percentage of the lithic fraction (values between 71 and 82 %) with the most common typology being characterized by reddish volcanic clasts, well-visible in the general appearance of the samples (**Fig. 2.36a**, image 1); the juvenile content shows

similar values ranging from 15 % to 26 %. The sample 080410-1 has a slightly higher percentage of juvenile particles (18 % of sideromelane and 27 % of tachylite). Crystals have been found with percentage of 2-5 % (**Fig. 2.35**).

The 25 August 2010 eruption from BN: The three analyzed samples show very similar component proportion, being characterized by very low percentages of sideromelane (2-6 %) and a slightly higher content of tachylite (15-22 %) (**Fig. 2.35**). The lithic fraction has the highest percentage (63-77 %) and within this class the most common types are the grey fragments (pre-existing lava clasts; **Fig. 2.36c, image 3**), the whitish lithics (altered volcanic and rarely sedimentary clasts; **Fig. 2.36c, image 4**) and the altered, yellowish to brownish glass fragments as shown in **Fig. 2.36c, image 2**. The remaining fraction (6-12 %) is made of plagioclase crystals.

The 15 November 2010 eruption from NEC: The sample is characterized by a high percentage of tachylite (45 %) and a poor content of sideromelane (2 %). The abundance of tachylite fragments gives a dark aspect to the total sample (**Figure 2.36a, image 3**). The lithic fraction, made up of both grey and reddish volcanic fragments, has a percentage of 35 %. Finally, we found 18 % of crystals, most of which plagioclases.

All the analyzed samples show peculiar morphologies especially regarding sideromelane and tachylite clasts (**Fig. 2.35**). In particular, the tachylite has blocky morphology (**Fig. 2.36b, image 4**), whereas sideromelane has been found both as equant and highly vesicular fragments (**Fig. 2.36b**, **image 1**) or scarcely to non-vesicular with smoothed surface, irregular-shaped particles (**Fig. 2.36b, images 2,3**). In **Table 2.6** a semi-quantitative evaluation of the different morphologies of sideromelane found in every analyzed sample is reported.

	Relative Percentage (0-100 %) of Morpology Types of Sideromelane		
Samples	Equant well vescicular	Smooth surfaced and irregular shapes	Acicular (like Pele's hair)
8 April	40	60	0
25 August	27	70	3
15 November	25	75	0

Table 2.6: Relative proportions of morphology types of sideromelane clasts distinguished in the ash samples from the study explosive events

SEM images allowed detailing the external morphology of the juvenile particles (**Fig. 2.37**). The most abundant type of sideromelane (**Table 2.5**) consists of fluidal clasts with variable shapes

(from elongated to convoluted to irregular), characterized by smooth glassy surfaces and vesicles ranging from elongated to subspherical (**Fig. 2.37a**). The other dominant sideromelane class is made up of almost equidimensional particles, with external surfaces intersected by large bubbles with polygonal shapes (**Fig. 2.37b**). Tachylite is generally equant to subequant, poorly to non-vesicular and characterized by smooth, planar to curviplanar surfaces and sharp edges (**Fig. 2.37c**); partially altered tachylites can also have isolated vesicles intersecting the surface filled by finer, pyroclastic fragments (**Fig. 2.37d**). Finally, **Fig. 2.37e** shows a reddish lithic typically found in the SEC samples, while **Fig. 2.37f** is an altered, transparent, yellowish glass shard.

Componentry and morphological data of the analyzed samples may be used to explain the origin of the ash, and integrated with the seismo-acoustic evidence in order to formulate a simple model of the eruptive dynamic producing the different explosive events.

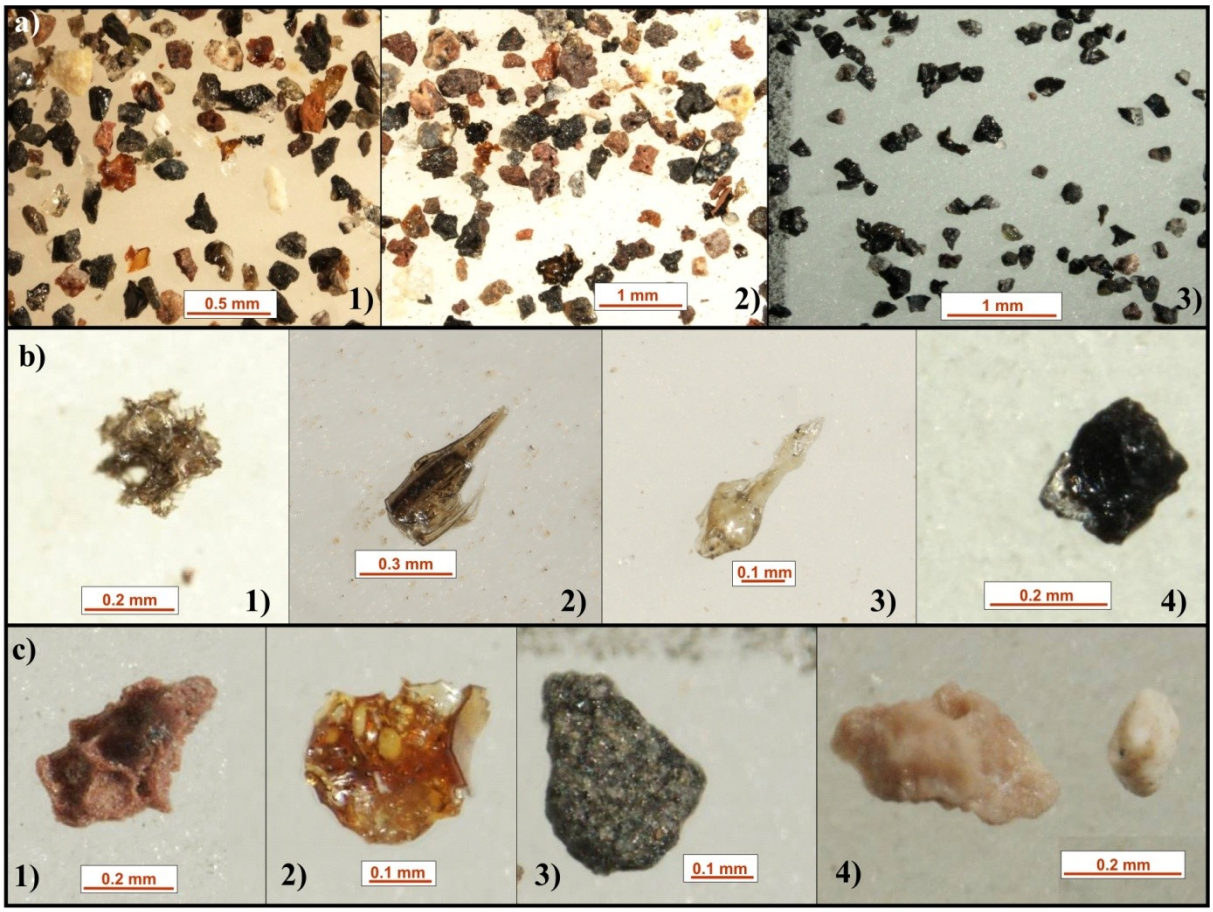

Figure2.36: Images acquired under stereomicroscope showing: a) the general appearance of ash samples erupted from 1) SEC, 2) BN and 3) NEC; b) different juvenile clasts: 1) well vesicular, equant shaped sideromelane; 2) poorly vesicular sideromelane particle with smoothed surface; 3) thread, acicular sideromelane particle; 4) black, equant blocky clast of tachylite; c) different lithic clasts: 1) reddish opaque and blocky; 2) transparent, yellowish altered glass; 3) greyish and blocky; 4) whitish volcanic (left) and sedimentary (right) particles.

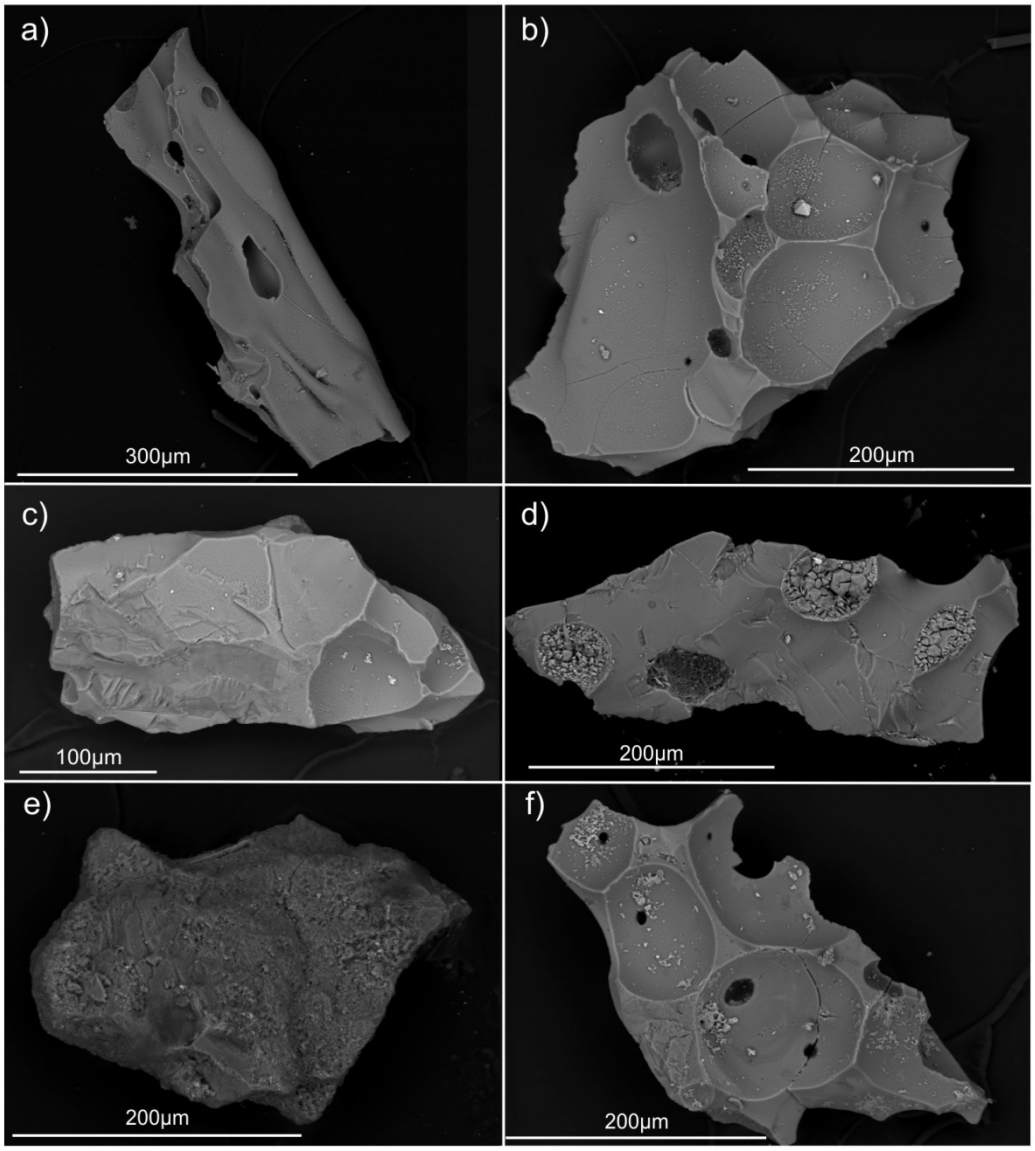

Figure 2.37: Images acquired under Scanning Electron Microscope (SEM) showing: a) fluidal and b) equidimensional fragments of sideromelane; c) non-vesicular particle of tachylite; d) clast of tachylite showing vesicles filled by finer, altered material; e) reddish lithic; f) altered glass shard.

2.4.3 Seismo-acoustic analysis

In order to characterize seismo-acoustic data collected during the 2010 explosive events of Mt Etna, the VASR (Volcanic Acoustic-Seismic Ratio) parameter, proposed by Johnson and Aster [2005], was adopted. To obtain VASR, seismic energy (E_{seism}), was calculated on the resultant vector of the three component traces of the recorded velocity (U) by the equation (**25**), and fixing the volcano density and P wave velocity, equal to 2500 kg/m^3 and 1800 m/s, respectively [Gresta et al., 2004; Lokmer et al., 2007; Sciotto et al., 2011]. Concerning the seismic wave radiation, the same assumptions discussed by Johnson and Aster [2005] were found to be valid, and therefore

adopted in this thesis. The parameter *A* accounts for intrinsic and scattering dissipation and *S* for the site response. At Etna, literature data demonstrated that frequency-dependent absorption coefficient has a weak influence on energy dissipation [Di Grazia et al., 2006; Patanè et al., 2008]. On the basis of this consideration and taking into account the short station-source distance [Johnson and Aster, 2005], *A* was fixed equal to 1. Regarding the site response, site correction factors for EBEL and EBCN stations were evaluated and found to be equal to ~ 1 [Di Grazia et al., 2006; Andrea Cannata, personal communications].

Successively, acoustic energy (E_{ac}) was estimated on the basis of the excess pressure (ΔP), assuming linear propagation of sound (infinitesimal excess pressure with respect to ambient pressure), by means of equation (**24**), where ρ_{atm} (density of the atmosphere) and c_{atm} (sound velocity in the atmosphere) were fixed equal to 0.9 kg/m^3 and 340 m/s, respectively. For microphones located at distance shorter than a few kilometres from the vent, as for the acoustic stations used for this analysis, the effects of the inhomogeneous atmosphere are negligible [Johnson, 2003]. Consequently, in this case, the main source of disturbance on the pressure recording could be the wind, which can generate a broadband noise. On checking the weather-conditions during the three analyzed episodes carefully, wind intensities were found lower than 7 m/s, and, consequently, could not have introduced errors in evaluating acoustic energies.

Many authors have acknowledged the utility of a quantitative analysis of the relative partitioning of acoustic and seismic energy to compare eruptive dynamics both between different volcanoes [e.g. Johnson and Aster, 2005] and at a single volcano among different explosive episodes [e.g. Sahetapy-Engel et al., 2008]. Nevertheless, some limitations are due to the assumptions and the parameters fixed for the energy estimations. Focusing on each parameter, the error in the measure of source-station distances is low enough to be neglected, while, concerning P-wave velocity, density of volcano edifice, site response and attenuation, literature data has been considered as reference (see references above). Regarding the acoustic wave velocity and density in the atmosphere, they are largely dependent on the temperature, but unfortunately there are no measures of this parameter at such altitude. In order to evaluate the influence of possible errors due to the fixed parameters, VASR was computed by systematically changing all those parameters inside cautelative ranges. In particular, for seismic energy computation, P-wave velocity in the range 1.7-2 km/s was adopted, and volcano edifice density from 2.3 to 2.5x10^3 kg/m^3. Then, in order to compute the acoustic energy, the acoustic wave velocity and density was evaluated on the basis of different temperature conditions (from -15 to 30 °C), obtaining ranges of

0.322-0.350 km/s and 0.83-0.99 kg/m^3, respectively. Finally, minimum and maximum values for the VASR were found. They differ from the values calculated by about 20 %.

In this thesis, VASR calculation, performed on the signals acquired by EBEL (08 April, 25 August episodes) or EBCN station (14-15 November episode), has been applied to investigate and compare the relative explosive behavior at the three different craters of Mt Etna producing ash emission in 2010. Further, to obtain information on the time variations of the seismo-acoustic source, likely related to changing conduit conditions, variations of VASR have been analyzed throughout a succession of discrete explosive events at every single vent. It is noteworthy that this analysis concerns a suite of ash emissions occurring at the same volcano, and therefore any eventual uncertainties on some aforementioned parameters (e.g. ρ_{volc} and c_{volc}), that remain unchanged during the different episodes, is not able to affect strongly the relative comparison among values obtained for the studied episodes.

Furthermore, localization analysis of infrasound events recorded during the main episodes of activity at the summit craters in 2010 were performed, by using the joint semblance and brightness method [Cannata et al., 2011]. A grid of 4x4 km^2, with a spacing of 25 m, coincident with topographical surface and centered below the summit craters was defined. The source point is identified where joint semblance-brightness values show their maximum.

Successively, volcanic tremor amplitude was computed at ECPN station during a period from 15 March to 15 December, including the three main episodes here described. The RMS (Root Mean Square) amplitude time series was computed over a 5-second-long moving window, filtered in the 0.5-2.5 Hz band. In order to remove the contribution of seismic transients (such as volcano-tectonic earthquake and long period events), a value of 25th percentile was obtained for each 1-minute-long RMS series. Then, volcanic tremor was located, by using the grid search amplitude decay [Battaglia et al., 2005; Patané et al., 2008] method on 1-hour-long filtered seismic windows (0.5-2.5 Hz). The 3D grid used for this work is 6x6x6 km^3, with spacing between nodes of 250 m and centered beneath the summit craters.

In the following **sections 2.4.3.1** and **2.4.3.2** volcanic tremor during 2010 and seismo-acoustic event recorded during each episode are analyzed, respectively.

2.4.3.1 Volcanic Tremor Analysis between March and December 2010

Volcanic RMS amplitude is plotted against time in **Fig. 2.38**. In order to emphasize the occurrence of migration of volcanic tremor sources, the locations were plotted in map and section view (**Fig. 2.39**). On the basis of the observed trends of tremor locations, we subdivided the analyzed period into three intervals: i) 15 March-14 May; ii) 15 May-14 October; iii) 15 October-15 December.

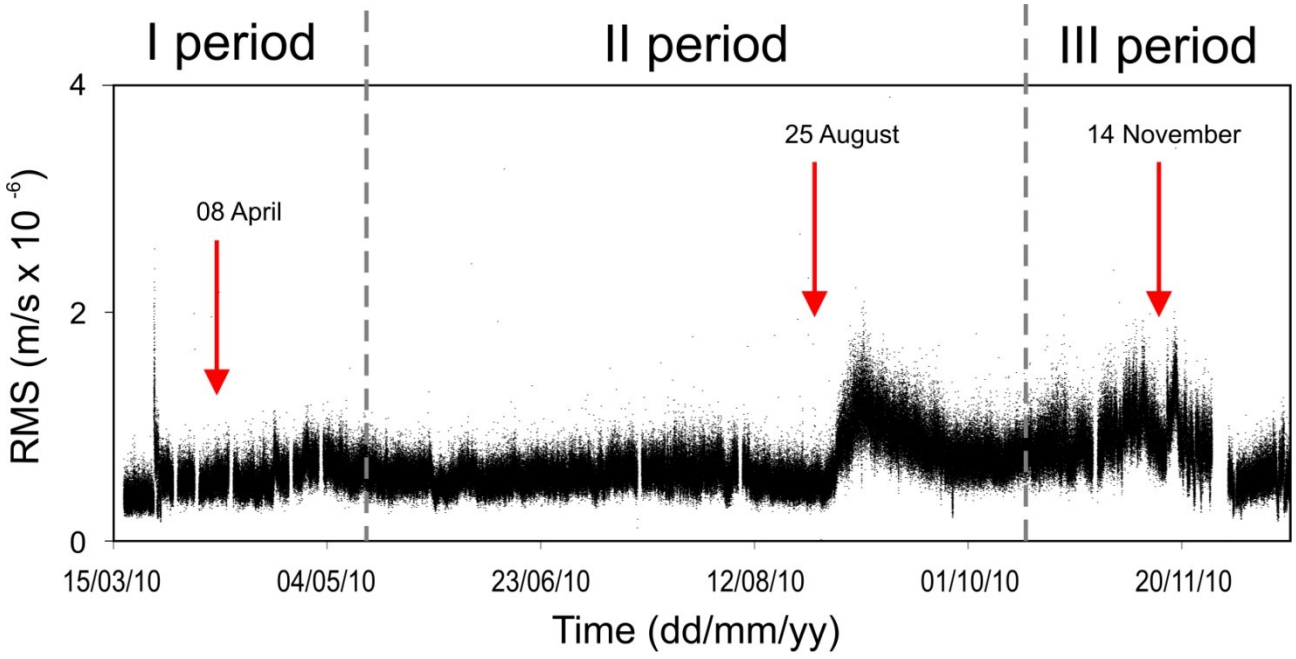

Figure 2.38: Variation over time of root mean square (RMS) amplitude of volcanic tremor. The dashed gray lines bound the three periods characterized by different volcanic tremor location trends. In particular, period I lasts from 15 March to 14 May, period II from 15 May to 14 October, and period III from 15 October to 15 December 2010.

During the onset of the first period the volcanic tremor originated below NEC at altitudes ranging between 0.5-1.0 km a.s.l. It is noteworthy that from the very first days of April volcanic tremor became progressively shallower (1.5-2.0 km a.s.l.), and moved southeastward, toward SEC. During the first period no significant amplitude variations were observed. During the second period tremor location remained stable roughly below SEC, while a slight increase in RMS amplitude started on 30th August, and lasted for about 15 days. During the third period, from early November, tremor locations progressively returned to their original position (North East of the summit area), roughly beneath NEC, deepening in the meantime (0.5-1.5 km a.s.l.). In mid-November the RMS amplitude sharply decreased reaching the minimum values of the whole period.

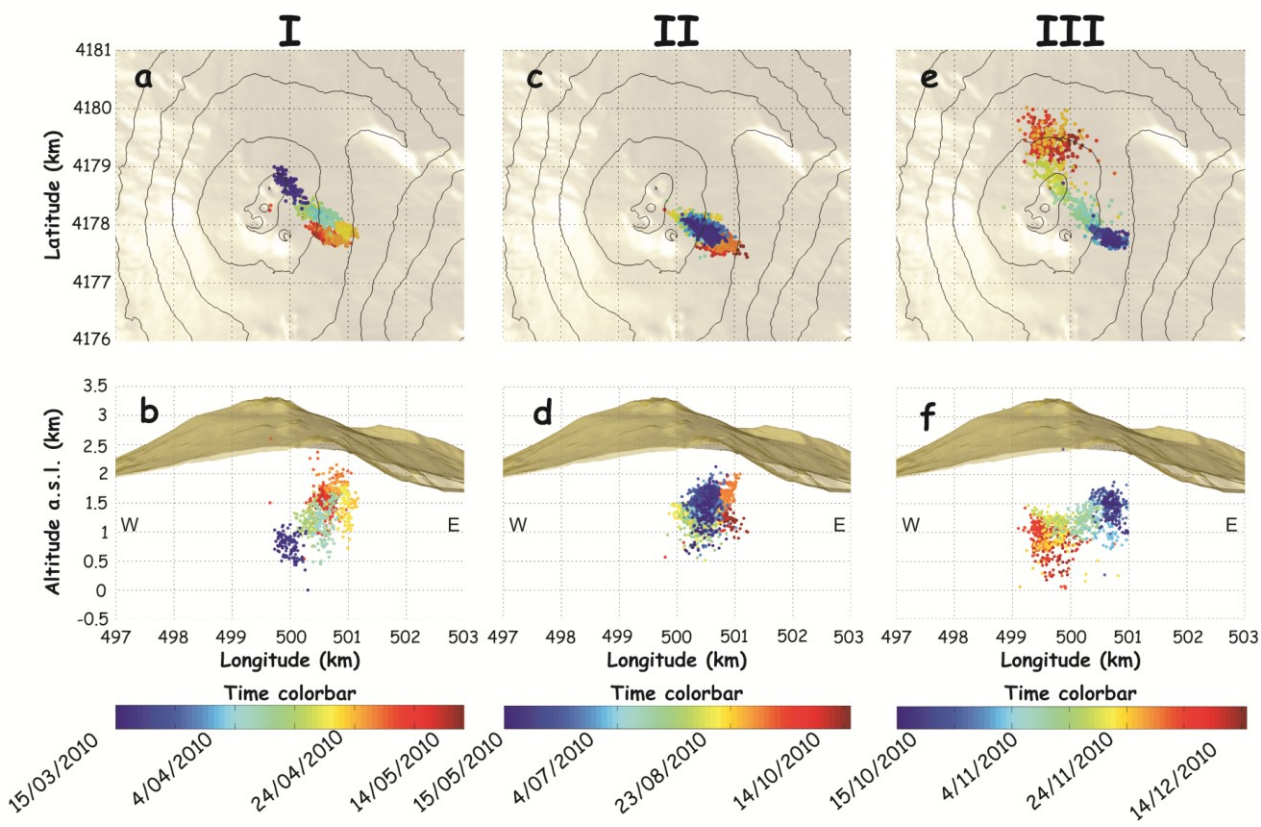

Figure 2.39: Maps and sections of Mt Etna with volcanic tremor source locations calculated during three periods (see the bottom time color bar). In particular, period I lasts from 15 March to 14 May (a and b), period II from 15 May to 14 October (c and d), and finally period III from 15 October to 15 December 2010 (e and f).

2.4.3.2 Seismo-Acoustic Data: VASR evaluation

During the ash emission of 8 April from SEC, more than 25 seismic events with the associated infrasound events were recorded in about an hour. The events are characterized by duration of about 15 s and frequency peak of 0.5-1 Hz (**Fig. 2.40a**). Infrasound events originated in the area of the pit-crater. Infrasound and seismic cumulative energies were evaluated for 19 events occurring between 15:50 and 16:30, assuming 0.34 km s^{-1} and 0.9 kg m^{-3} as sound velocity and air density, respectively. **Fig. 2.41** shows VASR values obtained from infrasound and seismic energies. Explosive events recorded on 8 April are mainly characterized by VASR between 0.001 and 0.1 and the respective acoustic and seismic energies display a fairly positive correlation (i.e. increasing seismic energy acoustic energy increases, too), except for the event of 16:18. The latter, indeed, exhibited a lower seismic energy and a VASR value of about 2.

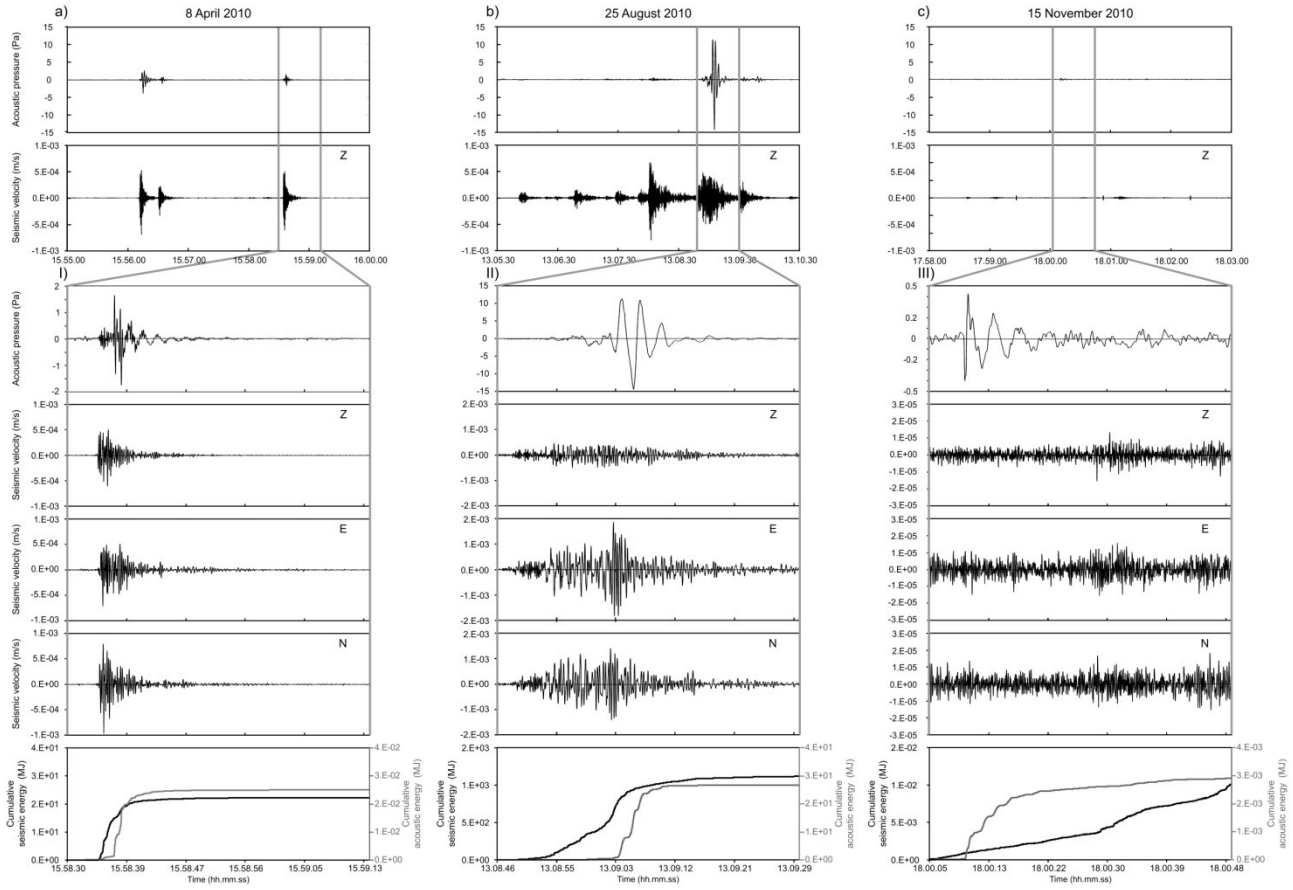

Figure 2.40: Infrasonic signals, three-component seismic signals, and relative cumulative energies for events recorded at EBEL station during the three analyzed eruptive episodes. In particular, the events shown in a, b, and c were recorded during explosive activity at the pit crater of SEC, BN, and NEC, respectively.

During the ash emission of 25 August from BN, 6 main seismic events took place between 13:05 and 13:10, and among these, the last two were accompanied by infrasound events and ash emission at about 13:09. Later, on 25 August and in the following days, other lower intensity ash emission episodes were accompanied by both seismic and infrasound events at the same source vent. The infrasound events of 25 August lasted about 30 s with frequency peak of ~0.4 Hz (**Fig. 2.40b**). Location analyses pointed to BN as the source of the infrasound events, recorded during the main episode (25 August) and the following explosions. The seismic events lacking in acoustic signals had VASR values between ~0.0001 and 0.001. On the other hand, for the seismic event recorded during the main explosion at BN (13:09), accompanied by the infrasound event, we obtained a VASR equal to 0.02 (**Fig. 2.41**; see the red dot label).

Concerning the ash emissions of November 2010 from NEC, we analyzed infrasound and seismic signals collected during 14-15 November. The numerous infrasound events analyzed have shown similar characteristics to those typically recorded at Mt Etna (see **section 2.2**). As also observed during 14-15 November (**Fig. 2.40c**), NEC infrasound events, recorded by G.R.A.S. microphones,

are generally characterized by duration up to tens of seconds and waveforms resembling decaying sinusoids. They usually have two frequency bands: one lower than 0.5 Hz, the other comprised between 0.8-2.5 Hz. Unlike the previous analyzed ash emission episodes, NEC events recorded on 14-15 November were accompanied by no evident seismic events, as also usual at this vent (see **section 2.2.1.3**). Indeed, the seismic events observed during 14-15 November (also visible in **Fig. 2.40c**) show a time lag with respect to the infrasound ones that is inconsistent with the hypothesis of a shared source. In particular, VASR was calculated between infrasound events and the corresponding seismic window aside from the presence of any evident seismic event. The analyzed events exhibited values of VASR comprised between 0.1 and 1 (**Fig. 2.41**).

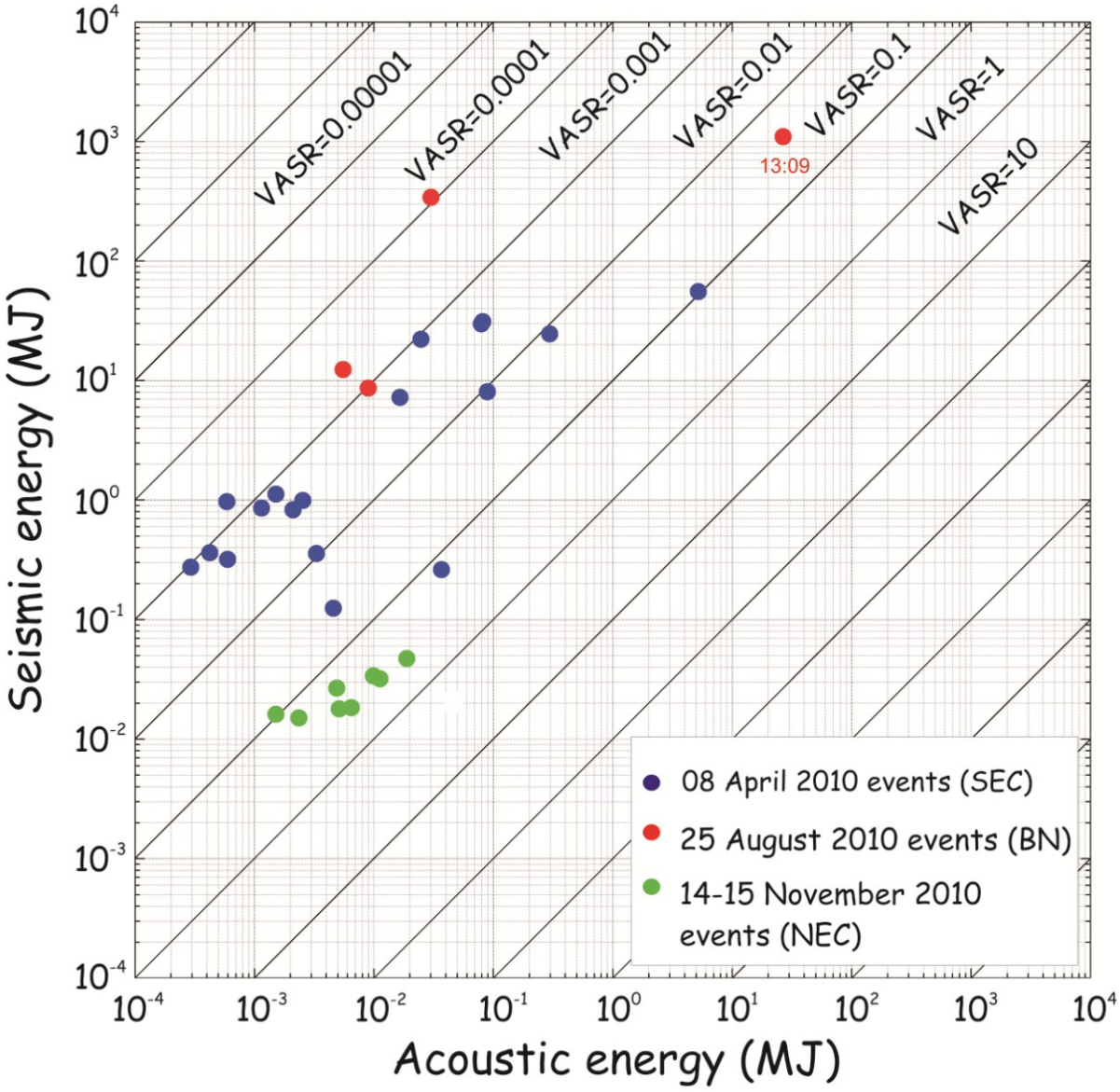

Figure 2.41:. Volcanic acoustic-seismic ratio (VASR) values calculated for seismo-acoustic events recorded during 8 April (blue dots), 25 August (red dots), and 14–15 November (green dots) eruptive episodes. Please note that an error of 20% due to the uncertainties of the fixed parameters could affect VASR values .

2.4.4 Discussion

2.4.4.1 Definition of 2010 ash emission types

Based on the texture analysis of the erupted deposits and the seismo-acoustic characterization of the explosive episodes, we can distinguish between an impulsive ash emission, named *type a*, and a more prolonged one, named *type b*. *Type a* was characterized by short duration (less than 1 minute) of the associated, well-distinct seismic signal, and followed by the formation of a 1-km high sustained eruption column. The top of the volcanic plume was then moved laterally by dominant winds producing light, relatively extended tephra fallout up to 20-30 km of distance from the vent. *Type a* ash emissions occurred from SEC (particularly from the lateral pit-vent) and BN, both craters sharing the presence of a several meters-thick layer of talus and detritus filling the crater bottom. Despite this similarity, in the last 13 years SEC has been the most active summit crater of Etna, being the location of very frequent Strombolian/lava fountaining activity and lava flow output; this resulted in the alternation of clearing and accumulation of ash and blocks on the top of the conduit constantly modifying the crater morphology, thus suggesting the presence of a persistent thermal and fumarolic activity within the lateral pit-crater. Conversely, BN was practically quiescent since the large explosion in January 2006, and the bottom of this crater was covered up to mid-2010 by a growing, relatively cold layer of debris mostly produced by failures of the inner walls and involved only by low fumarolic and degassing activity.

Type b ash emission, observed only at NEC, was characterized by a continuous, prolonged ash and steam venting. Remarkably, this activity was not correlated to evident seismic events or increasing of the volcanic tremor amplitude, but occurred a few days after the shifting of the tremor source, beneath the NEC. Coherently, the eruption plume was not sustained but passively rose upward and possibly bent over the summit of the volcano just outside of the crater, depending on the strength of the blowing winds. Unlike SEC and BN, in recent years NEC has been involved by intense degassing to puffing from its deep crater volcanic processes suggesting in some ways a definitive, continuous clearing of the conduit and the lack of a thick layer of old material on the top of the magma column residing in the conduit.

So, such simple observations lead to suppose different eruptive conditions for the three craters in 2010: i) the volcanic conduit below the pit-crater of SEC was the location of cooling magma,

caused by the frequent activity occurring at least up to 2008 and whose unrest produced the formation of the pit-crater itself since November 2009, ii) the bottom of BN was quiescent and practically inactive since 2006, and finally iii) NEC had a relatively free or at least permeable surface at the top of the residing, active magma column.

It is noteworthy that, both *type a* and *type b* ash emissions were characterized by the infrasonic wave radiation, but they can be distinguished on the basis of the presence or the absence of evident seismic counterpart. Indeed, explosions producing *type a* ash emissions generated infrasonic and seismic signal. On the contrary, *type b* ash emission exhibited infrasonic events not accompanied by evident seismic traces. This different coupling of the volcanic explosions with the atmosphere and the volcano edifice resulted in different VASR value associated with the two types of ash emission.

2.4.4.2 Indications from the ash texture

The texture analysis of the collected samples was helpful in order to distinguish the componentry and morphology of the ash particles erupted from SEC, BN and NEC during the 2010 volcanic activity. In particular, the absolute percentage of lithics vs. juvenile, the sideromelane/tachylite ratio and the morphological features of the ash samples, allowed drawing inferences on the eruptive dynamics accompanying the ash emissions of *type a* (SEC and BN) and *type b* (NEC).

In general, all the ash samples are characterized by high percentages of lithics with respect to the juvenile fraction, while within this class the amount of sideromelane is lower than tachylite. The NEC sample is further made up of a higher percentage of juvenile particles than SEC and BN samples showing also a lower sideromelane/tachylite ratio.

The morphological features (shape, surface and vesicularity) of sideromelane in the tephra deposits support the involvement of “fresh” magma during all the studied volcanic events; in other words, the activity at the three craters (SEC, BN and NEC) was undoubtedly magmatic. What is remarkable here is the quantity of sideromelane in the collected samples and their relative percentage with respect to the other juvenile components, i.e. the tachylite. The low amount of juvenile particles for SEC and BN may be correlated to the thick layer of relatively old and altered volcanic material, filling the crater bottom from months to a few years and therefore reworked and altered with time. When ejected during explosive activity, the old material (volumetrically larger than the low amount of magma involved) may significantly dilute the percentage of juvenile

particles (sideromelane and tachylite). The presence of an almost constant amount (12 to 27 %) of tachylite in the SEC and BN samples also indicates a similar involvement of portions of crystallized magma during the explosive process.

Conversely, together with a poor percentage of sideromelane, the NEC sample is also made up of abundant particles of tachylite (45%). Noteworthy, the origin of this component is attributed to portions of cooler magma; this means relatively low temperature and high degree of crystallization supporting the formation of a network of cracks favorable to permeable gas flow [Taddeucci et al., 2004] and suggesting the presence of a continuous process of brittle fragmentation of the magma during the volcanic activity at NEC. Here also the percentage (35 %) and typology (mainly two) of lithics are less than at SEC and BN (**Fig. 2.35**), while free-crystals are relatively abundant, giving further evidence of the different features of explosive activity (*type b*) and associated deposit of NEC with respect to the other two craters producing *type a* explosions.

However, significant differences among component classes have been found in the lithics from SEC and BN. In particular, the SEC samples are mainly made up of both opaque reddish and greyish blocky clasts (**Fig. 2.36c, images 1 and 3**), whereas BN samples show several transparent yellowish fragments with a clear morphology that could be ascribed to altered sideromelane glass (**Fig. 2.36c, image 2**) and whitish, altered clasts (**Fig. 2.36c, image 4**). Grey-fresh type lithics (**Fig. 2.36c, image 3**) could be lava fragments associated to portions of the conduit, whereas the whitish and altered types could be derived from old material (both lavas and pyroclasts erupted months to years before) that has been recycled, remobilized, or ejected from the bottom crater (**Fig. 2.36c**, **image 4**).

Both opaque reddish and transparent yellowish (**Fig. 2.36c**, **images 1** and **2**; **Fig. 2.37e,f**) lithic typologies, specific to SEC and BN respectively, may be the result of different kinds of volcanic glass alteration. Volcanic glass is one of the most thermodynamically unstable materials found in the Earth's surface and it can be affected by extensive secondary alteration after its emplacement, which could derive either by fumarolic activity or circulating hydrothermal solutions or, if emplaced far away from their source areas, extensive weathering by weakly reactive meteoric waters (generally considered less acid than fumaroles or hydrothermal solutions). When considering an active volcano environment, as in the case of Etna, exceeding 3000 m of elevation and subjected to intense rain and snow in the colder seasons, the kinetics of alteration processes is very rapid due to the interaction with high temperatures [up to 700 °C according to Allard et al., 2008] and diffuse emission of volcanic gases.

The process of alteration may be relatively rapid, or extremely slow, depending mainly upon the following physico-chemical parameters [Furnes, 1975] chemical composition of the glass, 2) chemistry of the aqueous environment in which the process takes place, 3) temperature and 4) time factor. Assuming the first two parameters are similar for the different craters, it is reasonable to assume that for Etna the latter two (temperature and time) could be the most crucial to deeply alter glass particles. Another important constraint comes from Spadaro et al. [2002] that, after exposition of basaltic glass within the Etna crater, demonstrated that morphological and chemical transformations of the clast surface occur in a very short time and become significant within a few hours. The same results have been confirmed by Schiavi et al. [2010] thanks to some experiments conducted on ash samples that were kept at high temperature (>700 °C) in a tube furnace. These experiments showed that an exposure of about 12 h at 750 °C in oxidizing conditions (fO_2 ~ atmospheric) produced a complete reddening of clast surfaces. Less oxidizing conditions resulted in observable surface modifications and precipitation of very small secondary crystals, giving a dull gray appearance to the clast surface. It is noteworthy that these characteristics are like those found in the SEC samples.

Moreover, different studies conducted on the rate of alteration of basaltic glasses showed that the color of the altered glass varies from light yellowish brown to dark brown. It appears, on the other hand, that the color shade is temperature-dependent, and the ones formed at the highest temperature (90 °C in this experiment) are darker than those formed at lower temperatures [Furnes, 1975]. Again, the different stage of alteration could influence the characteristics of clasts, and in particular at the incipient stage, glass is described as a light yellow brown to red brown isotropic material, which Peacock [1926] referred to as gel-palagonite; and this could be the case of BN samples. At a more advanced stage of alteration, clasts show an anisotropic variety characterized by a darker yellow brown color, granular to fibrous, often with scattered opaque granules, due to increasing degree of clay and Fe-oxide/hydroxide crystallization with time [Thorseth et al., 1990].

So, given the features of altered volcanic glass, we think that the relative abundance of reddish lithics (**Fig. 2.36**) related to the SEC activity could be ascribed to a higher temperature environment in different oxidation contexts, whereas lithics (altered glasses; **Fig. 2.37f**) and whitish minerals erupted from BN show a minor degree of alteration probably linked to lower temperatures. Conversely, NEC samples are characterized by the “fresher” particles of lithics and tachylite (the latter appearing shiny black-colored), while the presence of a significant amount of

bright crystals in the ash from volcanic activity at NEC further suggests the continuous, efficient process of crystallization and rapid clearing of magma fragments occurring in the conduit. Concerning the tachylite, different degrees of freshness may support dissimilar eruption dynamics between *type a* and *b* ash emissions; this is apparent by comparing **Fig. 2.37c**, showing a clean clast from NEC, with **Fig. 2.37d**, which on the contrary highlights a particle from BN whose vesicle hollows are filled by abundant, fine-grained, altered ash particles due to the preexistent debris layer in the crater bottom.

2.4.4.3 Indication from seismo-acoustic data

Indication from tremor analysis and LP sequences

The close link between Mt Etna volcanic tremor and the volcano feeding system was first highlighted by Schick and Riuscetti [1973]. The continuity in time of Mt Etna volcanic tremor, characterized by a low frequency content [0.5-6 Hz; Gresta et al., 1987; Alparone et al., 2007], allows us to make comparisons between its changes in amplitude and location and renewal of volcanic activity, as previously done by other authors, such as Patanè et al. [2008].

Analyzing the volcanic tremor source location it transpires that among the three main episodes, tremor migration toward the eruptive vent preceded the renewal of volcanic activity in two cases (08 April and 14-15 November episodes), suggesting important implications for early warning. On the contrary, no relevant information derived from the observation of the RMS analysis, considering that the only relevant significant was at the end of August, after the Bocca Nuova episode.

The 8 April eruptive episode was preceded by a seismic sequence of low frequency events localized below SEC, at 04:36, not accompanied by any infrasound evidence. In the same way, a seismic sequence was recorded at 08:50 on 24 August at BN. In accordance with the literature associating such seismic low frequency events with the dynamics of fluids within the plumbing system [e.g. Chouet, 1996; Almendros et al., 2002], we believe these seismic episodes, preceding the explosive activity by some hours, to be somehow related to the pressure transients excited by gas slugs rising and pushing at the top of the plugged conduit. Increases in amplitude and occurrence rate of low frequency events have also preceded eruptive activities at other volcanoes

such as Redoubt [Chouet et al., 1994], Mount St. Helens [Moran et al., 2008b] and Colima [Varley et al., 2010]. It is noteworthy that no seismic sequence preceded the eruptive episode at NEC.

Interpretation of the seismo-acoustic energy partitioning

The characteristics of each explosive episode were investigated by means of VASR calculation. As previously specified, there are many different parameters affecting this value. A fundamental role is played by the coupling between acoustic waves and the atmosphere. Indeed, good coupling, favored by factors such as low density of the eruptive plumes, or alternatively the absence of a cap rock plugging the conduit, increases acoustic waves energy which is transmitted through the air. Similarly, the energy associated to seismic waves, travelling inside rock medium from the source to the station, is affected by conduit conditions (e.g. explosive source depth, conduit width) as well as intrinsic attenuation and scattering.

For ash rich eruptions, a various range of acoustic energy is possible, depending on the mass of entrained ash into the eruptive plume. On the contrary, seismic energy is not affected by plume density. As a consequence, high values of VASR are indicative of scarce ash component into the eruptive plume. Alternatively, high values of VASR could be explained by explosions occurring through a magma free surface, lacking any cap rock obstructing the vent, and causing an efficient energy transfer into the atmosphere [Johnson and Aster, 2005]. Indeed, overlying material capping the vent causes an inefficient displacement of the atmosphere thus decreasing the acoustic energy radiated. For these reasons, VASR is known to give useful information on the amount of overlying material damping the acoustic source [Johnson and Ripepe, 2011]. Another possible cause of VASR variation consists in the change of the impedance contrast between magmatic fluid and surrounding medium, mainly influencing seismic energy. Severe impedance contrasts cause a decrease in radiated seismic energy, thus increasing VASR. For instance, gas-rich magma has both higher attenuation and impedance contrast, reducing seismic amplitude [Johnson and Aster, 2005]. Finally, energy loss due to the viscous upward flow in the conduit should be accounted for by a deep source. Indeed, seismic efficiency increases because of some energy loss to the conduit walls. Furthermore, for a narrow conduit, viscous losses cause decrease of infrasound production. Considering both these observations, a decrease in VASR values is expected for a long narrow conduit [Johnson and Aster, 2005]. In light of these considerations,

acoustic and seismic energies and VASR have been calculated and studied for each explosive event.

The 8 April eruptive episode consisted of a sequence of ash explosions, well-correlated with seismo-acoustic events. For these seismo-acoustic events, values of VASR mainly comprised between 0.001-0.1 were obtained (15 events out of 19 have VASR roughly in the 0.001-0.01 range). Such low values of VASR are likely due to a deep source or either to the presence of a dense cap rock topping the conduit. Between the described possibilities the latter is considered more probable. This is in perfect agreement with the low quantity of sideromelane, which, as previously mentioned, was diluted by the notable percentage of lithics in SEC ash samples, likely related to the presence of a conspicuous cap rock. This hypothesis is also supported by the aforementioned occurrence of a sequence of seismic low frequency events with no acoustic emissions, taking place in the early morning and suggesting the lack of coupling of the shallow plumbing system with the atmosphere before the main ash emission episode. Furthermore, seismic and acoustic energy roughly show a positive correlation: increasing seismic energy, acoustic energy increases, too. This general trend of correlated acoustic and seismic energies is typical of a fairly steady source and has been attributed to variations in explosive yield, likely related to eruption magnitude [Johnson and Aster, 2005]. Nevertheless, there are few VASR values scattered with respect to the general positive trend of the data. Taking into account the short time-span in which the events occurred and the characteristics of the eruptive episode, small variations in seismo-acoustic energy partitioning may likely be due to changes in plume density and/or in source depth.

On 25 August 2010 the explosive sequence started at 13:05 and mainly consisted of 6 seismic events. It culminated at 13:09 with the emission of a dense and dark cloud above the BN-1 crater. At the same time as the ash emission a high energy infrasound event, accompanying the seismic event, was recorded (**Fig. 2.40b**). It is noteworthy that the minor ash emissions occurring during 25 August, after the 13:09 explosive event, as well as the following days, were all accompanied by both seismic and infrasound radiation. Evaluation of energy emitted and the calculation of the VASR were carried out for the explosive events occurring between 13:05 and 13:09. Three events recorded before the ash emission exhibited VASR values between ~0.0001 and 0.001, while during the main explosion, at 13:09, VASR reached a value of 0.02. The temporal evolution of volcanic phenomena together with the absence of the infrasound events before the ash emission make the changing condition of the crater the most probable reason for such a variable VASR. In particular,

an obstruction of the conduit would have prevented the explosion from radiating infrasound signals before the main ash emission of 13:09. Once the conduit has become open, radiation of infrasound events would occur during the following minor ash emission episodes. This hypothesis is supported by the low quantity of sideromelane together with the high percentage of lithics observed in BN ash samples. Also in this case the sequence of seismic low frequency events preceding the explosions validate such a hypothesis.

All the seismo-acoustic features of the NEC eruptive episode highlight quite a different explosive mechanism from SEC-BN episodes. Indeed, first of all, from the deployment of the permanent infrasound network in 2006, this crater has been continuously active from the infrasound point of view [e.g., Sciotto et al., 2011]. Furthermore, except for the ash emission here described, NEC had not given rise to superficial volcanic activity since July 2006. Conversely SEC, and, from August 2010, BN, radiate acoustic waves only in coincidence with explosive activity. During the ash emission of 14-15 November 2010, no meaningful changes of NEC infrasound events, compared to their general features observed in the previous days, were found. No associated evident seismic trace was present. Consequently, we can suppose that the energy content of the seismic radiation associated with infrasonic transients was far below the noise level. Thus, in the NEC case, VASR was calculated by using seismic windows mostly containing noise, and then overestimating seismic energies. As a consequence, on the basis of the equation (**26**) the VASR values should be even higher, confirming the hypothesis of our model (VASR values higher for NEC explosions than for SEC/BN explosions). Such a VASR difference is related to the low coupling of the seismo-acoustic source with the medium, likely due to the absence of a cap rock obstructing the NEC top conduit (**Fig. 2.42c**). This confirms the hypothesis that NEC conduit should be relatively open, lacking any thick layer of old material capping the vent, thanks to the efficient degassing, as mentioned in **section 2.4.4.1** These considerations are confirmed by the higher percentage of juvenile component, particularly tachylite, into NEC samples. The idea of considering NEC conduit the main branch of degassing for the volcano was also highlighted by other acoustic studies [Marchetti et al., 2009; Cannata et al., 2009b].

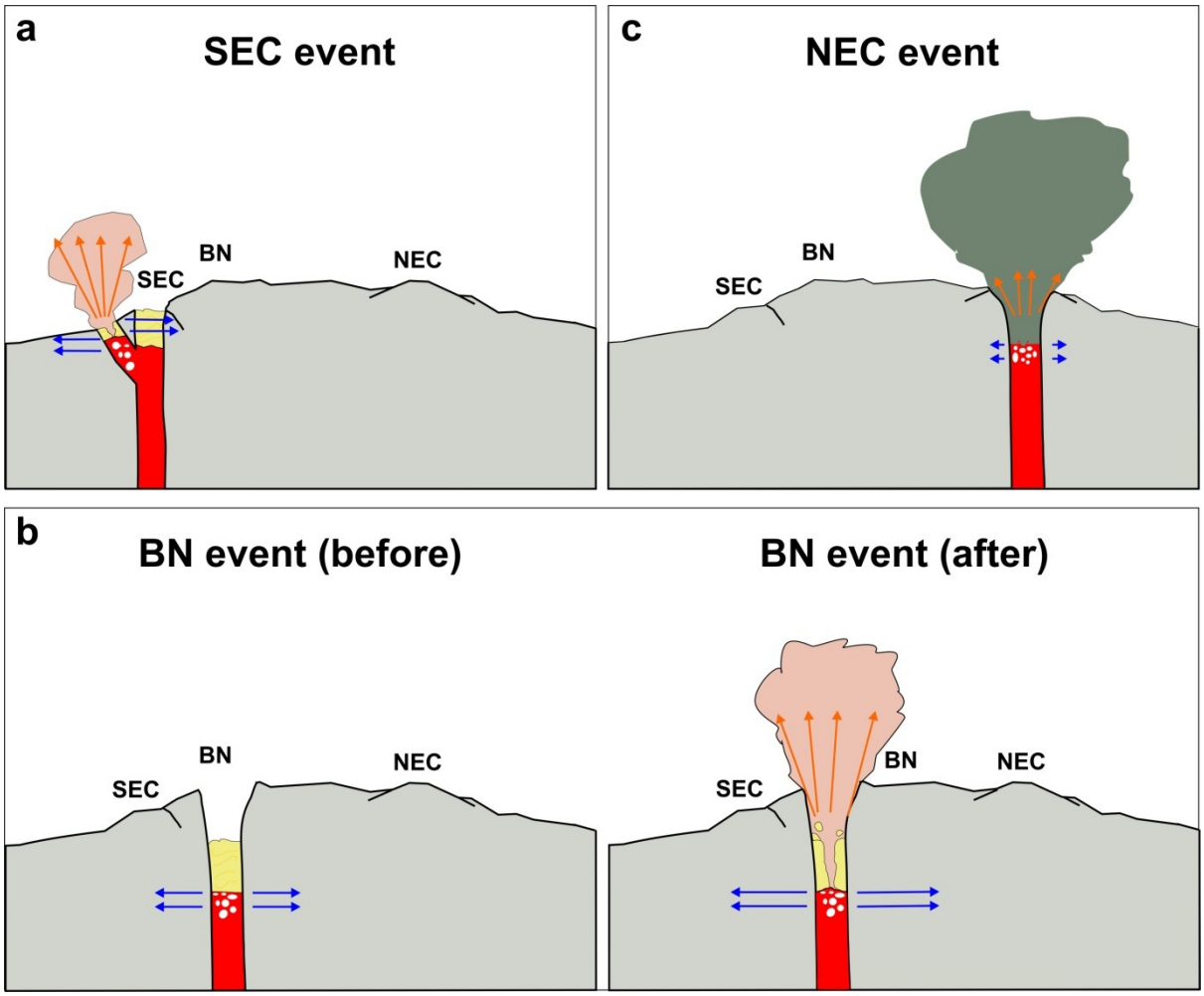

Figure 2.42: Sketches of eruptive events at (a) SEC, (b) BN, and (c) NEC. Note that distances in the sketches are exaggerated for graphical purposes. The length of the orange and blue arrows represents qualitatively infrasonic and seismic energy, respectively. The orange color in the SEC and BN conduits (a-b) indicate the relative clogging of the magma system, while the yellow color in the lateral conduit from SEC represents the relatively active degassing occurring there; conversely, the gray color in the sketches c suggests the relative clearing of the NEC conduit.

It is noteworthy that the difference of several orders of magnitude among VASR values (**Fig. 2.41**) of the main episodes, occurring at different vents, is not due to the variability of the parameters, which were fixed in order to compute seismic and acoustic energies. Indeed, uncertainties in the aforementioned parameters could produce a maximum error of 20 %, taking into account a precautionary range of variation. Thus, they should be due to changes in the mechanisms at the root of explosive activity, likewise the existence/absence of a plug in the conduit, which could prevent acoustic waves from coupling with atmosphere. For the same reason, the variability observed among explosions occurring at the same vent is likely due to changes in the explosive dynamics. In particular, during the 8 April eruptive episode, as aforementioned, we believe the variation in VASR value to be caused by changes in the source depth and/or plume density. During the 25 August eruptive episode, the main variation of VASR is directly reflecting the transition

from the closed conduit condition to the disruption of the plug and the consequent opening of the system. Finally, the 14-15 November episode exhibits low variability of VASR, in agreement with the hypothesis we made of a steady-state open system.

2.4.5 Volcanic hazards from minor explosive activity at Mt Etna

The 2010 will be remembered at Etna for the high number of short-lasting explosive events which affected the summit craters and the coeval absence of paroxysmal activity with higher energy (e.g. lava fountains or strong Strombolian eruptions). At least 35 of these events have been counted taking place from SEC and BN (**Table 2.4**); most were associated to small explosions, followed by weak ash emissions which formed low eruption plumes above the volcano up to heights of a few hundreds of meters. No coarser, lapilli-sized products were observed around the crater rim, so that -if potentially erupted- they fell into the crater itself.

However, some other events were related to higher energy explosions or in some cases to close sequences of a small number of explosions which caused ejection of up to metric-sized blocks (the 8 April explosive event), and the formation of an eruption plume up to several hundreds of meters, accompanied by ash fallout for several km away up to the lower-elevation inhabited areas of the volcano. Further, collapse and craterization phenomena affected the crater during the explosive event.

In general terms, volcanic hazards from minor explosive activity are lower than those related to lava fountains like the 2000 sequence [Alparone et al., 2003], or long-lasting explosive events like the 2001 and 2002-03 eruptions, lasting ~3 weeks and ~3 months, respectively [INGV-staff, 2001-2013; Andronico et al., 2008]. Indeed, high energy eruptions are typically associated to volcanic plumes higher than 1 km above the eruptive vents and usually reaching up to 3-4 km of height, active for tens of minutes up to a few hours (lava fountains) or prolonged from days to weeks (2001 and 2002-03 eruptions). Hence, the main consequences of these typologies are: i) the injection of tephra into the atmosphere for a long time with severe risks to aviation, and ii) the following tephra fallout which can cause complete covering of the ground, thus largely affecting vehicle traffic. Nonetheless, lava fountains and long-lasting explosive events may be heralded with sufficient signs to alert the authorities in charge of the territory [Alparone et al., 2007], so they may implement actions to mitigate the impact both in the air and on the ground. Previous studies have proven a good correlation between volcanic tremor and impending phenomena before,

during and after paroxysmal episodic activity [e.g. Alparone et al., 2003]; indeed, during the 64 events of the 2000 sequence, such a faithful correlation led to develop a first, well-working prototype of alert system to mitigate tephra fallout hazards [Alparone et al., 2007]. Similarly, the 2001 and 2002-03 long-lasting eruptions were preceded by a clear increase in seismic energy release hours to days before their occurrence [Barberi et al., 2004; Falsaperla et al., 2005].

Although the lower and shorter impact for the risks posed to the air and vehicle traffic (in terms of air volume affected and ground area covered by erupted tephra), the minor explosive activity is to date lacking evident geophysical precursors. The common aspect of the 2010 *type a* events was the unexpected, explosive nature which makes them particularly hazardous. In general, volcanologists and specialists visiting the summit of Etna are able to avoid the risks (and the bombs) from higher explosive eruptions because of the warning signs from the gradual increase in seismic tremor. Nonetheless, they cannot protect themselves from unforeseen explosions like those observed in 2010, which, especially along the crater rims, may prove unsafe or even lethal in the highly probable case of ejection of scoria and/or blocks. A minor, although possible risk is that posed to aviation, because even if the ash emission and the possible eruption column formation are clearly impulsive (and not visible in cloudy conditions on the top of the volcano), such phenomena are significantly lower in terms of duration and intensity than the higher energy eruptions. The hope for the future is to improve our understanding of the minor explosive activity from the summit craters of Etna, thus preventing any potentially dramatic situation.

Chapter 3: Explosive activity at Mt. Yasur

3.1 Geographical and tectonic setting

Mt. Yasur is an active volcano located in Tanna, one of 83 islands composing the archipelago of Vanuatu, South West of the Pacific Ocean. It is situated in the central part of the New Hebrides Island Arc (hereafter NH arc), 150 km east of the homonymous (New Hebrides) trench and 150 km above the Benioff zone [Carney and McFarlane, 1979; Louat et al., 1998] related to the subduction of the Indo-Australian Plate below the Pacific Plate (**Fig 3.1.a**). Along the 1400 km of the NH Arc, the rate of convergence varies several times. However, a value of about 180 ± 10 mm/y in the ENE direction was estimated for the southern Vanuatu [Taylor et al., 1995].

Tanna Island reaches a total extent of 550 km^2 and is built up by Pliocene to recent sub-aerial and subaqueous basaltic and andesitic volcanic units and reef limestone [Bani and Lardi, 2007]. The geological record of the island has been commonly divided into three Units [i.e., Carney and Macfarlane, 1979; Coulon and Maury, 1981]. The more ancient is the Upper Pliocene to Pleistocene Green Hill Group, which hosts the first evidences of volcanic activity, consisting of a series of basaltic lavas in the north and basaltic pyroclastics toward east [Allen, 2005]. Two former eruptive centers in the area of Green Hill and Waesisi have been identified. A third suspected eruptive center is suggested to be placed below the sea level [Coulon and Maury, 1981]. The second unit corresponds to the Tukosmeru Group in the south of Tanna Island, ascribable to the Late Pleistocene. Two main sub-units are part of it: the stratovolcano named Main Cone, and the so called Pyroclastic Apron, made up of tuffaceous andesitic deposits [Coulon and Maury, 1981]. Finally, the most recent Unit is the Siwi Group, in the south-easternmost sector of the area.

The Siwi Group comprises three Units: Yenkahe, Ombus and Yasur volcanics, all of them clustered in a narrow range of compositions [Coulon and Maury, 1981; Allen, 2005], mainly consisting of basaltic-andesite to andesite pyroclasts and lavas [Kelley, 2008]. The Yasur-Yenkahe complex is hosted into the Siwi Caldera, which extends for 9 x 4 km^2 and is bounded by the “Siwi Ring Fracture” on land [Peltier et al., 2012; Carnay and Macfarlane, 1979]. The Yenkahe volcanics originated about 0.23 Ma [K-Ar dating; Carnay and Macfarlane, 1979], whereas Ombus and Mt. Yasur are much younger.

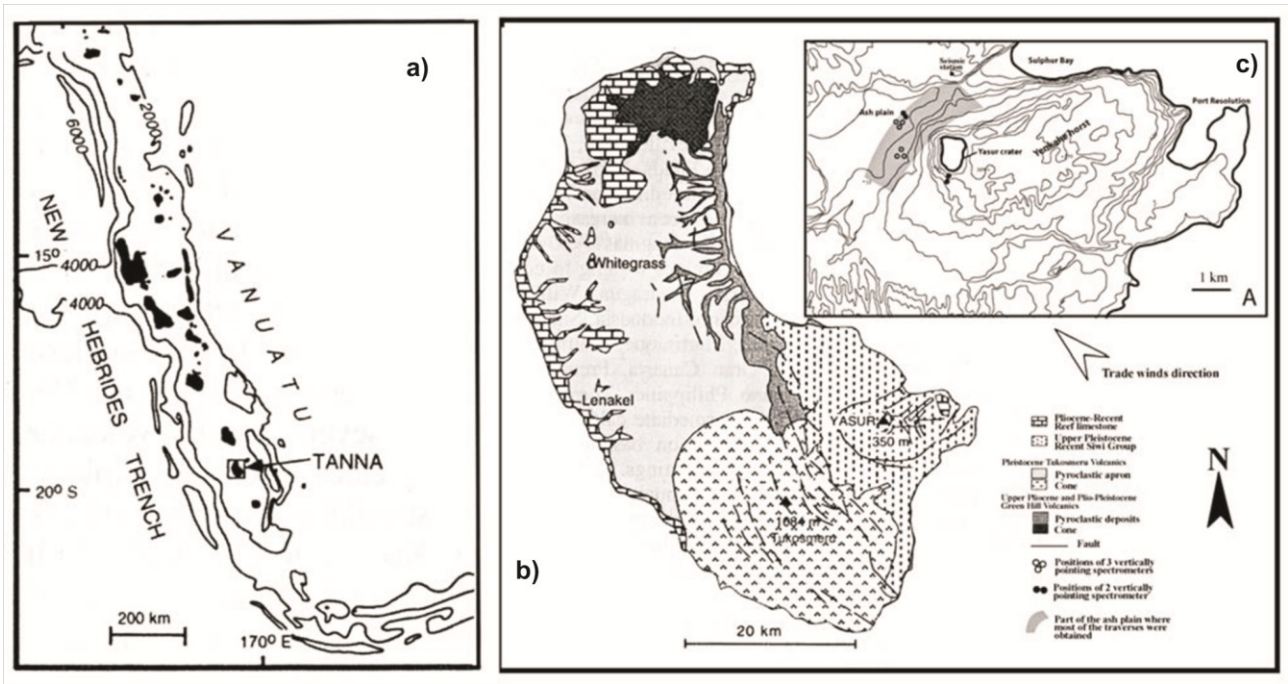

Figure 3.1 :(a) Map of Vanuatu. The black box, marked by the arrow, shows the position of Tanna. (b) Geological map of Tanna, redrawn after Carney and Macfarlane [1979]. c) Map of eastern Tanna, showing the Yenkahe horst and the Yasur crater. Modified from Bani and Lardi [2007].

Mt. Yasur is the only active eruptive center nowadays, situated in the western part of the Yenkahe Horst. It is a small stratovolcano (361 m a.s.l. high, 1500 m of diameter; see **Figs. 3.1c, 3.2b**) permanently active since the first report in 1774 [Aubert de La Rue, 1960]. Strombolian and vulcanian activities have been described since the first known human records in Vanuatu [about 1000 y; Cronin and Sharp, 2002]. The three small active craters at Mt. Yasur are aligned in the NE-SW direction, and are commonly referred (from South to the North) as vent A, B and C [i.e. Oppenheimer et al., 2006]. They are source of open vent degassing and recurrent explosions, propelling hot gases and fragments a few hundred meters above the craters [Nabyl et al., 1997; Oppenheimer et al., 2006; Bani et al., 2013]. The prevailing direction of the dominant winds toward south-east led to the accumulation of ash NW of Yasur cone into an ash plain [Carney and McFarlane, 1979].

It has been estimated that the volcano has an average uplift rate, due both to the regional tectonics and the inflation of the volcano edifice, of about 1.6 mm/y [in the last 5 kyr; Neef et al., 2003]. Recently, the uplift of the Yenkahe resurgent block, which amounts to 150 m over the last thousand years, was linked to the presence of 25 km^3 of degassed and not erupted magma [Metrick et al., 2011].

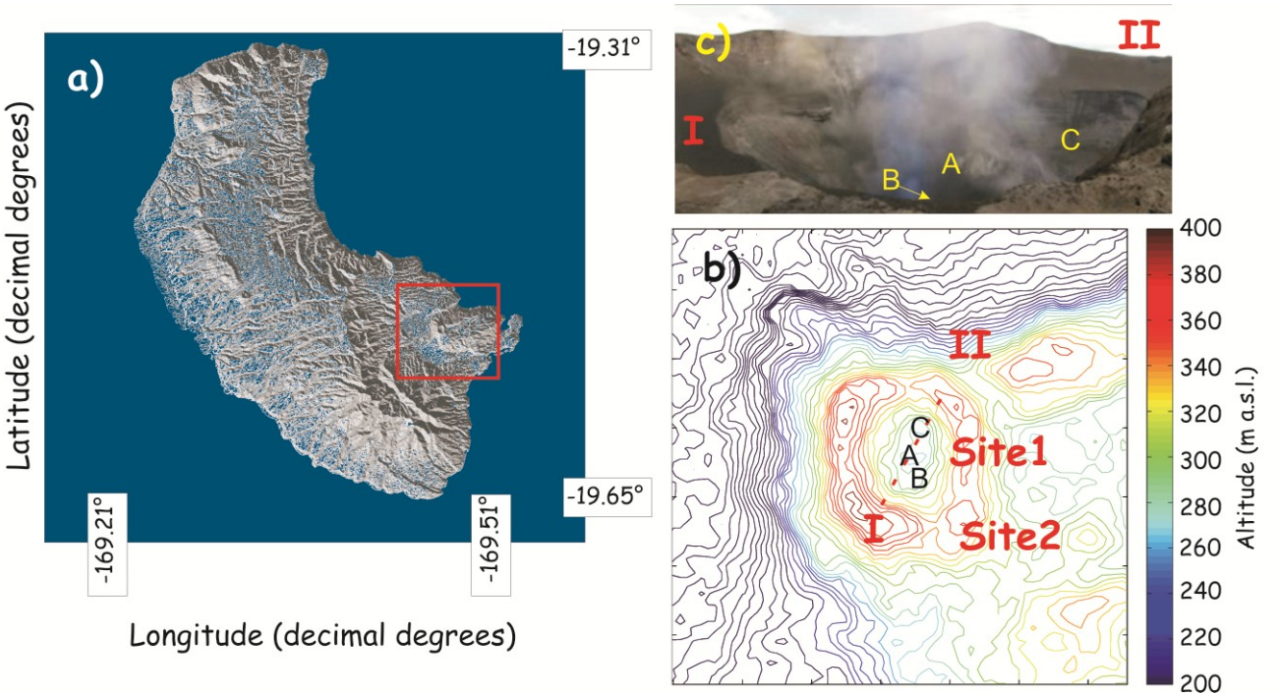

Figure 3.2: a) Digital elevation map of Tanna island. Mt. yasur is enclosed in the red box. b) Contour map of Mt. Yasur, the capitol letters (A, B and C) are the names of the active vents. Site1 and Site2 indicate the position of the recording site. c) Photo view of the crateric area with the indication of the active vents position (courtesy of Piergiorgio Scarlato).

3.2 Description of the experimental field study and setup

An experimental field study was carried out at Mt. Yasur, from 9th to 12th July 2011, in collaboration with Dr. Jacopo Taddeucci and Dr. Piergiorgio Scarlato of Istituto Nazionale di Geofisica and Vulcanologia, Dept. of Seismology and Tectonophysics, Section of Rome.

The multiparametric setup, named FAMoUS [Fast Multiparametric Setup for Real-time Observations; Freda et al., 2012], used for this temporary experiment, is composed by several kinds of instruments, time synchronized via a hand or microphone-operated trigger. The FAMoUS toolbox includes (see **Fig. 3.3.a**): 1) an Optronis CamRecord 600x2 high speed camera and data logger; 2) a FLIR SC655 thermal camera; 3) two InfraCyrus microphones. The visible and infrared high-speed videos were acquired at 500 and 50-200 fps and with resolutions of 1280 x 1024 and 480-120 x40 pixel, respectively. However, in this thesis, we will refer mainly to the acoustic signals, that were recorded both in infrasonic (1-20 Hz) and audible range (20 Hz-20 KHz).

Figure 3.3: a) Experimental setup emplaced at Site1. b) Particular of the experimental setup: high speed camera filming explosions at Mt. Yasur. Photo courtesy of Piergiorgio Scarlato.

The InfraCyrus microphones, used in the toolbox, were originally Panasonic WM034DM commercial electret microphones, recording in the audible range (20 Hz-20 kHz), successively adapted to the infrasonic range by researchers at the Osservatorio Vesuviano, Istituto Nazionale di Geofisica and Vulcanologia, Section of Naples [Buonocunto et al., 2011]. The resulting instrument response curve has a flat gain of 0 dB (1 V/Pa at 1 KHz) between 20 and 3000 Hz, while the instrumental response in the infrasonic range is shown in **Fig. 3.4.**

All the signals were corrected for the instrumental response on the basis of such information.

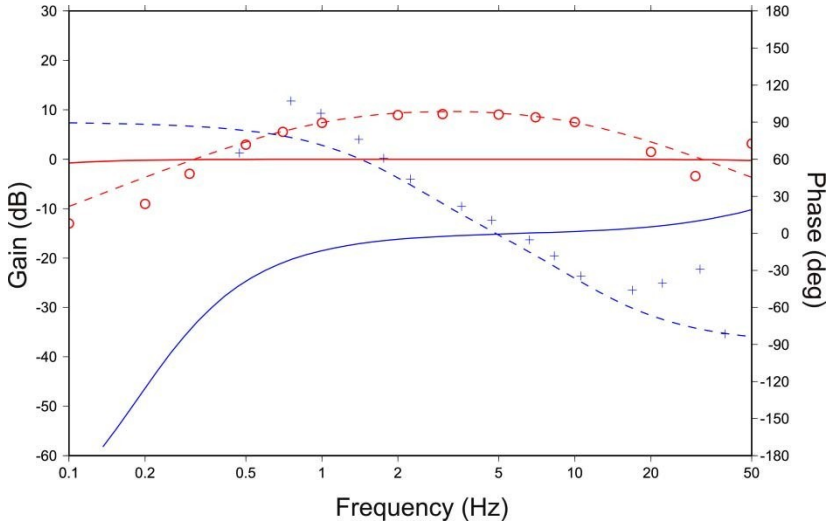

Figure 3.4: Response function of the InfraCyrus sensor (dashed lines) compared to the response of the Chaparral sensor (solid line) used as reference for the microphones calibration. Red lines represents the gain, and in particular circles represent experimental data, whereas the blue line represents the phase, with the crosses representing experimental data. Modified from Buonocunto et al. [2011].

Two locations were chosen as sampling site, namely Site1 and Site2 (see **Fig. 3.2b**). **Table 3.1** summarizes the principal steps of recording phase performed during the experiment. The equipment was placed near to the active crater rim, at roughly 300 m from the main active vents (horizontal distances: 283 and 312 m between Site1-Vent A and Site2-Vent A, respectively). Indeed, during the morning of 10 and 12 July, the station was placed into the saddle between A-B and C vents (the so called Site1), while during the other days, it was located in the western side of the crater rim of A-B vents (here named Site2), about 13 m in altitude below its position at Site1. In that condition, where microphones were at their most far location in respect of C vent, the instrumentation was partially occulted from the crater rim.

Sampling phase number	Day	Recoding time (GMT)	Recording site
1	9-10th July	11 p.m. - 1.40 a.m.	Site1
2	10th July	5.45 - 6.40 a.m.	Site2
3	11th July	4.45 - 6.13 a.m.	Site2
4	11-12th July	11.20 p.m. - 1.40 a .m.	Site1
5	12th July	6.50 - 7.10 a.m.	Site2

Table 3.1: Timing and location of the performed sampling phases.

Although the setup comprises two microphones, we will refer only to the microphone 1, as it showed the best signal to noise ratio, and provided the most reliable data.

3.3 Analyses of the dataset

3.3.1 Root Mean Square and events detections

On each acoustic trace RMS was computed using a 0.3 s moving window, with a shift of 0.1 s. Then, on the obtained RMS series, a percentile trigger [Cannata et al., 2011b] was applied in order to identify and count the recorded explosions, choosing a threshold value of percentile equal to 8 (i.e. see **Fig. 3.5b**).

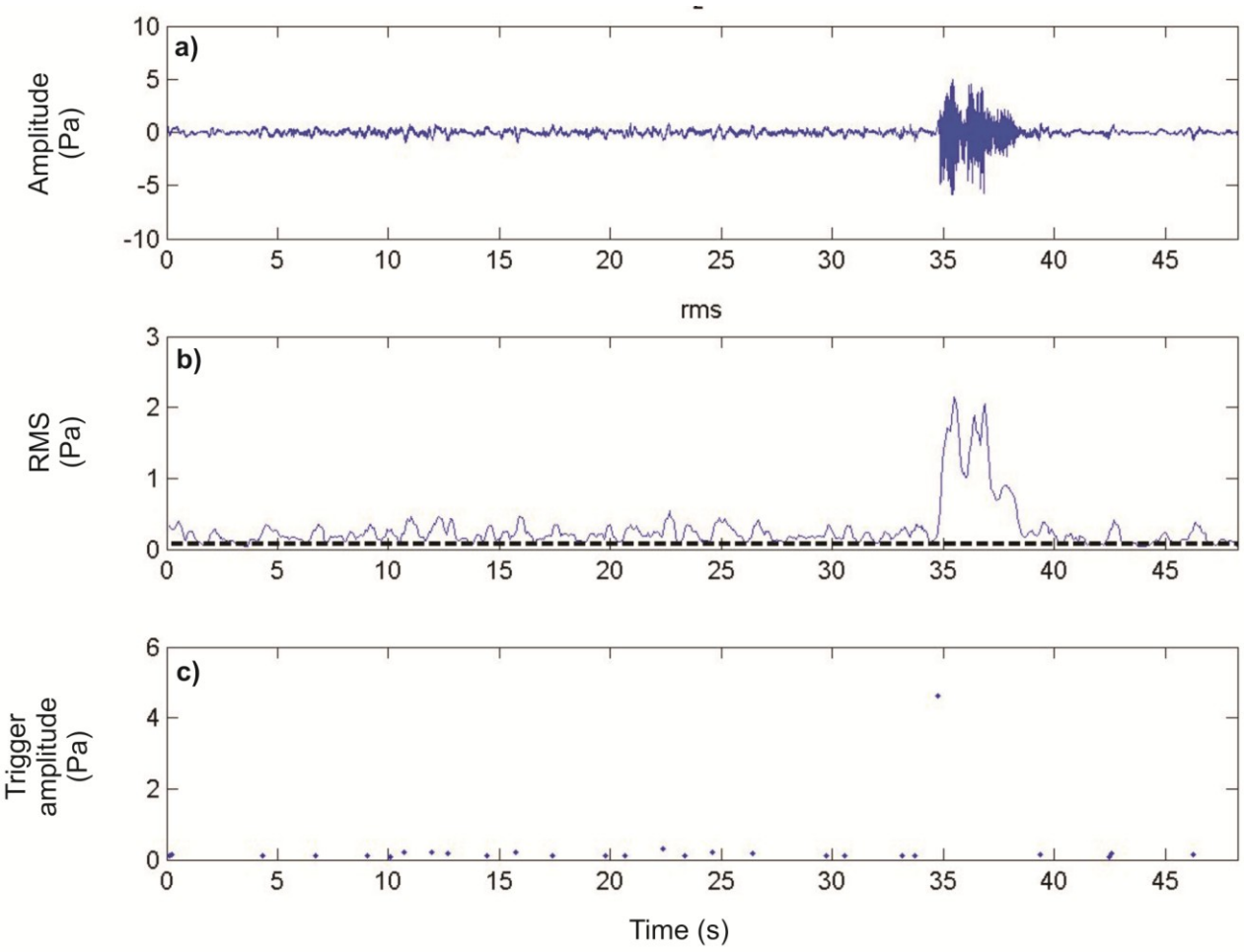

Figure 3.5: a) Acoustic signal recorded at Mt. Yasur (Begin time: 11/07/2011 23:22:00). b) RMS time series of the signal shown in a). The dashed line represents the percentile threshold applied to the dataset in order to detect events. c) Amplitude of triggered events.

Interestingly, a decrease in RMS amplitude is evident in connection with recordings performed at Site2 (**Fig. 3.6**). This topic will be extensively discussed in **section 3.5**.

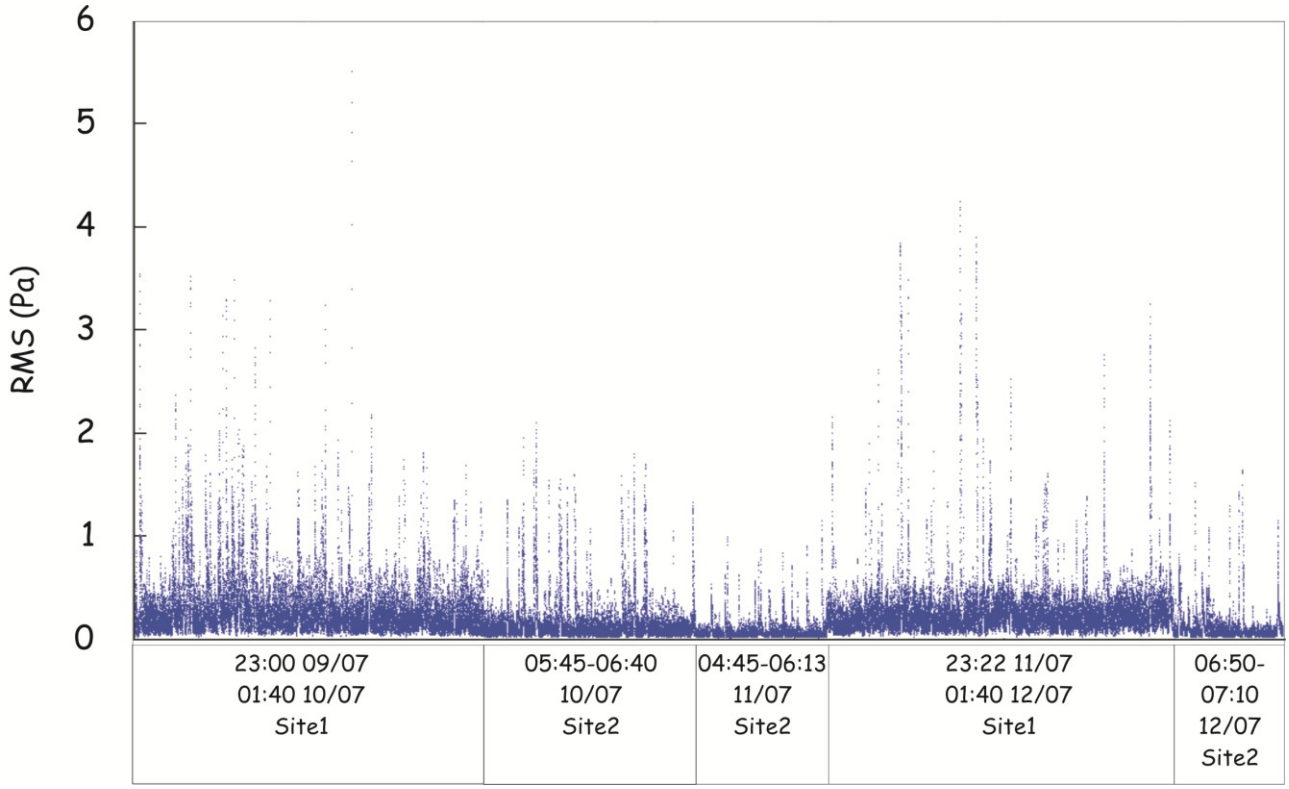

Figure 3.6: Plot of RMS values obtained for the whole dataset. The timing in the boxes along the x axis refers to the begin-time of the first and last recorded trace. The site of sampling is reported, too.

Fluctuations in the general trend of RMS amplitude are widespread. **Fig. 3.5a** shows a common example of recorded trace, with the relative RMS (**Fig. 3.5b)** and the amplitude of the triggered events (**Fig. 3.5c)**. As visible from this example, inter-eruptive phases -i.e., between strong explosions (hereafter named major events)- are often associated to small waveforms composed by one cycle, one cycle and an half (see **Fig. 3.7**) and small amplitude (generally <2 Pa) and duration (generally <2 s). The regular repetition of such small explosions produces the sequences of peaks, visible in almost all the RMS series (for instance, see **Fig. 3.5b**). The comparison with thermal and video cameras reveals that they correspond to small-scale explosions, related to the bursting of overpressurized pocket of gas, ejecting pyroclastic product in the atmosphere, known in literature as puffing [Ripepe et al., 2007]. Their occurrence rate (roughly 0.7 event/s) remained rather stable during the investigated period, as shown by **Fig. 3.8.**

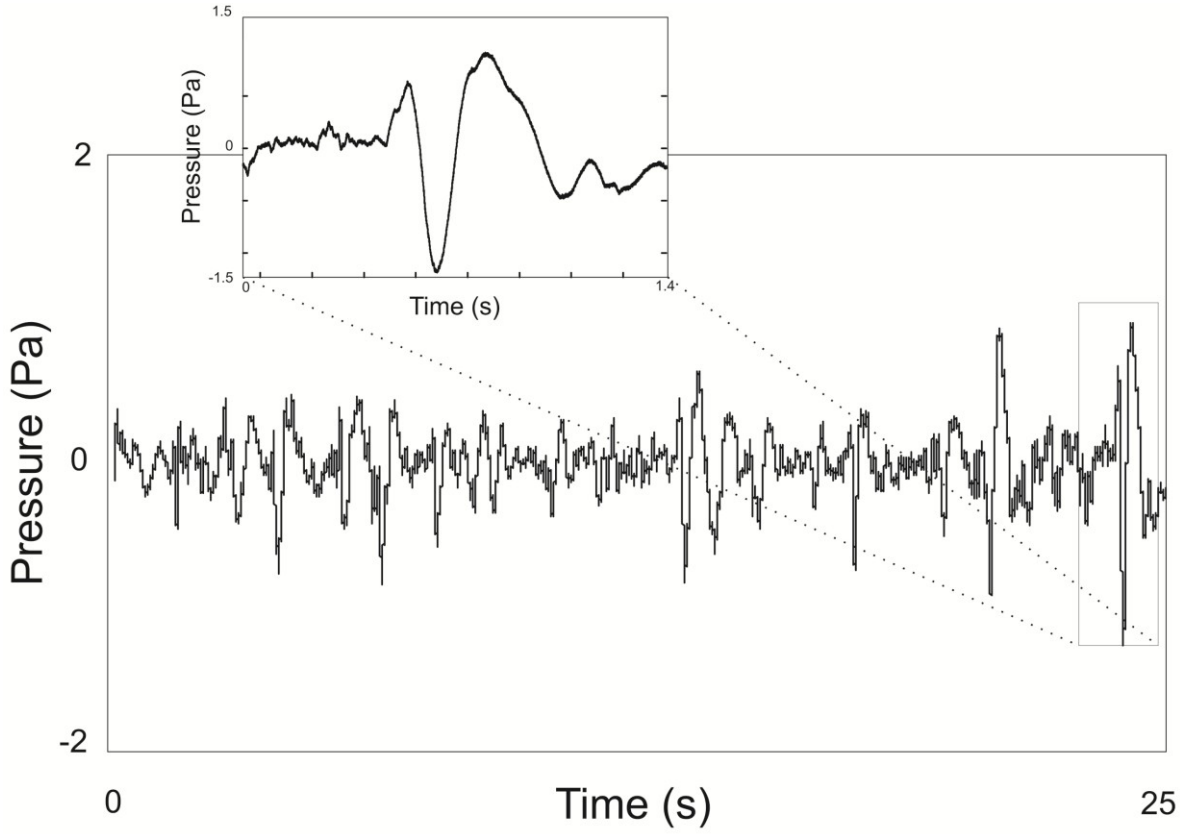

Figure 3.7: Example of a sequence of minor explosions occurring at Mt. Yasur.

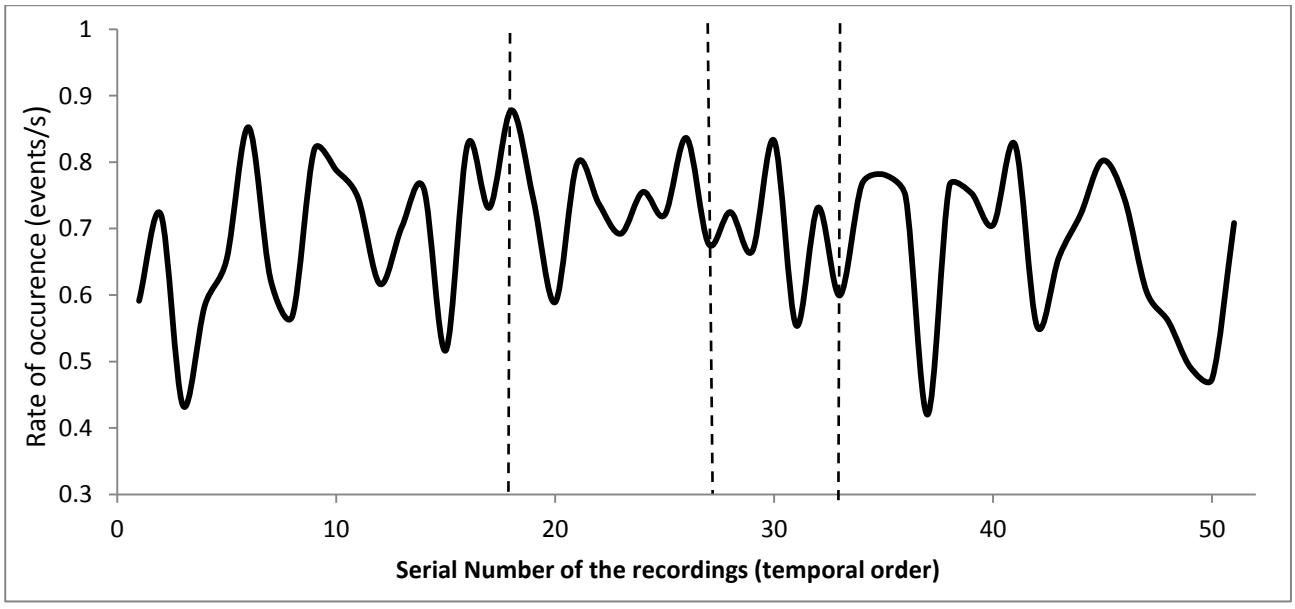

Figure 3.8.: Occurrence rate (event/s) of small explosions computed for each acoustic trace. Dashed line represents the switching among recording phases, where several hours of gap in the registration occurred.

The possible existence of a trend in the amplitude, frequency or rate of occurrence of such explosions in relation with the major events, has been verified. In particular, some events for each trace have been selected as template events and a correlation coefficient was estimated through

cross-correlation of the template event with the whole trace. No meaningful trend or evidences were found, and therefore this analysis will not be described further on.

The major events, instead, are characterized by bigger amplitude (from ≈2 to ≈15 Pa) and longer duration. Furthermore, an high waveform variability was noted, highlighting the existence of different phenomena dominant in the sound radiation. A total number of 106 major explosions were identified. On this dataset, detailed analyses were carried out, in order to get more information on the different dynamics active at the vents (see **section 3.4** for further details).

3.3.2 Spectral analyses

Spectrograms were performed on each acoustic trace by using different moving windows (1.28, 2.56, 5.12 s, overlap 50 %), in order to take into account the effect of the various length of the acoustic transient. Beyond the individual differences, it can be noted that in general the bulk of spectral energy is below 20 Hz in the infrasonic range, as expected. However, a certain amount of spectral energy is still present up to roughly 500 Hz, in coincidence of some major explosions. For a general example of the observed features see **Fig. 3.9b,c.**

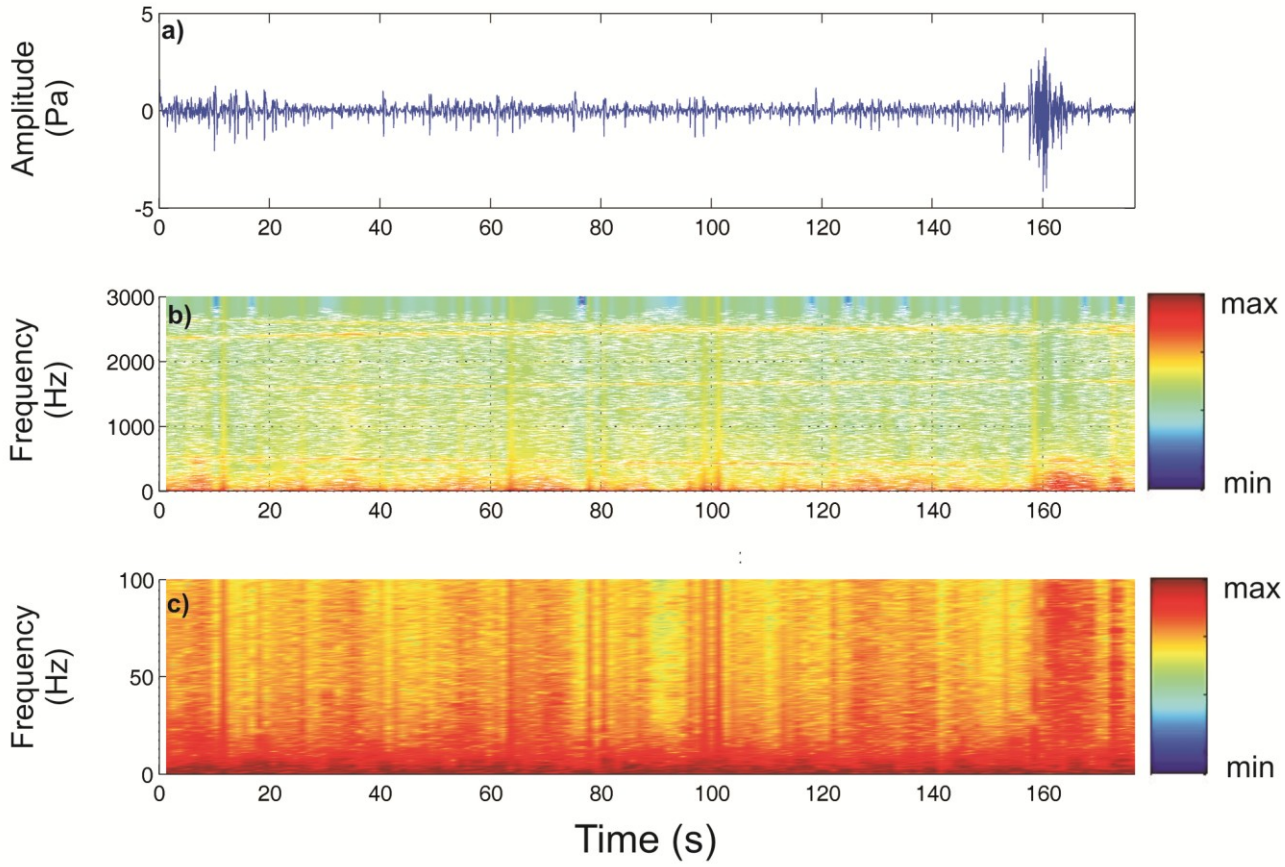

Figure 3.9: a) Acoustic recordings of Mt. Yasur explosive activity (begin time: 10/07/2011, 01:26:29). b) Normalized spectrogram obtained with a moving window of 2.56 s. c) Particular of b) in the range 0-100 Hz. Note that the colorbar in b and c represents the logarithm of spectral amplitude.

Contemporaneously, also the peak-to-peak amplitude has been estimated in the same windows. **Fig. 3.10** shows the plot of the peak frequencies estimated, that are generally clustered below 5 Hz.

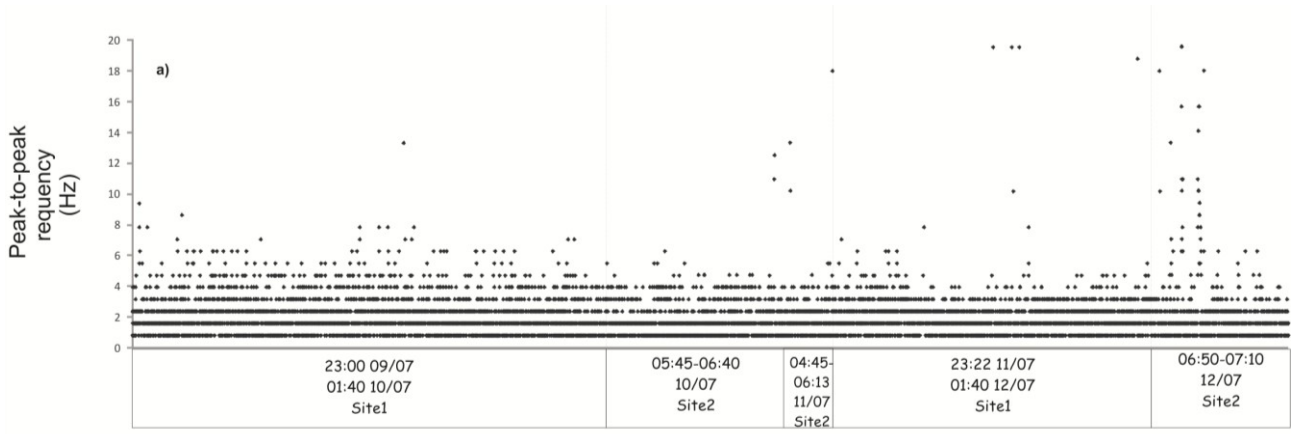

Figure 3.10: a) Peak frequency computed by using 2.56 s windows on the whole dataset. The timing in the boxes along the x axis refers to the begin-time of the first and last recorded trace. The site of sampling is reported, too.

3.4 Analysis of major events

A total number of 106 major explosions were manually selected from the traces. They are clearly distinguishable from minor events due to their bigger amplitude (generally higher than 2 Pa), the longer duration (≈2-20 s) and the waveform complexity. Furthermore, while minor explosions were characterized by high repeatability suggesting the stability of their source, major events feature an high level of variability. A first order distinction can be done on the base of the waveforms. Indeed, we can distinguish among impulsive events (**Fig**. **3.11 a**) , characterized by a sharp first arrival of the acoustic wave, and emergent signals, with slowly increasing amplitude and long codas tapering off (**Fig**. **3.11c**). The latter are often characterized by lower values of amplitude, but unlike minor explosions, they are accompanied by notable ash rich emissions.

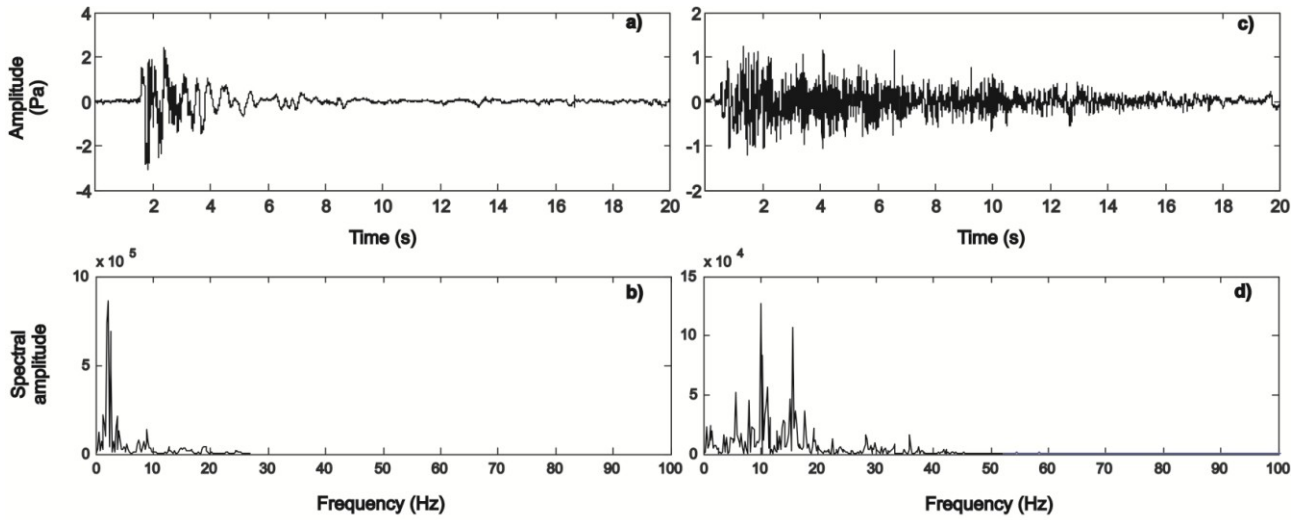

Figure 3.11: a) Waveform of an impulsive event (begin time: July 12th, 07:23:21). b) Spectrum of the signal shown in a), performed by using a 5.12 second long window. c) Waveform of an emergent event (begin time: July 12th, 07:05:56). d) Spectrum of the signal shown in c), performed by using a 5.12 second long window.

For each event the spectral characteristics have been investigated by performing FFT analyses with a window of 5.12 seconds, according to the average duration of the events (see for instance **Fig. 3.11 c,d**). The bulk of spectral amplitude is generally below 20 Hz. Remarkably, whereas in some cases spectra are monochromatic, several spectra with wider frequency content (up to 300 Hz) are present.

Furthermore, for each selected event, peak-to-peak amplitude as well as duration, was estimated (see **Fig. 3.12**).

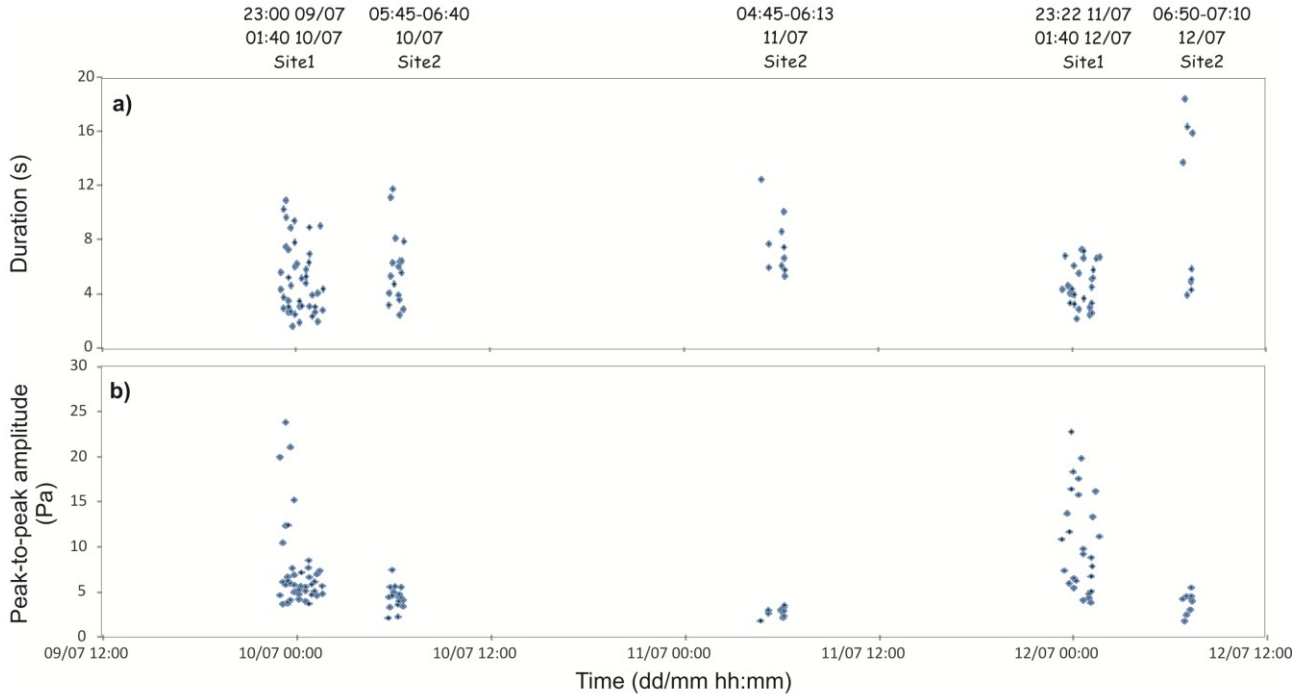

Figure 3.12: a) Total duration and b) peak-to-peak amplitude of the major 106 acoustic events. Each cluster of point corresponds to a sampling phase. The timing at the top of the figure to the begin-time of the first and last recorded trace for each sampling phase. The site of sampling is reported on the top of the figure.

As shown in **Fig. 3.12 a**, a wide range of duration was found, mainly comprised between 2 and 20 seconds, with an average of 5 ±3 s. However, the longest durations (values above 12 seconds) are clustered during the last sampling phase, and often associated to the occurrence of the so called "emergent-event", which were more frequent during this day. Peak-to-peak amplitudes are comprised between 2 and 25 Pa. It is noteworthy that systematically lower values are associated to the sampling phases carried out at Site2 (see **section 3.5**).

3.5 Diffraction at the crater rim

Several evidences have been found on the existence of site effects, which account for the differences between signals recorded at Site1 and Site2, the sampling sites chosen for the temporary experiment. Indeed, it was noted that both RMS and peak-to-peak amplitude are systematically lower when computed at Site2 rather than Site1. This is valid both for amplitude measurements computed on the whole dataset (thus including the minor events), as well as for analyses carried exclusively on the major events. Furthermore, this sort of attenuation effect was found to be more effective on the higher frequency content of the signals.

It is worthy to recall some information about the relative geometry of the recording station and the active vents. As previously specified, horizontal distances from the position of the sensor in Site1 and Site2 to the vent A (measured by using telemetric sensor, with a maximum error on the horizontal of 3 m) was respectively of 283 and 312 m. The vertical depth of the vent A from the crater rim measured at Site1 was of 161 m. Furthermore, the microphone at Site2 was partially retreated in respect of the crater rim, and this resulted in a difference of 13 m of altitude between the two sampling sites.

Unfortunately, there are no measurements of wind intensity during the investigated period. However, operators in the field reported low winds for all the duration of the experiment, except for the last sampling phase, in the afternoon of July 12th, when the effect of increased wind speed is evident in a slight worsening of the signal to noise ratio, but without any remarkable effect on the amplitudes. Thus the existence of systematic effect of dominant wind was discarded. Alternatively, source complexity and directional pattern effects due to non monopole sources must be taken into account. Johnson et al. [2008], for instance, inferred both monopole and dipole component in signals from Mt. Erebus. However, in the analyzed dataset, attenuation effects were evident both for minor events and major explosions. For such different type of event, source mechanisms are supposed to be different, and therefore the radiation pattern is expected to change. For this reason, it is more likely that such pervasive variations of amplitude are connected to the travel path of the acoustic wave rather than to any source fingerprint. For small differences in the travel path (≅30 m) the effect of geometrical spreading is almost the same at both recording site. Furthermore, anelastic attenuation and scattering in the atmosphere are negligible for such small distance from the source. Therefore, it is mostly probable that such variation in the property of the signal is due to some kinds of “barrier effect” related to the crater rim. Diffraction at the crater rim are already described in literature [Johnson, 2005; Li and Wong, 2004; Kim and Lees, 2011; Lacanna and Ripepe, 2013], although the existence of such effects is often not taken enough into account when dealing with volcano acoustics.

In order to quantify the attenuation effect at Site2 in respect of Site1, not having any contemporaneous recordings at the two stations, we assumed that –in average– the level of activity has been constant during the whole temporary experiment. This assumption seems to be reasonable, considering the quite stable rate of occurrence observed during the whole field experiment, the only difference consisting in the occurrence of slight major number of emergent events on July 12th.

For such reasons, the average amplitudes *A1* and *A2* of the signal respectively at Site1 and Site2, were taken into account in order to obtain a value of attenuation. The latter was computed at different frequencies f_n by filtering the signal into a narrow band (f_n±2), centered around the investigated frequency value.

Then, attenuation (also defined insertion loss) was calculated through the following equation (Li and Wong, 2004):

$$Att_{exp} = 20log_{10}(\frac{A_1}{A_2})$$

(27)

In order to test the hypothesis of diffraction, we referred to the empirically derived equations developed for acoustic barriers. An acoustic barrier is generally defined as any natural/artificial obstacle standing in the direct path between a source of sound and the receivers. Thus, in our case, it is possible to assume that the crater rim is acting as an acoustic barrier for the volcanic source, partially diffracting the sound at its edges. Analytical solutions for diffraction have been developed in literature through time [for an extensive discussion see Li and Wong, 2004], but they require computational time and costs not easily affordable in order to obtain the solution for spherical waves. Thus, in engineer field often the attenuation of acoustic barriers is computed via experimentally derived equations. Indeed, Maekawa [1968] realized a chart by measuring the attenuation, produced in anechoic environment, by a thin rigid plane barrier and considering different position of point sources. The variation in the geometry of the system was quantified by using the Fresnel number, defined as:

$$N = \frac{R' - R1}{\lambda/_2}$$

(28)

where *R'* is the effective travel path of the front wave due to the presence of the barrier, and *R1* is the direct travel path in the ideal case of the absence of the barrier and λ is the wavelength of the acoustic wave.

Many authors [i.e. Yamamoto and Tagaki, 1992; Kurze and Anderson, 1971] developed equations in order to fit the experimental data of Makeawa. Among them, one of the most widely used equation in order to compute the expected attenuation is given by [Kurze and Anderson, 1971]:

$$Att_{theor} = 5 + 20log\frac{\sqrt{2\pi N}}{tanh\sqrt{2\pi N}}$$

(29)

valid for attenuation values lower than 24, and with Att_{theor} equal to 0 or for N (see equation **28**) < -0.2.

Naturally, both the experimental studies and the equations have been developed for application into the audible range of frequencies. Indeed, Maekawa's chart was based on the result of experiments comprised between 500 Hz and 10 KHz.

However, our geometrical configuration lies in the range of Fresnel numbers defined by the equation. Indeed, an estimation of the Fresnel number is done considering the geometry of **Fig. 3.13,** where the dashed gray line represents the effective wave front path, composed of the two segments R_r and R_s, while R_1 represents the direct theoretical travel path from the source *S* to the station *R* in absence of the barrier. By simple trigonometric considerations, the values of R'(equal to Rr+Rs in the graph) and R1 were estimated, and then the Fresnel number for different wavelength was evaluated.

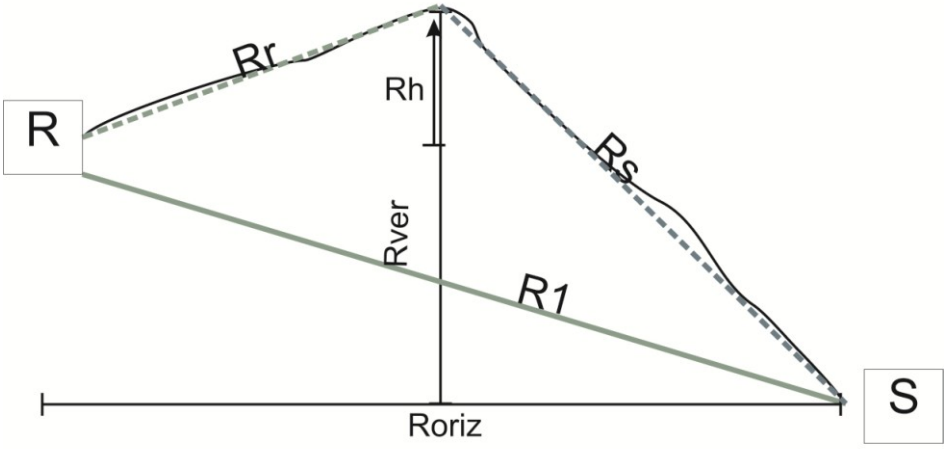

Figure 3.13: Geometry of the source-receiver system for recordings carried out at Site2. R and S represent respectively the locations of Receiver and Source, R1 is the direct path in absence of any acoustic barrier and Rr and Rs are the two segments which compose the effective travel path of the acoustic wavefront (R' in equation 28). Finally, note that Rver=161m, Roriz=312 m, Rh=13 m.

Considering frequencies comprised between 2 and 100 Hz, the obtained Fresnel number are in the interval 0.08-3.4, and therefore they are inside the investigated interval for Maekawa's chart [1968] and Kurze and Anderson equation [1971]. The expected values of attenuation for a total acoustic barrier is represented by the theoretical curve of **Fig. 3.14**, whereas the obtained values of attenuation, computed with equation (**27**) are represented by the experimental curve. The choice of investigating up to 100 Hz was due to the observation that, although the bulk of energy is generally below 20 Hz, many events have a discrete amount of spectral amplitude in the lower audible range, where diffraction effects are expected to be more effective.

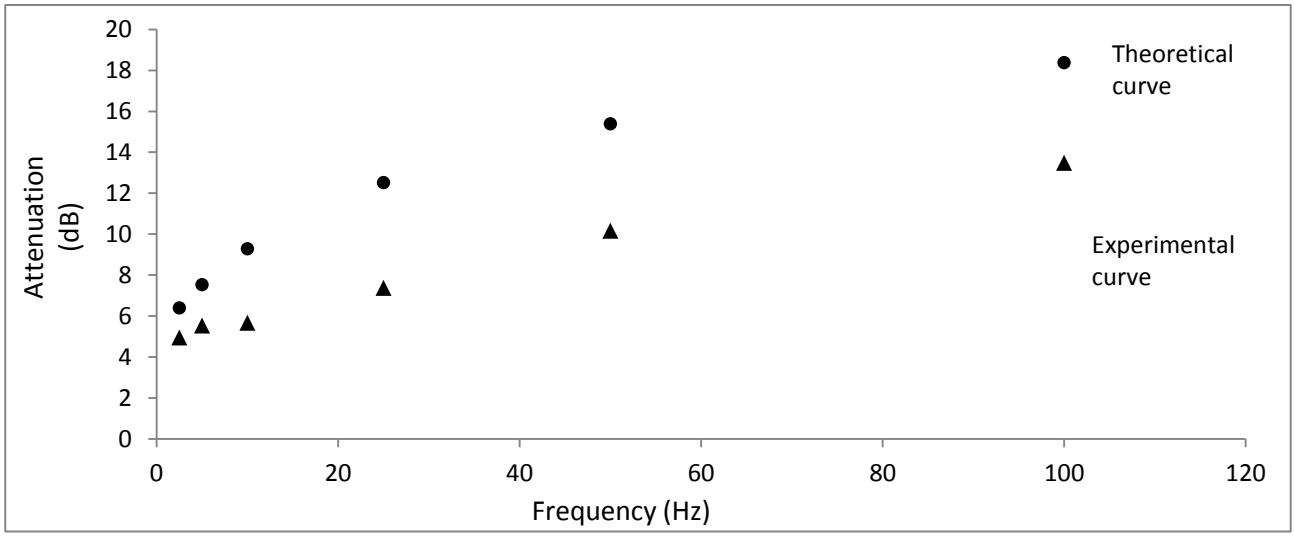

Figure 3.14: Attenuation values obtained from average peak-to-peak amplitude of signals recorded at Site2 (experimental curve, black triangles) and expected by applying the model of Kurze and Anderson [1971] (theoretical curve black dots) to our source-receiver geometry and frequencies of interest.

3.6 Discussion

In this chapter a dataset of acoustic signals of explosions from Mt. Yasur, recorded between 9th and 12th July 2011, is analyzed.

A first general distinction has been done, on the base of the waveforms appearance, amplitude and spectra, between major explosions and minor bursts. Indeed, whereas the first are characterized by rather complex and variable shapes, with durations spanning in a relatively wide interval (2-20 s) and individual differences in their spectra, minor explosions are characterized by an high level of self-similarity, and exhibit a series of steady features. Coupled analysis of the thermal and video images, shows that the minor explosions correspond typically to small-scale explosions, with ejection of little amount of pyroclastic products after the burst of pockets of gas. Furthermore, they are characterized by one cycle-one cycle and an half waveforms, resembling the typical acoustic signatures of strombolian explosions [Vergniolle and Brandeis 1996; Vergniolle et al., 2004], with commonly short duration (roughly < 2s; see **Fig. 3.7**), and frequencies slightly variable from one event to each other, but commonly below 5 Hz. Those events showed lower values of amplitude in respect of the major explosions (mainly < 2 Pa), but took place at an higher rate, that was in average constant and equal to 40 events/minute. We did not find any correlation between such minor explosions and the occurrence of the major events. This suggests an independence of the source dynamics feeding the two activities. The characteristics of minor

explosions recorded at Mt. Yasur are similar to the so called “puffing”, described at Stromboli [Ripepe et al., 1996; 2007], where a persistent (1 every ≈1-2 seconds) low amplitude (≈1 Pa) signal was associated to the release of hot steams containing droplets and hot ash particles [Harris et al., 2003]. Puffing activity was linked to the degassing of the magma column, occurring in over-pressurized conditions, independently from the occurrence of stronger strombolian explosions. Thus, even in the case of Stromboli, the two dynamics are totally decoupled. Interestingly, a recent study [Bani et al., 2013], performed at Mt. Yasur in September 2011 and based on the use of a thermal infrared thermometer, comes to similar conclusions. Indeed, authors [Bani et al., 2013] defined, on the base of the individual thermal energy of each explosion, two groups of bursting events. The first group comprised the majority of the recorded events (up to 87% of the dataset), each exhibiting low energy values. As a consequence the total amount of energy of the first group was overall lower than that of the bigger events, which made up only 13% of the whole dataset. The absence of any correlation between the two groups of events led the authors to infer the existence of two different source dynamics. The more quiet degassing-bursting activity was explained with a rise speed-dependent model of shallow bubble growth, whereas more violent high energy events required foam to collapse at depth. Thus, the repose-time between explosions is necessary to the system in order to generate the foam. The existence of a two scale dynamics was suggested also by the FTIR spectroscopy, investigating the content of SO_2/HCl ratio [Oppenheimer et al., 2006]. Authors found much higher values (≈30) of such ratio for high energy events rather than for passive degassing and small bursting (≈2) suggesting the existence of a deep source, rich in SO_2 and CO_2, and a shallow source enriched in HCl.

Our analysis confirms the existence and independence of two different source dynamics for minor explosion and major events. The continuity of small explosive activity in time is according with the hypothesis of a continuously active mechanism of generation/release of small pockets of gas, providing magma degassing. Notably, as specified in **section 3.1,** the continuous degassing of Mt. Yasur was inferred to have led the accumulation of 25 km^3 of degassed and not-erupted magma in the past thousand years [Metrick et al., 2011].

The major events correspond to the typically described activity of Mt. Yasur, spanning between Strombolian and mild Vulcanian intensity level. Despite the persistency of such kind of explosive activity, that has characterized the volcano since 800 years [McClelland et al., 1989], only sporadically interrupted by sub-plinian explosive phases [Nairn et al., 1988], huge variations in the number of the explosions (up to a factor of 5) and acoustic pressure (up to a factor of 4) were

observed since the deployment of permanent acoustic arrays in the area [Zielinski et al., 2010]. Indeed, from the observation of several years of activity (2003-2007) three regimes, characterized by different combination of two variables (occurrence rate and acoustic pressure of the events), were defined. The switch among these different conditions was linked to variations, which could either occur suddenly or take place during several months, of the gas fraction in the conduit [Zielinski et al., 2010]. Huge variation in the intensity and number of explosion was described also by Le Pichon et al. [2005], basing on events detected by the Global Infrasonic Network of the International Monitoring System (IMS).

Accordingly, a widespread range of amplitude values and rate of occurrence have been reported for Mt. Yasur. In our analysis the acoustic events showed amplitudes comprised between 2 and 15 Pa. This interval of values stands at the lower limit of the commonly reported range of pressure for this volcano. Marchetti et al. [2013], for instance, during an experiment carried out in July/August 2008, recorded acoustic events in the range 5-105 Pa, showing a surprising degree of self-similarity, with an high rate of occurrence, that may reach the value of 60 events/hours. Authors [Marchetti et al., 2013] inferred the existence of blast waves, i.e. the sudden release of large quantity of gas in very short time [Needham, 2011]. We do not have any evidence of blast wave sources for our acoustic dataset, accordingly with the lower level of activity, which probably was in the low rate of occurrence-low amplitude phase described by Zielinski et al. [2010]. Indeed, the hazard level for the volcano, defined by the Vanuatu Geohazard observatory, was lowered from the level 3 to the level 2 after June 11th, 2011, following the end of an high explosively phase.

Among the major events, we distinguished impulsive and emergent events. Similar distinction, based on the first arrival of the acoustic waveform, has been done on acoustic signals related to vulcanian activity at Mt. Augustin, Alaska [Petersen et al., 2006]. Impulsive events are characterized by sharp onset, generally higher values of amplitude and shorter duration. They constitute the majority of the dataset. Inside this group, several individual differences have been found. Notable is the evidence, for many events of the dataset –confirmed also by the observation in the visual camera- of overlapping or either closely related bursting events, as also previously described in literature [Bani et al., 2013]. Such sort of clustering of the explosions may suggest the existence of multiple batches of gas periodically arising, i.e. chains of bubbles, rather than a single slug. However, more detailed analyses are required in order to constrain the source mechanisms.

The emergent events, characterized generally by longest duration (up to 20 seconds) in the acoustic trace and lower amplitude, were associated in the visual and thermal camera to ash-rich

explosions. Interestingly also Kremers et al. [2013] recognize two different types of explosions from the seismic and acoustic traces recorded in August-September 2008: the ash-free and ash-loaded explosions. The emergent events here analyzed are undoubtedly ash-loaded. It is well known that propagation through volcanic plumes may modify amplitude and spectral features of infrasound signals [i.e., Johnson and Aster, 2005]. However, in our opinion, the presence of ash is not sufficient by itself to justify their emergent features, being considerable ash content entrained in several cases also in some impulsive events. The extended waveform, indeed, may result from a sustained emission of pyroclastic mixture, as suggested for similar acoustic events of Mt. Augustin [Petersen et al., 2006], highlighting a different source mechanism. However, the influence of the ash and of the temperature of gas cloud in the infrasonic signals cannot be ruled out, and requires further detailed analyses. Indeed, at Mt. Yasur strong alteration of the infrasonic signals caused from a fast-moving volcanic cloud and due to Doppler-shifting phenomena has been found by Meier et al. [2011].

Furthermore, not negligible site effects have been found by comparing the signals recorded in the two sampling sites (namely Site1 and Site2). Unfortunately, there are no contemporaneous recordings at the two positions. However, the evidence of a remarkable amplitude attenuation at Site2, where indeed the recording position was retreated in respect of the crater rim, suggests the existence of diffraction at the topography. We calculated the expected values of attenuation by assuming the crater rim equal to a semi-infinitive plane acoustic-barrier, and the source equivalent to a point source, as required by the most commonly used equation in engineer field for the computing of efficiency of acoustic barriers. These values were compared with the experimental attenuation, derived considering the average spectrum content of the volcano activity to be constant during the experiment. As shown in **Fig. 3.14**, there is a good agreement between the two curves, although the experimental one displays lower values. This could be justified by the error implied by the assumption of Site1 as the reference signal for the source. Indeed, signals at Site1 may be already partially diffracted, although less than those at Site2. Alternatively, the mismatch could be due to a more complex geometry of the crater rim-barrier rather than the simple semi-infinite plane considered by the equations.

It is noteworthy that Marchetti et al. [2013] invoke the diffraction effect at the topography (or alternatively reflections into the conduit) to justify a rather stable group of secondary peaks found in acoustic signals of Mt. Yasur in July/August 2008. The importance of taking into account distortion effects due to the topography nearby the crater rim is suggested by numerical

evidences and comparison with Karymsky acoustic waveforms also by Kim and Lees [2011]. At Stromboli, Johnson [2005] reported a frequency-dependent scatter of the location of the puffing, compatible with distortion effect at the crater rim.

Finally it is noteworthy that the effect of diffraction was identified and quantified at Stromboli by Lacanna and Ripepe [2013]. They found that amplitude decay distribution of the acoustic waves was different for varying source positions, being not correspondent to those expected assuming simple geometrical attenuation. By using a 2D finite difference time domain modeling they evaluated the effect of the ground-atmosphere topography on acoustic waveforms and amplitude. As in this thesis, authors assimilate the diffraction rim to an acoustic barrier, in order to model the diffraction properties of the topography. Results from Lacanna and Ripepe [2013] suggest that diffraction contaminate the amplitude and waveforms of the acoustic signals, and therefore the topography must be taken into account, especially when signals are inverted to obtain the source mechanism.

Chapter 4: Conclusions

4.1 Conclusions

The analysis of volcanic infrasound signals is an emergent and satisfying technique, through which many information on the dynamics of volcanoes can be acquired. However, there is a vast amount of open issues that still needs to be investigated. For instance, source mechanisms and related radiation patterns, may change substantially, even at the same volcano, with the eruptive style. The path geometry of the acoustic waves, often simplified in the propagation models, may in some cases be complicated by topography effects. In order to shed light into this phenomena, and finally to understand the eruptive mechanism and the dynamics of the plumbing systems, extensive analyses are required. With this aim, both Mt. Etna and Mt. Yasur, with their high rate of eruptive activity, represent perfect volcano laboratories.

Infrasound signals are continuously recorded at Mt. Etna, and nowadays they represent a fundamental key point for both monitoring purpose [Montalto et al., 2010] and for the study of the related source dynamics. Indeed, up to now, the analysis of their features has provided important information on the shallow plumbing system and on the characteristics of the explosive sources [i.e., Gresta et al., 2004; Cannata et al., 2009a,b; Marchetti et al., 2009; Sciotto et al., 2013; see **section 2.1.3** for further details]. Nevertheless, most of the researches were carried out in short intervals of time, eventually focusing on striking eruptive episodes.

In this thesis, we aimed to extend the analysis of infrasound signals to a wide range of time and eruptive activities, including degassing, minor ash emissions up to powerful fire fountains and effusive eruptions. This kind of approach, which benefits of several years of continuous recordings (August 2007-December 2010), allows to test the validity of the hypothesized source dynamics and investigating the steadiness of the reciprocal relations among shallow conduits through time.

In addition, strombolian/mild vulcanian activity from Mt. Yasur, recorded during a temporary experiment, was analyzed. Indeed, the comparison with other open conduits systems is fundamental in order to widen the knowledge on volcano behaviors and implement more realistic and valid models.

In the following bullet points, the main conclusions of this thesis are summarized.

1. NEC events featured periods with very steady waveforms and spectral features lasting from days to months, with slow or sudden variations. The steadiness of the waveforms during long periods highlights the repetitive nature of the NEC infrasound events, and then

of their source mechanism. Furthermore, as the source was inferred to be related to degassing activity, the stable character of NEC events, as also their almost-continuous radiation through the investigated time, suggests that NEC is a highly active branch of degassing of Mt. Etna. This is validated from the compositional and seismological analyses carried out on the ash emission of November 14-15th 2010, which suggests the existence of a free magma surface and open conduit condition for NEC crater (see also concluding remark number **5**).

2. The variations of NEC infrasonic events, taking place during the most important eruptive episodes at other vents, are systematic (see also **table 2.1**), implying a stable and "relatively" long lasting connection between NEC and SEC/EF plumbing systems. Indeed, even though a persistent degassing is active at NEC, increases of supply rate generally activate other vents (SEC/EF). The ongoing activity at SEC/EF affects deeply NEC events features, suggesting the existence of a link among the relative feeding systems.
3. The observations made in this thesis strengthen the interpretation of NEC infrasound event model, given also in previous studies [Sciotto et al., 2013], according to which two resonance mechanisms (standing wave and Helmholtz resonance), linked to the same trigger source, are contemporaneously active. The model implies that observed changes in spectral features are due to variations in the resonator length, mostly caused by level fluctuation of magma column inside the NEC conduit. The connections between NEC and SEC/EF feeding systems imply that level fluctuations of magma column inside the NEC conduit correspond to magmastatic pressure decrease/increase inside the main plumbing system. This finding opens up new and interesting possibilities for monitoring magma pressure changes inside the Mt. Etna plumbing system.
4. The detailed analyses carried out on infrasound signals generated by EF during May-September 2008, shed light on the relationship among closely spaced vents along the fissure. Indeed, by modeling the main sources of infrasound localized, periodical short-lasting increases of supply rate were identified. These episodes generally tend to activate the topographically highest altitude vent along the eruptive fissure (named V3), whereas moderate supply rate activity eruptive activity occurs exclusively at the topographically lower vents (V1-V2). In fact, the increase in the gas content leads to the activation of the most inclined portion of the feeding system of the fissure, while magma with minor gas

content is erupted from the less inclined branches. Furthermore, a collapse of the conduit wall of the vent V3 was inferred, on the basis of spectral changes of infrasound events.

5. The study of the 2010 ash emissions allowed distinguishing two main *types*, *a* and *b*: the former characterized by relatively powerful explosivity and impulsive nature, the latter by low explosivity and long-duration. The evaluation of volcanic events at SEC-BN (*type a*) suggests an accumulation of gas below the involved craters, followed by its "stepped" release as sequences of small/minor explosive events, and finally the main explosive event producing a significant eruption plume and tephra fallout. It was assumed that the presence of material plugging the upper portion of the conduit accounts for the low values of VASR computed. Different conditions are inferred for NEC (*type b*), where the abundance of tachylite particles within the tephra deposit, erupted by NEC, suggest the existence of a surface of cooling magma on the top of the conduit, as confirmed by the seismo-acoustic features of NEC explosions, compatible with the absence of a cap rock obstructing NEC top conduit.
6. The analysis of acoustic signals from a persistently active open-conduit volcano, Mt. Yasur, reveals the existence of different dynamics. Indeed, at Mt. Yasur puffing activity is accounting for the continuous degassing activity, which takes place independently from the occurrence of strongest strombolian/mild vulcanian events. The latter, indeed, are characterized by complex waveforms, often resulting from overlapping events, suggesting the arrival of multiple batches of gas slugs/bubbles. A distinction has been done for ash-loaded events, where either the source mechanism (prolonged pyroclastic mixture release) or attenuation effects, due to entrained ash in the plume, produce emergent long lasting waveforms. Finally, amplitude attenuation effects, not justifiable with geometrical spreading, were linked to diffraction at the crater rim. This observation suggests that, in future, the topography of the crateric area must be taken into account when planning measurements close to the crater rim.

ACKNOWLEDGMENTS

With these few lines I want to thanks all the people that contributed to my personal and scientific development up to now.

Firstly, I want to thank Professor Stefano Gresta. I was honored to be introduced to the volcano seismology by a skilled specialist like him, and grateful to receive his support, especially in the hardest time of those years. I thank Eugenio, particularly for the enthusiasm, that he is always communicating and for helping me with the development of my scientific work. A warm thanks to Andrea, for all the knowledge and time he gave me, for the indestructible patience with whom he supported my anxious crises, until the very last months.

This thesis has still a lot of people to acknowledge. In particular, I want to say thanks to Mariangela, who worked close to me as a colleague and as a friend, and to all of my colleagues who contributed directly to this work, as Daniele Andronico, Deborah Lo Castro, Letizia Spampinato, Luigi Lodato, Piergiorgio Scarlato and Jacopo Taddeucci, all from Istituto Nazionale di Geofisica and Vulcanologia. I am warmly grateful to all of those people in the Section of Catania, who contributed to make my working-time better, and especially those I was sharing the room with, and those I was (involuntarily) invading the office. Quoting each name would be rather long, but for every coffee, discussion or shared lunch, and for every laugh or suggestion, thanks.

I received a lot of support from my colleagues in Munich that I want to acknowledge. Amongst other, particularly Cristian for being a proactive colleague and listener friend, Alejandra for sharing time, open thoughts and project for a better word, and Betty for her useful advices and fruitful discussions.

But most of all, I want to say thanks to my parents, who gave me all the motivation and support in the most difficult time and to my sister, Eleonora, for being on my side, day by day. They were my best supporter and incentive to make better. I want to thank Daniele for believing me and for showing me always the best side of the world. Finally I want to say thanks also to all those people who were close to me during these three years, sharing this part of my life and contributing to it.

REFERENCES

Aiuppa, A., Cannata, A., Cannavò, F., Di Grazia, G., Ferrari, F., Giudice, G., Gurrieri, S., Liuzzo, M., Mattia, M., Montalto, P., Patanè, D., and G., Puglisi, (2010), Patterns in the recent 2007-2008 activity of Mount Etna volcano investigated by integrated geophysical and geochemical observations, *Geochem. Geophys. Geosys.*, 11, doi:10.1029/2010GC003168.

Aki, K., Fehler, M., and S., Das, (1977), Source mechanism of volcanic tremor: fluid-driven crack models and their application to the 1963 Kilauea eruption, *J. Volcanol. Geotherm. Res.*, 2, 259-287.

Aki, K., and R., Koyanagi, (1981), Deep volcanic tremor and magma ascent mechanism under Kilauea, Hawaii, *J. Volcanol. Geotherm. Res.*, 86, 7095–7109.

Allard, P., Aiuppa, A. , Burton, M., Caltabiano, T., Federico, C., Salerno, G., and A., La Spina, (2008), Crater gas emissions and the magma feeding system of Stromboli volcano, in: The Stromboli volcano. An integrated study of the 2002–2003 eruption, *Geophys. Monogr. Ser.*, vol 182, edited by S. Calvari et al., pp 65–80, AGU, Washington, D. C.

Allen, S.R., (2005), Complex spatter- and pumice-rich pyroclastic deposits from an andesitic caldera-forming eruption: the Siwi pyroclastic sequence, Tanna, Vanuatu, *Bull Volcanol*, 67, 27–41, DOI 10.1007/s00445-004-0358-6.

Almendros, J., Ibanez, J.M., Alguacil, G., Del Pezzo, E., and R., Ortiz, (1997), Array tracking of the volcanic tremor source at Deception Island, Antarctica, *Geophys. Res. Lett.*, 24, 3069-3072.

Almendros, J., Chouet, B.A., Dawson, P., and T., Bond (2002), Identifying elements of the plumbing system beneath Kilauea Volcano, Hawaii, from the source locations of very-long-period signals, *Geophys. J. Int.*, 148, 303–312.

Almendros, J., and B.A., Chouet, (2003), Performance of the radial semblance method for the location of very long-period volcanic signals, *Bull. Seism. Soc. Am.*, 93, 1890–1903.

Aloisi, M., Bonaccorso, A., Cannavò, F., Gambino, S., Mattia, M., Puglisi, G., and E. Boschi, (2009), A new dyke intrusion style for the Mount Etna May 2008 eruption modeled through continuous tilt and GPS data, *Terra Nova,* 21, 316–321.

Alparone, S., Andronico, D., Lodato, L., and T., Sgroi, (2003), Relationship between tremor and volcanic activity during the Southeast crater eruption on Mount Etna in early 2000, *J. Geophys. Res*., 108, doi:10.1029/2002JB001866.

Alparone, S., Andronico, D., Sgroi, T., Ferrari, F., Lodato, L., and D., Reitano, (2007), Alert system to mitigate tephra fallout hazards at Mt. Etna Volcano, Italy, *Nat. Hazards*, doi:10.1007/s11069-007-9120-7.

Alparone, S., Cannata, A., Gambino, S., Gresta, S., Milluzzo, V., and P., Montalto, (2010), Time-space variation of volcano-seismic events at La Fossa (Vulcano, Aeolian Islands, Italy): new insights into seismic sources in a hydrothermal system, *Bull. Volcanol*., 72, 803–816, doi: 10.1007/s00445-010-0367-6.

Alster, M., (1972), Improved calculation of resonant frequencies of Helmholtz resonators, *Journal of Sound and Vibration* 24, 63–85.

Andronico, D., Cristaldi, A., and Scollo, S. (2008), The 4-5 September 2007 lava fountain at South-East crater of Mount Etna, Italy, *J. Volcanol. Geotherm. Res.*, 173, 325-328.

Andronico, D., S. Scollo, A. Cristaldi, and F., Ferrari, (2009a), Monitoring ash emission episodes at Mt. Etna: the 16 November 2006 case study, *J. Volcanol. Geotherm. Res.*, 180 (2–4), 123–134, doi:10.1016/j.jvolgeores.2008.10.019.

Andronico, D., Spinetti, C., Cristaldi, A., and M.F., Buongiorno, (2009b), Observations of Mt. Etna volcanic ash plumes in 2006: an integrated approach from ground-based and polar satellite NOAA-AVHRR monitoring system, *J. Volcanol. Geotherm. Res*., 180 (2–4), 135–147, doi:10.1016/j.jvolgeores.2008.11.013.

Andronico, D., Lo Castro, M. D., Sciotto, M., and L., Spina, (2013), The 2010 ash emissions at the summit craters of Mt Etna: Relationship with seismo-acoustic signals, *J. Geophys. Res.*, doi:10.1029/2012JB009895.

Arciniega-Ceballos, A., Chouet, B.A., and P., Dawson, (1999), Very long-period signals associated with vulcanian explosions at Popocatépetl volcano, México, *Geophys. Res. Lett.*, 26, 30133016.

Arrowsmith, S., Johnson, J., Drob, D., and M., Hedlin, (2010), The Seismo-Acoustic Wavefield: A new paradigm in studying geophysical phenomena, *Review of Geophysics*, doi:10.1029/2010RG000335.

Aster, R., Zandomeneghi, D., Mah, S., McNamara, S., Henderson, D.B., Knox, H., and K., Jones, (2008), Moment tensor inversion of very long period seismic signals from Strombolian eruptions of Erebus Volcano, *J. Volcanol. Geotherm. Res.*, 177, 635647.

Aubert de la Rue, E., (1960), Les manifestations actuelles du volcanisme aux Nouvelles Hebrides (Melanesie), *Bulletin Volcanologique*, 23, 197–205.

Azzaro, R., (1999), Earthquake surface faulting at Mount Etna volcano (Sicily) and implications for active tectonics, *J. Geodyn*., 28, 193-213.

Azzaro, R., Barbano, M.S., Antichi, B., and R., Rigano, (2000), Macroseismic catalogue of Mt. Etna earthquakes from 1832 to 1998, *Acta Vulcanol*., 12, 3-36.

Azzaro, R., Mattia, M., and G., Puglisi, (2001), Dynamics of fault creep and kinematics of the eastern segment of the Pernicana fault (Mt. Etna, Sicily) derived from geodetic observations and their tectonic significance, *Tectonophysics,* 333, 401-415.

Bani, P. and M., Lardi, (2007), Sulphur dioxide emission rates from Yasur volcano,Vanuatu archipelago, *Geoph. Res. Lett.*, Vol. 34, L20309, doi:10.1029/2007GL030411.

Bani, P., Harris, A.J.L, Shinohara, H., and F., Donnadieu, (2013), Magma dynamics feeding Yasur's explosive activity observed using thermal infrared remote sensing, *Geophys. Res. Lett.*, Vol. 40, 3830–3835, doi:10.1002/grl.50722.

Barani, S., Ferretti, G., Massa, M., and D., Spallarossa, (2007), The waveform similarity approach to identify dependent events in instrumental seismic catalogues, *Geophys J Int* , 168, 100–108.

Barberi, G., Cocina, O., Maiolino, V., Musumeci, C., and E., Privitera, (2004), Insight into Mt. Etna (Italy) kinematics during 2002– 2003 eruption as inferred by seismic stress and strain tensors inversion, *Geophys. Res. Lett.*, 31, L21614, doi:10.1029/2004GL020918.

Barreca, G., Bonforte, A., and M., Neri, (2012), A pilot GIS database of active faults of Mt. Etna (Sicily): A tool for integrated hazard evaluation, *J. Volcanol. Geotherm. Res.*, http://dx.doi.org/10.1016/j.jvolgeores.2012.08.013.

Battaglia, J., and K., Aki, (2003), Location of seismic events and eruptive fissures on the Piton de la Fournaise volcano using seismic amplitudes, *J Geophys. Res.*, 108, NO. B8, 2364, doi:10.1029/2002JB002193.

Battaglia, J., Aki, K., and V., Ferrazzini, (2005), Location of tremor sources and estimation of lava output using tremor source amplitude on the Piton de la Fournaise volcano: 1. Location of tremor sources, *J. Volcanol. Geotherm. Res.*, 147, 268-290.

Boatwright, J., (1980), A spectral theory for circular seismic sources: simple estimates of source dimension, dynamic stress drop, and radiated seismic energy, *Bull. Seismol. Soc. Am.*, 70 (1), 1 – 27.

Bonaccorso, A., and P.M., Davis, (1999), Models of ground deformation from vertical volcanic conduits with application to eruptions of Mount St. Helens and Mount Etna, *J. Geophys. Res.*, 104, 10531–10542.

Bonaccorso, A., Bonforte, A., Del Negro, C., Di Grazia, G., Ganci, G., Neri, M., Vicari, A., and E., Boschi, (2011a), The initial phases of the 2008-2009 Mt. Etna eruption: a multi-disciplinary approach for hazard assessment, *J. Geophys. Res.*, doi:10.1029/2010JB007906.

Bonaccorso, A., Cannata, A., Corsaro, R. A., Di Grazia, G., Gambino, S., Greco, F., Miraglia, L., and A., Pistorio, (2011b), Multidisciplinary investigation on a lava fountain preceding a flank eruption: The 10 May 2008 Etna case, *Geochem. Geophys. Geosys.*, doi:10.1029/2010GC003480.

Bouche, E., Vergniolle, S., Staudacher, T., Nercessian, A., Delmont, J.-C., Frogneux, M., Cartault, F., and A., Le Pichon, (2010), The role of large bubbles detected from acoustic measurements on the dynamics of Erta 'Ale lava lake (Ethiopia), *Earth and Planetary Science Letters,* doi:10.1016/j.epsl.2010.03.020.

Branca, S., Carbone, D., and F., Greco, (2003) , Intrusive mechanism of the 2002 NE-Rift eruption at Mt. Etna (Italy) inferred through continuos microgravity data and volcanological evidences, *Geophys. Res. Lett.*, 30, No 20, 2077 doi:10.1029/2003Gl018250.

Buckingham, M.J., and M.A., Garcés, (1996), Canonical model of volcano acoustics, *J. Geophys. Res.*, 101(B4), 8129–8151, doi:10.1029/95JB01680.

Buonocunto, C., D'Auria, L., Caputo, A., Martini, M., and M., Orazi, (2011), The InfraCyrus sound sensor, *Rapporti tecnici INGV*, ISSN 2039-7941, Anno 2011_numero 188.

Burollet, P.F., Mugniot, G.M. and P., Sweeney, (1978), The geology of the Pelagian Block: the margins and basins of Southern Tunisia and Tripolitania. In: Nairn, A., Kanes, W., Stelhi, F.G. (Eds.), The ocean basins and margins, *Plenum Press, New York*, NY, pp. 331– 339.

Calvari, S., Spampinato, L., Lodato, L., Harris, A.J.L., Patrick, M.R., Dehn, J., Burton, M.R., and D., Andronico, (2005), Chronology and complex volcanic processes during the 2002–2003 flank eruption at Stromboli volcano (Italy) reconstructed from direct observations and surveys with a handheld thermal camera, *J. Geophys. Res*.110, B02201. doi:10.1029/2004JB003129.

Cannata, A., Catania, A., Alparone, S., and S., Gresta (2008), Volcanic tremor at Mt. Etna: Inferences on magma dynamics during effusive and explosive activity, *J. Volc. Geotherm. Res.*, doi:10.1016/j.jvolgeores.2007.11.027.

Cannata, A., Montalto, P., Privitera, E., and G., Russo,(2009a), Characterization and location of infrasonic sources in active volcanoes: Mt. Etna, September-November 2007, *J. Geophys. Res.*, 114, B08308, doi:10.1029/2008JB006007.

Cannata, A., Montalto, P., Privitera, E., Russo, G., and S., Gresta, (2009b). Tracking eruptive phenomena by infrasound: May 13, 2008 eruption at Mt. Etna, *Geophys. Res. Lett*., doi:10.1029/2008GL036738.

Cannata, A., Hellweg, M., Di Grazia, G., Ford, S., Alparone, S., Gresta, S., Montalto, P., and D., Patanè, (2009c), Long Period and Very Long Period events at Mt. Etna volcano: characteristics, variability and causality, and implications for their sources, *J. Volcanol. Geotherm. Res*., 187, 227–249, doi:10.1016/j.jvolgeores.2009.09.007.

Cannata, A., Sciotto, M., Spampinato, L., and L., Spina, (2011a), Insights into explosive activity at eruptive fissure closely-spaced vents by infrasound signals: example of Mt. Etna 2008 eruption, *J. Volc. Geotherm. Res.*, 208, 1-11.

Cannata, A., Montalto, P, Aliotta, M., Cassisi, C., Pulvirenti, A., Privitera, E., and D., Patanè, (2011b), Clustering of infrasonic events at Mount Etna using pattern recognition techniques, *Geophys. J. Int.*, 185, 253–264, doi: 10.1111/j.1365-246X.2011.04951.x.

Cannata, A., Di Grazia, G., Aliotta, M., Cassisi, C., Montalto, P., and D., Patanè, (2013), Monitoring Seismo-volcanic and Infrasonic Signals at Volcanoes: Mt. Etna Case Study, *Pure Appl.Geophys.*, doi:10.1007/s00024-012-0634-x.

Carnay, J.N. and A., Macfarlane, (1979), Geology of Tanna, Aneityum, Futuna and Aniva, *New Hebrides Geological Survey Report*, pp. 5–29.

Catalano, S., Torrisi, S., and C., Ferlito, (2004), The relationship between Late Quaternary deformation and volcanism of Mt. Etna (eastern Sicily) : new evidence from the sedimentary substratum in the Catania region, *J Volcanol. Geotherm. Res.*, 132, 311-334, doi:10.1016/S0377-0273(03)00433-5.

Chouet, B.A., (1986), Dynamics of a fluid-driven crack in three dimensions by the finite difference method. *J. Geophys. Res.,* 91, 967-992.

Chouet, B.A., (1988), Resonance of a fluid-driven crack: radiation properties and implications for the source of long-period events and harmonic tremor, *J. Geophys. Res.,* 93, 4375-4400.

Chouet, B.A., Page, R.A., Stephens, C.D., Lahr, J.C., and J.A., Power, (1994), Precursory swarms of long-period events at Redoubt Volcano (1989-1990), Alaska: their origin and use as a forecasting tool, *J. Volcanol. Geotherm. Res.*, 62, 95–135.

Chouet, B., (1996), Long-period volcano seismicity: its source and use in eruption forecasting, *Nature*, 380, 309–316.

Chouet, B., Saccorotti, G., Dawson, P., Martini, M., De Luca, G., Milana, G. and M., Cattaneo, (1999), Broadband measurements of the sources of explosions at Stromboli Volcano, Italy, *J. Geophys. Res.*, 26, 1937-1940.

Chouet, B.A., (2003), Volcano seismology, *Pure Appl. Geophys.* 160, 739788.

Chouet, B.A., (2009), Volcanoes, non-linear processes in, In "*Encycl. Complexity and System Sci.*" (R.A., Meyers Ed.), Springer-Verlag, Berlin, pp. 98729899.

Continisio, R., Ferrucci, F., Gaudiosi, G., Lo Bascio, D., and G., Ventura, (1997), Malta Escarpment and Mt. Etna: early stages of an asymmetric rifting process? Evidences from geophysical and geological data, *Acta Vulcanol.*, 9, 39-47.

Cooley, J.,W., and J.,W., Turkey, (1965), An algorithm for the machine calculation of complex Fourier series. *Math. Comput.*, 19, 297-301.

Corsaro, R.A., and M., Pompilio, (2004), Magma dynamics in the shallow plumbing system of Mt. Etna as recorded by compositional variations in volcanics of recent summit activity (1995–1999), *J. Volc. Geotherm. Res.*, 137, doi:10.1016/j.jvolgeores.2004.05.008.

Coulon C, and R.C., Maury, (1981), Petrology of tholeiitic lavas from Tanna Island (New Hebrides): importance of cumulative processes in island arc magmatism, *Bull Volcanol*, 44, 661–680.

Cristofolini, R., and R., Romano, (1982), Petrologic features of the Etnean volcanic rocks, *Mem. Soc. Geol. Ital.*, 23, 99–115.

Cronin, S.J., and D.S., Sharp, (2002), Environmental impacts on health from continuous volcanic activity at Mt. Yasur (Tanna) and Ambrym, Vanuatu, *International Journal of Environmental Health Research*, 12, 109-123

Crosson, R.S., and D.A., Bame, (1985), A spherical source model for low frequency volcanic earthquakes, *J. Geophys. Res.*, 90,10237-10247.

Dahm, T. and B., Brandsdóttir, (1997), Moment tensors of microearthquakes from the Eyjafjallajökull volcano in South Iceland, *Geophys. J. Int*., 130: 183–192. doi: 10.1111/j.1365-246X.1997.tb00997.

Dahlgren, R.A., Salgus, M., and F.C., Ugolini, (1989) The Nature, Properties and Management of Volcanic Soils, Advances in Agronomy, Vol. 82, 2004, pp 113-182.

De Angelis, S., and S.R., McNutt, (2005), Degassing and hydrothermal activity at Mt. Spurr, Alaska during the summer of 2004 inferred from the complex frequencies of long period events, *Geophys. Res. Lett*., 32, doi:10.1029/2005GL022618.

De Angelis, S., and S., McNutt, (2007), Observations of volcanic tremor during the January February 2005 eruption of Mt. Veniaminof, Alaska, *Bull. Volcanol*., 69, 927-940.

Del Bello, E., Llewellin, E., Taddeucci, J., Scarlato, P., and S.J., Lane, (2012), An analytical model for gas overpressure in slug-driven explosions: Insights into Strombolian volcanic eruption, *J. Geophys. Res*., Vol. 117, B02206, doi:10.1029/2011JB008747.

Di Grazia, G., Falsaperla, S., and H., Langer, (2006), Volcanic tremor location during the 2004 Mount Etna lava effusion, *Geophys. Res. Lett.*, 33, L04304, doi:10.1029/2005GL025177.

Di Grazia, G., Cannata, A., Montalto, P., Patanè, D., Privitera, E., Zuccarello, L., and E., Boschi (2009), A new approach to volcano monitoring based on 4D analyses of seismo-volcanic and acoustic signals: the 2008 Mt. Etna eruption, *Geophys. Res. Lett.*, 36, 18, doi:10.1029/2009GL039567.

Diehl, R.L., (2008), Acoustic and auditory phonetics: the adaptive design of speech sound systems, *Philosophical Transactions of the Royal Society,* B 363, 965–978.

Dobran, F., (2001), Volcanic Processes: Mechanisms in *Material Transport*. Kluwer Academic/Plenum Publishers.

Doglioni, C., Innocenti, F., and G., Mariotti, (2001), Why Mt. Etna?, *Terra Nova,* 13, 2531.

Dvorak, J. J., and A.T., Okamura (1985), Variations in tilt rate and harmonic tremor amplitude during the January–August 1983 East Rift eruptions of Kilauea volcano, Hawaii, *J. Volcanol. Geotherm. Res.*, 25, 249–258.

Dvorak, J.J., and D., Dzurisin, (1997), Volcano Geodesy: the search for magma reservoirs and the formation of eruptive vents, *Reviews of Geophysics*, 35, pp 343-384.

Erdem, J.E., and G.P., Waite, (2013), Temporal changes in eruptive behavior identified with coda wave interferometry and seismo-acoustic observations at Fuego Volcano, Guatemala, in Rose, W.I., N. Varley, and J. Palma, eds., Open Vent Volcanoes, *Geol. Soc. Am.*, Boulder, CO.

Falsaperla, S., Alparone, S., D'Amico, S., Di Grazia, G., Ferrari, F., Langer, H., Sgroi, T., and S., Spampinato (2005), Volcanic Tremor at Mt. Etna, Italy, Preceding and Accompanying the Eruption of July-August, 2001, *Pure App. Geophys.*, 162, 1-22, doi:10.1007/s00024-005-2710-y.

Fee, D., Garces, M., Patrick, M., Chouet, B., Dawson, P., and D., Swanson, (2010a), Infrasonic harmonic tremor and degassing bursts from Halema'uma'u Crater, Kilauea Volcano, Hawaii, *J. Geophys. Res.*,115, doi:10.1029/2010JB007642.

Fee, D., Garces, M., and A., Steffke, (2010b), Infrasound from Tungurahua Volcano 2006–2008: strombolian to plinian eruptive activity, *J. Volcanol. Geotherm. Res.*, doi:10.1016/j.jvolgeores.2010.03.006.

Ferrick, M.G., and W.F., St. Lawrence, (1984), Comment on 'Observations of volcanic tremor at Mt. St Helens volcano' by Michael Fehler., *J. Geophys. Res.,* 89, 6349-6350.

Firstov, P.P., and N.M., Kravchenko, (1996), Estimation of the amount of explosive gas released in volcanic eruptions using air waves, *Volcanol. Seismol*., 17, 547-560.

Freda, C., Taddeucci, J., Scarlato, P., Rao, S., Salvaterra, C., Gaeta, M., and D.M., Palladino, (2012), The FAMoUS toolbox goes to Yasur: field test of a FAst, MUltiparametric Set-up for real-time observation of explosive eruptions, *Geophysical Research Abstracts*, Vol. 14, EGU2012-9882, EGU General Assembly 2012

Furnes, H., (1975), Experimental Palagonitization of Basaltic Glasses of Varied Composition, *Contrib. Mineral. Petrol.*, 50, 105–113.

Garces, A.M., and S.R., McNutt, (1997), Theory of the airborne sound field genereted in a resonant magma conduit*, J. Volcanol. Geotherm. Res.*, 78, 155-178.

Garces, M., Harris, A., Hetzer, C., Johnson, J., Rowland, S., Marchetti, E., and P., Okubo, (2003), Infrasonic tremor observed at Kilauea Volcano, Hawaii., *Geophys. Res. Lett.*, 30, 2023. doi:10.1029/2003GL018038.

Ghisetti, F., (1979), Relazioni tra strutture e fasi trascorrenti e distensive lungo i sistemi Messina–Fiumefreddo, Tindari–Letoianni e Alia–Malvagia-Sicilia nord-orientale.: uno studio micro tettonico, *Geol. Romana*, 18, 23-58.

Giacomelli and Pesaresi (2003), La struttura e la storia eruttiva dell'Etna. Da http://vulcan.fis.uniroma3.it/gnv/etna/GNV1.PDF.

Goto, A., and J.B., Johnson, (2011), Monotonic infrasound and Helmholtz resonance at Volcan Villarrica (Chile), *Geophys. Res. Lett*., 38 (L06301).

Green, D.N., (2005), Multi-parameter monitoring and modelling of cyclic volcanic activity, *PhD Thesis.*

Green, D.N., and J., Neuberg, (2006), Waveform classification of volcanic low-frequency earthquake swarms and its implication at Soufrière Hills Volcano, Monserrat*, J. Volcanol. Geotherm. Res.*, 153, 51–63.

Gresta, S., Imposa, S., Patanè, D., and G., Patanè, (1987), Volcanic tremor at Mt. Etna: state-of-the-art and perspectives, *Pure App. Geophys.*, 125, 1079–1095.

Gresta, S., Ripepe, M., Marchetti, E., D'Amico, S., Coltelli, M., Harris, A.J.L., and E., Privitera, (2004), Seismoacoustic measurements during the July-August 2001 eruption at Mt. Etna volcano, Italy, *J. Volc. Geotherm. Res.*, 137, 219-230.

Hagerty, M.T., Schwartz, S.Y., Garces, M.A., and M., Protti, (2000), Analysis of seismic and acoustic observations at Arenal Volcano, Costa Rica, 1995–1997, *J. Volcanol. Geotherm. Res.,* 101, (1–2), 27–65.

Harris, A., Johnson , J., Horton, k., Garbeil, H., Ramm, H., Pilger, E., Flynn, L., Mouginis-Mark, P., Pirie, D., Donegan, S., Rothery, D., Ripepe, M., and E., Marchetti, (2003), Ground-based infrared monitoring provides new tool for remote tracking of volcanic activity, *Eos Trans.* AGU, 84(40), 409.

Hasada, Y., Kumagai, H., and M., Kumazawa, (2001), Autoregressive modeling of transfer functions in frequency domain to determine complex travel times, *Earth. Planet. Space*, 53, 3-11

Hasegawa, A and A., Yamamoto, (1994), Deep, low-frequency microearthquakes in or around seismic low-velocity zones beneath active volcanoes in northeastern Japan, *Tectonophysics*, 233, 233–252.

Havskov, J. and G., Alguacil (2004), Instrumentation in Earthquake Seismology, *Modern Approaches in Geophyisics*, vol. 22 - Springer.

Hill, D.P., (1996), Earthquakes and carbon dioxide beneath Mammoth Mountain, California, *Seis. Res. Lett.*, 67, 8–15.

Hori, S., Fukao, Y., Kumazawa, M., and M., Furumoto, (1989) A new method of spectral analysis and its application to the Earth's free oscillations: The "Sompi" method., *J. Geophys. Res.*, 94 (B6), 7535-7553.

Inguaggiato, S., Mazot, A., and T., Ohba, (2011), Monitoring active volcanoes: The geochemical approach, *Annals of geophysics*, 54, 2, doi: 10.4401/ag-5187.

INGV staff (2007-2013), Volcanological and geochemical reports, http://www.ct.ingv.it/index.php?option=com_content&view=article&id=130&Itemid=315.

James, M.R., Lane, S.J., Chouet, B., and J.S., Gilbert, (2004), Pressure changes associated with the ascent and bursting of gas slugs in liquid-filled vertical and inclined conduits, *J Volcanol. Geotherm. Res.*, 129, 61–82.

James, M.R., Lane, S.J,. and B.A., Chouet, (2006), Gas slug ascent through changes in conduit diameter: Laboratory insights into a volcano-seismic source process in low-viscosity magmas, *J. Geophys. Res.*, 111(B5), B05201, doi:10.1029/2005JB003718.

Jaupart, C., and S., Vergniolle, (1988), Laboratory models of Hawaiian and Strombolian eruptions, *Nature* 331, 58–60.

Johnson, J.B., and J.M., Lees, (2000), Plugs and chugs: seismic and acoustic observations of degassing explosions at Karymsky, Russia and Sangay, Ecuador, *J. Volc. Geotherm. Res.*, 101, 67-82.

Johnson, J.B., (2003), Generation and propagation of infrasonic airwaves from volcanic explosions, *J. Volcanol. Geotherm. Res*., 121 (1–2), 1 – 14.

Johnson, J. B., and R.C., Aster, (2005), Relative partitioning of acoustic and seismic energy during Strombolian eruptions, *J. Volc. Geotherm. Res.*, 148, 334–354, doi:10.1016/j.jvolgeores.2005.05.002.

Johnson, J.B., (2005), Source location variability and volcanic vent mapping with a small-aperture infrasound array at Stromboli Volcano, Italy, *Bull Volcanol*, 67:1–14 DOI 10.1007/s00445-004-0356-8.

Johnson, J.B., Aster, R., Jones, K., Kyle, P., and W., McIntosh, (2008), Acoustic source characterization of impulsive Strombolian eruptions from the Mount Erebus lava lake, *J. Volc. Geotherm. Res.,* 177, 673–686.

Johnson, J.B., and M., Ripepe (2011), Volcano infrasound: A review, J. *Volcanol. Geotherm. Res.*, doi:10.1016/j.jvolgeores.2011.06.006.

Johnson, K., (1997), Acoustic and Auditory Phonetics. MA, Blackwell Publishers, Malden.

Jones, K.R., Johnson, J.B., Aster, R., Kyle, P., and W., McIntosh, (2008), Infrasonic tracking of large bubble bursts and ash venting at Erebus volcano, Antarctica, *J. Volcanol. Geotherm. Res*., 177, 661–672.

Jones, K.R., and J.B., Johnson, (2010). Mapping complex vent eruptive activity at Santiaguito, Guatemala using network infrasound semblance, *J Volcanol. Geotherm. Res.*, doi:10.1016/j.jvolgeores.2010.08.006.

Kao, H., and S.J., Shan, (2004), The source-scanning algorithm: mapping the distribution of seismic sources in time and space, *Geophys. J. Int*., 157, 589–594.

Kawakatsu, H., Ohminato, T., and H., Ito, (1994), 10sPeriod volcanic tremors observed over a wide area in southwestern Japan, *Geophys. Res. Lett*., 21:1963–66.

Kawakatsu, H., Kaneshima, S., Matsubayashi, H., Ohminato, T., Sudo, Y., Tsutsui, T., Uhira, K., Yamasato, H., Ito, H., and D., Legrand, (2000), Aso94: Aso seismic observation with broadband instruments, J. Volcanol. Geotherm. Res., Vol. 101, Issues 1–2, pp 129-154.

Kedar, S., Sturtevant, B., H., Kanamori, (1996), The origin of harmonic tremor at Old Faithful geyser, *Nature,* 379, 708-711.

Keating, G.N., Krier, D.J., Valentine, G.A., and F.V., Perry, (2007), Shallow plumbing systems for small-volume basaltic centers, *Bull. Volcanol.*, 70, 563–582.

Kelley, J.K., (2008), Glassy Tephra of Yasur Volcano, Vanuatu: A Magnetic, Petrographic, and Crystallographic Study and Implications for Devitrification, *Thesis*, Southern Illinois University Carbondale, 2008 - 77

Kieffer, S.W., (1984). Seismicity at Old Faithful geyser: An isolated source of geothermal noise and possible analogue of volcanic seismicity, *J. Volcanol. Geotherm. Res*., 22, 59-95.

Kim, K., and J.M., Lees, (2011) Finite-difference time-domain modeling of transient infrasonic wavefields excited by volcanic explosions, *Geophys. Res. Lett.*, Vol. 38, L06804, doi:10.1029/2010GL046615.

Kinsler, L.E., Frey, A.R., Coppens, A.B., and J.V., Sanders, (1982), *Fundamentals of Acoustics*, Third edition. John Wiley and Sons (480 pp.).

Knopoff, K., (1964), Q, *Rev. Geophys*., 2, 625– 660.

Kokelaar, B.P., (2002), Setting, chronology and consequences of the Eruption of Sourfiere Hills Volcano, Montserrat (1995-1999), in The Eruption of Soufrière Hills Volcano Montserrat (1995-1999), Druitt, T. H. and B.P. Kokelaar editors, The Geological society of London , pp 1-44.

Kostantinou, K. I., and V., Schlindwein, (2002), Nature, wavefield properties and source mechanism of volcanic tremor: A review*, J. Volcanol. Geotherm. Res*., 119, 161–187.

Kremers, S., Wassermann, J., Meier, K., Pelties, C., van Driel, M., Vasseur, J., Hort, M., Inverting the Source Mechanism of Strombolian Explosions at Mt. Yasur, Vanuatu, using a Multi-Parameter Dataset, *J. Volcanol. Geotherm. Res*., doi: 10.1016/j.jvolgeores.2013.06.007.

Kumagai, H., and B.A., Chouet, (1999), The complex frequencies of long-period seismic events as probes of fluid composition beneath volcanoes, *Geophys. J. Int.*,138, F7-F12.

Kumagai, H., and B.A., Chouet, (2000), Acoustic properties of a crack containing magmatic or hydrothermal fluids, *J. Geophys. Res*., 105, 25493-25512.

Kumagai, H., Chouet, B.A., and P., Dawson, (2005). Source process of a long-period event at Kilauea volcano, Hawaii, *Geophys. J. Int.*, 161, 243-254.

Kumazawa, M., Imanishi, Y., Fukao, Y., Furumoto, M., and A., Yamamoto, (1990), A theory of spectral analysis based on the characteristic property of a linear dynamic system, *Geophys. J. Int.*, 101, 613-630.

Kurze, U.J. and G.S., Anderson, (1971), Sound attenuation by barriers, *Appl. Acoust*. 4, 35–53.

Li, K.M., and H.Y., Wong, (2004), A review of commonly used analytical and empirical formulae for predicting sound diffracted by a thin screen, *Appl. Acoustic*, 66, 45-76.

Lacanna, G., and M., Ripepe, (2013), Influence of near-source volcano topography on the acoustic wavefield and implication for source modeling, *J. Volcanol. Geotherm. Res*., Vol. 250, pp 9-18, http://dx.doi.org/10.1016/j.jvolgeores.2012.10.005.

La Spina, A., Burton, M., and G.G., Salerno, (2010), Unravelling the processes controlling gas emissions from the Central and Northeast craters of Mt. Etna, *J. Volcanol. Geotherm. Res*., 198, 368-376, doi:10.1016/j.jvolgeores.2010.09.018.

Lanzafame, G., Neri, M., and D., Rust, (1996) Active tectonics affecting the eastern flank of Mount Etna: structural interactions at regional and local scale. In: Gravestock, P.H., McGuire, W.J. (Eds.), Etna: fifteen years on. Proceedings of the conference held on 12 February 1996 at the Cheltenham and Gloucester College of Higher Education, pp. 25-33.

Lanzafame, G., and C., Bousquet, (1997), The Maltese escarpment and its extension from Mt. Etna to the Aeoloian Islands (Sicily): importance and evolution of a lithosphere discontinuity, *Acta Vulcanol*., 9, 113-120.

Le Pichon, A., Blanc, E., Drob, D., Lambotte, S., Dessa, J. X., Lardy, M., Bani, P., and S., Vergniolle, (2005), Infrasound monitoring of volcanoes to probe high-altitude winds, *J. Geophys. Res.*, 110, D13106, doi:10.1029/2004JD005587.

Lighthill, J., (1978), Waves in Fluids. Cambridge University Press, 504 pp.

Lo Castro, M.D., and D., Andronico (2008), Operazioni di base per la misura della distribuzione granulometrica di particelle vulcaniche tramite il CAMSIZER, *Rapporti Tecnici INGV*, 79, 1–35.

Lokmer, I., C. J. Bean, G. Saccorotti, and D., Patane`, (2007), Moment-tensor inversion of LP events recorded on Etna in 2004 using constraints obtained from wave simulation tests, *Geophys. Res. Lett.*, 34, L22316, doi:10.1029/2007GL031902.

Louat, R., Hamburger, M., and M., Monzier, (1998), Shallow and intermediate depth seismicity in the New Hebrides Arc: Constraints on subduction process, in Geology and Offshore Resources of Pacific Island Arcs-Vanuatu Region, Earth Sci.

Ser., vol. 8, pp 329-356, edited by H. G. Green and F. L. Wong, Circum Pacific Council for Energy and Mineral Resources, Houston, Tx.

Maekawa, Z., (1968),Noise reduction by screens, *App. Acoustic* , 1, 157-173.

Makris, J., Nicolich, R., and W., Weigel (1986), A seismic study in the western Ionian Sea. *Ann. Geophys*., 6, 665– 678.

Marchetti, E., M. Ripepe, G. Uliveri, S. Caffo, and E., Privitera (2009), Infrasonic evidences for branched conduit dynamics at Mt. Etna volcano, Italy, *Geophys. Res. Lett.*, 36, L19308, doi:10.1029/2009GL040070.

Marchetti, E., Ripepe, M., Delle Donne, D., Genco, R., Finizola, A., and E., Garaebiti, (2013), Blast waves from violent explosive activity at Yasur volcano, Vanuatu, *American Geophysical Union*, doi: 10.1002/2013GL057900, accepted.

Marcillo, O., and J., Johnson, (2010), Tracking near-surface atmospheric conditions using an infrasound network, *Journal of the Acoustical Society of America*, 128, 14–19.

Marti, S., and O., Shoham, (1997), A unified model for stratified-wavy two-phase flow splitting at a reduced T-junction with an inclined branch arm, *International Journal of Multiphase Flow*, 4, 725–748.

Matoza, R., Hedlin, M.A.H, and M.A., Garces, (2007), An infrasound array study of Mount St. Helens. *J. Volcanol. Geotherm. Res.*, 160, 249-262 doi:10.1016/j.jvolgeores.2006.10.006.

Matoza, R.S., Fee, D., Garces, M.A., Seiner, M., Ramoin, P.A., and M.A.H., Hedlin, (2009a), Infrasonic jet noise from volcanic eruptions, *Geophys. Res. Lett*., 36, L08303, doi 10.1029/2008GL036486.

Matoza, R.S., Garces, M.A., Chouet, B., D'Auria, L., Hedlin, H., De Grooth-Hedlin, C., and G.P., Waite, (2009b), The source of infrasound associated with long-period events at Mount St. Helens, *J. Geophys. Res.*, 114, doi:10.1029/2008JB006128.

Matoza, R.S., Le Pichon, A., Vergoz, J., Herry, P., Lalande, J.M., Lee, H.I., Che, I.Y., and R., Rybin (2010a), Infrasonic observations of the June 2009 Sarychev Peak eruption, Kuril Islands: implications for infrasonic monitoring of explosive volcanism, *J. Volc. Geotherm. Res*., 200, 35–48.

Matoza, R.S., Fee, D., and M.A., Garcés, (2010b), Infrasonic tremor wavefield of the Pu`u `O`o crater complex and lava tube system, Hawaii, in April 2007, *J Geophys. Res.*, 115. doi:10.1029/2009JB007192.

McClelland, L., Simkin, T., Summers, M., Nielsen, E., and T.C., Stein, (1989), Global Volcanism: 1975–1985, Prentice-Hall, Upper Saddle River, N. J.

McNutt, S.R., (1986), Observations and analysis of B-type earthquakes, explosions and volcanic tremor at Pavlof volcano, Alaska, *Bull. Seismol. Soc. Am*., 76, 153–175.

McNutt, S.R., Rymer, H., and J., Stix, (2000) , Synthesis of volcano monitoring , Encyclopedia of Volcanoes, H. Sirgudsonn, Acamedic Press, Imprinted by Elseviewer, 2000, Part VIII , pp 1165-1184.

McNutt, S.R., (2005) Volcanic Seismology, *Annu. Rev. Earth Planet. Sci*., 32, 461-491.

Meier, K., Hort, M., Tessmer, E., and J., Wassermann, (2011) An integrated geophysical appro, ach: Field and modelling studies for abetter understanding of infrasound signals at Yasur volcano, Vanuatu, *Geophysical Research Abstracts*, Vol. 13, EGU2011-7852, EGU General Assembly 2011

Miklós, A., Hess, P., and Z., Bozóki, (2001), Application of acoustic resonators in photoacoustic trace gas analysis and metrology, *Rev. Sci. Instrum*., 72, 1937-1955.

Miller T.P., and T.J., Casadeval, (2000), Volcanic ash hazard to aviation, , Encyclopedia of Volcanoes, H. Sirgudsonn, Acamedic Press, Imprinted by Elseviewer, 2000, Part VII, pp 915-930.

Molina, I., Kumagai, H., Garcia-Aristizabàl, A., Nakano, M., and P., Mothes, (2008), Source process of very-long-period events accompanying long-period signals at Cotopaxi Volcano, Ecuador, *J. Volcanol. Geotherm. Res.*, 176, 119-133.

Monaco, C., Petronio, L., and M., Romanelli, (1995), Tettonica estensionale nel settore orientale del Monte Etna (Sicilia): dati morfotettonici e sismici, *Studi Geolog. Camerti*, Vol. Spec. (2), 363-374.

Monaco, C., Tapponier, P., Tortorici, L., and P.Y., Gillot, (1997), Late Quaternary slip rate On the Acireale-Piedimonte normal faults and tectonic origin of Mount Etna, *Earth Planet. Sci. Lett*., 147,125-139.

Monaco, C., Catalano, S., Cocina, O., De Guidi, G.,Ferito, C., Gresta, S., Musumeci, C., and L., Tortorici, (2005), Tectonic control on the eruptive dynamics at Mt. Etna Volcano (Sicily) during the 2001 and 2002–2003 eruptions, *J. Volcanol. Geotherm. Res*., 144, 211-233.

Montalto, P., Cannata, A., Privitera, E., Gresta, E., Nunnari, G., and D., Patané, (2010), Towards an automatic monitoring system of infrasonic events at Mt. Etna: strategies for source location and modeling, *Pure Appl. Geophys*, doi: 10.1007/s00024-010-0051-y.

Moran S.,C., (2003),. Multiple seismogenic processes for high-frequency earthquakes at Katmai National Park, Alaska: Evidence from stress tensor inversions of fault-plane solutions, *Bull. Seis. Soc. Am.*, 93:94–108.

Moran, S., Matoza, R.S., Garces, M. A., Hedlin, M. A.H., Bowers S. D., Scott, E.W., Sherrod, D. R., Wallance, (2008a), Seismic and acoustic recordings of an unusually large rockfall at Mount. St. Helens, Washington, *Geophys. Res. Lett.*, 35, L19302, doi:10.1029/2008GL035176.

Moran S.C., Malone, S.D., Qamar, A.I., Thelen, W.A., Wright, A.K., and J., Caplan-Auerbach, (2008b), Seismicity associated with renewed dome building at Mount St. Helens, 2004-2005., Chapter 2, In A Volcano Rekindled: The Renewed Eruption of Mount St. Helens, 2004-2006. (eds. Sherrod, D.R., Scott, W.E., Stauffer, P.H.) (U.S. Geological Survey Professional Paper, 1750, 2008).

Morrissey, M.M., and B.A., Chouet, (2001), Trends in long-period seismicity related to magmatic fluid compositions, *J. Volcanol. Geotherm. Res*., 108, 265-281.

Morse, P.M., and K.U., Ingard, (1968), Theoretical Acoustics, 927 pp., Princeton Univ. Press, Princeton, N. J.

Métrich, N., Allard, P., Aiuppa, A., Bani,P., Bertagnini, A., Shinohara, A., Parello, F., Di Muro, A., Garaebiti, E., Belhadj, O, and D., Massare, (2011), Magma and Volatile Supply to Post-collapse Volcanism and Block Resurgence in Siwi Caldera (Tanna Island, Vanuatu Arc), *J. Petrol*., Doi:10.1093/petrology/erg019

Nabyl, A., Dorel, J., and M., Lardi, (1997), A comparative study of low frequency seismic signals recorded at Stromboli volcano, Italy, and at Yasur volcano, Vanuatu, *New Zealand Journal of Geology and Geophysics*, Vol. 40, 549-558.

Nairn, I.A.; Scott, B.J.; and W.F., Giggenbach, (1988), Yasur volcano investigations, Vanuatu, *New Zealand Geological Survey*, Department of Scientific and Industrial Research. December 1988,pp. 1-74

Nakada, S., (2000), Hazard from Pyroclastic flows and surges, Encyclopedia of Volcanoes, H. Sirgudsonn, Acamedic Press, Imprinted by Elseviewer, 2000, Part VII, pp 945-956.

Nakamichi, H., Hamaguchi, H., Tanaka, S., Ueki, S., Nishimura, T., and A., Hasegawa, (2003), Source mechanisms of deep and intermediate-depth low-frequency earthquakes beneath Iwate volcano, northeastern Japan, *Geophys. J. Int.*, 154, 811–828.

Napoli, R., Currenti, G., Del Negro, C., Greco, F., and D., Scandura, (2008), Volcanomagnetic evidence of the magmatic intrusion on 13th May 2008 Etna eruption, *Geophys. Res. Lett.*, 35, L22301. doi:10.1029/2008GL035350.

Needham, C.E., (2010), Bast waves, Springer, 339 pp.

Neef, G., Zhao, J.X., Collerson, K.D., and F.S., Zhang, (2003), Late Quaternary uplift and subsidence of the west coast of Tanna, south Vanuatu, southwest Pacific: U\Th ages from the raised coral reefs in the median sedimentary basin, *Australian Journal of Earth Sciences*, 50, 39–48.

Neidel, N., and M.T., Tarner, (1971), Semblance and other coherency measures for multichannel data, *Geophysics,* 36, 482–497.

Neri, M., Acocella, V., and B., Behncke, (2004), The role of the Pernicana Fault System in the spreading of Mt. Etna (Italy) during the 2002–2003 eruption, *Bull. Volcanol*., 66, 417-430.

Neuberg, J., Luckett, R., Ripepe, M., and T., Braun, (1994), Highlights from a seismic broadband array on Stromboli volcano, *Geophys. Res. Lett.*, 21, 749–52.

Neuberg, J., (2000), Characteristic and causes of shallow seismicity in andesite volcanoes, *Philos. Trans. R. Soc. London*, Ser. A. 358, 1533-1546.

Neuberg, J., Tuffen, H., Collier, L., Green, D., Powell, T., and D., Dingwell (2006), The trigger mechanism of low-frequency earthquakes on Montserrat, *J. Volcanol. Geotherm. Res*., 153, 37–50

O'Connel R., J., and B., Budiansky (1978), Measures of dissipation in viscoelastic media, *Geophys. Res. Lett*., 5, 5-8.

Ohminato, T., Chouet, B.A., Dawson, P., and S., Kedar, (1998), Waveform inversion of very long period impulsive signals associated with magmatic injection beneath Kilauea Volcano, Hawaii, *J. Geophys. Res.*, 103:23839–62.

Oppenheimer, C., Bani, P., Calkins, J.A., Burton, M.R., and G.M., Sawyer, (2006), Rapid FTIR sensing of volcanic gases released by Strombolian explosions at Yasur volcano, Vanuatu, *Appl. Phys*., B 85, 453–460, DOI: 10.1007/s00340-006-2353-4.

Oshima, H. and T., Maekawa, (2001), Excitation Process of Infrasonic Waves Associated with Merapi-type Pyroclastic Flow as Revealed by A New Recording System, *Geophys. Res. Lett.*, 28, 6, 1099-1102.

Parfitt, E. (2004), A discussion of the mechanisms of explosive basaltic eruptions, *J. Volcanol. Geotherm*. *Res*., 134, 77-107.

Patanè, D., Di Grazia, G., Cannata, A., Montalto, P., and E., Boschi, (2008), Shallow magma pathway geometry at Mt. Etna volcano, *Geochem., Geophys. Geosys.*, 9, 12, doi:10.1029/2008GC002131.

Patanè, D., Aiuppa, A., Aloisi, M., Behncke, B., Cannata, A., Coltelli, M., Di Grazia, G., Gambino, S., Gurrieri, S., Mattia, M., and G., Salerno, (2013), Insights into magma and fluid transfer at Mount Etna by a multi-parametric approach: a model of the events leading to the 2011 eruptive cycle, *J. Geophys. Res.*, in press.

Patané, G., La Delfa, S., and J.C., Tanguy (2004), L'Etna e il mondo dei vulcani. Maimone editore, 285 pp.

Patrick, M.R., Harris, A.J.L., Ripepe, M., Dehn, J., Rothery, D.A., and S., Calvari, (2007), Strombolian explosive styles and source conditions: insights from thermal (FLIR) video, *Bulletin of Volcanology*, 69, 769–784.

Peacock, M.A., (1926), The petrology of Iceland. Part I. The basic tufts, Trans. Roy. Soc. Edinburgh, 55, 51–76.

Peltier, A., Finizola, A., Douillet, G.A., Brothelande, E., and E., Garaebiti, (2012), Structure of an active volcano associated with a resurgent block inferred from thermal mapping: The Yasur–Yenkahe volcanic complex (Vanuatu), *J. Volcanol. Geotherm. Res*., 243-244, 59–68.

Penmatcha, R., Ashton, P.J.N., and O., Shoham, (1996), Two-phase stratified flow splitting at a T-junction with an inclined branch arm, *International Journal of Multiphase Flow*, 22, 1105–1122.

Petersen, T., De Angelis, S., Tytgat, G., and S. McNutt, (2006), Local infrasound observations of large ash explosions at Augustine Volcano, Alaska, during January 11-28, 2006, *Geophys. Res. Lett*., Vol 33, L12303, doi: 10.1029/2006GL026491,2006.

Petersen, T., and S.R., McNutt, (2007), Seismo-acoustic signals associated with degassing explosions recorded at Shishaldin Volcano, Alaska, 2003–2004, *Bull. Volcanol.*, 69, 527–536. http://dx.doi.org/10.1007/s00445-006-0088-z.

Peterson, D.W., and R.I., Tilling, (2000), Lava flow hazard, Encyclopedia of Volcanoes, H. Sirgudsonn, Acamedic Press, Imprinted by Elseviewer, 2000, Part VII, pp957-972

Pinkerton, H., Wilson, L., and R., Macdonald, (2002), The transport and eruption of magma from volcanoes: a review, *Contemp. Phys*., 43, 197–210.

Pitt, A.M., and D.P., Hill, (1994), Long-period earthquakes in the Long Valley caldera region, eastern California, *Geophys. Res. Lett. ,* 21, 1679–1682

Pompilio, M., Trigila, R., and V., Zanon, (1998), Melting experiments on Etnean lavas: the calibration of an empirical geothermometer to estimate the eruptive temperature, *Acta Vulcanol*., 10, 1-9.

Power J.A., Stihler, S.D., White, R.A., and S.C., Moran, (2004). Observations of deep long-period (DLP) seismic events beneath Aleutian arc volcanoes; 1989–2002, *J. Volcanol. Geotherm. Res*., 138:243–66.

Raichel, D.R., (2006),The science and applications of acoustics, New York, Springer.

Ripepe, M., Poggi, P., Braun, T., and E., Gordeev, (1996), Infrasonic waves and volcanic tremor at Stromboli, *Geophys. Res. Lett.*, 23, 181-184.

Ripepe, M., Coltelli, M., Privitera, E., Gresta, S., Moretti, M., and D., Piccinini, (2001a), Seismic and infrasonic evidences for an impulsive source of the shallow volcanic tremor at Mt. Etna, Italy, *Geophys. Res. Lett.*, 28, doi:10.1029/2000GL011391.

Ripepe, M., Ciliberto, S., and M., Della Schiava, (2001b), Time constraint for modelling source dynamics of volcanic explosions at Stromboli, *J. Geophys. Res*., 106, 8713–8727, doi:10.1029/2000JB900374.

Ripepe, M., and E., Marchetti, (2002), Array tracking of infrasonic sources at Stromboli volcano, *Geophys. Res. Lett.*, 29, 2076. doi:10.1029/2002GL015452.

Ripepe, M., Marchetti, E., and G., Ulivieri, (2007), Infrasonic monitoring at Stromboli volcano during the 2003 effusive eruption; insights on the explosive and degassing process of an open conduit system, *J. Geophys. Res*., 112. doi:10.1029/2006JB004613.

Ripepe, M., Marchetti, E., Bonadonna, C., Harris, A.J.L., Pioli, L., and G., Ulivieri, (2010), Monochromatic infrasonic tremor driven by persistent degassing and convection at Villarrica Volcano, Chile, *Geophys. Res. Lett*., 37, L15303, doi:10.1029/2010GL043516.

Rossing, T., D., (2007), Handbook of Acoustic, springer editor.

Saccorotti, G., Lokmer, I., Bean, C.J. , Di Grazia, G., and D., Patanè, (2007), Analysis of sustained long-period activity at Etna Volcano, Italy, *J. Volcanol. Geotherm*. Res., 160, 340–354, doi:10.1016/j.jvolgeores.2006.10.008

Sahetapy-Engel, S.T., Harris, A.J.L., and E., Marchetti, (2008), Thermal, seismic and infrasound observations of persistent explosive activity and conduit dynamics at Santiaguito lava dome, Guatemala, *J. Volcanol. Geotherm. Res.*, 173, 1–14, doi:10.1016/j.jvolgeores.2007.11.026.

Sanchez, J.J., and S.R., McNutt, (2004), Intermediate-term declines in seismicity at Mt. Wrangell and Mt. Veniaminof volcanoes, Alaska, following the November 3, 2002, Mw 7.9 Denali Fault earthquake, *Bull. Seis. Soc. Amer.*, 94, 6B, S370-S383, 2004.

Schaff, D., Bokelmann, G., Ellsworth, W., Zanzerkia, E., Waldhauser, F., and G., Beroza, (2004), Optimizing correlation techniques for improved earthquake location, *Bull. Seis. Soc. Amer*, 94, 705–721.

Schiavi, F, Kobayashi, K., Moriguti, T., Nakamura, E., Pompilio, M., Tiepolo, M., and R., Vannucci, (2010), Degassing, crystallization and eruption dynamics at Stromboli: trace element and lithium isotopic evidence from 2003 ashes, *Contrib Mineral Petrol*, 159, 541–561, doi:10.1007/s00410-009-0441-2.

Schick, R., and M., Riuscetti, (1973), An analysis of volcanic tremors at South Italian volcanoes, *Z. Geophysik*, 39, 247–262.

Sciotto, M., Cannata, A., Di Grazia, G., Gresta, S., Privitera, E. and L., Spina, (2011), Seismoacoustic investigations of paroxysmal activity at Mt. Etna volcano: New insights into the 16 November 2006 eruption, *J. Geophys. Res*., 116, doi:10.1029/2010JB008138.

Sciotto, M., Cannata, A., Gresta, S., Privitera, E., and L., Spina, (2013), Seismic and Infrasound Signals at Mt. Etna: Modelling of North-East Crater Conduit and its Relation with the Feeding Cannata, A., Montalto, P., Privitera, E., Russo, G., and S., Gresta, (2009a), Tracking eruptive phenomena by infrasound: May 13, 2008 eruption at Mt. Etna, *Geophys. Res. Lett*., 36, L05304, doi:10.1029/2008GL036738.

Seidl, D., Schick, R., and M., Riuscetti, (1981), Volcanic tremors at Etna: a model for hydraulic origin, *Bull. Volcanol*., 44, 43-56.

Smith, S.V., (1999), *The scientists and engineer' s guide to signal processing*, II edizione.

Spadaro, F.R., Lefèvre, R.A., and P., Ausset, (2002), Experimental rapid alteration of basaltic glass: Implications for the origins of atmospheric particulates, *Geology*, 30, 671–674.

Spampinato, L., Calvari, S., Oppenheimer, C., and L., Lodato, (2008), Shallow magma transport for the 2002–3 Etna eruption inferred from thermal infrared surveys, *J. Volcanol. Geotherm. Res*., 177, 301–312.

Sparks, R.S.J. (2003), Forecasting volcanic eruptions. *Earth Planet. Sci. Lett*., 210, 1-15.

Spera, F.J., (2000), Physical properties of magma. In: Sigurdsson, H. (Ed.), Encyclopedia of Volcanoes. Academic Press, San Diego, Calif, pp. 171–190.

St Lawrence, W.F., and A., Qamar, (1979), Hydraulic transients: A seismic source in volcanoes and glaciers. *Science,* 203, 654-656.

Stix, J., and H., Gaonach'h, (2000), Gas, plume and thermal monitoring, Encyclopedia of Volcanoes, H. Sirgudsonn, Acamedic Press, Imprinted by Elseviewer, 2000, Part VIII, pp 1141-1164.

Strachey, R., (1888), On the Air Waves and Sounds Caused by the Eruption of Krakatoa in August, 1883. In: G.J. Symons (Ed.), The Eruption of Krakatau and Subsequent Phenomena, Report of the Krakatau Committee of the Royal Society, Trubner & Co, London (1888), pp. 57–88

Simkin, T., Fiske, R.S.(Eds.), Krakatau 1883 (published 1983). Smithsonian Institution Press, pp. 368-374.

Taddeucci, J., Pompilio, M. and P., Scarlato (2002), Monitoring the explosive activity of the July–August 2001 eruption of Mt. Etna (Italy) by ash characterization, *Geophys. Res. Lett*., *29 (8),* 1029–1032, 1230, doi:10.1029/2001GL014372.

Taddeucci, J., Pompilio, M., and P., Scarlato (2004), Conduit processes during the July–August 2001 explosive activity of Mt. Etna (Italy): inferences from glass chemistry and crystal size distribution of ash particles, *J. Volcanol. Geotherm*. Res. 137, 33–54.

Taylor, F.W., Bevis, M.G., Schutz, B.E., Kuang, D., Recy, J. , Calmant, S., Charley, D., Regnier, M., Perin, B., Jackson, M., and C., Reichenfeld, (1995), Geodetic measurements of convergence at the New Hebrides island arc indicate arc fragmentation caused by an impinging aseismic ridge, *Geology*, November, vol.23, pp 1011-1014.

Thorseth, I.H., Furnes, H., and O., Tumyr, (1990), A textural and chemical study of Icelandic palagonite of varied composition and its bearing on the mechanism of the glass-palagonite transformation, *Geochimica and Cosmochimica Acta*, 55, 731–749.

Uhira, K., and M., Takeo, (1994), The source of explosive eruptions of Sakurajima volcano, *Japan. J. Geophys. Res.,* 99 (B9), 17775– 17789.

Valentine, G.A., and K.R., Groves, (1996), Entrainment of country rock during basaltic eruptions of the Lucero volcanic field, New Mexico, *Journal of Geology*, 104, 71–90.

Varley, N., Arámbula-Mendoza, R., Reyes-Dávila, G., Stevenson, J., and J., Harwood (2010), Long-period seismicity during magma movement at Volcán de Colima, *Bull. Volcanol*., 72, 1093–1107, doi:10.1007/s00445-010-0390-7.

Vergniolle, S., and G., Brandeis, (1996), Strombolian explosions: a large bubble breaking at the surface of a lava column as a source of sound, *J. Geophys. Res*., 101. doi:10.1029/96JB01178.

Vergniolle, S., Brandeis, G., and J.C. Mareschal, (1996), Strombolian explosions: Eruption dynamics determined from acoustic measurements, *J. Geophys. Res*., 101, 20449–20466, doi:10.1029/96JB01925.

Vergniolle, S. and J., Caplan-Auerbach, (2004) Acoustic measurements of the 1999 basaltic eruption of Shishaldin volcano, Alaska 2. Precursor to the Subplinian phase, *J. Volcanol. Geotherm. Res*., 137, 135-151

Vergniolle, S., Boichu, M., and J., Caplan-Auerbach, (2004) Acoustic measurements of the 1999 basaltic eruption of Shishaldin volcano, Alaska 1. Origin of Strombolian activity*, J. Volcanol. Geotherm. Res*., 137, 109-134

Vergniolle, S., and M., Ripepe, (2008), From Strombolian explosions to fire fountains at Etna Volcano (Italy): What do we learn by acoustic measurement? In: Lane, S.J., Gilbert, J.S. (Eds.), Fluid motions in volcanic conduits: a source of seismic and acoustic signals: *Geol. Soc. Spec. Publ*., 307, pp. 103–124.

Waite, G.P, and R.B., Smith, (2004), Seismotectonics and stress field of the Yellowstone volcanic plateau from earthquake first motions and other indicators, *J. Geophys. Res*., 109:10.1029/2003JB002675.

Wassermann, J., (2009) , Volcano Seismology. In: Bormann, P. (Ed.), New manual of seismological observatory practice. IASPEI 42 pp. doi:10.2312/GFZ.NMSOP_r1_ch13.

Witham, F., and E.W., Llewellin, (2006), Stability of lava lakes*, J. Volcanol. Geotherm. Res*., 158, 321–332.

White, R., (1996), Precursory deep long-period earthquakes at Mount Pinatubo: Spatiotemporal link to a basalt trigger. In: Newhall CG and Punongbayan RS (eds.) Fire and Mud: Eruptions and Lahars of Mount Pinatubo, Philippines, pp. 307–327. Seattle: University of Washington Press.

Withers, M., Aster, R., Young, C., Beiriger, J., Harris, M., Moore, S., and J., Trujillo, (1998), A comparison of select trigger algorithms for automated global seismic phase and event detection, *Bull. Seismol. Soc. Am*., 88, 95-106.

Yamamoto, K., and K., Tagaki, (1992), Expressions of Maekawa's chart for computation, *Appl. Acoustic*, 37, 75-82.

Zielinski, C., Vergniolle, S., Bani, P., Lardy, M., Le Pichon, A., Ponceau, D., Gallois, F., Herry, P., Todman, S., E., Garaeibiti, (2010), The potential of continuous near-field recording of infrasound produced by volcanoes in Vanuatu for probing the state of the atmosphere, *Geophysical Research Abstract*, Vol. 12, EGU2010-1055, 2010, EGU General Assembly 2010

Zobin ,V.,M., (2012), Introduction to volcano seismology,Second Edition 2012, Elseviewer.